



HAL
open science

MERCURY In-flight calibration of the PHEBUS UV instrument and Monte Carlo modelling of the hydrogen exosphere

Mea Simon Wedlund

► **To cite this version:**

Mea Simon Wedlund. MERCURY In-flight calibration of the PHEBUS UV instrument and Monte Carlo modelling of the hydrogen exosphere. Planetology. Université Pierre et Marie Curie - Paris VI, 2011. English. NNT: 2011PA066114 . tel-00667491

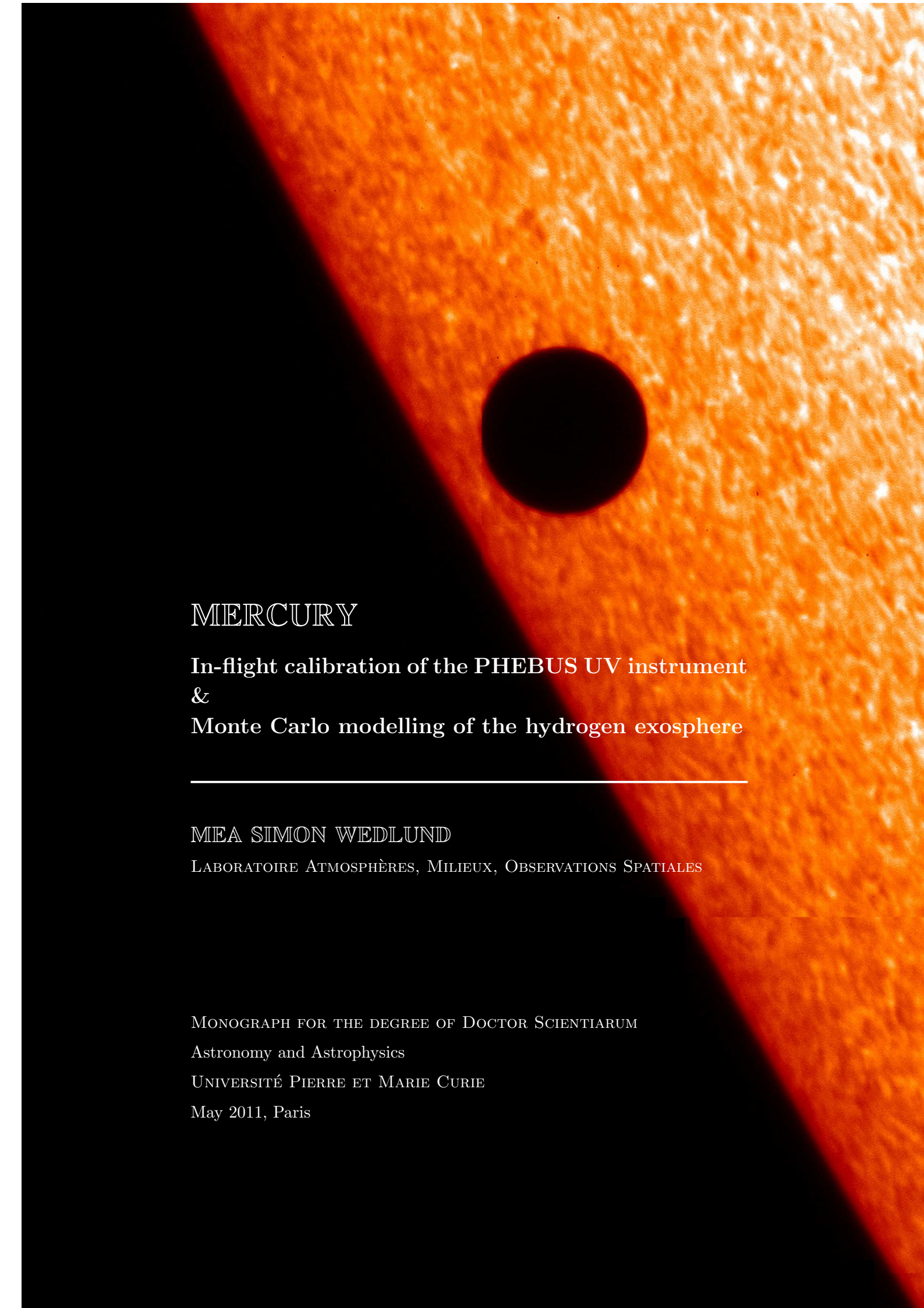
HAL Id: tel-00667491

<https://theses.hal.science/tel-00667491>

Submitted on 7 Feb 2012

HAL is a multi-disciplinary open access archive for the deposit and dissemination of scientific research documents, whether they are published or not. The documents may come from teaching and research institutions in France or abroad, or from public or private research centers.

L'archive ouverte pluridisciplinaire **HAL**, est destinée au dépôt et à la diffusion de documents scientifiques de niveau recherche, publiés ou non, émanant des établissements d'enseignement et de recherche français ou étrangers, des laboratoires publics ou privés.



MERCURY

In-flight calibration of the PHEBUS UV instrument
&
Monte Carlo modelling of the hydrogen exosphere

MEA SIMON WEDLUND

LABORATOIRE ATMOSPHÈRES, MILIEUX, OBSERVATIONS SPATIALES

MONOGRAPH FOR THE DEGREE OF DOCTOR SCIENTIARUM

Astronomy and Astrophysics

UNIVERSITÉ PIERRE ET MARIE CURIE

May 2011, Paris

Transit of Mercury on 8 November 2006 captured by the Solar Optical Telescope on board the Japanese solar satellite SOLAR-B/Hinode, just after it crossed the solar limb (Image JAXA/NASA/PPARC)

ASTRONOMY AND ASTROPHYSICS

MONOGRAPH FOR THE DEGREE OF
DOCTOR SCIENTIARUM
UNIVERSITÉ PIERRE ET MARIE CURIE

MERCURY

**In-flight calibration of the PHEBUS UV
instrument**

&

Monte Carlo modelling of the hydrogen exosphere

MEA SIMON WEDLUND

LABORATOIRE ATMOSPHÈRES, MILIEUX, OBSERVATIONS SPATIALES

Publicly presented and defended

3 May 2011

JURY

Dr. Bruno Sicardy	LESIA, Meudon	President of Jury
Dr. Helmut Lammer	IWF, Graz	Referee
Dr. Iannis Dandouras	CESR, Toulouse	Referee
Dr. Gabriele Cremonese	INAF, Padova	Examiner
Dr. Mathieu Barthélemy	LPG, Grenoble	Examiner
Dr. Eric Chassefière	IDES, Orsay	Supervisor
Dr. François Leblanc	LATMOS, Paris	Advisor

This thesis was in collaboration with Centre National de la Recherche Scientifique (CNRS), financed by Centre National d'Études Spatiales (CNES), prepared at Service d'Aéronomie (SA), Laboratoire Atmosphères, Milieux, Observations Spatiales (LATMOS) and Université Pierre et Marie Curie (UPMC), Paris, France.



ASTRONOMIE ET ASTROPHYSIQUE

THÈSE POUR OBTENIR LE GRADE DE
DOCTEUR
DE L'UNIVERSITÉ PIERRE ET MARIE CURIE

MERCURE
Calibration en vol de l'instrument UV PHEBUS
&
Modélisation Monte Carlo de l'exosphère
d'hydrogène

MEA SIMON WEDLUND
LABORATOIRE ATMOSPHÈRES, MILIEUX, OBSERVATIONS SPATIALES

Présentée et soutenue publiquement le

3 Mai 2011

JURY

Dr. Bruno Sicardy	LESIA, Meudon	Président du Jury
Dr. Helmut Lammer	IWF, Graz	Rapporteur
Dr. Iannis Dandouras	CESR, Toulouse	Rapporteur
Dr. Gabriele Cremonese	INAF, Padova	Examineur
Dr. Mathieu Barthélemy	LPG, Grenoble	Examineur
Dr. Eric Chassefière	IDES, Orsay	Directeur de Thèse
Dr. François Leblanc	LATMOS, Paris	Superviseur

Abstract

A unique feature of Mercury's space environment is its strongly coupled surface-exosphere-magnetosphere-solar wind system, which can be remotely monitored by space missions such as Mariner 10, MESSENGER and soon BepiColombo and by ground-based observatories. Mercury's exosphere is a very complex medium with only a few species detected so far, including atomic hydrogen. H has only been detected once by Mariner 10 in 1974-1975 and represents a tracer of the interaction between the solar wind and Mercury.

The PHEBUS instrument onboard the BepiColombo ESA/JAXA mission to Mercury is a dual-channel EUV-FUV spectrometer capable of detecting faint emissions including H I Lyman- α at 121.6 nm. The first part of this thesis focuses on the radiometric modelling and simulation of the optical return of PHEBUS. To prepare for in-flight and orbit spectral calibrations, a set of reference stars is determined and evaluated to match the resolution and spectral range of the detector. Predictions on the possibility of detection of a wide range of emission lines in space and in Mercury's exosphere are given (science performance).

PHEBUS is based on SPICAV, the UV spectrometer onboard Venus Express and can use similar techniques to perform the relevant calibrations. Therefore, a study of the star occultation events of SPICAV is performed in the second part of this thesis. The stars' spectra are extracted, analysed and convoluted with the instrument function for possibility of future use with PHEBUS. The results are stored in the calibration database for the "Cross-calibration of past FUV experiments" workgroup of ISSI.

In parallel to the development of new dedicated instruments, such as PHEBUS with high sensitivity and spectral resolution, state-of-the-art simulations of the exosphere of Mercury are also needed. In the third part of this thesis the 3D Monte Carlo hydrogen model SPERO is constructed. SPERO is the first fully consistent 3D exospheric model of hydrogen at Mercury, taking into account source and loss mechanisms such as thermal desorption, photoionisation and solar radiation pressure. Thermal desorption is assumed to be the dominant source of exospheric hydrogen. Surface densities as well as exospheric densities, temperatures and velocities are computed up to 8 Mercury radii. A sensitivity study is carried out highlighting the uncertainties in the source and loss mechanisms, and resulting in a day/night density and temperature asymmetry. Using the computed densities in a radiative transfer model makes it possible to compare with the Mariner 10 Lyman- α emission data and later on possibly the hydrogen data return of the MASCS instrument onboard NASA MESSENGER.

Résumé

Une caractéristique unique de l'environnement spatial de Mercure est le fort couplage qui existe entre la surface, l'exosphère, la magnétosphère et le vent solaire. Ce système peut être étudié par des méthodes de télédétection embarquées sur les missions spatiales telles que Mariner 10, MESSENGER et bientôt BepiColombo, ainsi que par les observatoires au sol.

L'exosphère de Mercure est un milieu complexe avec seulement quelques espèces détectées jusqu'ici, dont l'hydrogène atomique H. H a seulement été détecté une fois par la sonde Mariner 10 en 1974-1975 et représente un traceur de l'interaction entre le vent solaire et la planète Mercure.

L'instrument PHEBUS à bord de la mission ESA/JAXA BepiColombo vers Mercure est un spectromètre double canal EUV-FUV capable de détecter les émissions les plus faibles, comme H I Lyman- α à 121.6 nm. La première partie de cette thèse se concentre sur la modélisation radiométrique et la simulation des performances de PHEBUS. Pour préparer la calibration spectrale en vol et pendant la phase orbitale, un ensemble d'étoiles de référence est déterminé et évalué pour tirer partie au mieux de la résolution et du domaine spectral du détecteur. Des prévisions sur la possibilité de détection des raies d'émission exosphériques sont également données (science performance).

Comme PHEBUS est basé sur SPICAV, le spectromètre UV de Venus Express, des techniques semblables de calibration spectrale peuvent être utilisées. Une étude des occultations stellaire de SPICAV est réalisée dans la deuxième partie de cette thèse. Les spectres des étoiles sont extraits, analysés et convolués avec la fonction instrumentale en vue de préparer les futures observations de PHEBUS. Les résultats sont disponibles dans la base de données de calibration du groupe de travail à l'ISSI *Cross-calibration of past FUV experiments*.

En parallèle aux nouveaux instruments de grande sensibilité et à haute résolution spectrale, comme PHEBUS, le développement de simulations numériques est nécessaire à la compréhension de l'exosphère de Mercure. La troisième partie de cette thèse présente le modèle SPERO, premier modèle auto-cohérent 3D Monte Carlo dédié à l'hydrogène exosphérique de Mercure, prenant en compte toutes les sources et les pertes, tels que la désorption thermique, la photoionisation ou la pression de radiation solaire. La désorption thermique est par hypothèse la source dominante d'hydrogène exosphérique. La densité surfacique ainsi que les densités, températures et vitesses exosphériques sont calculées jusqu'à 8 rayons mercuriens. Une étude de sensibilité est effectuée en se basant sur les incertitudes dans les mécanismes de source et de perte, donnant lieu à des asymétries jour/nuit en densité et en température. En utilisant les densités calculées dans un modèle de transfert radiatif, il est possible de comparer les sorties de SPERO avec les données d'émission Lyman- α de Mariner 10, et d'anticiper le retour de données hydrogène grâce à l'instrument MASCS embarqué sur la mission MESSENGER de la NASA.

For URANIE...

Acknowledgments

"As for yourself, Uranie continued, know that knowledge is the surest foundation of intellectual worth; seek neither poverty nor riches; keep yourself free from ambition, as from every other species of bondage. Be independent; independence is the chiefest of blessings and the first condition of happiness."

In the course of this thesis I have had one supervisor, two advisors, two lab affiliations, worked on four separate projects and learnt a new language¹. At times it was, mildly put, confusing, disturbing and extremely entertaining.

And sometimes I felt like I was closed into a small black bag without any hope of finding my way out...

... but when it was as darkest I could always rely on the thin red thread guiding me: the connection to the planet Mercury. No matter how distant the projects seemed to be from this subject, I always found the connection I needed to my favourite planet.

This thesis is the accumulation of that.

*

All along I was working on this thesis I frequently got the question: "*Why do you like Mercury so much?*"

My reply then was: "*Because it differs from the rest of the planets in the most extreme ways and it is closer to the Sun than anything we know. We practically know nothing of it.... It wasn't even until two years ago that we had enough photographs to know what the entire planet looked like. Isn't that amazing?*"

Today my answer is: "*Because it is just like me.*"

¹French

It is passionately burning² on one side and frostily cold³ on the other, it has the weirdest path⁴ through life, of all planets, and it is just as slow⁵ as me.

Despite all this, it is also the planet I find most harmonious with its beautiful 3/2 ratio around the Sun and the heavily scarred and roasted surface.

It is as if it has gone through a lot for a very long time and finally found its place in the Universe and now, at last, it can lazily enjoy the warmth of the Sun and continuously annoy the Earth-bound scientist with its weirdities, to its own pleasure.

Yes, Mercury is extreme, mostly unexplored and very, very appealing. For as long as humans have looked to the sky, Mercury, despite its closeness to Earth, has always been neglected. This is understandable since it is drowned in the glare of the Sun, but today we do not have that problem anymore. Let us use the advantage technology can give us today, that the ancient astronomers didn't have.

Let's explore and learn more, after all, isn't that what life is all about?

*

Thanks

First I would like to give my everlasting thanks to Prof. David Milstead at Stockholm University, whom without I would not have reached this far, for several reasons:

- He is unbearably clever in solving quantum mechanical problems, making me opening my mind to the endless possibilities of solutions.
- He is an everlasting source of positive energy as radiant as a small star.
- He was there for me when I needed him most. His reply when I asked him to be my reference for applying to this PhD: "*I would be honoured!*"

*

In chronological order from my arrival in France

Florence, Frédéric and Camille,
who kindly housed a complete stranger until I could find an apartment

*

Verrières-le-Buisson

Eric Chassefière,
who kindly gave me the chance to take on this PhD and who has supported me in a distance

²surface temperature of 600 K

³surface temperature of 100 K

⁴most elliptic orbit

⁵in rotation

Marie-Sophie Clerc,
the first person to welcome me to France and, while in Verrières-le-Buisson, was my
constant source of help and advice

Cécile Takacs,
who never hesitated to help me find obscure literature no matter how difficult

Jean-Luc Maria,
who welcomed me in the PHEBUS team straight away and helped, without holding back

The entire PHEBUS team of engineers: Pierre-Olivier, Jean-Baptiste, Jean-François,
Sébastien and especially Nicolas Rouanet, who kindly shared his programs and knowledge
without restraint

Eric Quémerais,
who showed me true French candor when he thought I needed it as most

Rosine Lallement,
who kindly helped me with star spectra catalogs

Everyone else in Verrières-le-Buisson who has crossed my path...

*

Natalia Vale Asari,
*"But it struck me to say, while so far away, You are with me today.
You are here are in my head, in my heart...Dear friends"*

Kazuo Yoshioka and Go Murakami,
tomodachi de ite kurete, arigatou gozaimasu

*

Jussieu

François Leblanc,
who gracefully accepted to be my advisor when no one else would

Maryse Grenier,
who fought and succeeded to help me get my Carte Vitale, after 3 years of administration

Christophe Merlet, my office mate in Jussieu,
who bravely withstood my constant comings and goings and my very loud music

Olivier Thauvin,
who managed to transform my mediocre laptop to a high-performance modelling tool,
thus making my job much, much easier

Ronan Modolo,
who spent hours debugging and programming with me

Jean-Yves Chaufray,
who took care of the entire radiative transfer for me when time became too short

Everyone else in Jussieu who has crossed my path...

My PhD defense Jury,

Dr. Bruno Sicardy
Dr. Helmut Lammer
Dr. Iannis Dandouras
Dr. Gabriele Cremonese
Dr. Mathieu Barthélemy,
for taking the time to read, correct and question my report and science

I would also like to thank them for graciously sitting through my 3-hour long presentation, caused by my poor health - it meant the world to me.

*

Honorary mention

Dr. Patrick Boissé,
who put in a great effort to steer my thesis when it seemed to take a wrong path

Jean Lilensten,
who, in his love and passion for science, became my unsuspecting mentor

Hervé Lamy,
who, generously and repeatedly, offered up his office so I had a place where I could finish my thesis

*

My mother, father and brother,
who are always there to remind me of my Swedish heritage, when I sometimes forget it

My mother-in-law, father-in-law and sister-in-law,
who are always there to remind me of my husband's French heritage, when I sometimes forget it

*

Last on my list, but first in my heart,
my beloved husband Cyril,
You are Uranie, to my Spero...

*

For I am Ta-Meaut, the Triumphant!

footnote

One of my childhood dreams was realised when I came to Paris and got to visit Observatoire de Paris.

This is where Camille Flammarion studied to become an astronomer and this is where the story in his book "Uranie" takes place.

I discovered "Uranie" in my father's library, when I was around 12 years old. It was a very small, old book that really wasn't impressive at all, but the content was.

The book tells the story of a young astronomer's voyage through the solar system with his guide Uranie, the muse of astronomy.

The book saturated my mind with the endless possibilities and the fervent wish to do science.

So I saturated this thesis with "Uranie".

My Fortran simulation is named after one of the main characters in Uranie, Georges Spero, a genius in science that completely lacked social skills but made marvelous discoveries, and all the quotes in this thesis are from "Uranie".

Contents

1	Introduction	1
1.0.1	Layout of thesis	3
2	Mercury: History and context	5
2.1	The Planet Mercury	5
2.1.1	Orbital parameters	5
2.1.2	Internal structure, the magnetic field and magnetosphere	8
2.1.3	Surface	9
2.1.4	Exosphere	10
2.2	History and science: Ancient	13
2.3	Science: In modern times	16
2.3.1	Early Optical observations	16
2.3.2	Modern ground-based observations	19
2.3.3	Missions	22
2.3.4	Modelling the exosphere of Mercury: a brief history	27
2.4	Summary	30
3	SPICAV: Differentiate ultraviolet signatures	31
3.1	Stellar occultations and calibrations of the SPICAM and SPICAV instruments	31
3.2	The UV spectrometers on board the Mars Express and the Venus Express missions	32
3.2.1	General overview of the instruments	32
3.2.2	SPICAM and SPICAV datasets	34
3.3	Star calibration	41
3.3.1	Theoretical background	41
3.3.2	Observation of intensity decrease in high wavelengths	50
3.4	Summary	55
4	PHEBUS: Instrumentation for a harsh environment	57
4.1	Radiometric Modelling and Scientific Performance of PHEBUS	57
4.2	Theoretical background	58
4.2.1	Instrument	58
4.2.2	Objectives and demands on the instrument	60
4.2.3	Sources	60
4.2.4	Optical layout	61
4.2.5	Photometric assessment and spectral resolution	69
4.3	Theoretical Results	73
4.3.1	Radiometric modelling of star spectra	73
4.3.2	In-flight calibrations of stars	74
4.4	Summary	74

5	Modelling Mercury's hydrogen exosphere	77
5.1	Introduction	77
5.2	SECTION I: The physics behind	85
5.2.1	Definitions and basic exospheric theory	85
5.2.2	Mechanisms of ejection from the surface: Maxwell-Boltzmann distributions	86
5.2.3	Temperature mapping	88
5.2.4	Ballistic motion of particles in the exosphere and external conditions	89
5.2.5	Sources of hydrogen at Mercury: Thermal processes	91
5.2.6	Sinks of hydrogen at Mercury: Ionisation	99
5.2.7	Deriving emission line brightness: radiative transfer and optical thickness (<i>with Jean-Yves Chaufray</i>)	100
5.3	SECTION II: Monte Carlo model	103
5.3.1	Coordinate system	103
5.3.2	Flow of program	103
5.3.3	Time evolution of the particle	108
5.3.4	Euler solution to ballistic motion	109
5.3.5	Outputs	113
5.4	Validation	114
5.4.1	Convergence criteria	114
5.4.2	Chamberlain	114
5.4.3	Thermalisation at surface	120
5.5	Sensitivity study	121
5.5.1	MB and MBF Velocity distribution functions	122
5.5.2	Accommodation coefficient	129
5.5.3	Source regions	129
5.5.4	Comparison to Mariner 10 data	132
5.5.5	Prediction of expected PHEBUS signal	139
5.6	Summary	142
6	Conclusion	145
	Appendices	147
A	SPICAM star table of 39 stars with flux above 800 R at 164 nm	147
B	PHEBUS radiometric simulation brightness of emission lines	149
C	SPICAV star table of 183 stars with flux above 60 R at 164 nm	157
D	Short-term variations of Mercury's sodium Na exosphere observed with very high spectral resolution	163
	Bibliography	169

Chapter 1

Introduction

”For us who seek the truth without pre-conceived ideas, and without having a theory to support, it seems to us that the principle of matter remains as much unknown as the principle of force, the visible universe not being at all what it appears to our senses. ”

The planet Mercury is the first planet from the Sun, situated around one third of the distance between the Sun and the Earth, making it a privileged witness of solar-planetary interactions.

It also occupies a unique niche in the Solar System with its huge ground temperature amplitudes spanning hundreds of degrees (from 100 K to 600 K) as it faces the scorching whims of the Sun, with its weak but appreciable magnetic field for such a small body, and its tenuous exosphere bounded to the surface, made mostly of neutral atoms.

In this respect the Mercurian environment is a marvelous in-situ laboratory for complex plasma physics, involving dust, neutral-ion particle interactions and acceleration processes.

Different tools can be used to study Mercury as a planet and probe its vicinity:

- Remote sensing: ground-based observatories such as the solar telescope THEMIS (Tenerife)
- In-situ observations: past missions such as Mariner 10, current space missions such as MESSENGER
- Models or physical simulations of the 3D neutral/ion environment, including Monte Carlo simulations of the ballistic motion of a great number of particles

All three tools working in synergy are necessary to gain the most detailed understanding: observations show which species and mechanisms are present, while models try to explain them with state-of-the-art physical approaches. In turn, models can predict many observables that can be compared with new (or old) observations.

It is not surprising that since the advent of modern techniques (spectroscopy, radars, high-resolution imagers), Mercury has been unveiling more and more of its hidden characteristics, despite the fact that after more than 50 years of investigations, it remains one of the least known planetary bodies in the Solar System. For instance, the very

location of Mercury close to the Sun and the difficulty to observe it directly has impeded a more systematic examination from ground-based observatories. Only since the 1980s have they become sufficiently sensitive and adapted to the study of Mercury's exosphere.

This developmental state of flow in science history, described by the philosopher of science Thomas S. Kuhn, is what Mercury science has been experiencing for the last 50 years, with many outstanding discoveries and new theories that have to be tested against measurements and coming from many different science groups. These theories will eventually lead to a paradigm, characterised by scientific consensus, thanks to the science outputs of current and incoming efforts such as the ESA/JAXA BepiColombo mission.

One of the main science problematics in today's Mercury science concerns the formation, sustaining and evolution of the tenuous atmosphere of the planet, called the exosphere, as the planet is not large enough to retain by gravity a permanent thick atmosphere. From Mariner 10 in the 1970s, MESSENGER since 2008 and ground-based observations, the species that have been detected include H, He, O, Na, K, Ca and Mg.

Generally speaking, an exosphere is the uppermost layer of the atmosphere of a planet, where the particle density is so low that the particles no longer collide with each other and some are moving fast enough to reach the escape velocity and escape to space.

In the case of Mercury, the exosphere starts at the surface, which gives rise to many original and peculiar processes, which can be classified into two categories:

- release from the surface: thermal, photon/electron desorption, meteoroid impact, solar wind sputtering
- depletion: Jeans escape, photoionisation, charge exchange or solar radiation pressure

These processes depend on the location of the particle on the planet, whether it is on the cool 100-K nightside or the hot 600-K dayside.

Hydrogen

One of the first species discovered in the exosphere of Mercury was atomic hydrogen H, through its characteristic emission at 121.6 nm, called Lyman- α . Since its discovery very few studies have been performed and even less observations are available. Analogy with the Moon has been used with much success and has managed to constrain the mechanisms at the origin of the release and loss of hydrogen around Mercury, namely (1) thermal desorption, (2) Jeans escape, (3) photoionisation and (4) solar radiation pressure.

The reason hydrogen is interesting is that not only is it one of the fourth most abundant species on Mercury, although not the most bright, but it is also an "end-member"; it is the species that is most extreme in every way because of its very low mass and its high velocity mobility in the exosphere. Using comparisons with the Moon it is also obvious that despite the similarities between the Moon and Mercury hydrogen does not react the same way on both these planets.

Also, despite being one of the first species detected on Mercury by Mariner 10, together with helium, no real attempts to model hydrogen have been done so far. In the tenuous exosphere of Mercury, all species are important for a complete understanding of its mechanisms. Hydrogen is no exception.

1.0.1 Layout of thesis

This thesis deals with two aspects of hydrogen at Mercury, observational and theoretical, with the preparation of the UV spectrometer PHEBUS on board BepiColombo and the modelling of the neutral hydrogen exosphere.

Chapter 2 is intended to be an overview of Mercury's science through history, browsing through its orbital characteristics and discussing the main scientific areas of investigation: surface, magnetosphere and magnetic environment, exosphere. A specific focus is put on recent exospheric studies, both observational and theoretical, dealing with other species than hydrogen. This chapter presents the background science necessary for the next chapters and briefly discusses the science objectives of the Mariner 10, MESSENGER and BepiColombo missions, as well as the use of the solar telescope THEMIS (situated in Tenerife) for observing the exosphere of Mercury.

Chapter 3 is aimed at setting up an in-flight calibration procedure for PHEBUS, based on that of the SPICAM/SPICAV UV spectrometers on board ESA Mars Express and Venus Express. As PHEBUS primary design is based on SPICAM/SPICAV, star calibration is performed from two stars chosen in the SPICAV star catalogue and tested for assessing the sensitivity of PHEBUS and the plausibility of in-flight/in-orbit calibrations. The list of stars, their spectral type and fluxes are presented at the end of the chapter.

Chapter 4 introduces the UV spectrometer PHEBUS (Probing of Hermean Exosphere By Ultraviolet Spectroscopy) on board BepiColombo, and the radiometric modelling which is used to predict the expected science performance of the instrument, developed in close collaboration by N. Rouanet. A list of emissions and their brightness is provided, which proves that PHEBUS with both high spectral resolution and high sensitivity will be able to measure all the existing exospheric emissions and more, including hydrogen for which the wavelength range of the instrument has especially been chosen.

Chapter 5 presents the theoretical follow-up of the PHEBUS in-flight calibration. This chapter is a detailed description of the model SPERO for hydrogen neutral atoms that was developed in the last part of this thesis. SPERO (Simulation and Parsing of Exospheric neutRal atOms) is a full 3-D Monte Carlo numerical model that calculates the ballistic orbits of hydrogen particles released from the surface of Mercury up until 8 Mercury radii.

After an historical report of previous studies on hydrogen, the classical theory of exospheres is discussed and presented. All theoretical release and loss processes are also discussed in the case of atomic hydrogen. The development of the Monte Carlo model, with the different algorithms and assumptions concerning the distribution function of the ejecta, is also thoroughly described, while a sensitivity study of all known parameters is presented.

Finally, thanks to the use of radiative transfer model of J.-Y. Chaufray (LMD), key notions are deducted and a comparison to the Mariner 10 original hydrogen Lyman- α data is possible and shown. Preliminary results concerning the dusk-dawn asymmetry and predictions are also highlighted which could be confirmed either by data from the ongoing MESSENGER mission (MASCS) or the future BepiColombo mission to Mercury.

An application to PHEBUS is also shown, with hydrogen emissions applied to the instrument function giving the possible count rates of the EUV detector.

THEMIS observation

In the scope of studying the exosphere of Mercury, an observation campaign dedicated to the sodium exosphere, was carried out at the THEMIS observatory in Tenerife. This work lead to the publication in *Geophysical Research Letters* of an article entitled "Short-term variations of Mercury's sodium Na exosphere observed with very high spectral resolution", which can be found in Appendix D.

*In this manuscript, the subsolar point designates the point on the surface of the planet facing the Sun at zenith, thus on the dayside of the planet. To mirror this expression the opposite point on the surface of the Sun and directly facing the interplanetary space on the nightside of the planet is then referred to as the **antisolar**. However at some instances I do refer to this point as **subspace**, since it was a term that somehow fitted the description very well.*

Chapter 2

Mercury: History and context

"From this it results that the histories of all the worlds are traveling through space without disappearing altogether, and that all the events of the past are present and live forever in the bosom of the Infinite."

2.1 The Planet Mercury

Mercury is the small, rocky planet located closest to the Sun in the solar system and the smallest of the terrestrial planets, Figure 2.1. Its main physical characteristics are summarised in Table 2.1 and compared to those of the Moon and Earth. In appearance Mercury resembles the Moon by its size, its cratered surface, the lack of satellites¹ and the absence of a substantial atmosphere, see Figure 2.2.

2.1.1 Orbital parameters

Mercury is in many ways the most extreme of all planets. Its orbit is the most eccentric with a value of 0.21 making it have a large variety in distances from the Sun, from 46×10^6 km at aphelion to 70×10^6 km at perihelion. This causes the solar flux received by the planet to change by more than a factor of two throughout a Mercurian year.

The orbital tilt to the ecliptic is 7 degrees, making it possible to see transits of Mercury across the Sun only 13 to 14 times per century from Earth. The last observed transit occurred on 08 November 2006, see Figure 2.3, while the next one will take place on 09 May 2016.

¹Although it is not common that satellites have satellites due to the instabilities they might infer, it is not impossible. For example, there is proof that the satellite Rhea has had shepherd moons in the past (Jones et al., 2008).

Physical parameters	Mercury	Moon	Earth
Mean radius (km)	2439.7	1737.1	6371.0
Mass (kg)	$3.30 \cdot 10^{23}$	$7.35 \cdot 10^{22}$	$5.97 \cdot 10^{24}$
Mean density (g cm^{-3})	5.43	3.34	5.51
Equat. surf. gravity (m s^{-2})	3.70 (0.38 <i>g</i>)	1.62 (0.16 <i>g</i>)	9.81 (1 <i>g</i>)
Escape velocity (km s^{-1})	4.25	2.38	11.18
Obliquity/axial tilt ($^\circ$)	0.02	6.68	23.44
Sidereal rot. period (days)	58.6	27.3	1
Rotation velocity (m s^{-1})	3.02	4.63	465.1
Albedo ^a	0.142	0.136	0.367
Aphelion (AU) ^b	0.47	–	1.02
Perihelion (AU) ^b	0.31	–	0.98
Eccentricity	0.21	0.05	0.02
Orbital period (days)	87.97	27.32	365.27
Orbital speed (km s^{-1})	47.87	1.02	29.78
Inclination to ecliptic ($^\circ$)	7.00	5.41	0
Main atmospheric constit. <i>trace</i>	Na,H ₂ ,He H,K,Ca,Mg,O	Ne,He,Ar CH ₄ ,CO ₂	N ₂ ,O ₂ O,Ar,H,He
Pressure at surface (nPa)	~ 1.0	0.1	$1013 \cdot 10^{11}$
Max. surface temp. (K)	700	390	279
Min. surface temp. (K)	100	100	
Altitude of exobase (km)	~ 0	~ 0	~ 500
Magn. field, equator (nT)	230 – 290	none	50000
Magn. field tilt ($^\circ$)	5 – 12	–	11.5
Satellite	none	–	Moon

Table 2.1: Mercury planetary data compared to that of the Moon and Earth. The most recent measurements (MESSENGER) were chosen when available, especially for the *B*-field values. The composition of Mercury’s exosphere is not well constrained and was measured by Mariner 10, MESSENGER and ground-based facilities to be He, H, O, Na, K, Ca and Mg. ^a The albedo, ranging between 0 and 1, is the ratio of the total brightness backscattered by the surface of a planetary body to that of a perfect reflector ($A = 1$). ^b 1 AU = $1.496 \cdot 10^6$ km.

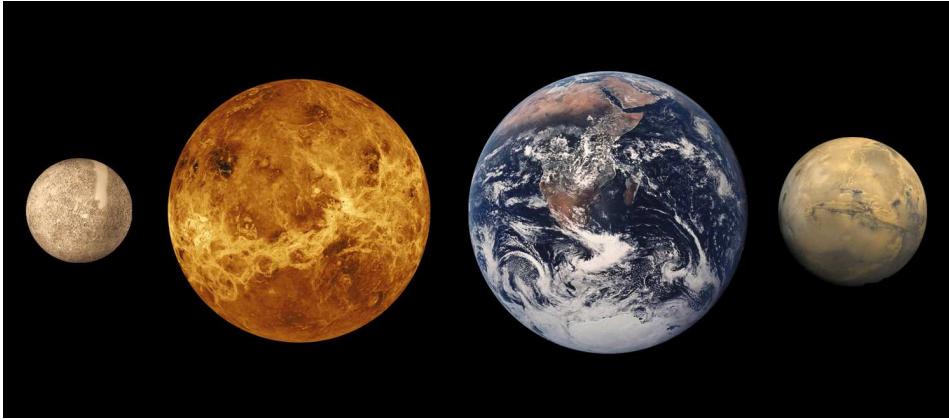


Figure 2.1: Size comparison of the terrestrial planets. From left to right: Mercury, Venus, Earth and Mars (Image NASA/ESA).

Due to its elliptic orbit, it is from Earth only possible to see Mercury, by the naked eye, in morning or evening when the Sun has not yet risen or when the Sun has just gone down the horizon. Mercury, with a maximum apparent diameter of only $13''$, is a very bright object in the sky, and has a magnitude that varies from -2.6 to $+5.7$ depending on its orbital location. Because of its close proximity to the Sun (it never strays more than 28° away from the Sun), it is usually lost in the strong background sunlight.

Mercury's period around the Sun is 88 days, and speeds through space at nearly 50 km per second, faster than any other planet. Its axial tilt is almost zero, 0.027 degrees, which is much smaller than even Jupiter at 3.1 degrees, preventing the planet from displaying its poles to the Sun and leaving them always in relative shadow.

In 1965 Pettengill and Dyce (1965) discovered from radar Doppler observations that the rotation of Mercury was not synchronously locked as had been believed for many years and equaled ~ 58 days instead of 88 days. Mercury has a very slow rotation period that is exactly half of its synodic period making for a very peculiar counting of days and years; a single day (solar day) lasts exactly two Mercury years (sidereal). This is thought to be due to the eccentricity of Mercury's orbit in combination with the gravitational influence from the Sun and other planets in the solar system, creating a 3:2 spin-orbit resonance, as shown in Figure 2.4.

Correia and Laskar (2004, 2010) have shown that as the orbital eccentricity of Mercury varied chaotically from near zero to more than 0.45 in the last 4×10^9 years and adding the viscous friction at the core-mantle boundary, the capture probability in a 3:2 resonance increases and can be favoured.

Mercury's advance of perihelion amounts to 43 arcseconds per century with respect to classical Newtonian mechanics, an anomalous rate discovered first by Urbain Le Verrier in 1859 and ascribed to possible planetary bodies inside Mercury's orbit (often nicknamed "Vulcan"). This served historically as a test of the validity of Einstein's General Theory of Relativity in 1916 and played a major role in the adoption of the then young theory.

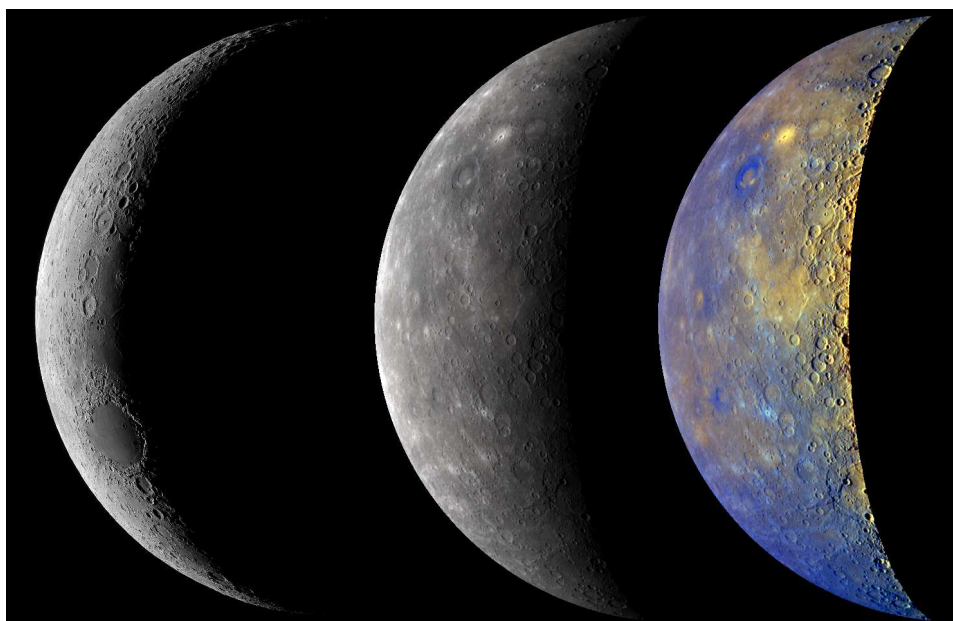


Figure 2.2: The Moon seen from Earth (left) and Mercury imaged in true colours by the Wide Angle Camera (WAC) of the Mercury Dual Imaging System (MDIS) on board NASA MESSENGER in 2009 (right). The enhanced-colour view of Mercury on the right shows surface features not unlike the Moon's. (Image Thierry Legault, NASA/Johns Hopkins University Applied Physics Laboratory/Carnegie Institution of Washington).

2.1.2 Internal structure, the magnetic field and magnetosphere

Models predict that the core of Mercury is very large (42% in volume) (see Fig. 2.5) and consists of mostly metallic (70%) and silicate (30%) materials, making it one of the densest planets in the solar system (5.43 g cm^{-3}), only topped by Earth (5.51 g cm^{-3}).

While the Moon completely lacks a magnetic field, Mercury possesses a very large liquid iron core sustained by tidal effects and generating through a dynamo effect a weak but stable dipolar magnetic field, probably fueled by the cooling of the core and the contraction of the entire planet after the "late heavy bombardment" period, between 4.1 and 3.8 billion years ago (Breuer et al., 2007; Glassmeier et al., 2007).

The intensity of the magnetic field reaches around 300 nT at the equator, which is about 1.1% the corresponding value of Earth's. Following the recent measurements of the MESSENGER probe, the magnetic field poles were found to be tilted between 5 and 12° from the spin axis of the planet (Anderson et al., 2008).

The stable magnetic field is strong enough to make an obstacle to the solar wind creating a magnetospheric cavity probed by Mariner 10 and more recently by MESSENGER (Fig. 2.5). The magnetosphere traps solar wind ions and electrons that participate to the space weathering of the surface.

During its first flyby on 14 January 2008 followed by a second flyby on 06 October 2008, NASA MESSENGER showed that Mercury's magnetic field can be extremely dynamic (Slavin et al., 2008, Fujimoto et al., 2007) with the discovery of recurrent flux transfer

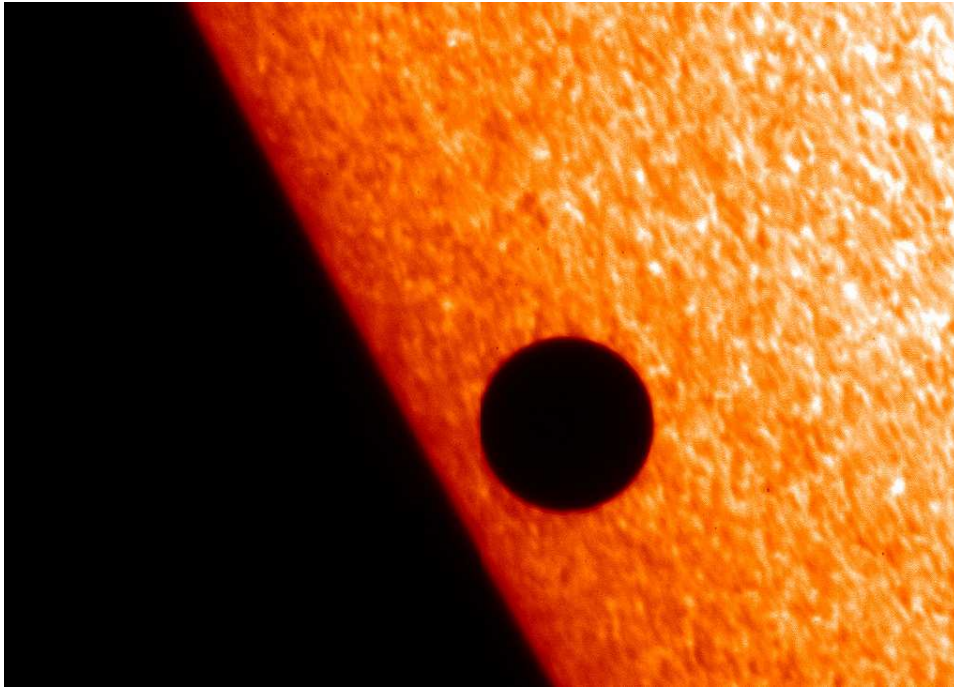


Figure 2.3: Transit of Mercury on 8 November 2006 captured by the Solar Optical Telescope on board the Japanese solar satellite SOLAR-B/Hinode, just after it crossed the solar limb (Image JAXA/NASA/PPARC).

events being a signature of magnetic reconnection between the solar wind frozen-in field and the planet's own magnetic field (Slavin et al., 2009; Slavin et al., 2009).

MESSENGER's third flyby on 29 September 2009 showed that the solar wind plasma can then be allowed to enter the magnetosphere in bursts lasting 2 to 3 minutes and at a uniquely high rate owing to the proximity of Mercury to the Sun (Slavin et al., 2010). Following this new picture, two sources are thought to contribute to the existence of a magnetospheric plasma: the solar wind (through reconnection or direct entry along open field lines), but also pick-up ions created by UV photoionisation and electron impact ionisation of the neutral exosphere and subsequently driven along magnetic field lines (Slavin et al., 2008).

Accelerated by intense electric fields in the magnetotail, the magnetospheric plasma can in turn impact the surface of the planet and release volatiles (Orsini et al., 2007). In doing so, it contributes as an additional source to the formation of the neutral exosphere. Charged particle acceleration mechanisms occurring at Mercury are now under close investigation by MESSENGER (Zelenyi et al., 2007). The study of the magnetosphere of Mercury, its energy content and dynamics is only starting.

2.1.3 Surface

Morphologically speaking, Mercury shows an astonishing similarity to the Moon (see Figure 2.2) with its mare-like plains, montes, planitiae, rupes and valles, and heavy cratering (Figure 2.6), proving that it has been partly geologically inactive for billions of years.

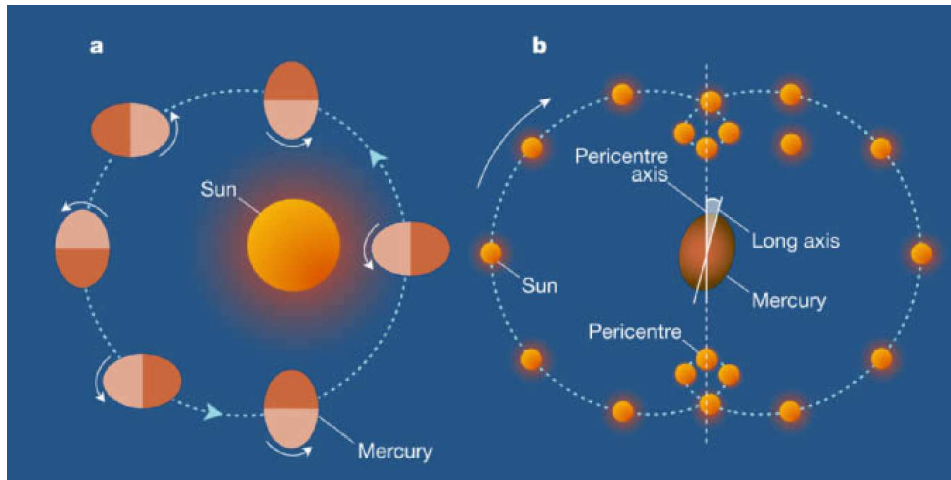


Figure 2.4: The 3:2 spin-orbit resonance of Mercury. *a* The planet presents the same face to the Sun every two passages at pericenter. *b* Dynamical stability of the resonant orbit: the Sun's position is shown in a reference frame centered on Mercury and rotating with the solid body of the planet. The angle between the pericenter axis and the long axis of the planet oscillates like a pendulum. (Image Dermott (2004))

Strom et al. (2008) concluded from new observations of the cratering record during the first flyby of MESSENGER that the plains formed no earlier than 3.8 billion years ago while lower densities of craters on certain basins (like Raditladi) may be younger than 1 billion year. The curious feature of high ridges in Mercury's surface is believed to be due to the cooling of the core and mantle and their subsequent shrinking, when the surface had already solidified (Solomon et al., 2008).

The discovery of volcanic evidence at Mercury was one of the main highlights of the first MESSENGER flyby (Head et al., 2008) and is thought to explain the formation of plains on Mercury. By comparison with the Moon, high resolution images (150 m) showed deformation vents of pyroclastic origin around the Caloris basin (the youngest known large basin) which were significantly different from the lunar impact basins known properties (albedo, geomorphological structure) (Murchie et al., 2008).

New images and data from the second and third flybys suggested that the role of volcanism was predominant in explaining these formations, while volcanic activity might have spanned previously unsuspected long periods, from the planet's formation to well into the second half of its history (Prockter et al., 2010).

2.1.4 Exosphere

Mercury, with an equatorial radius of 2440 km, is the smallest planet in the solar system but is also too small to retain a thick atmosphere. However, Mariner 10, ground-based instruments and now MESSENGER have shown that a tenuous surface-bound exosphere exists, where barely any collisions between constituents occur. It is mainly composed of (see Hunten et al., 1988; Killen et al., 2007, Table 2.1):

- Light species such as hydrogen (H and H₂)
- Noble gases such as helium He

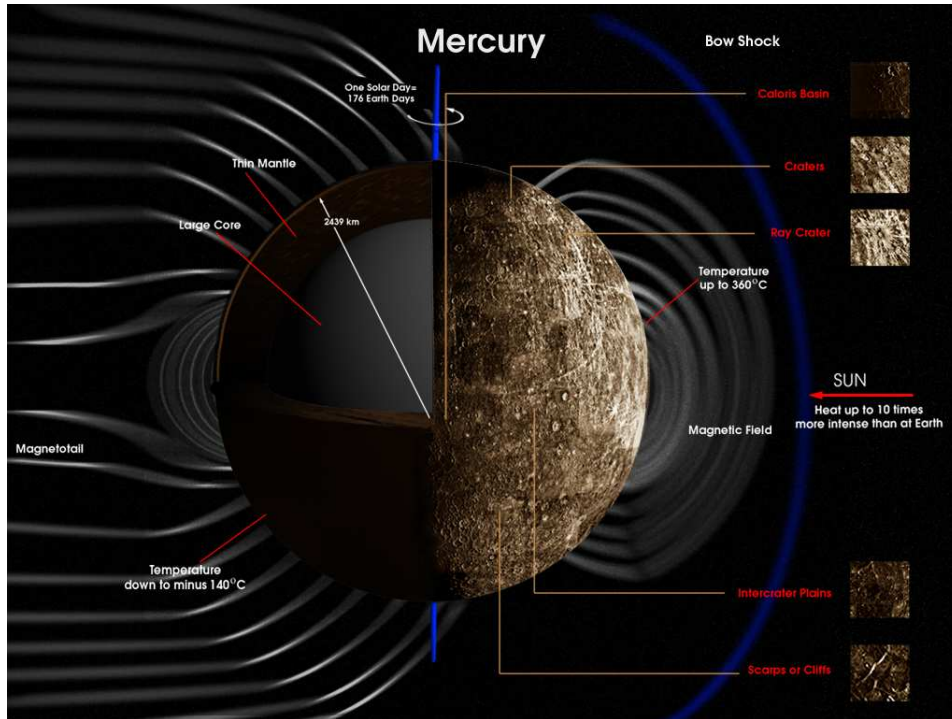


Figure 2.5: Mercury's space environment and surface features (Image ESA/BepiColombo)

- Alkali species such as sodium Na, potassium K, calcium Ca and magnesium Mg.
- Heavier species such as oxygen O, with expected traces of molecular oxygen O₂, nitrogen N₂ and carbon dioxide CO₂

The relative abundances of these species are badly constrained and need further investigation from current and upcoming space missions (Killen et al., 2007). It is also believed that Mercury has traces of water ice H₂O located in the eternally dark polar regions. Species such as C, CO, CO₂, N₂ and Li have been suggested (Sprague et al., 1996; Hunten et al., 1988) but were never detected, while hypothetical OH or S species were suggested to account for bright deposits at the poles.

According to models and observations (see for instance Leblanc and Johnson, 2003), the neutral species originate from the surface of Mercury and are released in the atmosphere by a number of processes that will be detailed in Chapter 2. They can be classified into three categories:

- Photon- and low energy electron-induced mechanisms (photon-stimulated desorption, electron-stimulated desorption) due to electronic excitation of a surface atom
- Sputtering effects due to impact (solar wind, magnetospheric ions, meteorites)
- Thermal vaporization of atoms (hydrogen and alkali atoms mostly) due to the high surface temperature of Mercury

Typical dayside densities at the surface range between 100 and 4×10^4 cm⁻³ while strong nightside variations are seen (Hunten et al., 1988). For instance, as shown in Table 2.2, hot (475 K) and cold (100 K) populations have been observed for hydrogen H, interpreted

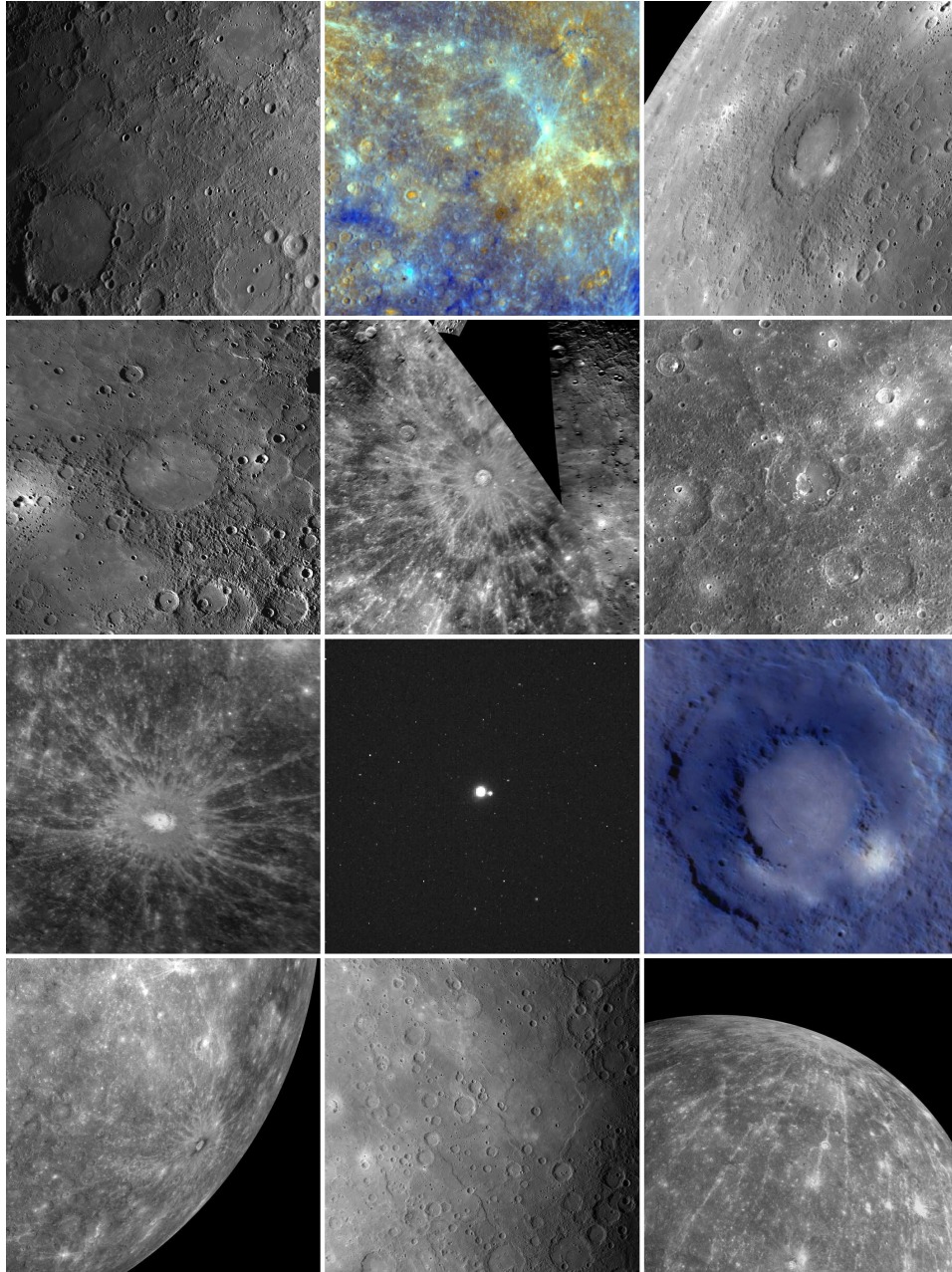


Figure 2.6: The surface of Mercury as seen by MESSENGER. Geddes Crater, smooth plains, young volcanism and the rays of Hokusai. (Image NASA/Johns Hopkins University Applied Physics Laboratory/Carnegie Institution of Washington)

Species	Densities ^a (10^7 cm^{-3}) <i>expected/measured</i>	Column abundance ^b (10^{13} cm^{-2}) <i>measured</i>	Temperature ^c (K) <i>measured</i>
H	~ 0.02	0.005	110 (night), 420 (day)
He	2.6	2.0	575
Na	11	0.02	750 – 1200
K	14	1.0×10^{-4}	
O	4.2	0.7	
Ca	–	1.0×10^{-6}	

Table 2.2: Upper limit of number densities and column abundances at Mercury inferred from Mariner 10 occultation experiment (Broadfoot et al., 1976 and Hunten et al., 1988). Large variations reported by Milillo et al. (2005) and references therein are expected. Temperatures derived from scale heights are also mentioned for a few species. ^a see Hunten et al. (1988), ^b see Strom and Sprague (2003), ^c see Milillo et al. (2005).

as a dayside and a nightside component (see Milillo et al., 2005) The column density of observed constituents has an upper limit of 10^{12} cm^{-2} (Killen and Ip, 1999).

During the different flybys of Mariner 10 in 1974 (Shemansky and Broadfoot, 1977) and more recently by MESSENGER (discovery of Mg by McClintock et al., 2009) as well as ground-based observations (discovery of Na and K by Potter and Morgan, 1985, 1986, and of Ca by Bida et al., 2000), the exospheric emissions arising from the excitation (resonant or not) of neutral species were observed and can serve to get an estimate of exospheric neutral densities.

Vervack et al. (2010) performed observations with the spectrometer on board MESSENGER of Na, Ca and Mg atoms with evidence of Ca^+ ions extending far back in the magnetotail. The neutral species exhibited very different distributions (for instance, sodium Na displayed a two-temperature distribution, while the weak Mg emission appeared to be nearly uniformly distributed) which indicated that multiple processes might drive the formation of these exospheric species.

2.2 History and science: Ancient

Surprisingly old records of Mercury have been discovered. The Mul.Apin tablets, dating back to 500 BC account for observations describing the risings and settings of stars believed to have been made by Babylonian astronomers around 1000 BC. The tablets, containing the earliest and most comprehensive surviving star catalogue from Mesopotamia, refer to Mercury as *Ninurta*, a planet who "rises or sets in the east or in the west within a month" (Hobson, 2009).

The Greeks knew around 450 BC that there were five planets, called *Astra Planeta* –the wandering stars–, and named them *Phainon* (Saturn), *Phaethon* (Jupiter), *Pyroeis* (Mars), *Eosphoros* (Venus), and *Stilbon* (Mercury). Believing Mercury to be two planets they named it *Stilbon/Apollo* in the morning and *Hermeaon/Hermes* in the evening. However around the 4th century BC they came to realise that it was two aspects of the same planet, naming it as the messenger of the gods, *Hermes*. The Romans later named the planet 'Mercury', in reference to the Greek God *Hermes* in their mythology.



Figure 2.7: Skull owl (left) and Shooting owl (right), aspects of Mercury by the Mayans, as depicted in the *Popol Vuh* (Image Tedlock, 1985).

Cicero, the famous Roman rhetorician of the first century BC, mentioned Mercury in his *De Natura Deorum*:

Below this [the orbits of Saturn, Jupiter and Mars] in turn is the Stella of Mercurius, called by the Greeks Stilbon (the gleaming), which completes the circuit of the zodiac in about the period of a year, and is never distant from the sun more than the space of a single sign, though it sometimes precedes the sun and sometimes follows it.

Cicero, *De Natura Deorum*, 45 BC.

In Southern America, the Mayas charted the motion of the visible planets including Mercury. Records of their detailed observations are found in the *Dresden Codex*, a Mayan book from 1000 AD, that is deemed to be a copy of an earlier text at least 300 years older. The astonishingly accurate text describes Mercury's visibility, location in the sky and a description of conjunctions with other planets at specific dates. The Mayans also calculated that Mercury would rise and set in the same place in the sky every 2200 days.

The Mayan had the notion of Mercury as the messenger of the gods of the underworld *Xibalba*, represented by four owls, two for the waxing/waning morning star aspect and two for the waxing/waning evening star aspect (Tedlock, 1985). Skull owl and Shooting owl, two of these aspects, can be seen in Figure 2.7.

Around 100 AD the Roman-Egyptian astronomer Ptolemy described a complex system of circles to describe the motion of the planets, based on a geocentric world view. In this system, Earth was in the middle instead of the Sun, and then Mercury went in a circular orbit around it, moving in an epicycle, see Figure 2.8. Later, in his large treatise *Almagest*, Ptolemy correctly suggested that no transits of planets, such as Mercury, across the face of the Sun had been observed either because it was too small to see, or because the transits were too infrequent.

1200 years after Ptolemy, Ibn al-Shatir (1304–1375), an Arab astronomer, mathematician and inventor from Syria, wrote an astronomical treatise *The Final Quest Concerning*

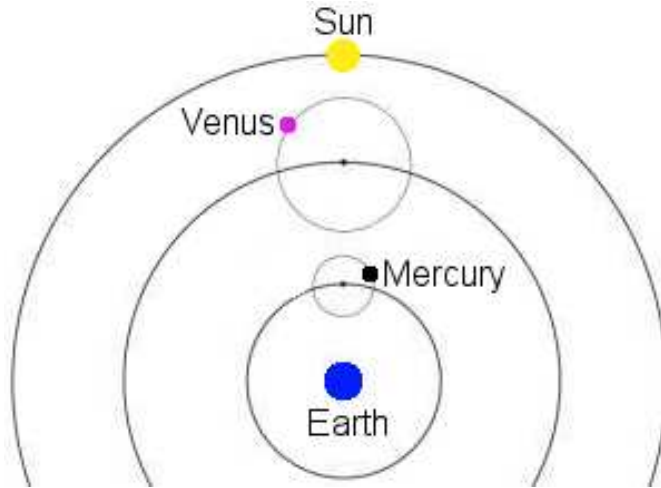


Figure 2.8: Ptolemaic system of the inner planets. The Earth is in the middle, while Mercury, Venus and the Sun all follow epicycles around it.

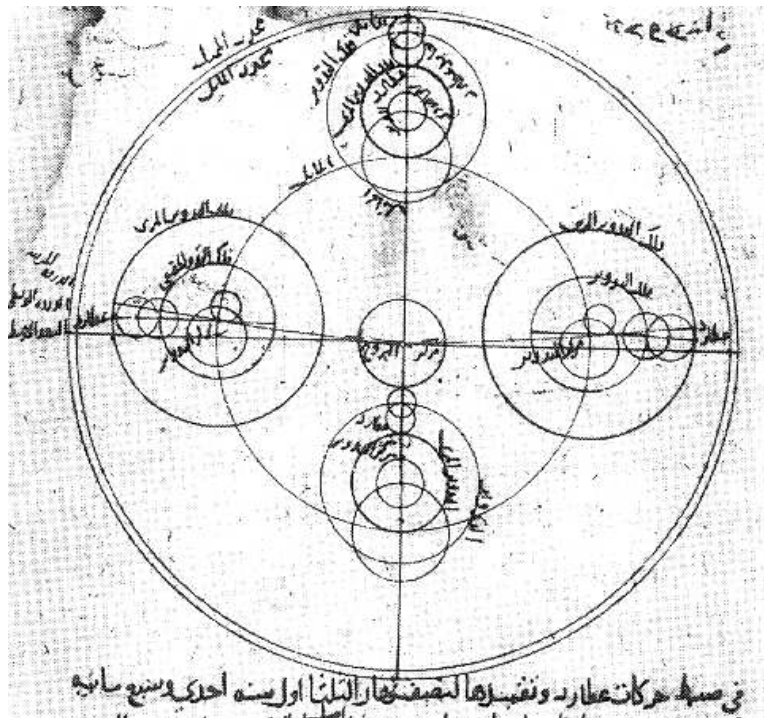


Figure 2.9: Ibn al-Shatir's drawing circa 1350 showing his reformation of the Ptolemaic system, predicting the motion of Mercury around the Sun (Image Huff (1993)).

the Rectification of Principles, see Saliva (1987), in which he drastically reformed the Ptolemaic model by introducing extra epicycles, subsequently eliminating the Ptolemaic equant and eccentrics, for an example applied to Mercury's orbit see Figure 2.9. This reform was one of the major ones that led to the evolution of the heliocentric system that, curiously enough, left Mercury in exactly the same orbit as in the Ptolemaic system, only revolving around the Sun this time instead of the Earth.

2.3 Science: In modern times

2.3.1 Early Optical observations

Even though Mercury is a very bright object in the sky with magnitude varying from -2.6 to $+5.7$ depending on its orbital location, it is very hard to observe the planet from Earth because of its close proximity to the Sun and because of its eccentric orbit. Therefore it is only possible to see it, by eye, in morning or evening when the Sun has not yet risen or when the Sun has just gone down the horizon.

The difficulty in observing Mercury from the ground has led to it being the planet least studied, with most erroneously attributed features that have later been disproved. The first known observation using a telescope was made by Galileo early in the 17th century but his telescope was not powerful enough to observe any phases.

In 1631 Pierre Gassendi observed the transit of Mercury on the Sun, as predicted two years before by Johannes Kepler (from his newly completed Rudolphine tables): he used a telescope to project an image 20 cm in diameter of the sun upon a white screen (see *Gassendi and the Transit of Mercury*, *Nature*, 128, 3236, 787, 1931).

Using a telescope only slightly more powerful than Galileo, Giovanni Battista Zupi (Zupus) discovered in 1639 that Mercury had phases just like the Moon and Venus, a potent evidence that Mercury was orbiting the Sun and giving strength to the argumentation of heliocentric theories, Figure 2.10. This was later observed independently by Johannes Hevelius in 1644 who also observed a transit in 1661 (Hevelius, 1662), see Figure 2.11.

The very rare occultation of Mercury by Venus in 1737 was recorded by John Bevis. The next one is expected to take place in 2133.

By the turn of the 19th century, with the increasing size of reflecting telescopes, several scientists, like Johann Schröter and his assistant Karl Harding in Germany, Giovanni Schiaparelli in Italy, had described some surface features of Mercury, Figure 2.12. Schröter claimed that due to irregularities in brightness, mountain ranges existed on Mercury, among which one towered at 18 km (Schröter, 1800). Both Schröter and Bessel (1813) incorrectly derived a period of 24 hours with a rotation axis at 70° to the orbital plane. At the end of the same century, Schiaparelli estimated a new, though incorrect, value of 88 days for the period (Schiaparelli, 1891), which was not corrected until the advent of radar observations in 1965. By his own words:

Among the planets known by the ancients, none is so difficult to observe as Mercury and none presents as many difficulties for the study of its orbit as well as its physical nature. Being impossible to observe during the night, and rarely possible during twilight, there is no other solution than studying it in full daylight, in the presence of the Sun always in the vicinity, and through an illuminated atmosphere.

G.V. Schiaparelli, *Sulla Rotazione di Mercurio*, 1890.

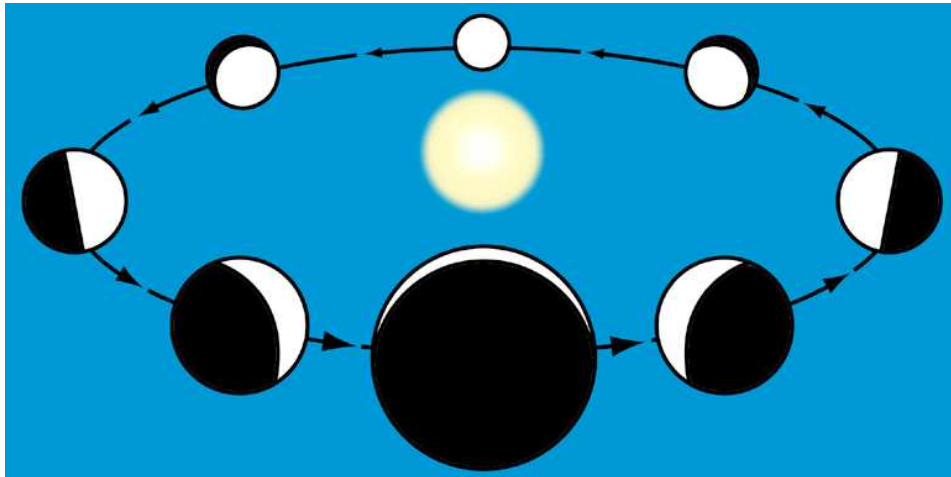


Figure 2.10: Mercury's phases seen from Earth (Image adapted from NMS University).

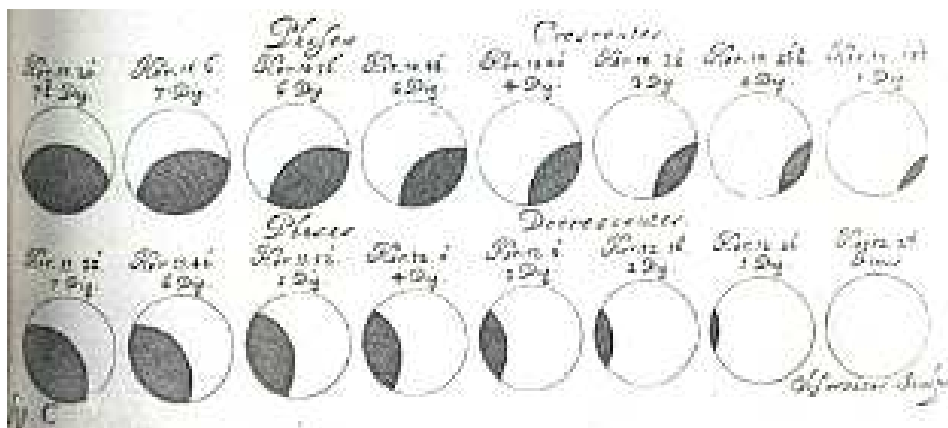


Figure 2.11: Part of Hevelius' report of the transit of Mercury across the Sun with the corresponding phases (Image Hevelius (1662)).

2.3.2 Modern ground-based observations

Use of radar techniques

The first modern radio observation was in 1962 when Soviet scientists under V. Kotelnikov in Crimea managed to reflect not less than 53 radar signals off the surface of Mercury. Three years later, using the newly built incoherent scatter radar of Arecibo (Puerto-Rico), Pettengill and Dyce (1965) showed that its rotational period was 59 ± 5 days completely overturning all that had been believed for the past 150 years. As any change of scientific paradigm, the implications were fascinating, indicating that *"either the planet has not been in its present orbit for the full period of geological time or that the tidal forces acting to slow the initial rotation have not been correctly treated previously"* (Pettengill and Dyce, 1965).

Between 1960 and 1961, it was also confirmed by analysis of the planetary radio wave emission between 3.45 and 3.75 cm wavelength with the 25.9 m reflector of Michigan University that Mercury's nightside was warmer than commonly assumed (Howard, 1962), questioning the accepted idea of the 1:1 ratio orbit, as this would have left the planet much colder on the nightside.

Dyce, Pettengill and Shapiro (1967) from the Smithsonian Astrophysical Observatory (SAO) were working on the interpretation of the new puzzling radar data, when Giuseppe 'Bepi' Colombo (1920 – 1984), an Italian astronomer who was a visiting scientist of SAO, hypothesised that Mercury could be in a 3:2 resonance (Colombo, 1965). As a main collaborator of Colombo (Colombo and Shapiro, 1966), Shapiro recalls:

Colombo realized almost immediately that 58.65 days was exactly two-thirds of 88 days. Mercury probably was locked into a spin such that it went around on its axis one-and-a-half times for every once around the planet. The same face did not always face the Sun. That meant that [...] the orbital motion and spin rotation of Mercury were very closely balanced, so that Mercury almost presented the same face to the Sun during this period.

Irwin Shapiro, quoting Giuseppe Colombo, in Butrica (1996).

The 3:2 resonance was later confirmed at the arrival of the American mission Mariner 10 in 1974 and explained why observers had always managed to see only one side of Mercury since it is always showing the same side every second orbit, while all other sides would not be properly viewed due to poor viewing conditions. The formidable intuition of Colombo fostered many studies on the origin and consequences of the rotation of Mercury from Liu and O'Keefe (1965) to Correia and Laskar (2010).

The story of Colombo with Mercury did not stop there: he also suggested in 1970 how to put the Mariner 10 spacecraft into an orbit that would bring it back repeatedly to Mercury, using the gravitational slingshot maneuver provided by Venus to bend its original flight path and decelerate the spacecraft on its way to the inner solar system.

The advent of spectroscopy and polarimetry

As soon as 1932, attempts were made to detect an atmosphere at Mercury using either IR spectroscopy (Adams and Dunham, 1932, who failed to detect CO₂) or polarimetry (Lyot, 1929). The optical studies of Lyot paved the way to increase the resolution of the observations always pushing away the observational limits: in 1942, he managed to observe Mercury at an angular distance of 2° from the Sun using a 11-m long sunshade mounted on a bamboo stick (Dollfus, 1953). Lyot concluded from his early polarimetric attempts

(Lyot, 1930) that Mercury's polarisation was almost identical to that of the Moon at a wavelength of 580 nm.

By using the polarisation of light, it is possible to detect an atmosphere around a planet or a natural satellite, since the scattering by molecules or aerosols may polarise the reflected light of the studied body. In the 1950s, Mercury was thought, because of its small size, to have lost its atmosphere due to atomic and molecular escape into space.

Performing polarisation measurements at the Pic du Midi Observatory in the French Pyrénées, Audouin Dollfus (1924–2010) set an upper limit to the atmosphere, estimating the maximum molecular atmospheric pressure to be under 25 Pa (Dollfus, 1961, Dollfus and Aurière, 1974), the real value being around 1 nPa. Dollfus and Aurière (1974) also confirmed Lyot's first results by showing that Mercury's surface was made of the same pulverised basalt, or regolith, as the lunar samples that the Apollo missions had returned.

In parallel to polarimetric measurements, IR spectroscopy were undertaken but failed to detect any sign of molecules such as CO₂, O₂ or H₂O (Spinrad et al., 1965; Poppen et al., 1973) even though H and CO₂ were reported by Kozyrev (1964) and Moroz (1964) but never confirmed (Kellermann, 1966). Radiogenic ⁴⁰Ar seemed at the time the likeliest species to be detected (Field, 1964). Mariner 10 later confirmed the absence of detectable molecules and inquired the suggestion about the preeminence of Ar by setting stringent limits on the constituents with the UV spectrometer experiment (Kumar, 1976).

The discovery of sodium Na by resonance scattering of sunlight from sodium atoms (Potter and Morgan, 1985) launched a new era in the observation of Mercury's exosphere. Potter and Morgan (1986) also detected potassium K using the McMath telescope at the Kitt Peak observatory and showed that the ratio of emission between sodium and potassium could reach anomalously large values of Na/K \sim 80 – 100, larger than any other known body in the solar system (except comets).

Many studies have tentatively tried to explain this ratio with different datasets (Potter and Anderson, 2002; Killen et al., 2010), until Doressoundiram et al. (2010), using the NTT (ESO, Chile) and CFHT (Hawaii) 3.6-m telescopes, measured in high resolution spectroscopy Na/K ratios ranging between 80 and 400 depending on the position in the exosphere. They reported also that potassium and sodium exospheres exhibited very different spatial distributions, which could be at the origin of the anomalous rate. The sodium and potassium modelling approach of Leblanc and Doressoundiram (2011) corresponding to these observations pointed the global day/night transport, the loss rate and the desorption efficiencies as the main factors responsible for the spatial distribution of the observed ratios.

Another fascinating facet of the sodium exosphere is its high temporal and spatial variability, documented since the start of the alkalis observation era (Potter et al., 2006, Leblanc et al., 2009). Long-term observational surveys have given a good statistical sampling of annual (Potter et al., 2007) and diurnal cycles (Potter et al., 2006) of the sodium exosphere, which have been associated with the solar wind.

Reconnection between the interplanetary magnetic field lines and those of Mercury on the dayside magnetopause may favour the bursty entrance of solar wind plasma into the cusp, which in turn may impact the surface and trigger, via ion-sputtering, the refilling of the Na exosphere (Masseti et al., 2007). Exospheric temperatures inferred for sodium are of the order of 1000 K as in shown by Killen et al. (1999) using the echelle spectrograph of McDonald Observatory or more recently by Leblanc et al. (2009) using the Franco-Italian solar telescope THEMIS.



Figure 2.13: The solar observatory THEMIS in Tenerife (Image M. Simon Wedlund).

THEMIS: a new window on Mercury

The solar telescope THEMIS (Télescope Héliographique pour l'Étude du Magnétisme et des Instabilités Solaires) is situated in Tenerife, Canary Islands, Figure 2.13). Its originality lies in its versatility and different modes ranging from high resolution spectrometry to spectropolarimetry, offering a unique perspective on Mercury's exospheric emissions. Built in 1996, THEMIS is perfect to observe Mercury in close proximity to the Sun, even during daylight, since the telescope was originally built to observe the Sun directly. It consists of a 90-cm primary mirror with a focal length of 15.04 m (López Ariste et al., 2000).

Several studies have been performed looking at the D_1 (589.6 nm) and D_2 (589.0 nm) lines of Na (Leblanc et al., 2008, 2009) and characterising the spatial and temporal variations of brightness and Doppler shifts. Scans across the bright side of Mercury were made and reveal asymmetries between North and South hemispheres and the dynamics of these emissions, see Figure 2.14. Polarimetric measurements of D_1 and D_2 were successfully carried out in 2010 (A. López Ariste, personal communication), and could help characterise the weak magnetic field of Mercury as the polarisation/depolarisation is thought to be arising from the Hanle effect.

A description of the observatory and the observational modes of THEMIS is available here: <http://www.themis.iac.es/>.

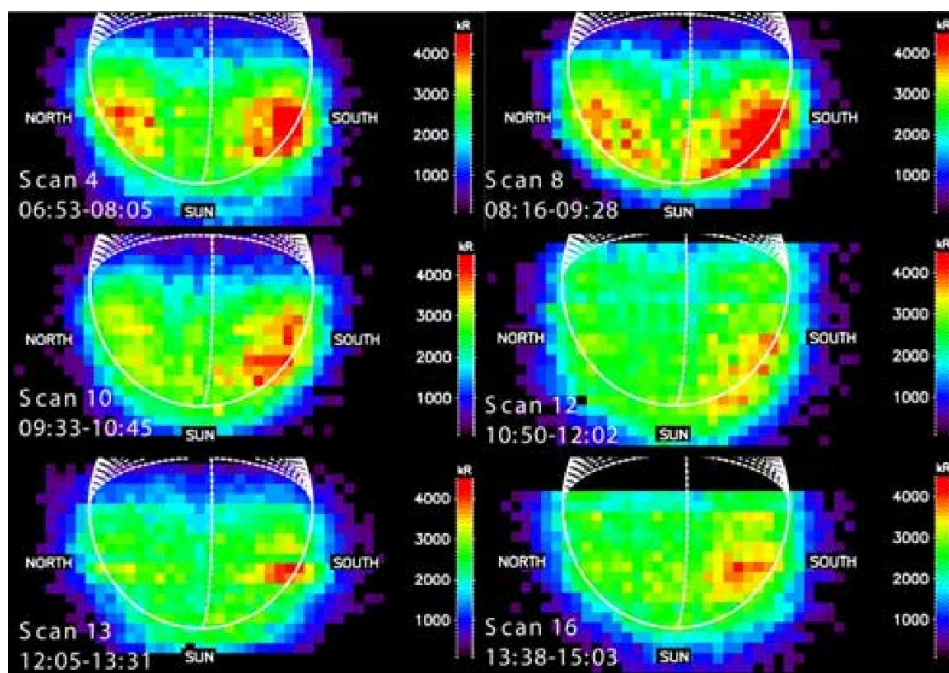


Figure 2.14: Brightness of the Sodium emission during six consecutive scans performed with THEMIS (CNRS/CNR) on 13 July 2008. The disk of Mercury is highlighted in white (Image Leblanc et al. (2009)).

2.3.3 Missions

So far only two space missions have successfully been deployed and reached Mercury, Mariner 10 and MESSENGER. A third, BEPI-COLOMBO, is in its building stage and will be launched in 2014. Due to Mercury's close proximity to the Sun, missions to Mercury have to take extra precautions to protect the instruments from the intense heat and radiation emitted from the star. To counteract these problems the spacecrafts have to be equipped with specially designed sunscreens and solar panels to keep the instruments in a safe working environment. Another problem is the difficult maneuver to make the spacecraft slow down and enter an orbit around Mercury due to the powerful gravitational field of the Sun that could easily accelerate the satellite and send it in a trajectory out of the solar system.

Mariner 10

In 1974-75 the first space probe reached Mercury.

Mariner 10, Figure 2.15 carried on board seven experiments to investigate Mercury: extreme ultraviolet spectroscopy, magnetometer, television imaging, infrared radiometry, plasma, charged particles, and radio wave propagation, see Figure 2.16.

Mariner 10, a successful NASA collaboration was not only the first mission to Mercury but also the first mission ever to use gravitational assisting in order to reach it, the first mission to visit more than one planet at the same time and also the first to make multiple flybys of a planet (Mercury) In Figure 2.17 the complex trajectory of Mariner 10 can be seen.



Figure 2.15: Artist view of Mariner 10 mission to Mercury (Image JPL)

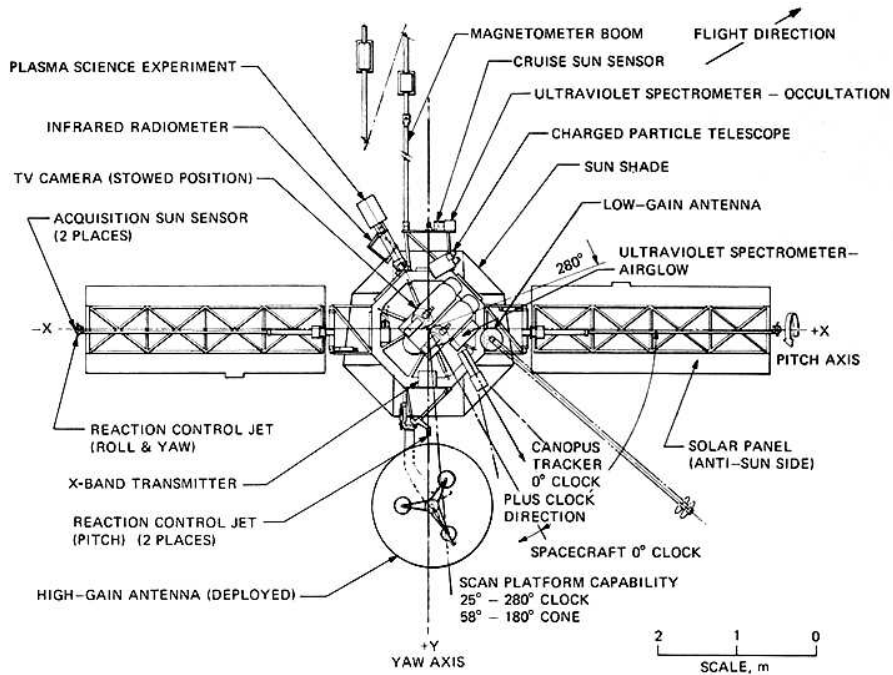


Figure 2.16: Payload of Mariner 10 mission to Mercury (Image Dunne and Burgess (1978))

It also managed, for the first time ever, to take magnificent photographs of parts of the surface of Mercury. Unfortunately Mariner 10 was aligned such that it looked upon the same surface each time, leaving half the planet unexplored.

The main objective of Mariner 10 was to explore Mercury's (and Venus) atmosphere, surface, environment and physical characteristics. Among the many discoveries was the Moon-like appearance of the surface that was revealed in the over 2800 photos taken. Another discovery was of the tenuous surface-bounded exosphere that separates it from the Moon together with the weak dipolar magnetic field.

Mariner 10 was a flyby mission, never meant to be inserted into orbit, and as such was limited in science to the three flybys performed. Because of this several features, such as the hydrogen exosphere, was never observed long enough to give conclusive data, despite this and several technical problems, it managed to greatly improve the existing knowledge of Mercury while at the same time raising a multitude of other questions.

MESSENGER

In 2004, 30 years after the Mariner 10 mission, the second mission to Mercury was launched. Also a NASA mission, the MESSENGER (MErcury Surface, Space ENvironment, GEochemistry and Ranging) probe has so far managed to make three flybys of Mercury, making a huge contribution to the understanding of Mercury. Among these, MESSENGER as depicted in Figure 2.19, has successfully managed to image the before unseen side of Mercury, completing the global map of the planet and made spectroscopic studies of the multitude of species in its exosphere, including for the first time Mg (McClintock et al., 2009).

Messengers main objective is to complete and complement the observations made by Mariner 10 and specifically to explore the nature of Mercury's exosphere and magnetosphere, characterize the chemical composition of the surface, the geological history and the size and state of the core.

MESSENGER has an extensive payload of eight highly sensitive instruments. The instruments include the Mercury Dual Imaging System (MDIS), the Gamma-Ray and Neutron Spectrometer (GRNS), the X-Ray Spectrometer (XRS), the Magnetometer (MAG), the Mercury Laser Altimeter (MLA), the Mercury Atmospheric and Surface Composition Spectrometer (MASCS), and the Energetic Particle and Plasma Spectrometer (EPPS), Figure 2.20.

The MESSENGER, just as Mariner 10, uses gravity assisted trajectories to reach Mercury and in doing so has made, as of yet, both Earth, Venus and Mercury flybys. However, unlike Mariner 10 who only made flybys, the MESSENGER is expected to be inserted into orbit around Mercury in early spring 2011 after its third flyby.

BepiColombo

The scientific objectives of the ESA/JAXA mission to Mercury, BepiColombo, are very similar to those of NASA's mission MESSENGER. This is due to historical collaboration between the missions to increase the scientific return of the instruments. BepiColombo is in the building stages for launch in 2014 on an Ariane 5 rocket and is composed of two orbiters, the Mercury Magnetospheric Orbiter (MMO) developed by JAXA and the Mercury Planetary Orbiter (MPO) developed by ESA.

The scientific payload of MPO consists of eleven instrument packages: the BepiColombo Laser Altimeter (BELA), the Mercury Radiometer and Thermal Infrared Spectrometer (MERTIS), the Ultra-Violet Spectrometer (PHEBUS), the Spectrometer and Imagers for

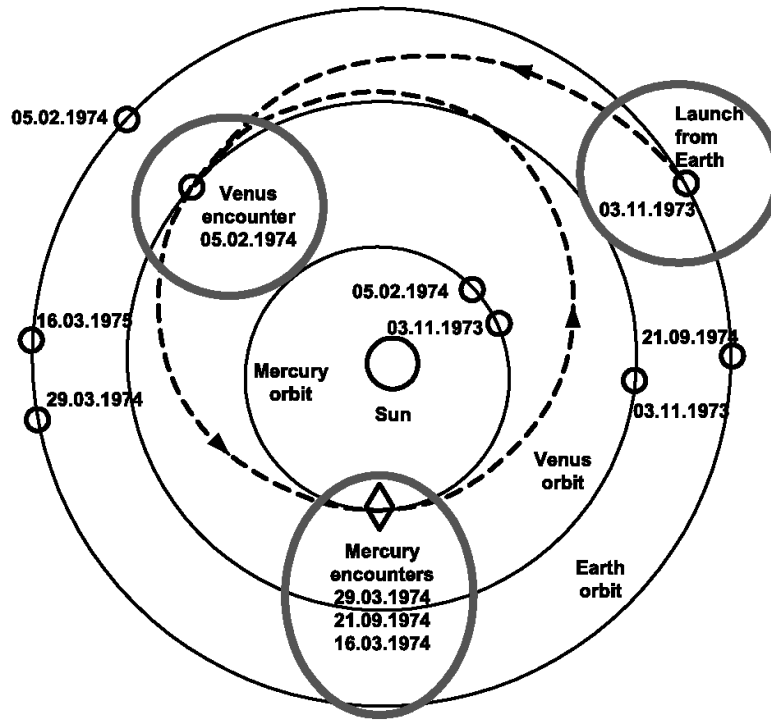


Figure 2.17: Mariner 10's gravity assisted trajectory past Venus on its way to Mercury (Image Balogh et al. (2007)).

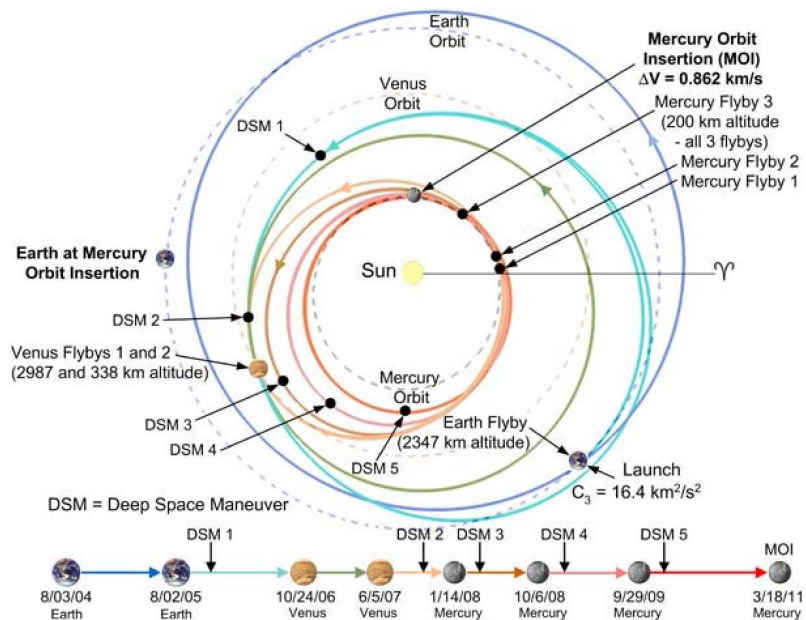


Figure 2.18: Messenger's gravity assisted trajectory to Mercury (Image Balogh (2007)).

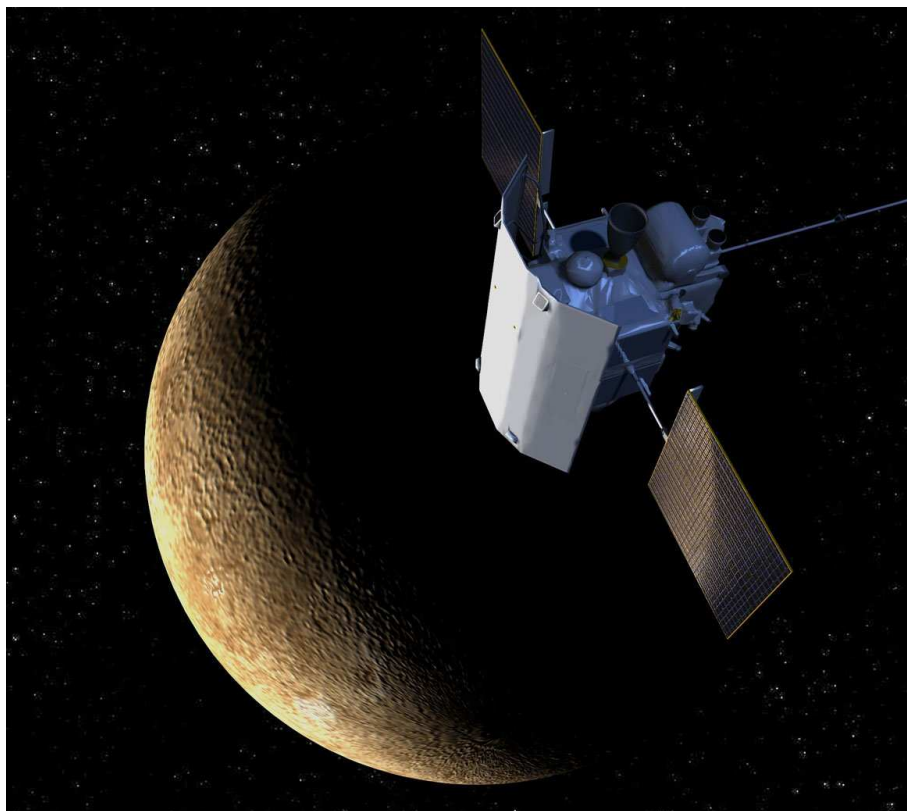


Figure 2.19: Artist view of MESSENGER mission to Mercury (Image NASA)

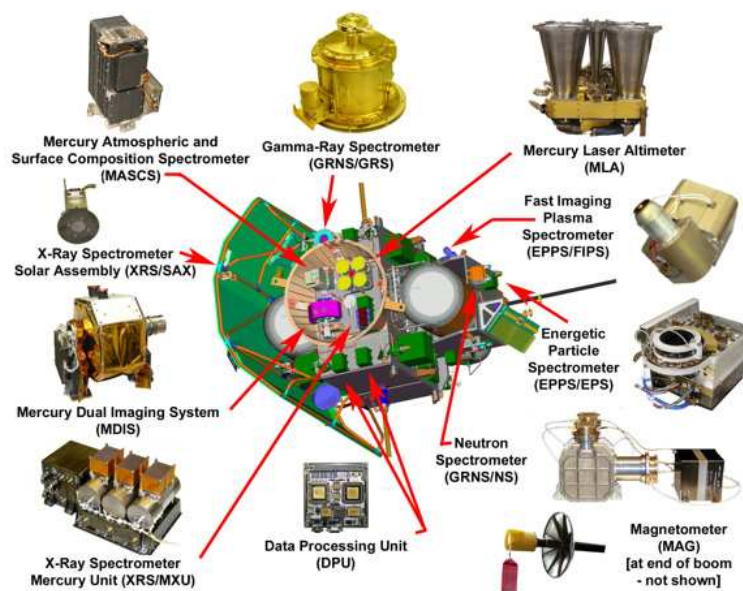


Figure 2.20: Payload of MESSENGER mission to Mercury (Image JHU/APL)

MPO BepiColombo Integrated Observatory System (SIMBIO-SYS), the Solar Intensity X-ray and particle Spectrometer (SIXS), the Search for Exospheric Refilling and Emitted Natural Abundances (SERENA) composed of four spectrometers – ELENA (Emitted Low-Energy Neutral Atoms), STROFIO (STart from a ROTating Field mass spectrOm-eter), MIPA (Miniature Ion Precipitation Analyser), PICAM (Planetary Ion CAMera) –, the Mercury Magnetometer (MERMAG), the Italian Spring Accelerometer (ISA), the Mercury Orbiter Radio-science Experiment (MORE), the Mercury Imaging X-ray Spectrometer (MIXS), the Mercury Gamma and Neutron Spectrometer (MGNS).

MMO carries five instruments: the Mercury Plasma Particle Experiment (MPPE) – divided into Mercury Electron Analyzer (MEA), Mercury Ion Analyzer (MIA), Mass Spectrum Analyzer (MSA), High-Energy Ions (HEP-ion), High-Energy Electrons (HEP-ele) and Energetic Neutrals Analyzer (ENA) –, the Magnetic Field Investigation (MGF), the Plasma Wave Investigation (PWI), the Mercury Sodium Atmosphere Spectral Imager (MSASI), the Mercury Dust Monitor (MDM).

MMO will perform observations of the magnetic field, the magnetosphere and exosphere of Mercury. MPO will observe Mercurys surface, chemical composition, gravity, magnetic field and to some degree the exosphere.

On board BepiColombo the ultraviolet spectrometer PHEBUS will play a huge role in adding to the data already collected from previous missions and especially on hydrogen.

For more information on BepiColombo and the PHEBUS instrument, see 4.

2.3.4 Modelling the exosphere of Mercury: a brief history

Due to the difficulty in observing Mercury, modelling has become a major tool in the understanding of the Hermean exosphere. Since Mercury, unlike most other rocky planets in the solar system, has a clearly identified surface-bounded exosphere with multiple sources and sinks with its space environment, exospheric modelling is also a clue to the surface composition, see Figure 2.21. For example, local surface inhomogeneities are expected to directly influence the exospheric composition (Leblanc et al., 2007).

Three classes of exospheric models have been used over the past decades:

- Chamberlain analytical models: first developed for Earth’s exosphere by Chamberlain (1963), these analytical models assume gravity as the only force and a strict separation between collisional and collisionless regions.
- Boltzmann transport: these models are particularly indicated to simulate the hot component and transition regions in one dimension (1D) by solving the Boltzmann transport kinetic equation and taking into account the chemical and physical reactions at work (Nagy and Banks, 1970; Nagy et al., 1990).
- Monte Carlo simulations: they are by essence stochastic and usually used for large 3D simulations. They are equivalent to the Boltzmann approach and often deal with multiple species (Chamberlain and Campbell, 1967; Barakat and Lemaire, 1990). They also take advantage of the intrinsic nature of gas interaction and the increasing computer power available.

These models have also been applied to other planets such as Mars (Nagy et al., 1981; Fox, 1993; Kim et al. 1998; Chaufray et al. 2007; Cipriani et al. 2007), Venus (Kumar et al., 1978; Bishop, 1989), Titan (Michael and Johnson, 2005), Europa (Leblanc and Johnson, 2003; Schematovich et al., 2005) and the Moon (Hodges, 1973; see Stern, 1999). Predictions derived from these models, such as the abundance of specific atoms or molecules, have been confirmed or infirmed by remote sensing measurements, showing the

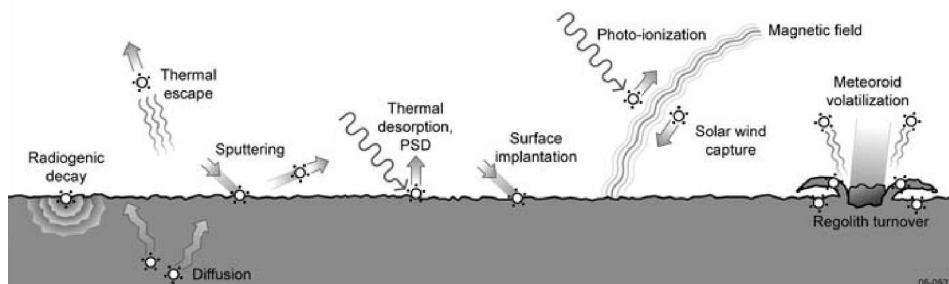


Figure 2.21: A coupled system between surface, exosphere and magnetosphere. Sources, sinks and interaction with the magnetic field are displayed schematically (Image Domingue et al. (2007)).

efficient and necessary synergy between observations and modelling. The main advantages of a simulation are:

- provide spatial distributions of the species
- separate temporal from spatial variations
- identify physical processes responsible for the dynamic creation of a given species

At Mercury, as soon as the Mariner 10 spacecraft reported a tenuous exosphere composed of H, He and O, modelling efforts started focusing mostly on He (Hodges, 1974; Hartle et al., 1975). Smith et al. (1978) used for example a Monte Carlo model to reproduce the exospheric He densities due to thermal desorption and concluded that only poor agreement could be obtained with the measurements of Mariner 10.

Since the recent discovery of alkali atoms (Na, K and Ca) and their spatial/temporal distribution at Mercury, many studies have been concentrating on these species.

One of the first sodium models was proposed by Ip (1986) to account for the observations of Potter and Morgan (1985). Ip used a Monte Carlo model to trace the orbital history of sodium atoms under the effect of solar radiation pressure and photoionisation loss. He concluded that photoionised Na (and hypothetical other heavy metallic ions such as Ca^+ , Al^+ or Fe^+) could be a major source of magnetospheric plasma and proposed that there exists at Mercury an extended sodium tail (Smyth and Marconi, 1995). The existence of a faint suprathermal sodium tail reaching at more than one planetary radius from the surface was confirmed by the observations of Potter and Morgan (1997).

The high variability of the sodium exosphere, up to a factor three in total content, warranted further investigation by models. In order to assess the impact of solar wind-magnetosphere interactions, Killen et al. (2001) used an open magnetosphere model in combination with a Na source model taking into account ion sputtering, photon-stimulated desorption and meteoritic vaporisation. They concluded that the variations of ion sputtering over regions open to the solar wind bombardment (in the case of southward interplanetary magnetic field for instance) could be responsible for the variation of the observed emission, while impact vaporisation plays the least significant role.

One of the first Monte Carlo multi-species exospheric models was developed by Wurz and Lammer (2003) in support to the incoming MESSENGER and BepiColombo spacecraft. Following the ballistic trajectories of particles, they computed densities for various atomic species including H, He, O, Na, K, Ca, Mg and expected molecular species such as CO_2 , H_2 , O_2 , etc. Complete accommodation of the reimpacted atoms was assumed and most release and loss processes were taken into consideration, except thermal desorption. Preliminary

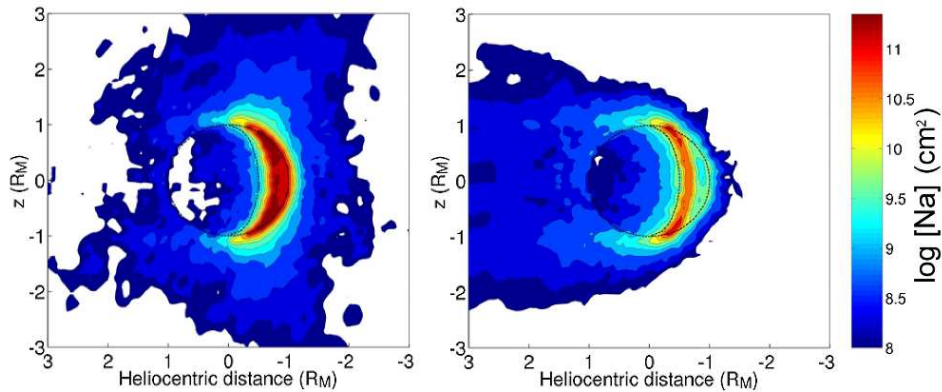


Figure 2.22: Spatial extension of the Na exosphere at aphelion (left) and at a true anomaly of 252° (right), showing the influence of solar radiation pressure that pushes away the Na atoms toward the dusk side. The column abundance of Na is expressed in atoms cm^{-2} . (Image Leblanc and Johnson (2003)).

results show good agreement with the measured intensity profiles of H and He (Broadfoot et al., 1976), and Ca (Bida et al., 2000). Despite the large uncertainties on most species and processes, Wurz and Lammer (2003) concluded that, within the upper limits set by their model, remote-sensing observations from an orbiting spacecraft would allow the detection of all species released from the surface.

The most comprehensive model of the sodium exosphere is that of Leblanc and Johnson (2003) who developed a 3D Monte Carlo model with a quantitative approach to thermal desorption, photon stimulated desorption, micro-meteoroid vaporisation and solar wind sputtering. They also treated realistically with time-dependent the surface composition, computed as an equilibrium between trapping/depletion from ejection. Their results were in good agreement with the large set of observations gathered by, for instance, Sprague et al. (1997).

Several studies have followed, showing the effects of separate sources on the overall distribution of the exospheric components (see Table 2 of Domingue et al., 2007) such as solar radiation pressure (Leblanc and Johnson, 2003, see Figure 2.22) solar energetic particle events (Leblanc et al., 2003a) and magnetospheric ion recycling (Leblanc et al., 2003b), and more recently Leblanc and Johnson (2010) and Leblanc and Doressoundiram (2011), where the authors adapted their sodium model to potassium K in order to investigate the Na/K ratio.

The observed dawn/dusk asymmetry, with a morning maximum followed by a three-fold depletion of the exosphere toward dusk, was explained by Leblanc and Johnson (2003) in terms of migration of atoms from hot to cold hemispheres, with an accumulation of atoms on the nightside. The models predicts also that the true anomaly angle² is one of the main proxies of the sodium exosphere, and that the total Na content is larger at aphelion than at perihelion, partly corroborated by observations compiled in Killen et al. (2004).

Mura et al. (2007, 2009) developed a Monte-Carlo model for the description of ion-sputtering, photon stimulated and thermal desorption from the surface of Mercury. Ballistic trajectories of the ejected particles are calculated using the full equation of

²True anomaly angle is the angular distance of Mercury along its orbit measured from perihelion

motion. Analytical fits of the modelled densities are then used to characterise each process separately. Unlike Leblanc and Johnson (2003), sodium concentration in the planetary surface was considered constant and uniform. This study showed possible strong variations in the exospheric profiles and that different surface compositions and morphologies should be properly taken into account in models.

For a comprehensive explanation and a state-of-the-art perspective on Mercury's complex exosphere, both from an observational and theoretical point of view, several reviews can usefully be consulted: Hunten et al. (1988), Hunten and Sprague (1997), Killen and Ip (1999), Leblanc et al. (2007), Killen et al. (2008) and, more specifically on ground-based techniques, Cremonese et al. (2010).

2.4 Summary

The planet Mercury is in many aspects a very peculiar planet. Locked in a 3:2 spin-orbit resonance and orbiting close to the Sun, it is one of the least known major bodies in the Solar System.

The presence of a weak magnetic field creating a very dynamic magnetospheric cavity in interaction with the solar wind plasma, where fast energy exchanges and acceleration processes take place, and of a tenuous surface-bounded exosphere makes Mercury a formidable in situ laboratory for plasma physics. A unique feature of Mercury's space environment is its strongly coupled surface-exosphere-magnetosphere-solar wind system, which can remotely be monitored by space missions (Mariner 10, MESSENGER and soon BepiColombo) and by ground-based observatories (Kitt Peak, McDonald observatory, THEMIS, etc.).

Mercury's exosphere is a very complex medium with only seven species detected so far, either from space (H, He, O and Mg) or from the ground (Na, K and Ca). Despite this success and owing to the inherent difficulty of observing Mercury near the Sun, few direct observations have been made. From ground, sodium Na Fraunhofer D_1 and D_2 lines are the brightest and the easiest to observe, motivating observational surveys and extensive modelling of its associated neutral species Na.

One particular species, hydrogen H, has only been detected once (Mariner 10 in 1974-1975) and warrants further investigation both on the observational and modelling sides, as it has never been consistently modelled. The processes of formation of exospheric hydrogen at Mercury, involving surface-bounded source and loss mechanisms, represent a key element/tracer of the interaction between the solar wind and Mercury and may serve as a test of current exospheric theories. The feedback is twofold:

1. Exospheric models on other bodies (like the Moon) help build a rough description of Mercury's exosphere.
2. Mercury's exospheric model adapted to simulate in-situ measurements help improve the existing theories and may be ported in turn on other bodies.

These aspects highlight the need to develop new dedicated instruments, such as PHEBUS, with high sensitivity and spectral resolution, in partnership with state-of-the-art simulations, such as the Monte Carlo model SPERO: the ambition is not only to prepare for the upcoming observations of hydrogen and its scattered emissions like Ly- α but also to achieve a global theoretical understanding of the Sun-Mercury connections.

Chapter 3

SPICAV: Differentiate ultraviolet signatures

"The Earth is a satellite of a star. Now, as in the future, we are inhabitants of the skies. Whether we know it or whether we are ignorant of it, we live, in reality, among the stars."

3.1 Stellar occultations and calibrations of the SPICAM and SPICAV instruments

The goal of this study is to analyse stellar spectra used for ground- and flight/orbit calibration. To inquire as to what can cause problems and how the spectra are influenced by outside and inside factors and how to counteract them when possible.

The end result should generate a mean spectrum per star, with errors, as free from perturbations as possible. These can in turn be compared to earlier stellar observations made by for example the Hubble Space Telescope (HST) or the International Ultraviolet Explorer (IUE) to confirm the accuracy and resolution of the SPICAM/SPICAV instruments.

Since the instrument PHEBUS is very similar to SPICAM and SPICAV, who in turn are nearly identical, the calibration of these instruments is also similar. Therefore this study is an excellent introduction to how the ground- and in-flight calibration for PHEBUS can be performed and optimised.

This chapter has been divided into three parts. The first part describes the characteristics and comparison of all three instruments. The second part is focused on the basic understanding of what a stellar calibration spectrum is and what problems can arise and how to treat them. The third part focuses on the very common problem of aging with instruments in space, that also has affected the SPICAV instrument.

3.2 The UV spectrometers on board the Mars Express and the Venus Express missions

3.2.1 General overview of the instruments

The instruments SPICAM and SPICAV are nearly identical. SPICAM was the first instrument launched and its design was reused for the SPICAV on the Venus Express mission. PHEBUS, though still in conception phase, is also a UV spectrometer and can therefore take use of the lessons learned from SPICAM and SPICAV.

SPICAM UV spectrometer on the Mars Express mission to Mars

SPICAM is a dual spectrometer (UV and IR) primarily dedicated to the study of the atmosphere of Mars (Bertaux et al., 2006). The UV imaging spectrometer was designed with a range of 118–320 nm and a resolution ranging between 1.5 nm (low sensitivity with narrow slit) and 6 nm (high sensitivity with wide slit), the UV atmospheric absorption of CO₂ (below 200 nm) and the Hartley ozone absorption (220–280 nm) decided the wavelength range for the instrument.

The CCD detector is an array of physical dimensions 408×288 pixels. The spectra are spread along the 288 lines of the CCD that are perpendicular to the slit axis and parallel to the dispersion plane of the grating. Of the 408 pixels in each line, only 384 pixels are used to measure the spectra while the remaining pixels, of which some are masked, are used to calculate the dark current of the CCD.

Every measurement has an integration time of several hundreds of milliseconds, typically 640 ms and the gain of the CCD is adjusted according to the brightness of the source.

Due to limited telemetry bandwidth, only 5 bands are read and transmitted to Earth while the rest is lost. To increase the signal to noise ratio, the five transmitted spectra are the sum of a chosen number of physical lines of the CCD. A line is defined as a line of pixels along the spectral dimension of the CCD, in this case typically 1, 2, 4, 8, 16 or 32. Usually, for stellar occultations, this number is either 8 or 16 physical lines of the CCD.

Up to 90% of the stellar signal is located in the central band while the other bands contain the rest of the signal (Bertaux et al., 2006).

The 'modes' define which lines are read and how many lines of pixels are summed. The mode most used is the 'binning' mode shown in Figure 3.1. For a more thorough description of the optical design and the gratings, see Figure 3.2 and Figure 3.3 and Bertaux et al., (2006).

SPICAM has a great versatility of observation modes: nadir and limb viewing (both day and night) and solar and stellar occultations. This is because of the large capacity to orient the spacecraft in its orbit and also because of the retractable slit. The slit placed at the focus of the entrance mirror can, during a star occultation, be removed from the light path.

Scientific results so far include findings relevant to CO₂, dust (Montmessin et al., 2006), cloud vertical profiles, the ozone column (Lebonnois et al., 2006), dayglow and nightglow (Leblanc et al., 2006, 2007; Simon et al., 2009) and aurora-like structures linked to Mars' crustal magnetic field anomalies (Bertaux et al., 2005; Leblanc et al., 2008).

The SPICAM IR spectrometer is not relevant for this study so it is only mentioned but not discussed.

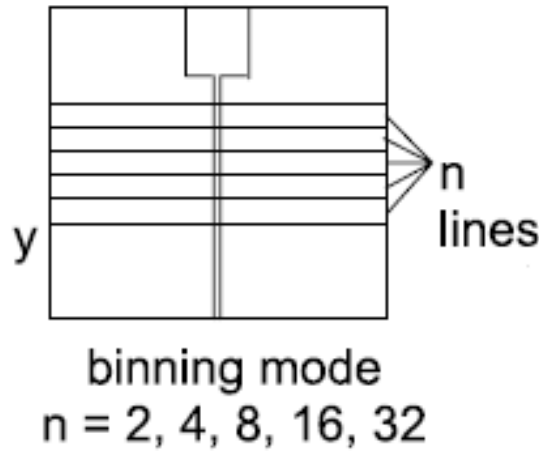


Figure 3.1: Layout of the CCD read-out mode. The mode most used is the 'binning mode', with five bins of 2, 4, 8, 16 and 32 lines are read at the same time. This corresponds to five bands that are distributed spatially along the slit. The band located furthest away from the wide slit is therefore least contaminated by solar stray light entering the spectrometer through the wide part of the slit (Image Bertaux et al. (2005)).

SPICAV UV spectrometer on the Venus Express mission to Venus

As a follow-up spectrometer to SPICAM, SPICAV is the acronym for 'Spectroscopy for the Investigation of the Characteristics of the Atmosphere of Venus' (Bertaux et al., 2007). It consists of three spectrometers on board the Venus Express mission, working in the UV and IR ranges. With a total mass of 13.9 kg its scientific objective is the study of the atmosphere of Venus from the surface to the exosphere.

In addition to the original design taken from SPICAM (Service d'Aéronomie, France), a high-resolution IR spectrometer called SOIR (Solar Occultation in the InfraRed), made in Belgium at BIRA-IASB, has been included.

The UV spectrometer channel (118 – 320 nm, resolution 1.5 nm) is identical to that of SPICAM. A summary of the characteristics of the SPICAV UV spectrometer with respect to SPICAM and PHEBUS is given in Table 3.1.

PHEBUS UV spectrometer on the BepiColombo mission to Mercury

The double spectrometer PHEBUS, see Figure 3.4 covers the range of Extreme Ultraviolet (55 – 155 nm) and Far Ultraviolet (145 – 315 nm). Focusing on the characterisation, composition, dynamics and surface-exosphere coupling of Mercury, PHEBUS addresses the following main scientific objectives: determination of the composition and the vertical structure of the exosphere, determination of the exospheric dynamics: day to night circulation, active to inactive regional transport, study of surface release processes, identification and characterisation of the sources of exospheric constituents, detection and evaluation of the ionosphere and its relation with the neutral atmosphere, space and time monitoring of exosphere/magnetosphere exchange and transport processes, study

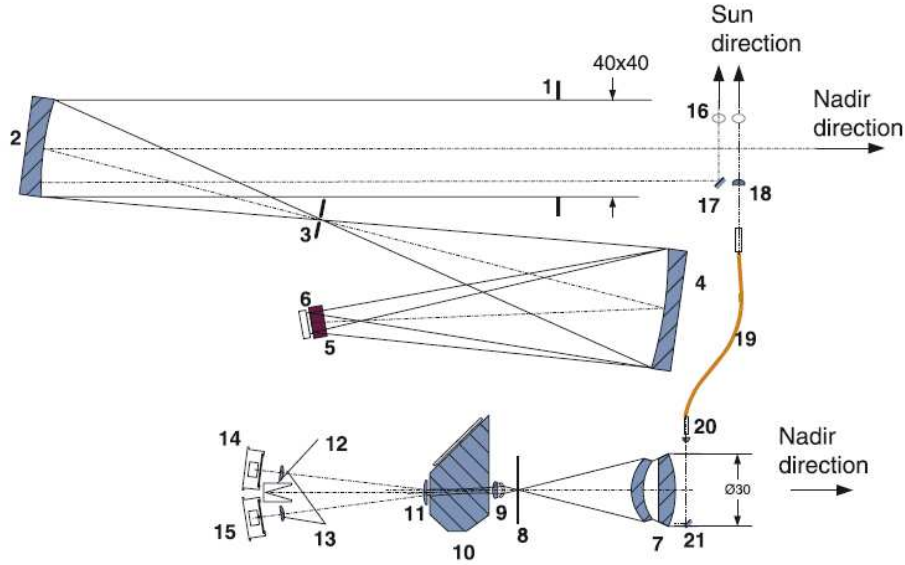


Figure 3.2: Optical layout of the UV and IR channels of SPICAM and SPICAV. **1** mechanical stop of the UV channel aperture, **2** off-axis parabolic mirror, **3** slit (can change from wide to narrow by a mechanical actuator), **4** concave UV grating, **5** intensifier, **6** CCD, **7** IR channel objective, **8** IR FOV diaphragm, **9** and **11** collimating lenses, **10** Acousto-optic tunable filter crystal, **12** light trap for undiffracted light, **13** detector proximity lenses, **14** "extraordinary" beam detector, **15** "ordinary" beam detector, **16** solar opening (is closed by shutter when not observing the Sun), **17** and **21** flat mirrors, **18** IR solar entry, **19** optical fiber, **20** fiber collimator (Image Bertaux et al. (2005)).

and quantification of escape, global scale source/sink balance and geochemical cycles synergistically with other experiments of BepiColombo (MSASI, MPPE on MMO and MIXS, SERENA on MPO).

3.2.2 SPICAM and SPICAV datasets

The data derived from the UV channels from both SPICAM and SPICAV consists of several observing modes with different objectives such as in Nadir, Star or Limb mode.

- In Nadir mode the line of sight is pointed directly to the planet, to analyse the solar radiation that has been filtered through the atmosphere and then reflected on the surface of the planet. These kinds of observations allow the measurement of total column abundance of atmospheric components.
- In Star or Sun mode, the instrument points tangentially through the atmosphere toward a star, or the Sun, which is observed through the atmosphere as it rises or sets. The instrument then analyses the light filtered by the atmosphere allowing derivation of vertical concentration profiles for atmospheric components. This is the mode used for occultation observations.
- Limb mode where the instrument points across the atmosphere to analyse the atmospheric glow just as in Star mode, but without a target star.

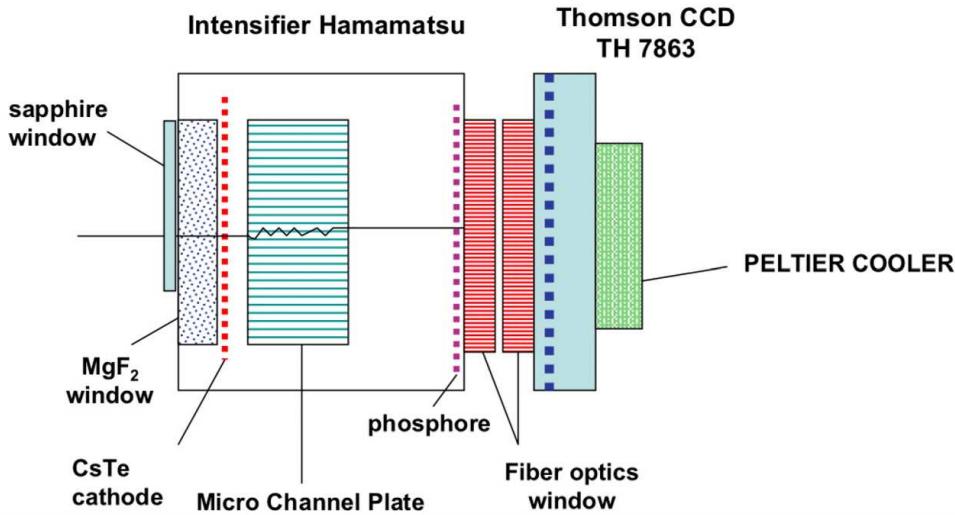


Figure 3.3: Layout of the SPICAM and SPICAV UV detector. Light pass through the sapphire window which is placed at the entrance to block second order grating diffraction, this feature does not exist on SPICAV. The light then passes through the UV image intensifier (Hamamatsu) which transforms each photon into a light pulse generated by the phosphor output screen. The image is then conveyed through two blocks of fiber optics until it reaches the Thomson CCD. The Peltier cooler has the purpose of cooling the CCD and thus lowering the dark current (Image Bertaux et al. (2005)).

Star mode and stellar occultations

The general principle of the Star mode or stellar occultation is quite simple, see Figure 3.5.

As the instrument is moving along its orbit, the planets limb is located opposite or perpendicular to the velocity vector. The instrument is then, at a predetermined time, oriented in such a way that the line of sight is pointed toward a given star.

When the star is high above the horizon of the planet, at least 300 km of altitude for Venus where the atmosphere has substantially thinned down.

The instrument records the spectrum of the star chosen while still unaffected by atmospheric absorption, as a reference spectrum. Then, as the spacecraft is maintaining its line of sight to the star, the star intersects deeper and deeper into the atmosphere, down to total occultation when it arrives completely behind the planet.

The spectra recorded, while the star is occulting, is the spectra from the star but altered by the absorption of all atmospheric constituents integrated over the line of sight from the instrument to the star (Bertaux et al., 2007).

The stellar occultation technique offers three critical features:

- Star occultations are a self calibrated method since a reference spectrum, the star spectrum, is taken at each observation. Even though the method is a relative measurement the result is an absolute concentration in no need of instrument calibration.
- The result has an excellent vertical resolution, no matter what distance to the planet, since the star is treated as a point source.

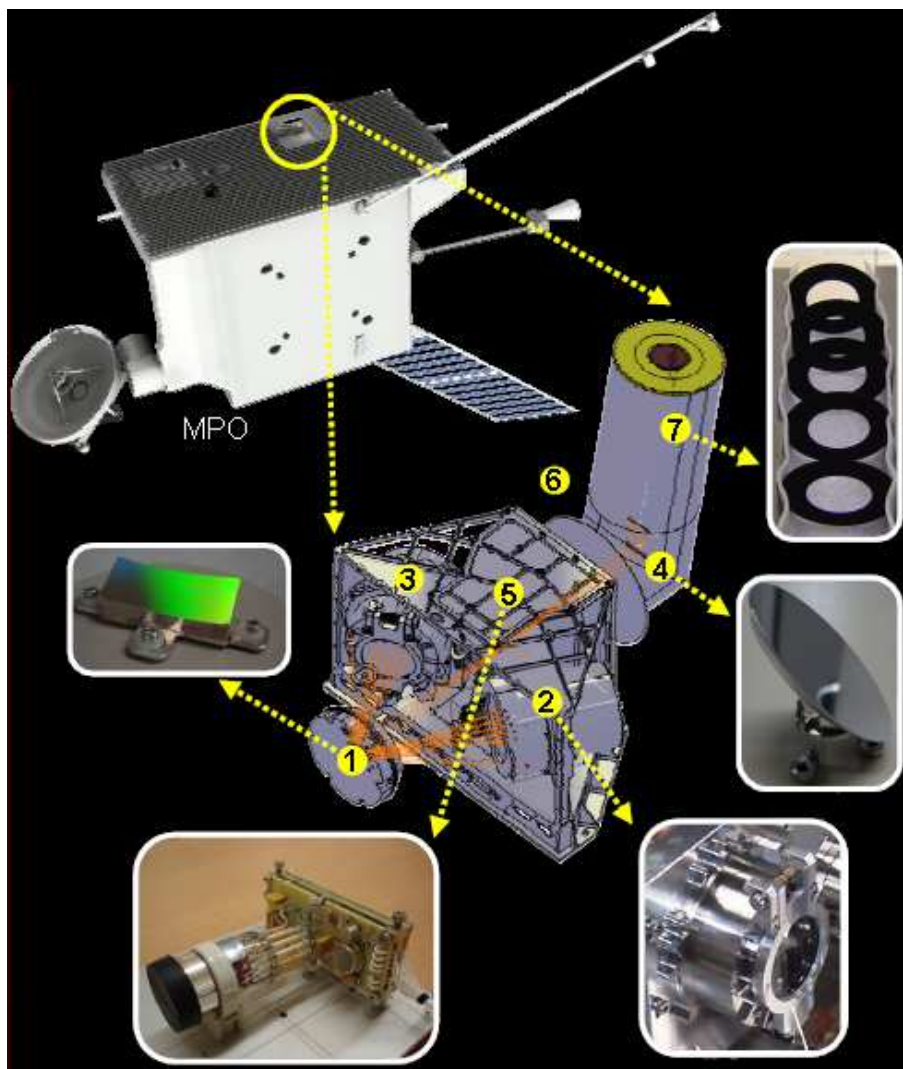


Figure 3.4: PHEBUS consists of two holographic gratings (1) and two detectors EUV (2) and FUV (3) which are fitted within a very compact design. In order to prevent sensitivity losses which are critical in UV ranges, a minimum of reflections is achieved inside the instrument using only an off-axis parabola mirror (4) and the set of two gratings. The spectrum detection is based on the photon counting method using Micro Channel Plate (MCP) detectors with resistive anode encoder, coated with CsI for the EUV range and CsTe for the FUV range. Extra visible lines (K at 404.7 nm and Ca at 422.8 nm) are monitored using photomultipliers (5), also used in photon counting mode. A one degree-of-freedom (360 angle) scanning system (6) with its baffle (7) to reduce stray light, allows probing at the highest possible signal-to-noise ratio in the selected regions and altitude ranges of interest (Image ESA and PHEBUS Team, LATMOS).

	SPICAM UV	SPICAV UV	PHEBUS
Slit width (mm)	0.05, 0.5	0.05, 0.5	0.28
Slit length (mm)	6.6	6.6	5.6
Field of view ($^{\circ}$)	1×3.16	1×3.16	$2^{\circ} \times 0.1$
λ range (nm)	118-320	118-320	55-310
			404, 422 (NUV)
Detector	CCD	CCD	MCP
Detector size (pixel)	384×288	384×288	512×512
Resolution (nm)	1.5	1.5	$1.5^1, 1^2$
Type	Holographic	Holographic	Holographic
Coating	MgF_2	MgF_2	$\text{CsTe}^1, \text{CsI}^2$
Dimensions (mm)	50×50	50×50	42×15
grooves per mm	280	280	$1600^1, 2700^2$

Table 3.1: Comparison of the characteristics of the SPICAV, SPICAM and PHEBUS channels and diffraction gratings. ¹FUV, ²EUV

- The accuracy of the altitude measurements are independent of the position in flight of the spacecraft. The line of sight is entirely determined by the placement of the star in the sky and the position of the instrument in its orbit.

Several occultations per orbit can be performed, preferably on the night side of the planet to avoid contamination by the bright limb. The only limiting factors being the spacecraft orientation and the amount of stars suiting the instrument.

It can be noted that when the star is first observed and then disappears behind the planet its referred to as a *occultation* while if the star appears behind the planet first and then rises out from behind its referred to as a *de-occultation*.

Calibration stars

The orbit of SPICAV is fixed in inertial frame, so when a star is occulted at one orbit, the same star will be occulted during the following orbits at the same latitude. Therefore stars, that are suitable to be occulted at various latitudes, have to be found so that the occultations can be observed in a repetitive manner to increase the statistics.

The stars chosen to be used for calibration purposes are all a small part of the list of stars that have previously been recorded by the Hubble Space Telescope (*HST*) and the International Ultraviolet Explorer (*IUE*). In general hot stars have been favoured for these two instruments since they have a wide spread in the UV wavelengths. PHEBUS, which has an even wider range in UV, will, in addition to the stars already listed, most definitely need even hotter stars, for example the Wolf-Rayet stars, than the ones used for SPICAM and SPICAV.

The stars that are referred to as hot usually have the Morgan-Keenan spectral type 'O' or 'B' with a temperature ranging between 10000–30000 K (B) and above 30000 K (O) and in the Hertsprung-Russel diagram they appear as blue or blue-white.

Hot stars are preferred for calibration purposes for these kind of instruments because they are brighter in UV wavelengths (Bertaux et al., 2006). The brightness of these stars can be as much as above 25000 solar luminosities. Since they are bright they also have reasonably constant signal over the whole wavelength range.

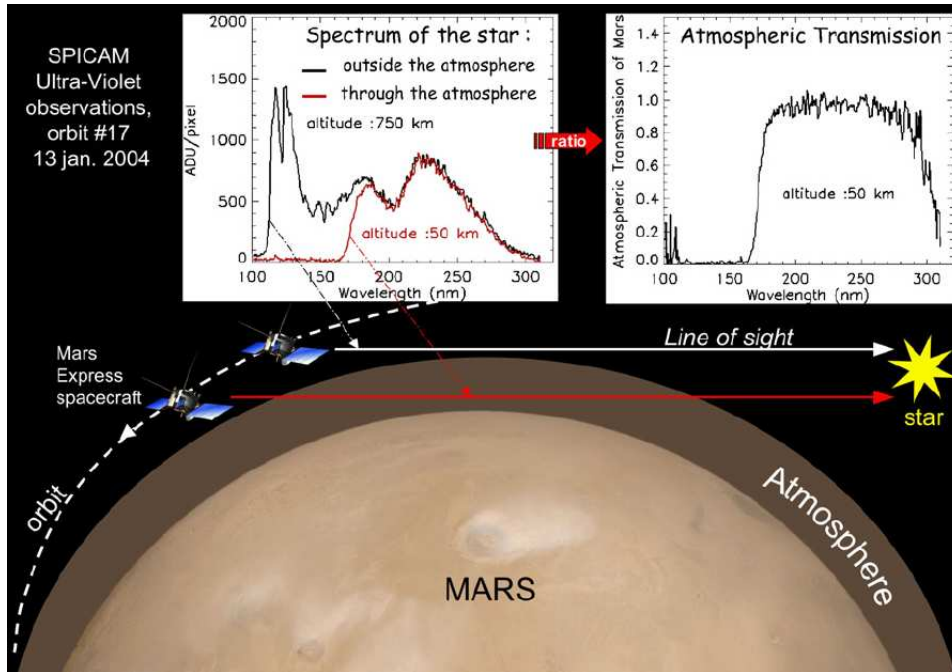


Figure 3.5: Schematics of a star occultation. The spectra in the image come from the very first stellar occultation made by SPICAM, although the principle is also similar for SPICAV. From these two spectra, obtained before and after the occultation, the atmospheric transmission can be derived as a function of wavelength. Below 180 nm in wavelength the signal from the star is almost completely absorbed by CO_2 (Image Bertaux et al. (2007)).

The negative point of using these bright hot stars for calibration purposes is that the latitude range is very restricted since these stars are not distributed uniformly on the sky, but concentrated along the galactic plane (Quemerais et al., 2006). They are also very rare (less than 0.1% of all main sequence stars).

SPICAM stellar data set

As mentioned in Bertaux et al. (2006), the stars used for the calibration of the UV channel in SPICAM are:

- Zeta Puppis (*O36/HR3165*)
- Eta Uma (*O57/HR5191*)
- Beta Cen (*O60/HR5267*)
- Zeta Oph (*O77/HR6175*)

The first number in the parentheses is a reference number of the star in the SPICAM star catalogue while the second number (HRxxxx) stands for the Harvard Revised Number or the Bright Star Number in the Bright Star Catalogue. This catalogue lists all stars of stellar magnitude 6.5 or brighter, which is roughly every star visible to the naked eye from Earth. See Table A.1 for a full list of all the stars used by SPICAM.

The orbits used in this study and with these calibration stars all date between August 2006 and September 2008. The amount of observations differ between 3 to 41 orbits depending on which star was being used. With one spectrum taken each second a typical observation will yield around 800 spectra per orbit.

The usable frequency of these spectra for calibrations completely depends on the pointing and observation conditions such as placement of CCD in the line-of-sight, the actual orbit altitude, the illumination of the atmosphere and the instrument and star problems that can arise.

Instrument problems showing in the spectra

- **Stray light inside instrument**

As seen in Figure 3.1 the design of the CCD reading opens for a large chance of stray light pollution coming from the wide slit. This is because light entering the wide slit will spread over a larger surface than the light coming from the narrow slit when both of them are illuminated. This stray light can account for as much as up to 10% of the total signal recorded (Bertaux et al., 2006).

In star occultations the star is centered on the third band, thus reducing the stray light contamination although not completely.

- **Offset**

Star occultations are usually made without the slit since the star is considered a point source. Although this is true, some star occultations were performed on the day side with the slit. This is because the slit helps in partially eliminating the scattered solar light, due to dust and atmosphere at the limb.

Some of these observations were successful. The star signal from these observations is about two times weaker than without the slit because of the optical aberrations emanating from the off axis parabolic mirror. But many others failed because the pointing turned out to be non-repeatable.

With exactly the same offset angles¹ the spectrum of star Zeta Puppis should be at the same place on the detector, but it is not. As shown in Figure 3.6, the spectra collect in two places differing by about 6 nm in wavelength shift.

The problem was traced to the use of either the star tracker A² or the redundant star tracker B, whose offsets with the XYZ body axis of the spacecraft are not identical. In the spacecrafts on-board software only the offset of the nominal star tracker A is taken into account even though some early observations were made with star tracker B. This is something that has to be carefully examined and corrected in all the observations to exactly determine the wavelength assignment³ (Bertaux et al., 2006).

SPICAV stellar data set

Since SPICAV is an almost identical copy of the SPICAM instrument, all the factors that have been previously mentioned for this instrument will also affect the SPICAV including

¹Defined as the angle from NADIR to the point where the S/C line of sight intersects the surface, as seen from Mars center, positive toward the orbital angular momentum.(MEX Instrument Request (MREQ) File Format Definition and Conventions, MEX-SGS-IF-002 Issue 1.2, 13 March 2009).

²The primary function of a star tracker camera is to provide stellar images that are processed against an on board star catalog to find pointing, thus establishing absolute angular references for attitude determination (Kordas et al., 1995).

³The wavelength of each pixel.

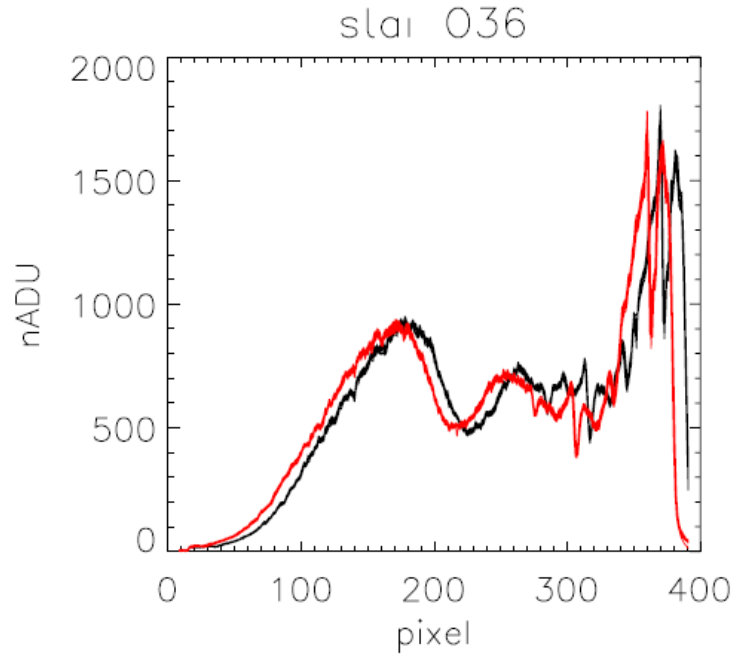


Figure 3.6: Typical example of the offset shifting problem with SPICAM. Overplot of 31 spectra of the star Zeta Puppis (O36 in the SPICAM catalogue) recorded by SPICAM as a function of pixel position. Please note that the x-axis in pixels is reversed scale in wavelength. 23 spectra (red line) are falling at the expected position, determined by the strong Lyman- α absorption line. 13 spectra (black line) are shifted by about 12 pixels, corresponding to a pointing error of 0.12 degrees (Image Bertaux et al. (2006)).

additional problems specific to SPICAV. Therefore, from now on, this study will only treat spectra from SPICAV. Of course all the applications made can also be used for star spectra from SPICAM observations - although not necessary for this study.

The stars used for the calibration of the UV channel in SPICAV are the same four as for SPICAM but with one extra addition:

Alpha Eridanus (*O5/HR0472*).

Please see Table A.1 and Table C.1 for a full list of all the stars used by SPICAV.

Typical datasets include stars which yield very different qualities in the star occultation data. A good example is the star Alpha Eridanus (HR0472/O5) which has a large consistent dataset: most of the data has been observed for a long time, more than 80% of the flux is located in the middle band (band 3) and most spectra are observed above 300 km altitude. All of this adds to the possibility of having reliable statistics, something that increases the confidence in the results. A bad example is Eta Ursae Majoris (HR5191/O57) which has a small inconsistent dataset: the star has only been observed for a short time, almost no data have more than 80% flux in the middle band and almost all data was observed under 300 km of altitude. This results in an extremely small dataset practically unusable for calibration (or any other kind of work).

3.3 Star calibration

The goal of a star calibration is to produce from observations an average spectrum in the UV range calibrated in wavelength and intensity. The spectrum of the star measured at regular interval during the mission provides a reference to monitor the sensitivity degradation of the instrument with time, which has to be taken into account for the retrieval of species abundances in the exosphere of Mercury.

3.3.1 Theoretical background

Star calibrations refers to the calibration of an instrument performed on ground, in space, in flight or orbit on a set of stars that spectrally suit the instrument.

Usually an absolute photometric calibration is performed on the ground before an instrument can be sent into space, but due to the limited accuracy to simulate the conditions in space the instrument always has to be double checked and fine-tuned when they reach space. This is of utmost importance for the observations since a good knowledge of the absolute sensitivity is necessary to perform a correct analysis of emission measurements. Figure 3.7 shows the difference between the ground calibration and the in-flight calibration very clearly, emphasizing the need for the in-flight calibration to be performed and, if possible, perfected during the course of the mission.

A typical stellar observation can be seen in Figure 3.8.

Star observation problems showing in the spectra

It does not always have to be that the faults recorded in the datasets are originating from the instrument, for example the choice of stars can have a deep impact on the result.

Unstable stars

A star initially chosen for calibration from the IUE reference library, Delta Scorpii, proved to be a very bad choice. Firstly because it is a multi-companion star, something that can affect the brightness in general since the companions will orbit the primary star and thus creating a variable brightness. Secondly because the primary star had a close encounter with one of its companions, in the beginning of year 2000, triggering an outburst of the primary star, increasing its magnitude from 2.3 to 1.5. This eruption is still continuing today.

Most stars are actually double, or multi-companion, stars. This is something that has to be taken into account when the calibration stars are chosen. It does not always have to be a problem since often the companion star is so small and dim that it does not affect the apparent spectrum from the primary star. But in certain cases it can cause problems such as the one mentioned above with delta Scorpii.

Solar stray light

Solar stray light can be a problem in itself or cause problems when reflected off another surface, such as an atmosphere or a planetary surface. Figure 3.9 shows typical wavelength ranges for such pollution and a typical spectra polluted by solar stray light can be seen in Figure 3.10.

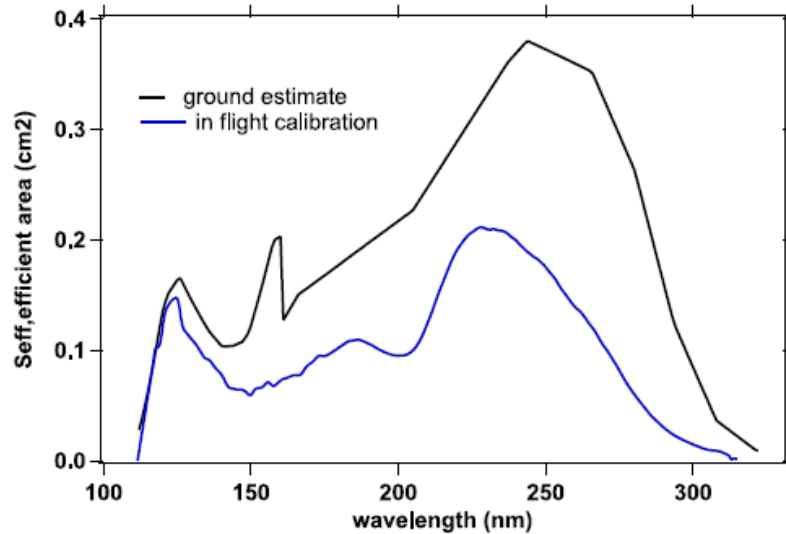


Figure 3.7: Efficient area (cm^2) vs wavelength, which is a measure of the sensitivity of SPICAM to a stellar source. Black curve shows the estimation made from the ground calibration before flight. The blue curve shows the in-flight sensitivity determined by comparing measured spectra (in ADU) of the star Zeta Puppis to the IUE absolute spectrum of the same star. The long wavelength decrease is due to the CsTe on the CCD, while the short wavelength decrease is due to the cut-off of the MgF2 window of the detector. It is also the MgF2 window that causes the sharp peak at around 160 nm, something that does not exist on SPICAV since this window is not present in the instrument. The reason it cannot be seen in the blue curve is because the photo cathode near the mechanical edge is seeing a part of the grating through the sapphire window and another part without the sapphire window so the curves smoothes out (Image Bertaux et al. (2006)).

Before raw spectra can be used for calibration, or other purposes, they need to be processed. The spectra that is used in this study come from observations made of stars that have been previously used as the calibration stars of the UV channel on SPICAV.

To get a general idea of the spectra and their characteristics before any processing, all spectra recorded for one star are plotted in the same graph. This gives an idea of the eventual irregularities that can occur within the spectra or other features that will need processing. It also shows how the spectra change with respect to the gain applied at the observation, see Figure 3.11.

A typical example of a normal spectrum that is in no need of processing can be seen in Figure 3.12 while Figure 3.13 gives an example of a spectra in need of processing.

The processing of the star spectra includes calibration and correction of wavelength shifts and is performed in a step-by-step approach:

Step by step approach

- Choice of stars

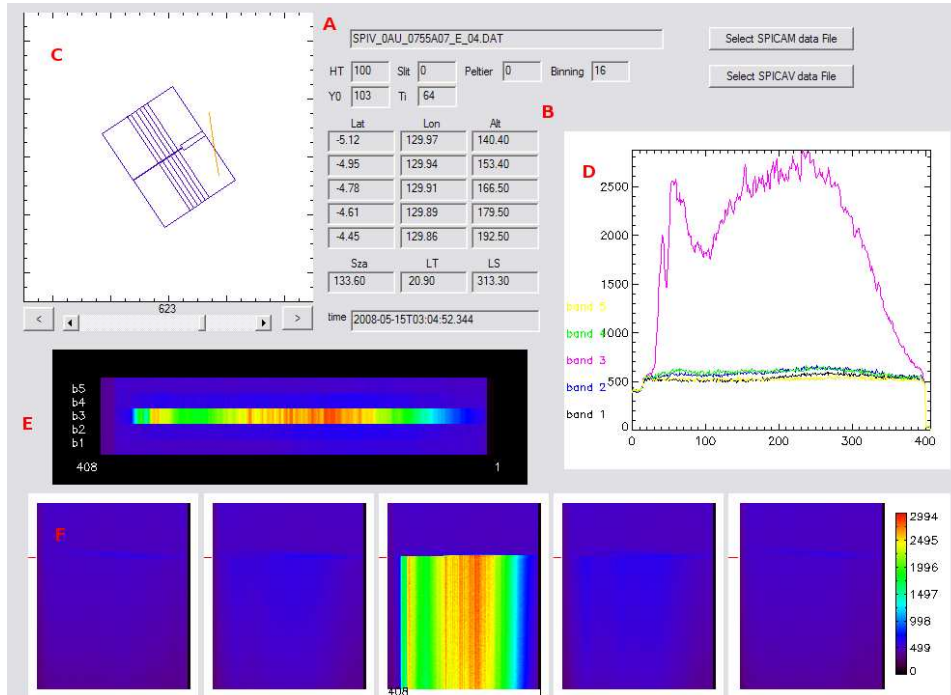


Figure 3.8: Typical display of all the original spectra from one observation. These spectra are from the SPICAV observation of the star HR0472 from the orbit 0755A07 the 15 May 2008 and are thus very recent. The entire display was generated by a program, courtesy of A. Reberac, LATMOS. This program can step by step go through all the spectra in the entire observation and show the position of the CCD at a specific time and in relation to the distance of the planets surface. Then for each step it also displays the spectrum divided into the five bands on the CCD. Legend: **A:** The observation filename and all general information about the instrument settings at the time of observation, such as HT, slit (on=1, off=0) and Peltier cooling (on=1, off=0). **B:** The latitude and longitude for the center of the CCD and the calculated distance from the surface of the planet. It also displays the solar zenith angle - an angle of above 90 degrees (classified as 'day') could lead to solar contamination. **C:** The blue square represents the CCD with the five bands and the two differently sized slits while the orange line represents the limb of the planet. For each time step the orange line will move, in this case, either to the right or left representing the CCD's line of sight moving closer or farther away from the limb. The bar right underneath this window is used to move backwards or forwards in time. **D:** Graphical plot of the spectra observed at a certain time step, here all five bands are separated showing band 3 as the band with most of the flux. **E:** Intensity map of the spectrum showed in **D**:. **F:** Graphical representation of the entire observation made in all the five bands.

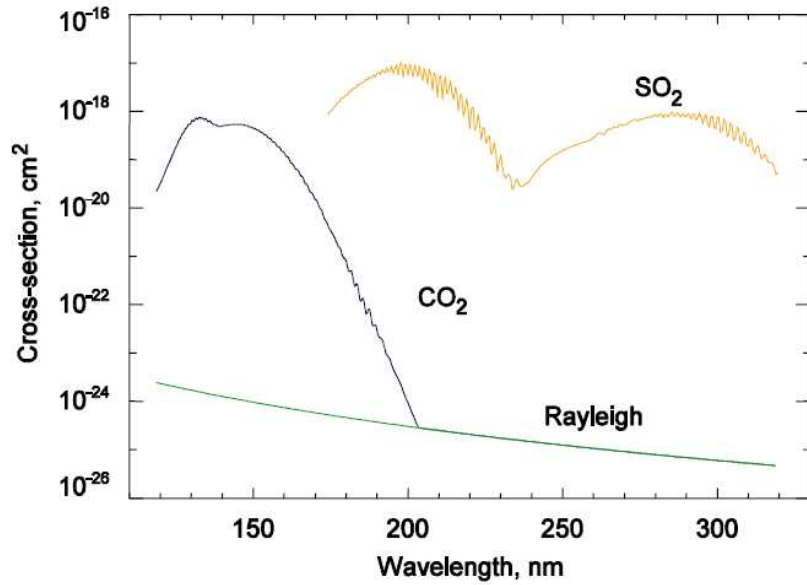


Figure 3.9: Typical example of the different interference that can pollute the observations; extinction cross-sections of CO₂ and SO₂ a characteristic for the Venus atmosphere in the spectral range of SPICAV and the Rayleigh extinction of CO₂ (Image Bertaux et al. (2007)).

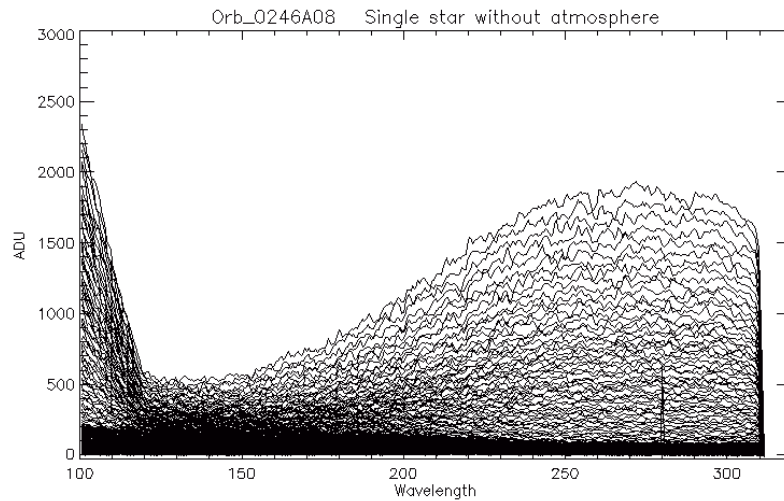


Figure 3.10: Typical spectrum with a large amount of solar stray light due to the fact that the pointing was done on the dayside too close to the sun and that the slit was off. The spectrum is from the SPICAV observation of the star HR3165 from the orbit 0246A08 the 23 December 2006, with the criteria that the entire CCD should be above 300 km of altitude.

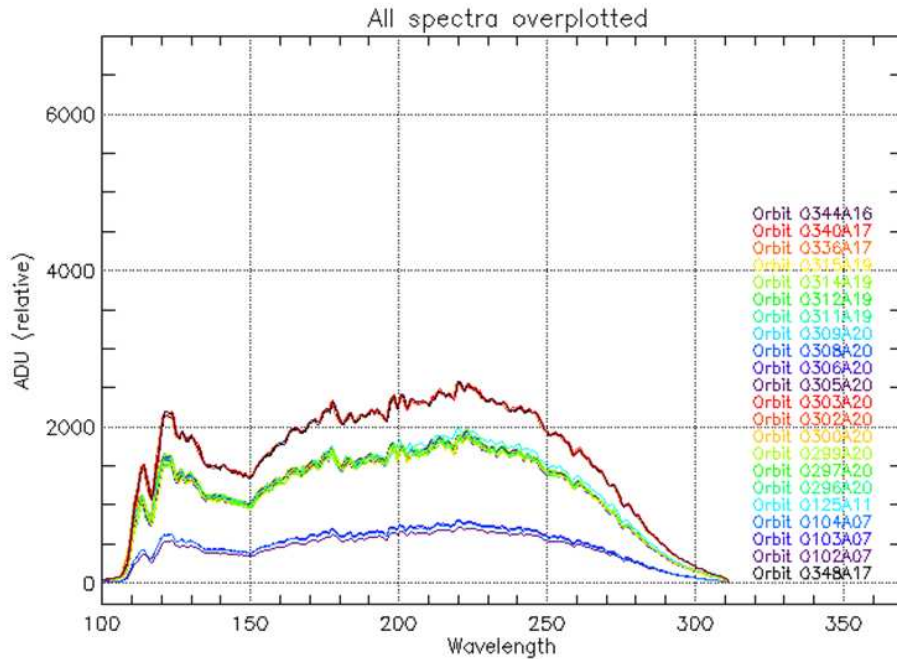


Figure 3.11: Example of original accumulated spectra of the SPICAV calibration star HR0472, of band 3 from 100 to 320 nm in ADU units for different orbits of Venus Express. The grouping of similar spectra depend on the instrumental gain set for that group of orbits. Here red is gain 100, green is gain 90 and blue is gain 60.

The stars chosen in this study are the five calibration stars used for SPICAM and SPICAV. These stars are the stars with most recorded observations among all the stars in the entire SPICAM/SPICAV lists.

- **Get raw data**

To get just the star spectra that are of interest, all other observations in the data that are not of a pure stellar nature, need to be discarded. This have to be manually selected for each star since the data can differ from star to star.

- **Flux criteria**

To have a significance, the spectra need to have a flux of more than 80% in the middle band. This was added so as to calculate the amount of flux in each band and then discard the data that contained less flux. It can be mentioned that calibrations need spectra that contain the flux in all the bands because it will contain all the photons collected while for variations in datasets only the middle band is needed as it usually contains most of the flux.

- **Offset**

As mentioned earlier the offset which is a static shifting of a set number of pixels needs to be performed to center the spectra, see Figure 3.6.

- **Correction for pointing shift**

Problem: In an ideal observation all the spectra will very neatly lie on top of each other if plotted in the same graph, though it happens that spectra does not exactly

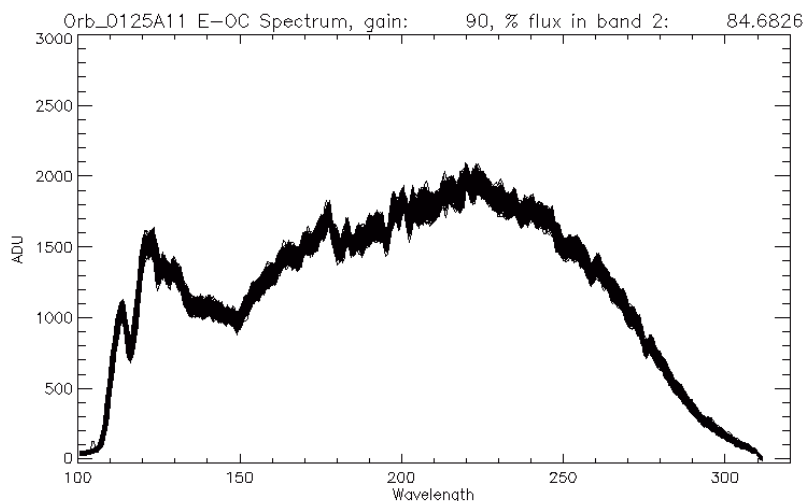


Figure 3.12: Example of original accumulated spectra from 24 August 2006, of the SPICAV calibration star HR0472 from one observation in band 3. The range is from 100 to 320 nm and in ADU units. These spectra are in no obvious need of processing and can therefore be used as is.

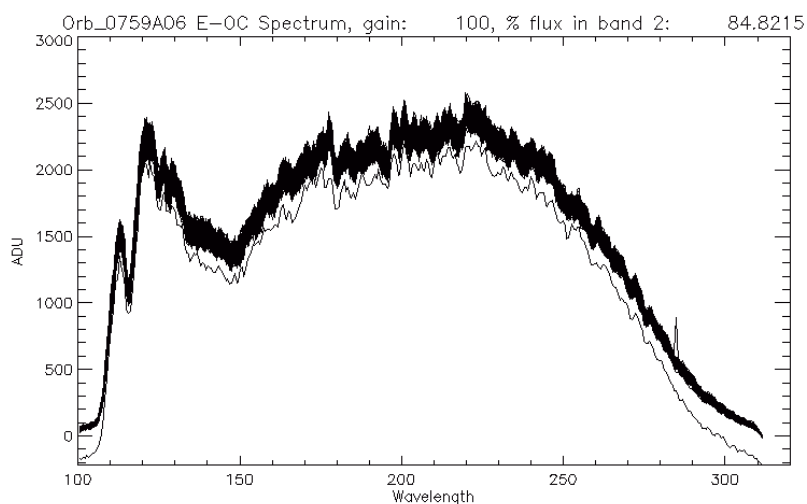


Figure 3.13: Example of original accumulated spectra from 19 May 2008, of the SPICAV calibration star HR0472 from one observation in band 3. The range is from 100 to 320 nm and in ADU units in obvious need of processing before being usable. Both cosmic radiation peaks and bad dark current removal is present.

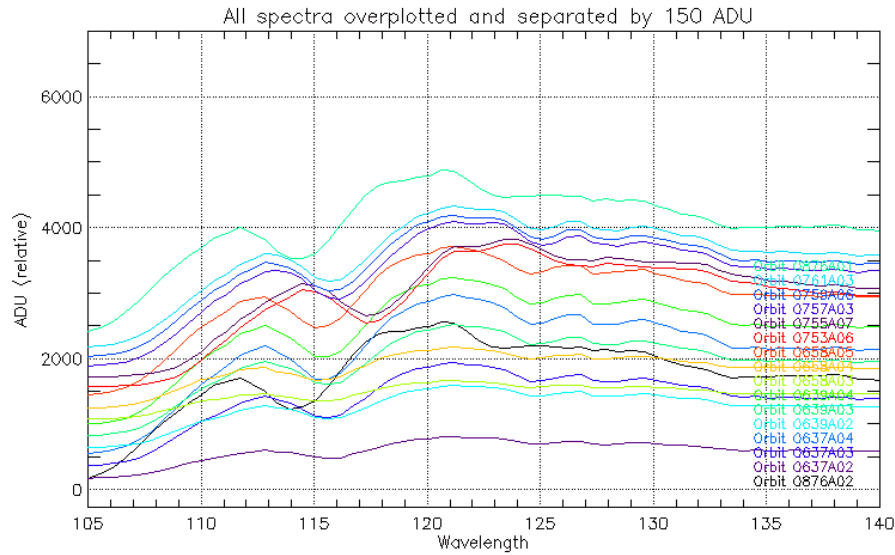


Figure 3.14: Zoom of band 3 from 100 to 320 nm in ADU units showing the spectral shift problem with the pointing. Spectra of the SPICAV calibration star HR0472 for the same orbit gets slightly shifted when the line-of sight to the star get shifted.

coincide even after calibration. This is because the line of sight can slightly change angle during the observation. This does not mean that the spectra cannot be compared, just that they need to be aligned. A typical example of this can be seen in Figure 3.14.

Solution: One of the first spectrum in the observation is used as a reference spectrum and then used together with the rest of spectra to calculate a correlation value that in turn tells if the spectra should be shifted or not. An allowance of ± 5 pixels are used.

- **Removing of data points derived from cosmic radiation**

Problem: The spectra are littered with data points that do not belong to the observation made but that arise when cosmic radiation from elsewhere impacts the CCD. These data points often give a very strong peak in the spectra as can be seen in Figure 3.15.

Solution: The average of all the accumulated spectra in one observation is calculated, to in turn calculate a variance, $\sigma = \sqrt{mean}$. This variance is used to remove data points that lie over two sigma outside of the mean curve already calculated.

- **Removal of data that has CCD LOS below 300 km**

Problem: Stray light from the sun reflected of the atmosphere can pollute the spectra so much that they are virtually unusable for calibration purposes, see Figure 3.10. This feature can arise from the fact that the field of view depends on how the orbit is planned for the instrument. In a close orbit the field of view will be much larger, and therefore the chance of stray light entering the line of sight is also much larger than in a far orbit.

Solution: To be sure that no atmospheric pollution enters the spectra, the CCD

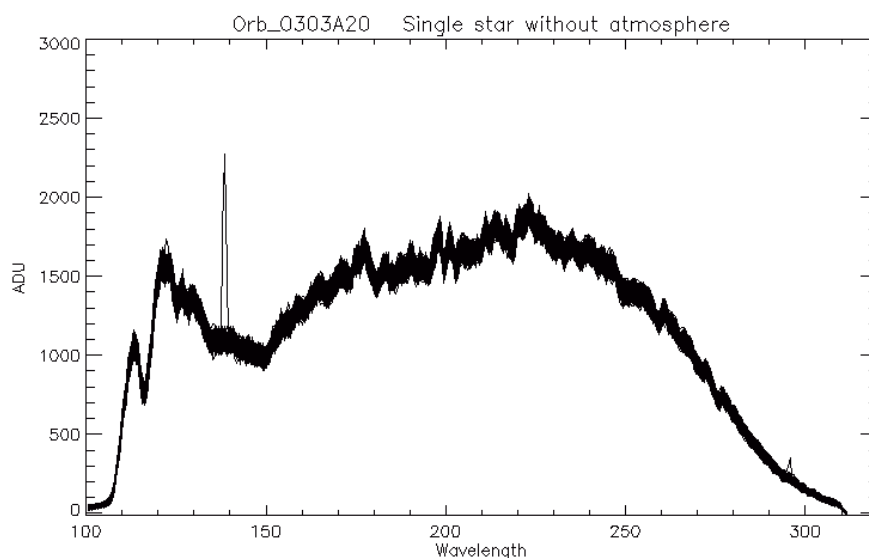


Figure 3.15: Typical example of cosmic radiation peaks - located at around 140 nm and 295 nm. The accumulated spectra is from 18 February 2007, of the SPICAV calibration star HR0472 from one observation in band 3. The range is from 100 to 320 nm and the x -axis is in ADU units.

has to be completely outside the atmosphere. Even a corner of the CCD inside the atmosphere can lead to contamination of the entire spectrum. To prevent this, a script has been added that removes all the observations that are within a certain height above the ground. In this case that limit has been decided to be 300 km, to be perfectly certain of having no contamination.

- **Removal of data that has bad dark current removal**

Problem: For reasons unknown as of now, there are some data that does not respond well to the removal of the dark current. These data appear in a graph as lying well below the mean of all other data in the same observation. See Figure 3.13

Solution: The data whose tenth pixel from the left is located below zero is subsequently removed from the dataset since this proves that the dark current that has been removed has been calculated to be too large in comparison to the observation made.

- **Calculation of mean and sigma**

Since the spectra consist of events that occur at random but at a definite average rate, the spectra can be assumed to have a Poisson distribution⁴.

Given this, a mean, and not a median should be calculated. The variance of this mean can be calculated as $\sigma = \sqrt{\text{mean}}$, as seen earlier. An example of this can be seen in Figure 3.16 and Figure 3.17.

- **Final output**

The final output from this data processing has been formatted into one .png image of the mean spectra from one observation, as seen in Figure 3.16, and as a .txt with

⁴This is assuming the spectra are in photo events and not ADU. To be noted is that all spectra up until now has been in ADU to simplify calculations.

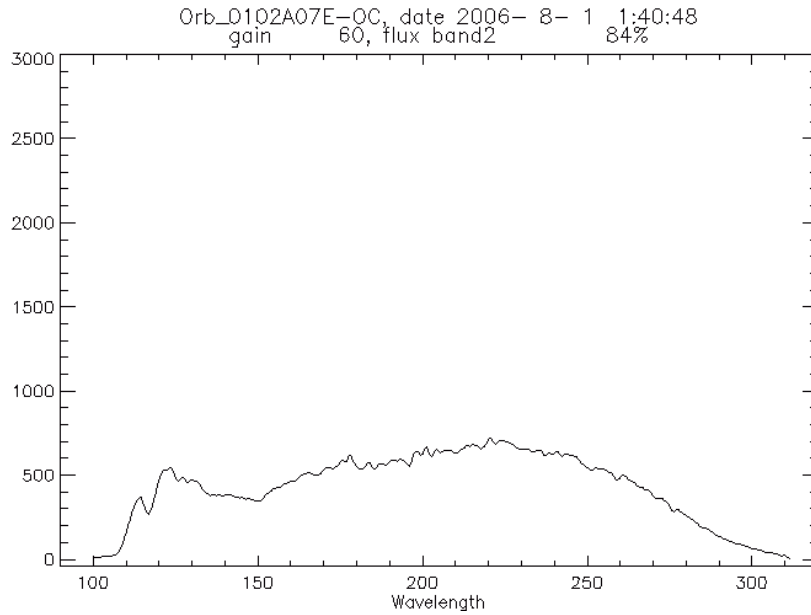


Figure 3.16: Calculated mean for one observation. The accumulated spectra are from 1 August 2006, of the SPICAV calibration star HR0472 from one observation in band 3. The range is from 100 to 320 nm and the x-axis is in ADU units.

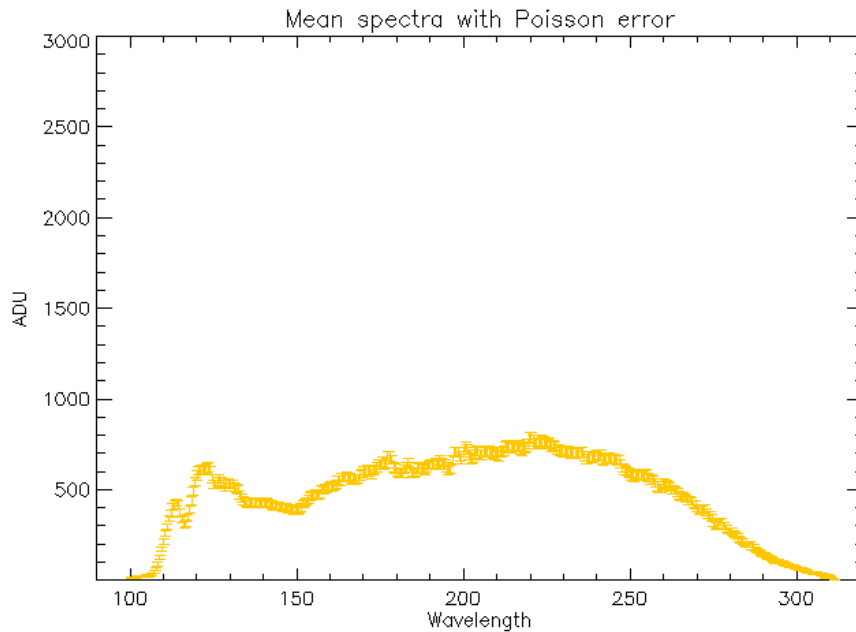


Figure 3.17: Calculated mean and variance for one observation. The accumulated spectra is the same as in Figure 3.16, 1 August 2006, of the SPICAV calibration star HR0472 from one observation in band 3. The range is from 100 to 320 nm and the x-axis is in ADU units.

```

Orbit :0102A07
Year  :   2006
Month :    8
Day   :    1
Binning:   16
ht    :    60
ti(ms) :  640.000
1st line read:  103
slit on(1)/off(0):  0

384
Lambda (nm) Intensity (ADU) Sigma
311.387      4.85517      2.20344
310.846     12.6307      3.55397
310.306     19.4158      4.40633
309.765     22.2081      4.71255
309.224     18.1149      4.25616
308.683     20.6608      4.54541
308.142     29.3366      5.41632
307.602     31.3951      5.60313
307.061     32.6632      5.71517

```

Table 3.2: Example of the header of the .txt file produced with calculated mean and variance for one observation. In this example the accumulated spectra is the same as in Figure 3.16, 1 August 2006, of the SPICAV calibration star HR0472 from one observation in band 3.

all the information about the mean spectra and its variance including gain, date, star name and more information located in the header of the file, see Table 3.2 for an example of the header.

3.3.2 Observation of intensity decrease in high wavelengths

A common feature of instruments in space is that the detector undergoes a steady deterioration that decreases the sensitivity of the instrument. The main cause of this is the usage, the aging and the conditions in space. The instruments are constantly surrounded by radiation, the extremely low temperature in space and the atmospheric conditions around the planet or object it is observing. All of these features can have an impact on the instruments and since they are all of natural occurrence they are practically impossible to completely remove, but they can be anticipated and calculated for to a certain degree.

To envisage what could affect an instrument, knowledge on the conditions in space and the reactions of metals and electronics are crucial. Also earlier information collected from instruments already in space can give information on these reactions.

It is very important to check for these occurrences since they can affect the entire calibration procedure and all other observations.

One way to see if there are any changes in the detector is simply by calculating the ratio of all the observation spectra for one star and plot them in the same graph. This is done by taking one mean spectrum (any spectrum) from one observation and divide all the

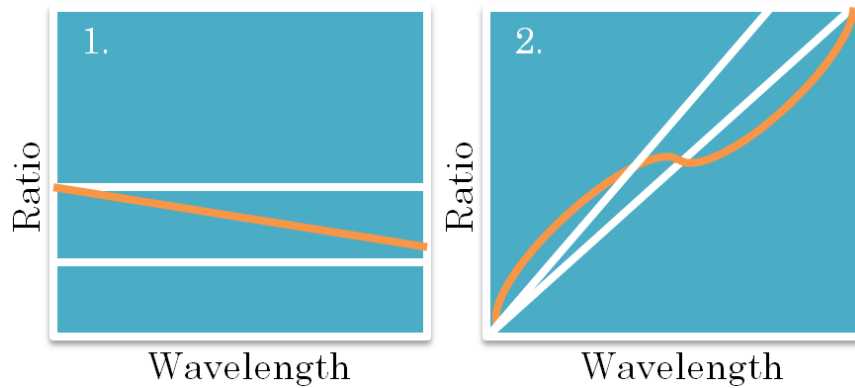


Figure 3.18: Schematic view of the ratio curves made with plotting a spectrum against another. White lines show ratios that are uniform and unchanging with wavelength, orange lines show ratios that are not uniform but change with wavelength.

other mean spectra from the other observations by this reference spectra. This will yield a straight line with different height (on the y-axis) depending on the gain setting of the instrument at the time of observation, see (1) in Figure 3.18.

If the spectra have all been taken in similar conditions, similar settings and of the same object they should normally show very little differences and thus give a straight line without any systematic errors. But sometimes the line can show a leaning or other instabilities such as can be seen in Figure 3.18.

A version of this ratio can be found if the same reference spectrum is plotted straight away against the rest of spectra. This yields a leaning line with different angles from the x-axis depending on the gain setting for the instrument, just as can be seen in (2) in Figure 3.18.

The two versions of these ratios were calculated for an example star from the SPICAV catalogue, HR0472 and the result can be seen in Figure 3.19, 3.20, 3.21 and 3.22.

The most striking feature in these plots is the obvious lean of all the ratio curves in Figure 3.19. The ratio was calculated using the earliest spectrum taken, with this star as object, as reference spectrum. All other spectra were observed between the 17 January 2008 and 12 September 2008 and are thus much younger than the reference spectrum.

One can easily see that the ratio gets higher and higher in the low wavelengths, and even more so for the spectra which has the highest gain settings.

The same data with the same reference spectrum is also plotted in Figure 3.21. The plot is showing lots of stray pixels and the lines are not sharp but blurry and show a slight falling of in the top and the bottom.

Figure 3.20 shows something different. Here the reference spectrum was picked to be much younger, from 17 January 2008, and the rest of the spectra are the same as earlier. Here all the lines are fairly straight and very little leaning is showing. The same trend is shown in Figure 3.22 where all the lines are very sharp and straight.

The conclusion from these four figures can be interpreted as that these spectra ratios display a decrease in sensitivity in lower wavelengths which becomes even worse with higher gain.

The reason this shows in the ratios, where the early spectrum has been used as reference, is because usually an instrument or a detector undergoes the greatest changes straight

after the launch when the instrument finally arrives in space. This is due to the fact that the surrounding conditions are as most extreme at this point and the instrument is not used to the conditions.

After a while (the time depends on the instrument and the conditions) the instrument gets used to the new environment and thus these changes slow down. This is what Figures 3.20 and 3.22 show, since here the reference spectrum is closer to the rest of the spectra in time the decrease has slowed down and thus the ratio lines are not leaning.

As was seen in Figure 3.11 the different spectra have different intensity (different ADU count even though the spectra look the same), the connection is the gain settings for that orbit or observation. The importance of instrumental gain is also shown in Figure 3.19, 3.20, 3.21 and 3.22.

Instrumental gain

The output of the SPICAM and SPICAV CCD is in analogue-to-digital units or ADU.

The gain G is defined as the number of ADU/photo event and is controlled by the High Voltage (which is redefined as the housekeeping parameter HT which vary from 1 to 255) setting on the MCP of the intensifier. The gain G was determined to vary from 1.0 to 79, on ground, for various levels of the High Voltage.

A photo event is defined as a pulse of light triggered in the intensifier by creating a photo electron at the intensifiers cathode. It creates in the CCD a number G of ADU (spread over a few pixels).

The star observations are done without the slit put in place in the spectrometer and since a star is considered a point source the spectral flux (ϕ) of any chosen star is photons $\text{cm}^{-2} \text{s}^{-1} \text{nm}^{-1}$.

Therefore the calibration factor of SPICAM and SPICAV is the product:

$$G \cdot S_{eff} \quad (3.1)$$

where S_{eff} is the 'efficient area' in cm^2 defined in the equation:

$$N_{phot ev} = \phi S_{eff} \quad (3.2)$$

where $N_{phot ev}$ is the number of photo-event detected by the CCD per second and per nanometer. The definition:

$$N_{ADU} = G N_{phot ev} \quad (3.3)$$

leads to the calibration equation:

$$G \cdot S_{eff} = N_{ADU} / \phi \quad (3.4)$$

In flight the gain can be checked by statistical methods: by counting the mean number of photo-events contained in the band where the star signal is located. The total ADU of the signal is analysed, and thus the gain G is determined as:

$$G = \frac{\text{Var}(\langle S_{ADU} \rangle)}{2 \langle S_{ADU} \rangle} \quad (3.5)$$

where $\langle S_{ADU} \rangle$ is the mean value of a series of measurements, $\text{Var}(\langle S_{ADU} \rangle)$ is the variance of the same series and the factor 2 comes from the non-Gaussian distribution of the number of electrons coming from a single photo-event (Sandel and Broadfoot, 1986; Bertaux et al., 2006).

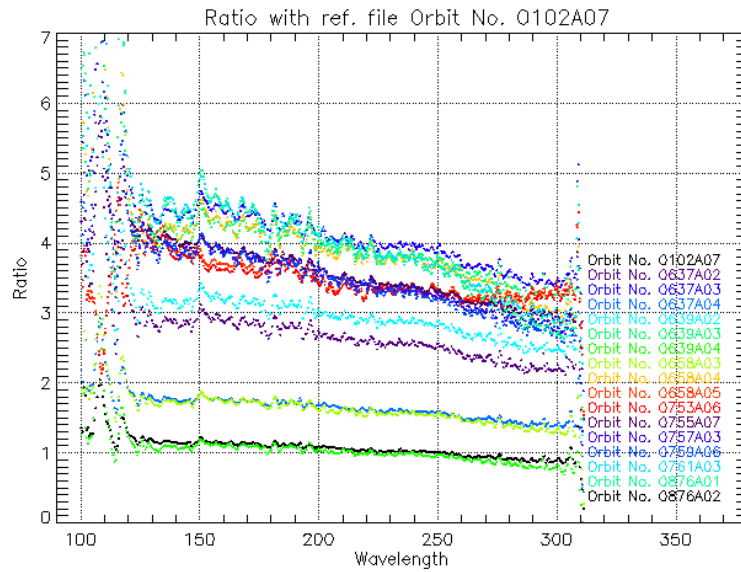


Figure 3.19: Ratio of several spectra using an early spectrum (orbit 0102A07 from the 1 August 2006) as reference, the gain for the groupings of spectra is, counting from below, 60, 75, 90, 95, 100 and 105. The lines show a steady ratio increase toward lower wavelengths.

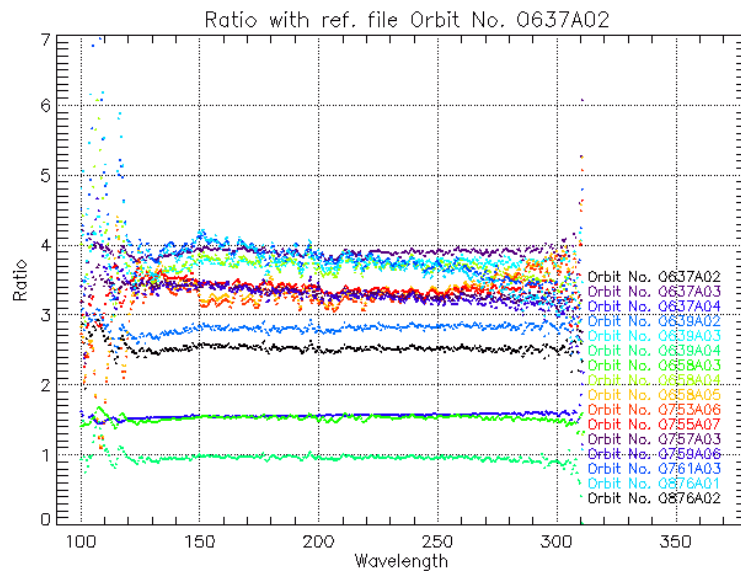


Figure 3.20: Ratio of several spectra using an early spectrum (orbit 0637A02 from the 17 January 2008) as reference, the gain for the groupings of spectra is, counting from below, 60, 75, 90, 95, 100 and 105. The lines are straight and show little or no decrease in any direction.

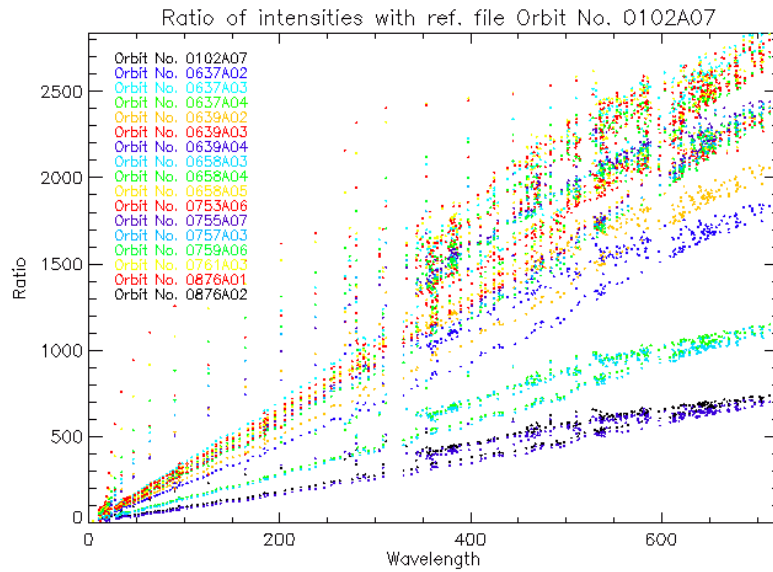


Figure 3.21: Ratio of several spectra using an early spectrum (orbit 0102A07 from the 1 August 2006) as reference, the gain for the groupings of spectra is, counting from below, 60, 75, 90, 95, 100 and 105. The lines are blurry and show non-linear features at the top and bottom.

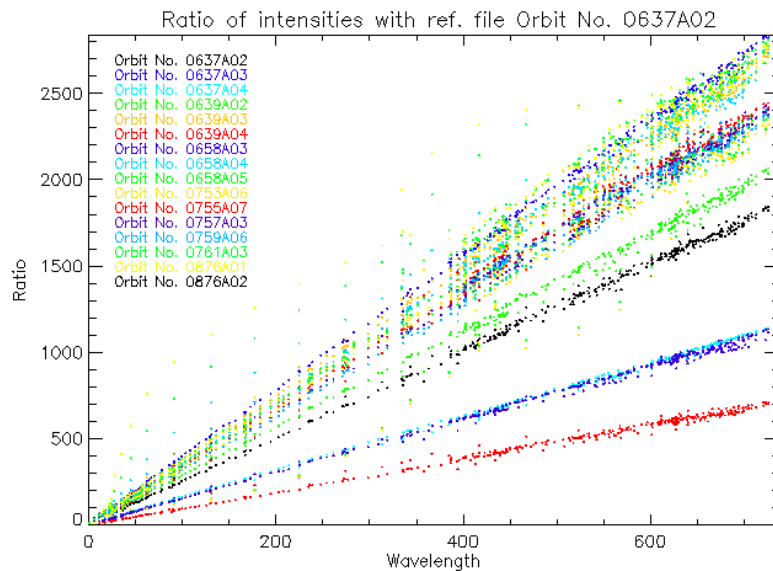


Figure 3.22: Ratio of several spectra using an early spectrum (orbit 0637A02 from the 17 January 2008) as reference, the gain for the groupings of spectra is, counting from below, 60, 75, 90, 95, 100 and 105. The lines are sharp and well defined showing little or no irregularities.

3.4 Summary

The present study supports the idea that earlier instruments can aid in the understanding of how to perform and improve stellar calibrations for similar types of instruments.

SPICAV and SPICAM, the UV/IR spectrometers on board the Venus Express and Mars Express missions, are nearly identical and can therefore be used for data comparison and instruments reactions to different environments in space.

SPICAM is primarily dedicated to the study of the atmosphere of Mars in the UV. As a follow-up, SPICAV consists of three spectrometers working in the UV and IR ranges observing the atmosphere of Venus. The UV spectrometer channel (118 – 320 nm, resolution 1.5 nm) is identical to that of SPICAM.

Since both instruments are nearly identical and very similar to PHEBUS in many aspects, the calibration of these instruments is also similar. Therefore this study is an excellent introduction to how the ground- and in-flight calibration for PHEBUS can be performed and optimised.

As with all instruments, the need for calibration is acute where a number of external and internal factors can affect both the instruments and the observations.

As these instruments all work in the UV range, stars are used for these calibrations and both SPICAV and SPICAM have an extensive list of such "calibration stars" from which recorded spectra can be compared to other official observations, for example HST or IUE.

Hot stars are preferred for calibration because they are brighter in the UV wavelength range and since they are bright, they also have reasonably constant signal over the whole wavelength range.

However PHEBUS is also working in the EUV range (55 – 155 nm), which means that the "calibration stars" listed for the SPICAM/SPICAV cannot all be used for calibration. Therefore in this chapter, an evaluation was performed into the greatest detail of the flux of the stars, their locations and their amount of clear spectra recorded. The spectra were then cleaned up and sorted according to usage (in-flight or orbit calibration purposes) and summarised in a list of usable stars that can be used for the calibration of PHEBUS.

A common feature of instruments in space is that the detector undergoes a steady deterioration that decreases the sensitivity of the instrument with time. The main cause of this is the usage, the aging and the conditions in space. All of these features can have an impact on the instruments and since most are of natural occurrence, they are practically impossible to completely remove, but they can be anticipated and calculated. This can be done by comparing star spectra taken with long time intervals in between. If the spectra have all been taken in similar conditions, similar settings and of the same object, they should normally show very little difference. If differences are seen, the problem is most probably instrumental.

If the instruments in turn are very similar, any eventual impact these changes could have on the first instrument could be translated to the next instrument.

In the evaluation of "calibration stars" from SPICAM/SPICAV, this study clearly show that spectra ratios calculated from these stars display a decrease in sensitivity in lower wavelengths, which becomes worse with higher gain. The reason, in this case, is that the instrument underwent greater changes in the beginning of its arrival in space and even though it stabilised after a while, the higher the gain, the greater the stress on the instrument.

This can be taken as a warning to PHEBUS to keep the gain lower in order to keep spectra from showing this decrease in sensitivity.

In conclusion despite the fact that the knowledge of calibrations gained from SPICAM and SPICAV is a valuable tool to apply to PHEBUS, it is impossible to really tell what will happen in the much harsher environment around Mercury. It is, however, obvious that in-flight calibrations have to be performed for the instrument to be in nominal conditions when arriving at Mercury.

Chapter 4

PHEBUS: Instrumentation for a harsh environment

”The space existing between the worlds scattered throughout the universe, does not isolate them from one another. They are all in perpetual communication with each other through the force of attraction which is constantly exerted through space.”

4.1 Radiometric Modelling and Scientific Performance of PHEBUS

The goal of any radiometric model is to simulate the foreseen observations as realistic as possible through a photometric model of the instrument. This is done by firstly making a photometric flux assessment of the instrument by modelling the flux of photons received by the detector. Knowing the intensities of the lines of the different species to be measured, a complete calculation of the path and transmission of photons along the full optical chain allows an estimation of the instrument’s theoretic spectral resolution and detection capabilities.

This computation combines the instruments geometric characteristics and the efficiency of the components used.

The PHEBUS radiometric model, developed by N. Rouanet, uses a combination of a ray-tracing software and a numerical computing software which produces a matrix representing the image recorded by the detector. A binned spectrum profile can then be calculated by summing along the spatial axis of the detector (PHEB-SC).

The radiometric model of the PHEBUS instrument has the following main objectives, which are vital for the development of the instrument:

- to calculate the instrumental response in terms of counts per second per Rayleigh of emission,

- to simulate observations of exospheric spectra and produce detector matrix images as result of this,
- to anticipate real in-flight observations in order to plan efficient observation sequences,
- to validate the scientific objectives and to prove that PHEBUS will meet the scientific requirements,
- to provide help for technological choices in the instrument for example in the choosing of the coating for the EUV photocathode and the slit width.

As always with these kinds of models it has some limits. There are large uncertainties about the expected emission lines used as reference¹, because the abundance of the exospheric species to be measured are not well known and are expected to be extremely variable from time to time and from place to place. There are also some uncertainties about the efficiencies of the optical components of the instrument itself². The straylight and noise are not well known in advance, because they are quite dependent on the details of the assembly of the final instrument and scattering by the gratings has similarly not yet been implemented. However refinement can be done with effective measurements on real optical components and with the in-flight calibrations (Chassefière et al. 2010).

This chapter has been divided into two parts. The first part describes the theoretical background, scientific demands and technical details of the development of any radiometric model. The second part shows the result of the developed radiometric model applied to the instrument PHEBUS for different species and star spectra.

4.2 Theoretical background

A radiometric model consists of several parts:

1. calculation of the UV emissions of the observed species
2. modelling of the transmission of light through the optical chain of the instrument
3. accounting for the (spectral) response of the detectors.

To be able to build an accurate model, several key factors need to be examined and collected such as spectral data tables of the different considered emission lines, their wavelength and brightness. Also information regarding the reflection coefficients of the entrance mirror and of the two gratings are needed as well as the quantum efficiencies of the detectors and the transmission coefficient of the protection window³.

These factors then need to be coupled with the instrument parameters such as pupil size and shape, mirror focal length, slit size, field of view and the size of the detectors. A deeper study of these terms can be found in the following chapter.

4.2.1 Instrument

The PHEBUS is a double UV spectrometer basically composed of two ultraviolet spectrophotometers with the wavelength ranges of 55-155 nm and 145-315 nm, including two small NUV detectors for 404 nm and 422 nm, and one scanning mirror, devoted

¹about a factor 10 or more

²at worst several tens of %

³if applicable



Figure 4.1: Artist view of the BepiColombo mission to Mercury with the PHEBUS visible to the left side of the sun shield. (Image Astrium)

to the characterisation of Mercury's exosphere composition and dynamics, and surface-exosphere connections. The instrument is French-led (PI E. Quémerais, LATMOS and co-PI F. Leblanc, LATMOS) and implemented in a cooperative scheme involving Japan (EUV/FUV detectors), Russia (scanner system) and Italy (ground calibration).

The instrument is part of the ESA/JAXA BepiColombo mission to Mercury that will be launched in 2014, at earliest, see Figure 4.1.

A movable mirror takes the light from the exosphere of Mercury above the limb onto the entrance slit of the spectrometers. This is done with a minimum of reflections in order to maximize the count rate of the Micro Channel Plate (MCP) detectors. Two gratings and two detectors are used according to a specific, compact design. The spectrum detection is based on the photon counting method and is realized using Micro Channel Plate (MCP) detectors with Resistive Anode Encoder (RAE). Extra visible lines are monitored using a Photomultiplier (PM) that is also used in photon counting mode.

4.2.2 Objectives and demands on the instrument

To rightfully assess the need and demands on any instrument, firstly a study of the observation environment needs to be done, such as what will the instrument observe and how.

Main measurement objectives

The PHEBUS instrument has been determined to have the following measurement objectives (Chassefière et al., 2010):

- In addition to the previous species detected, one objective of PHEBUS is to confirm the evidence of the presence of Si, Mg and Fe, atoms such as C, N and S, molecules and radicals (H_2O , H_2 , OH and CO), noble gases (Ar and Ne), ions (He^+ , Na^+ and Mg^+) in addition to the already detected species (Na, K, Ca, O, H, He and Mg) on Mercury (Broadfoot et al., 1976; McClintock et al., 2009)
- To measure an average Hermean exosphere such as the number densities of constituents and vertical structure with as many species as possible monitored together at different positions of Mercury around the Sun
- To measure local and temporal variations of the exosphere at specific times and places
- To search for albedo variations of the nightside surface of Mercury, lighted by the interplanetary H I Lyman- α glow at 121.6 nm, in order to exhibit possible signatures of surface ice layers (H_2O , SO_2 , N_2 and CO_2) in high latitude polar craters and other signatures of interest

These scientific criteria give rise to general design requirements as follows

- The requirement for line detection is a typical signal-to-noise ratio of 3,
- A spectral resolution better than 1 nm (to distinguish H from N). The range also needs to include 404 and 422 nm with a lower resolution to observe the Calcium (Ca) and Potassium (K) lines, since these lines are of great importance in the Hermean exosphere,
- A vertical scanning range equivalent to 0 - 1500 km,
- A vertical resolution of at least half a scale height on most species (around 20 km for the heaviest one) when observing from apoherm, translating into an angular resolution better than 0.37 degrees,
- Sensitivity to lines as weak as 0.1 Rayleigh, depending on the brightness of the stray light background⁴.

4.2.3 Sources

The light sources observed by PHEBUS are the emission lines coming from atoms and ions in the exosphere of Mercury. The major detection issue is the very large dynamic range required to observe as many lines as possible in the UV.

⁴The stronger the stray light background is, the harder it is to observe weak lines since they are drowned in the background noise. So the value of 0.1 Rayleigh is only plausible if the background noise has a brightness of around or lower than this value.

Dimension	Formula	Numerical Value
\varnothing Entrance pupil diameter		25.4 mm
H Pupil position		130 mm (arbitrary)
D Working angle		100°
L Mirror working focal length		170 mm
f Paraboloid absolute focal length	$f = \frac{L}{2}(1 + \cos(D))$	70.240 mm
a Point M x-coordinate (\bar{X}_p)	$a = L \cos(D - 90^\circ)$	167.417 mm
b Point M z-coordinate (\bar{Z}_p)	$b = f + L \sin(D - 90^\circ)$	99.760 mm
Slit full width (small dimension), along (\bar{Y}_s)		283 μm
Slit full height (large dimension), along (\bar{Z}_s)		5.667 mm

Table 4.1: Table of optical properties of the PHEBUS. See Figure 4.5 for a graphical layout.

Emission line brightness is given in a CGS unit called Rayleigh. By definition:

$$1 \text{ Rayleigh} = 10^6 \text{ photons s}^{-1} \text{ cm}^{-2} \quad (4.1)$$

This represents the photon flux emitted in 4π steradians by a column of 1 cm^2 area. For photometric calculations the radiance of such an extended source is expressed in radiance defined as:

$$\frac{10^6}{4\pi} \text{ photons s}^{-1} \text{ cm}^{-2} \text{ sr}^{-1} \quad (4.2)$$

The data for the source is a compilation of the species detected on the Mariner 10 mission to Mercury, based on ground-based observations and estimated abundances for non-detected species (Leblanc et al., 2007). See Table B.1 for a full list of emission lines used in the radiometric modelling. All these values are only rough estimations, since the local densities of the expected species can vary by a factor of 10 for several reasons (Leblanc et al., 2004).

4.2.4 Optical layout

The instrument can be divided into two parts. The first part collects the UV photons emitted by a source in the instruments field of view, while the second part is the spectrometer itself and the Micro Channel Plate.

The collecting part is composed of a baffle, see Figure 4.2, that shields from stray light, and its exit pupil. Right after the pupil an off-axis parabolic mirror concentrates the light collected onto the spectrometer entrance slit, see Figure 4.4, Figure 4.5 and Table 4.1.

Pupil and slit

The amount of photons entering the spectrometer is characterised by the geometrical product of the pupil and the slit field-of-view.

Instrument geometric extent G (in $\text{cm}^2 \text{ sr}$) is defined as

$$G = S_{pupil} \cdot \text{FOV} \quad (4.3)$$

where

$$S_{pupil} = \pi \varnothing^2 / 4 \quad (4.4)$$

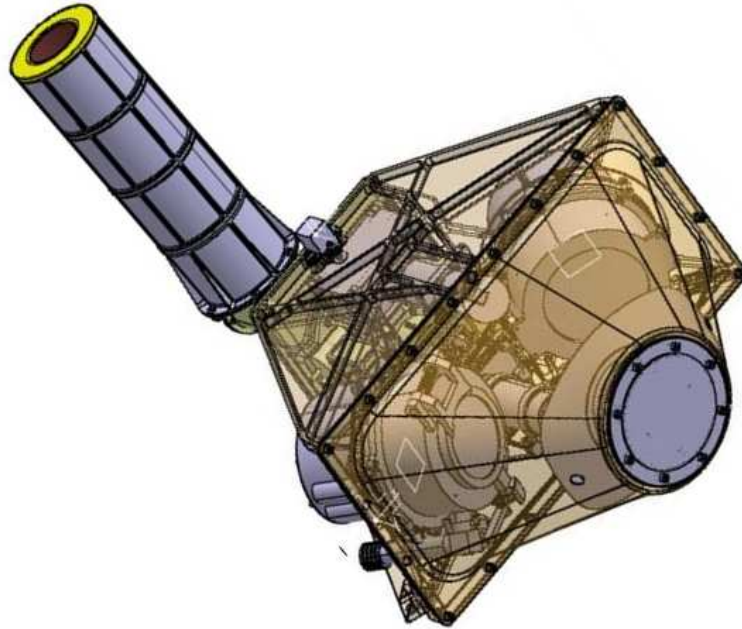


Figure 4.2: PHEBUS instrument with the compact design visible and the observation baffle. For the optical path in 3D see Figure 4.3

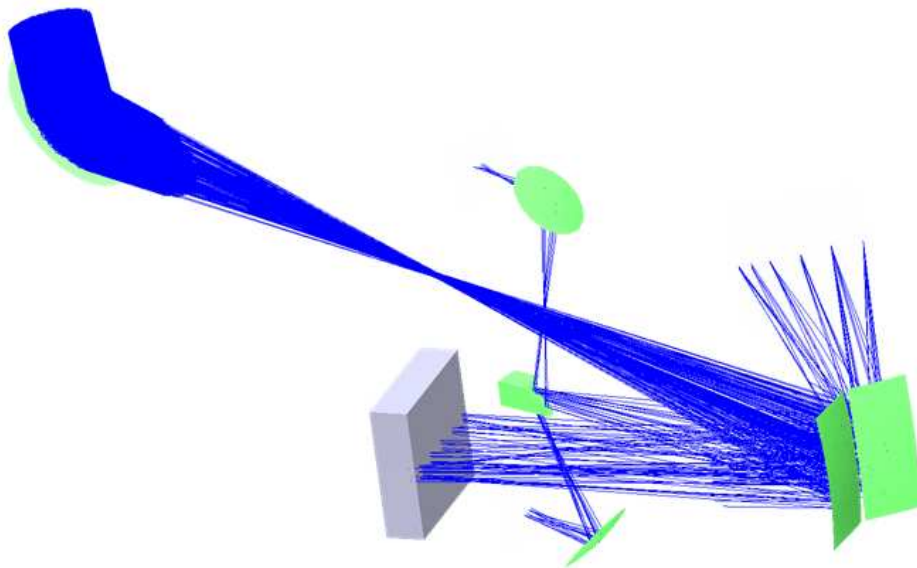


Figure 4.3: 3D view of the optical path of the PHEBUS making full use of the compact design (Image PHEBUS Team, LATMOS).

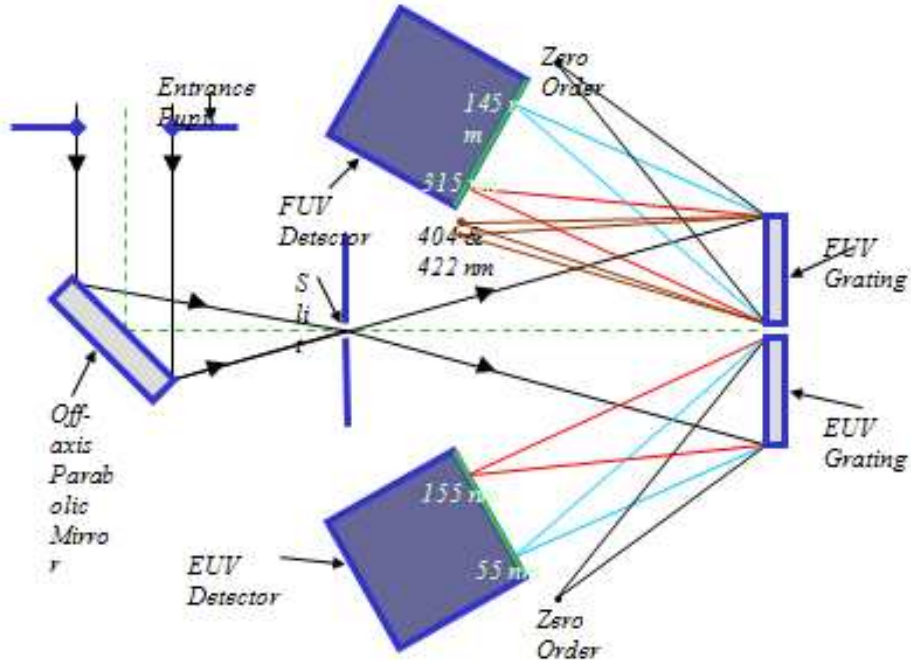


Figure 4.4: 2D representation of the optical layout of the PHEBUS (Image PHEBUS Team, LATMOS). Details in Figure 4.5

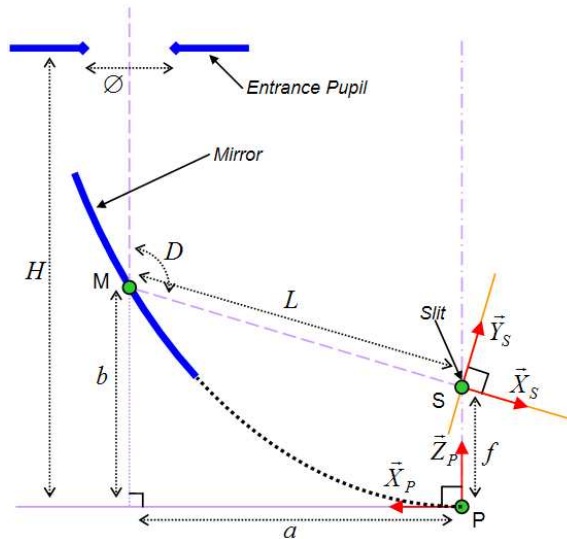


Figure 4.5: Optical layout of the PHEBUS. \varnothing is the entrance pupil diameter, H the pupil position, D is working angle, L is mirror focal length and f is the absolute focal length (Image PHEBUS Team, LATMOS).

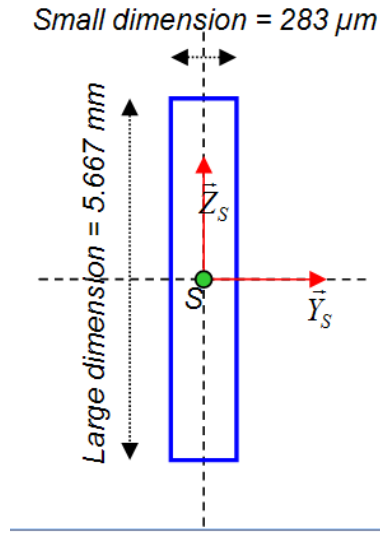


Figure 4.6: Graphical layout of the slit for the PHEBUS instrument (Image PHEBUS Team, LATMOS).

is the area of the entrance pupil and

$$\text{FOV} = a \cdot b / L^2 \quad (4.5)$$

is the field of view of the slit at the mirror focus, see Figure 4.6, where a , b and L (the focal length of the mirror) are defined in Table 4.1.

Mirror

The entrance mirror, made of silicon carbide, is not a perfect reflective surface. It has a SiC reflective coating which has a reflectance of $<100\%$, wavelength dependent. The spectral reflectance coefficient of the entrance mirror is $R_M(\lambda)$. Figure 4.7 shows this reflectance coefficient variation as a function of the wavelength.

The useful flux collected by the entrance mirror and passing through the slit is (in photons s^{-1}):

$$F(\lambda) = \frac{10^6}{4\pi} B(\lambda) R_M(\lambda) \quad (4.6)$$

where $B(\lambda)$ (Rayleigh) is the total amount of flux entering the baffle.

Spectrometer

The collected light entering the spectrometer is divided into two distinct paths: one path is reflected by the EUV grating while the other is reflected by the FUV grating. The loss of light on each path can thus be considered to be around 50% of the total light. Also because there is a small gap between the two gratings an additional small fraction of light is physically lost.

As a consequence, the photon flux entering the spectrometer has to be multiplied by two factors, before any other efficiency considerations. The factor is 0.5 for the spectral range separation and the factor g (< 1) for the gap.

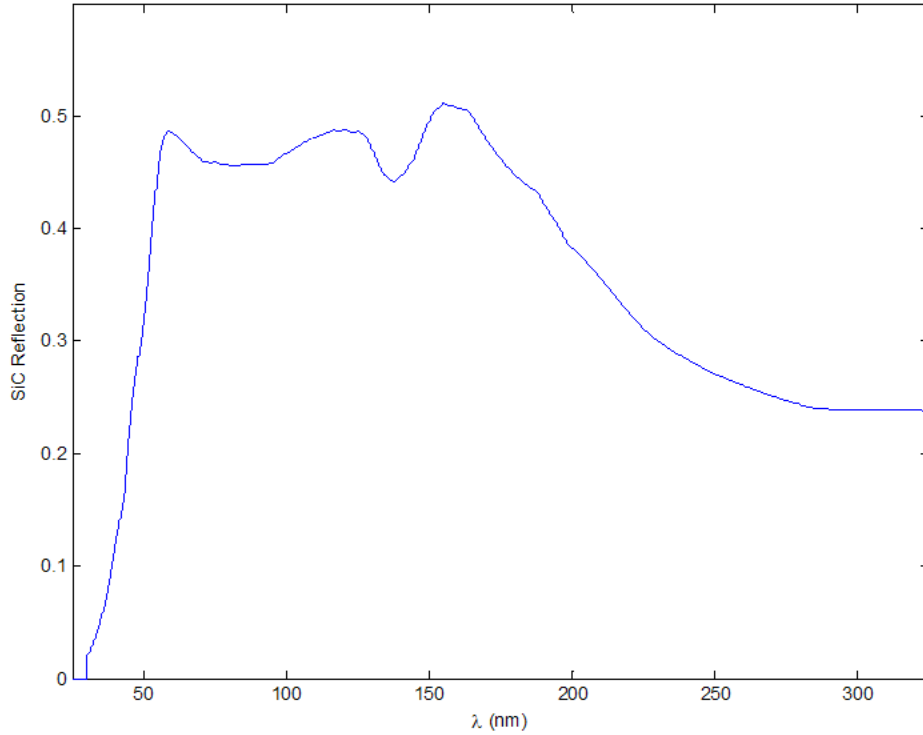


Figure 4.7: Spectral reflectance coefficient variation of the silicon carbide entrance mirror for the PHEBUS. Shown plotted against wavelength.

The spectral grating efficiency is called $Eff(\lambda)$ and the grating equation is:

$$\sin \alpha + \sin \beta = k \lambda / a \quad (4.7)$$

where α is the angle of incidence, β is the angle of diffraction, k is the order of diffraction, λ is the wavelength and a is the size of the grooves in the grating.

Relative grating efficiency is calculated using the formula:

$$Eff_{rel} = \text{sinc}^2 \left(a \frac{\cos B}{\lambda} (\sin(\alpha - B) + \sin(\beta - B)) \right) \quad (4.8)$$

where B is the blaze angle of the grating surface and $\text{sinc}(x)$ is defined as:

$$\text{sinc}(x) = \frac{\sin \pi x}{\pi x} \quad (4.9)$$

Absolute efficiency is the product of the relative efficiency by the reflectance of the material, in this case the gratings are coated with Platinum (Pt). Figure 4.8 shows the absolute efficiencies of the two gratings, at first and second order of diffraction.

Detectors

PHEBUS detectors are composed of three elements:

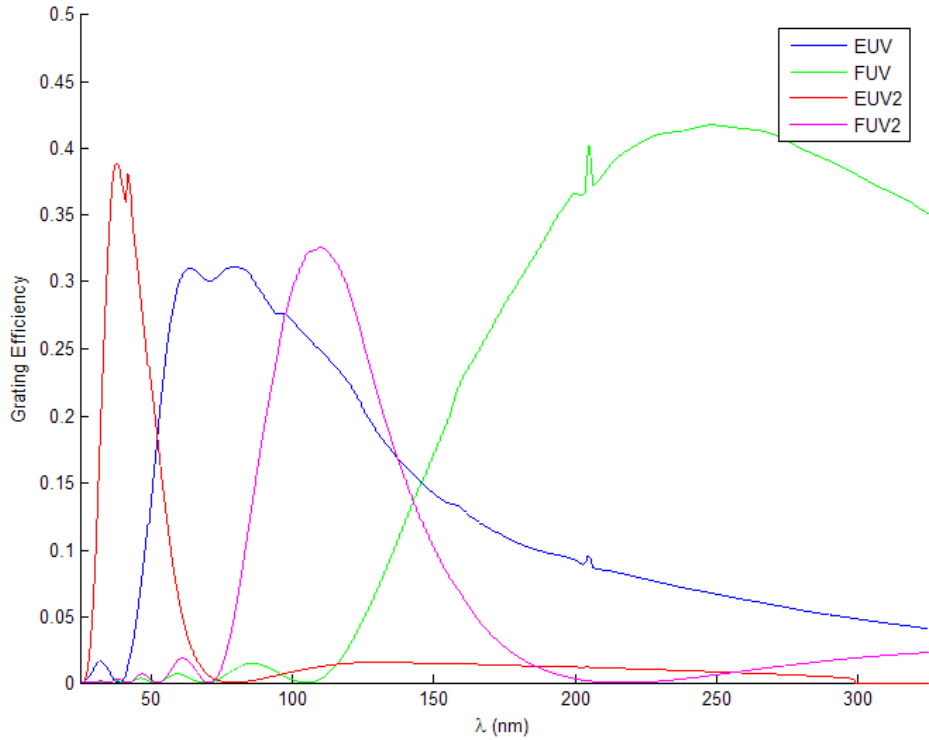


Figure 4.8: Absolute efficiency for the platinum coated gratings for both first and second order. The curves are traced using the following approximate properties for the gratings. EUV Grating: Groove period = $0.46 \mu\text{m}$, blaze angle = 5° , incidence angle = 17.5° . FUV Grating: Groove period = $0.79 \mu\text{m}$, blaze angle = 8° , incidence angle = 20° .

- a UV sensitive photocathode of appropriate material
- a micro channel plate (MCP)
- a resistive anode

A photo event is defined as a pulse of light triggered in the intensifier by creating a photo electron that will be amplified by the MCP in order to generate a cascade of electrons. This avalanche then impacts on the resistive anode, which is coupled to an encoder that measures the impact position. The process is quantified by the Quantum Efficiency (QE) of the photocathode. It creates in the MCP a number G of ADU (spread over a few pixels).

Each value assigned to one pixel is calculated as one count. Then, after a given integration time, the result is an image matrix that represents the number of counts for each pixel.

For a given integration time T , the final number of counts (for one emission line) is given by

$$\begin{aligned} \text{FUV : } N &= \frac{g}{2} \frac{10^6}{4\pi} \cdot B(\lambda) \cdot G \cdot \text{Eff}(\lambda) \cdot QE(\lambda) \cdot W(\lambda) \cdot T \\ \text{EUV : } N &= \frac{g}{2} \frac{10^6}{4\pi} \cdot B(\lambda) \cdot G \cdot \text{Eff}(\lambda) \cdot QE(\lambda) \cdot T \end{aligned} \quad (4.10)$$

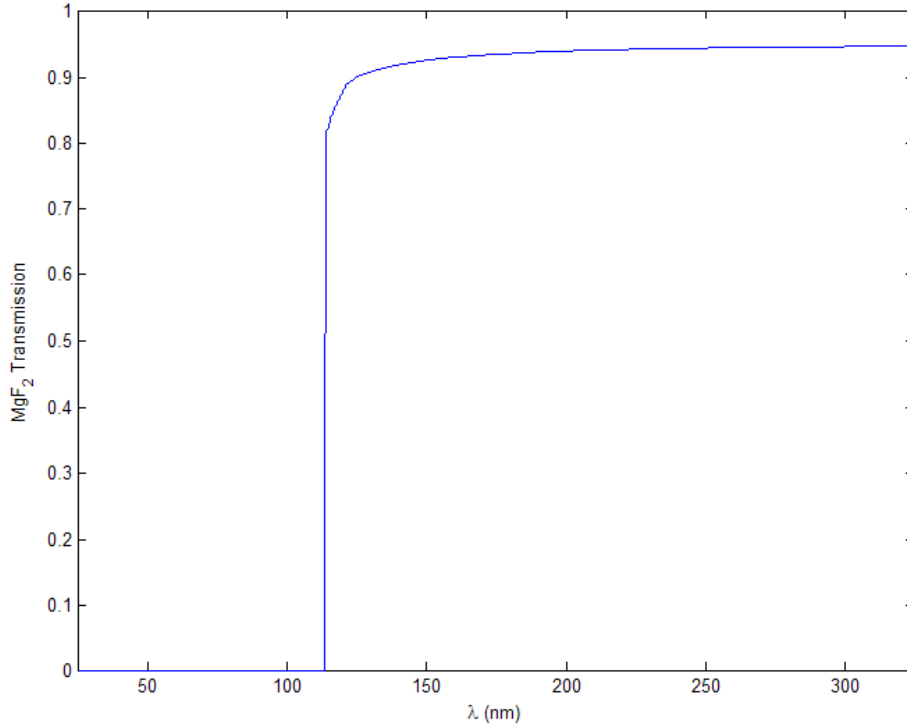


Figure 4.9: MgF₂ window transmission for the FUV detector. Below a certain wavelength the EUV photocathode can not observe any more since the MgF₂ window blocks all incoming flux.

where g is the gap factor, defined as the amount of light lost because of the physical gap between the EUV and the FUV gratings. g is typically very close to 1 (for a 1-mm gap, $g = 0.915$). The factor 2 in $g/2$ accounts for the initial beam being separated into two between the EUV and FUV channels, hence the flux in one channel is divided by the according amount.

The two spectral ranges use different photocathodes:

- for the EUV detector CsI has been chosen since it is very sensitive in the EUV-FUV overlapping range (145 to 155 nm) where crossed calibrations are needed
- for FUV detector a photocathode of CsTe has been chosen

The FUV detector is protected behind an MgF₂ window, see Figure 4.9. The MgF₂ window transmission is called $W(\lambda)$. A compilation of the quantum efficiencies is shown in Figure 4.10.

Global Instrument Efficiency

Global Instrument Efficiency GIE is the product of all spectral efficiencies, transmission and reflection coefficients according to:

$$\begin{aligned}
 \text{FUV : } GIE &= R_M(\lambda) \cdot Eff(\lambda) \cdot QE(\lambda) \cdot W(\lambda) \\
 \text{EUV : } GIE &= R_M(\lambda) \cdot Eff(\lambda) \cdot QE(\lambda)
 \end{aligned}
 \tag{4.11}$$

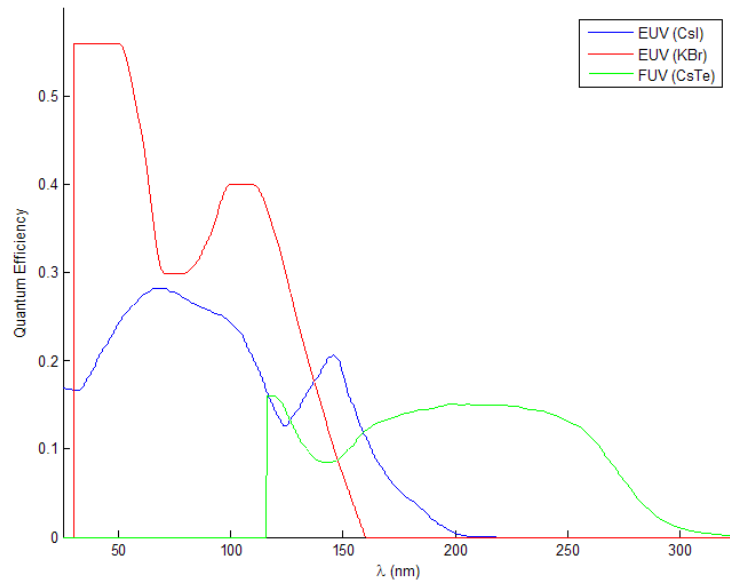


Figure 4.10: Compilation of the quantum efficiencies for EUV (CsI) and FUV (CsTe) ranges. Please note that the EUV (KBr) was another option as coating for the EUV detector but is now obsolete since the decision has been made to use the more well known CsI.

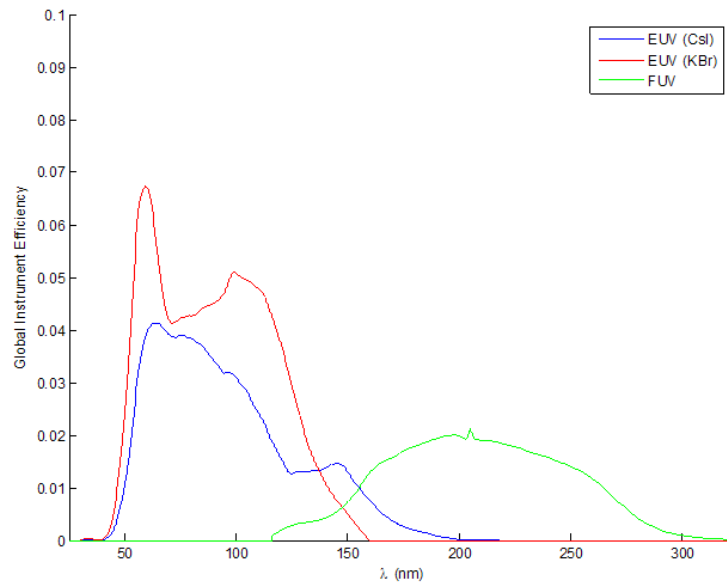


Figure 4.11: Global instrument efficiency, the product of all spectral efficiencies, transmission and reflection coefficients, for both the EUV (CsI) and the FUV (CsTe) detector. The EUV (KBr) is now obsolete since the decision has been made to use the more well known CsI.

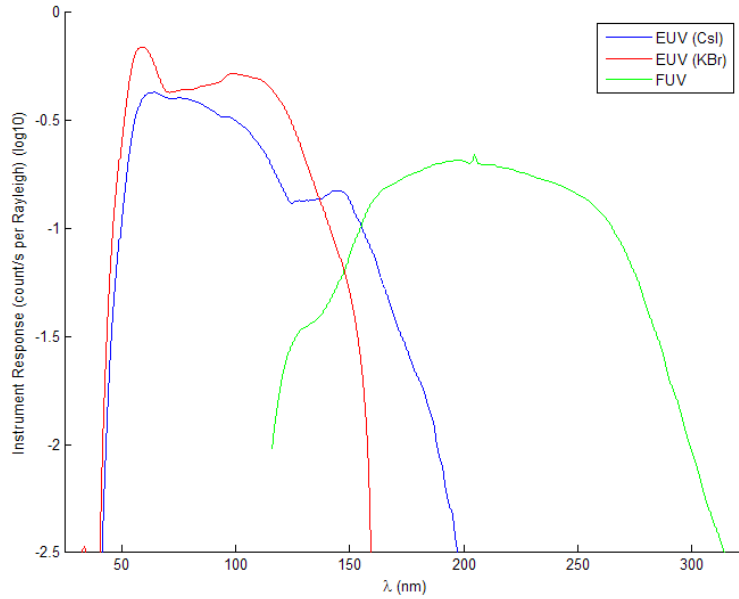


Figure 4.12: Total instrument response is the expected spectral count rate per Rayleigh of emission. It takes into account all efficiencies that can be traced for the EUV (CsI) range and the FUV (CsTe) range. The EUV with KBr photocathode is now obsolete.

as seen in Figure 4.11.

Instrument Response

The total instrument response IR is the expected spectral count rate per Rayleigh of emission as can be seen in Figure 4.12. It is expressed as follows:

$$\begin{aligned} \text{FUV : } IR &= \frac{g}{2} \frac{10^6}{4\pi} \cdot R_M(\lambda) \cdot Eff(\lambda) \cdot QE(\lambda) \cdot W(\lambda) \\ \text{EUV : } IR &= \frac{g}{2} \frac{10^6}{4\pi} \cdot R_M(\lambda) \cdot Eff(\lambda) \cdot QE(\lambda) \end{aligned} \quad (4.12)$$

4.2.5 Photometric assessment and spectral resolution

Implementation

The implementation of all these theoretical values from external sources, from other instruments and from the instrument is done with the two softwares: Matlab and Zemax.

A Matlab program calculates the expected count rates for each wavelength on each range, EUV and FUV, then writes a Zemax file. These files are opened with Zemax together with the spectrometer configuration and for each WAV-file a simulation of the illumination of a pixelized detector is performed.

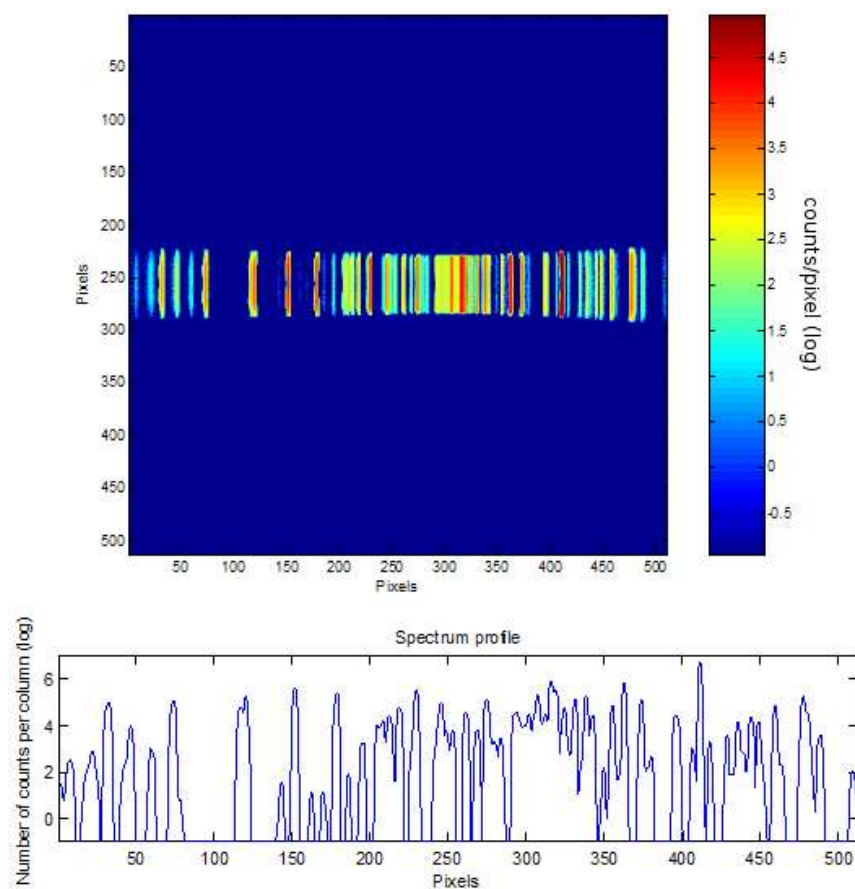


Figure 4.13: Simulated noise-free spectrum from the radiometric model of PHEBUS. The spectrum profile below the matrix is derived by integrating across the signal on the matrix for 1 second. Both x- and y-axis are in pixels.

Matlab is used to calculate the total number of rays to trace with Zemax to rightfully simulate the amount of photons reaching the detector and each wavelength is attributed a weight proportional to the number of photons it contains.

The program Zemax is then chosen to have either an extended source, for observations of all but stars, or a point source if the simulation is of a star.

This uniform source, with the same size as the field of view (square source of width 2.5°) will then be beamed toward the instrument so that some light enter.

The end result is an image, a matrix containing the number of impacts or simulated photons per pixel. A typical example of this noise-free spectrum can be seen in Figure 4.13.

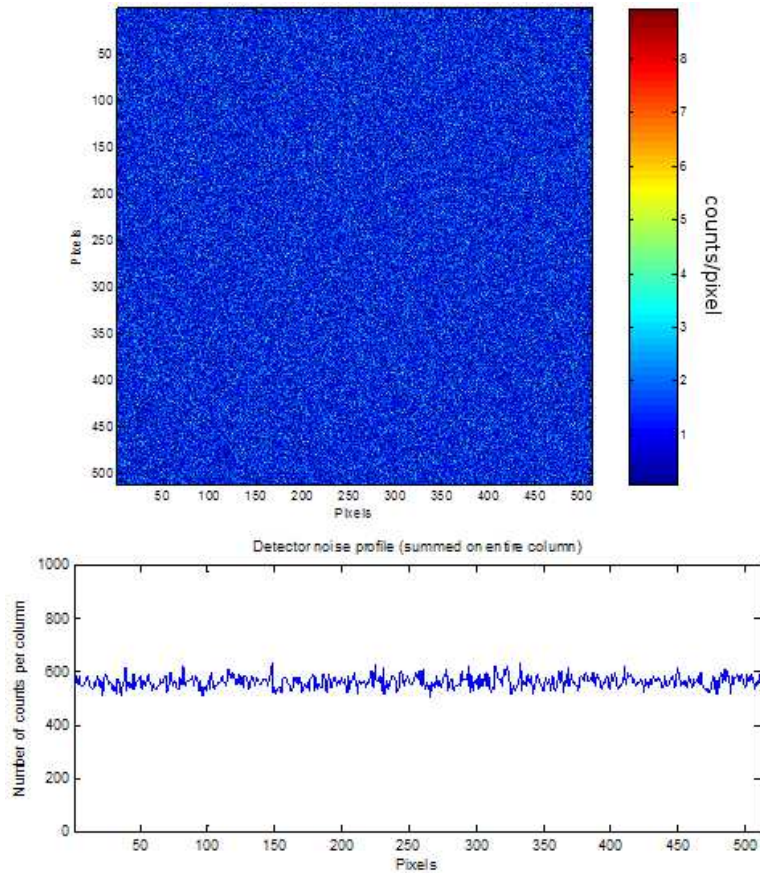


Figure 4.14: Simulated white noise spectrum. Used as the detector noise from the radiometric model of PHEBUS. The spectrum profile below the matrix is derived by integrating across the signal on the matrix. Both x- and y-axis are in pixels.

Adding Imperfections

Adding detector noise and internal stray light noise

Both the detector noise and the internal stray light noise can be considered to be a uniform white noise (Poisson noise) specified at 1 count per second per square centimeter of detector. Thus these two factors can be added together in a global parameter of 5 counts $\text{s}^{-1} \text{cm}^{-2}$ as can be seen in Figure 4.14.

Adding baffle stray light noise

The baffle on the PHEBUS is designed to reduce stray light as much as possible. This stray light is the solar flux reflected by the surface of Mercury that can obscure the other emissions. The fraction of this light coming from outside the guard angle and going through the entrance slit has been calculated as the solar flux reflected of the surface of Mercury (solar flux at Mercury \times albedo at surface = 0.06) reduced by $10^{-6} R$, see Figure

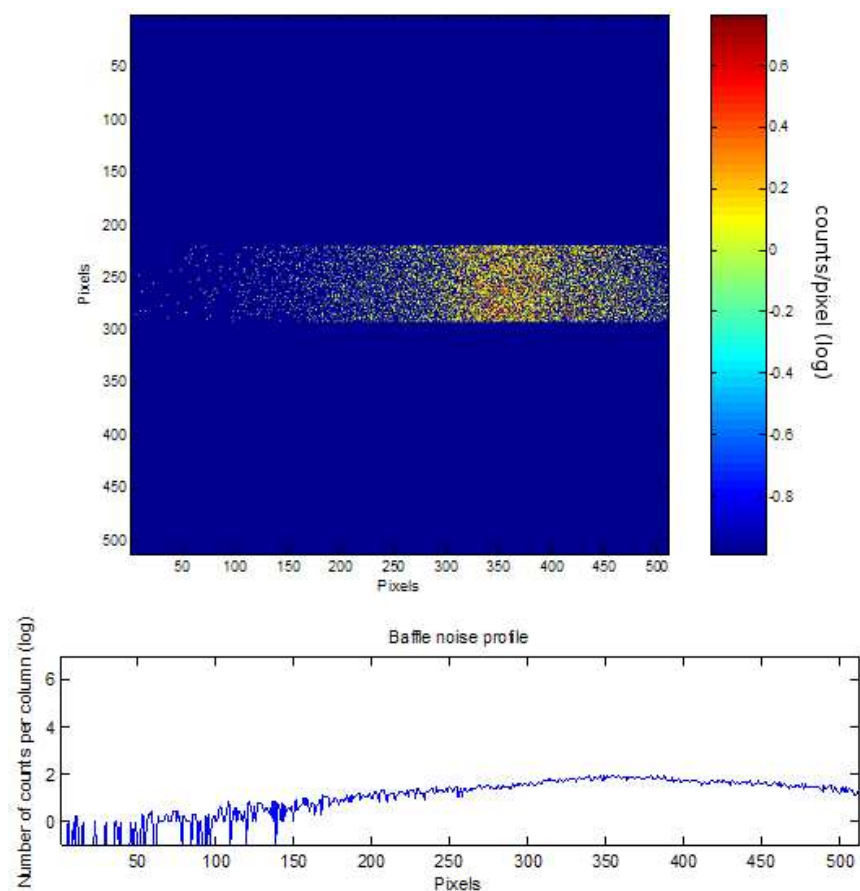


Figure 4.15: Simulated stray light noise spectrum. Used as the baffle noise from the radiometric model of PHEBUS. The spectrum profile below the matrix is derived by integrating across the signal on the matrix. Both x - and y -axis are in pixels.

4.15.

It is calculated for each column of the detector, equivalent to a certain wavelengths range, taking into account all efficiencies and they are randomly distributed on these columns.

Results: Noisy Spectrum

Then finally a full noisy spectrum can be simulated which is a matrix of counts or a spectral profile with the x axis in pixels or wavelengths.

In Figure 4.16 this matrix and the emission line spectrum can be seen.

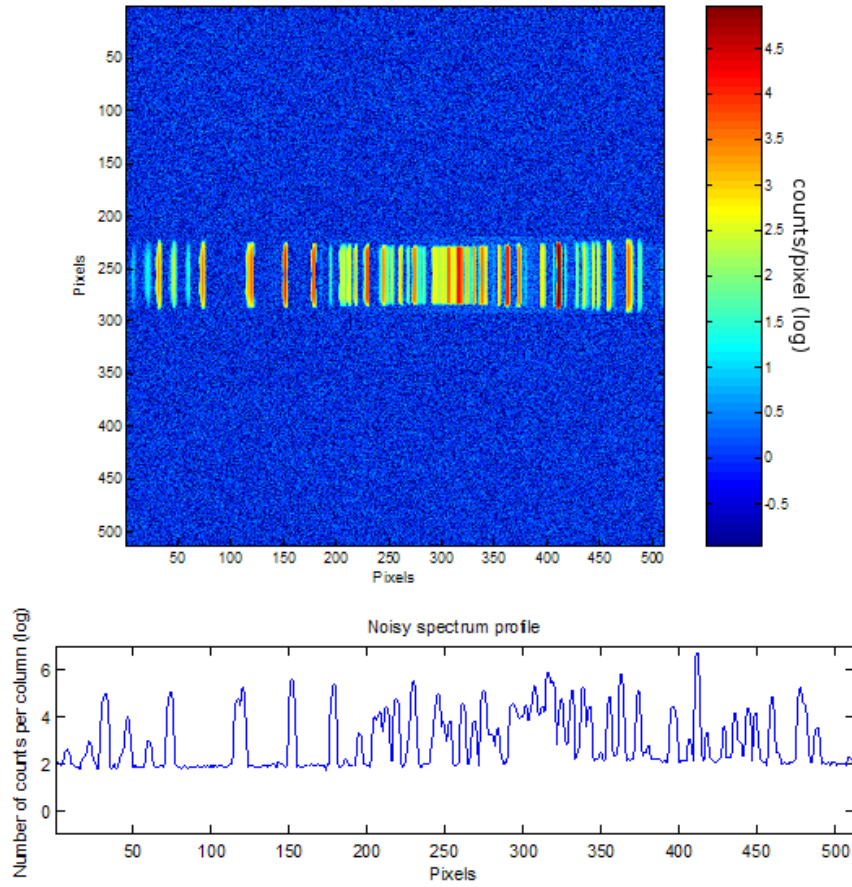


Figure 4.16: Complete simulated noisy spectrum from the radiometric model of PHEBUS. This matrix is the combination of the noise-free spectrum in Figure 4.13 and the noise from Figures 4.14 and 4.15. The spectrum profile below the matrix is derived by integrating across the signal on the matrix. Both x - and y -axis are in pixels.

4.3 Theoretical Results

4.3.1 Radiometric modelling of star spectra

I apply the radiometric model, as depicted earlier, to two chosen stars from the SPICAM catalog as defined in the earlier Chapter 3 which are summarised in Table 4.2.

No regards are taken, at this moment, to the position of these stars in relation to the spacecraft in flight; they are only used to evaluate the radiometric model for the case of star spectra calibration. This is because at the time of this evaluation the orbit and flight path of the BepiColombo mission is still in evaluation phase. Although care is taken to the quality and suitability for calibration of the PHEBUS. The spectra from both these stars have been taken from the IUE catalog of reference stars.

The reason I chose these two stars is that they are of very different classification and thus temperature. For use in the EUV range only very hot stars can come of use in the

SPICAM nr	Name	Spectral type	Temperature (K)
O2	Gamma Cassiopeia	B0IVe	6700
O19	Epsilon Orion	B0Ia	25000

Table 4.2: Table of basic information for the two chosen stars for the calibration radiometric model for the PHEBUS.

calibration (usually O-class stars) but for calibration of the FUV, most stars in B-class can certainly be of use. The "cool" SPICAM-2 star, in comparison with the very "hot" SPICAM-19 star, is therefore very interesting to note in the radiometric modelling of the calibration⁵.

Both of these star spectra were applied to the radiometric model and the result can be seen in Figure 4.17 for the SPICAM-2 star and in Figure 4.18 for the SPICAM-19 star.

It is clear that the radiometric model gives very good results that could most definitely be used for the FUV calibration. The spectra are well defined and have a good resolution. This seems then to be a plausible choice for in-flight calibration.

However this option for the EUV range must be looked more into details since it demands much hotter stars. For example, the star zeta Puppis, 036, could be very interesting since it is classified as a O5f star, which is both unique and very hot - ideal for extreme UV spectra. For a list of the stars used in as the SPICAM calibration stars please see Table A.1.

4.3.2 In-flight calibrations of stars

Regular calibration of the spectral response of detectors and optics, and its time evolution, by using stars and interplanetary medium, needs to be performed during flight. It is only the stellar calibration that will allow tracking the degradation of the channels as a function of wavelength and time.

A few interplanetary lines will also be available to follow the variation of the detectors (H I Ly- α at 121.6 nm first and second order, H I Ly- α at 102.5 nm, and He resonance line at 58.4 nm).

Cruise observations will be very important to establish the absolute calibration of the instrument and make comparisons with other measurements (at Earth and Venus also).

Since the number of bright hot stars is limited (about 10 to 20 according to the actual sensitivity of the instrument), a request will be put forward on off-pointing⁶ of the spacecraft during the "autumn" and "spring" seasons of the orbit to be able to point the line of sight of the instrument toward the desired stars.

4.4 Summary

PHEBUS is a dual channel EUV-FUV spectrometer that is currently being built in LATMOS and will span the 55 – 155 and 145 – 315 nm wavelength ranges. Its purpose is

⁵Both these stars are only used in the FUV range

⁶The off-pointing requirement for the star calibration in flight/orbit will be decided at later date given by ESA. It will depend on the actual orbit of the spacecraft and will be subject to change if the orbital plane is not the expected one.

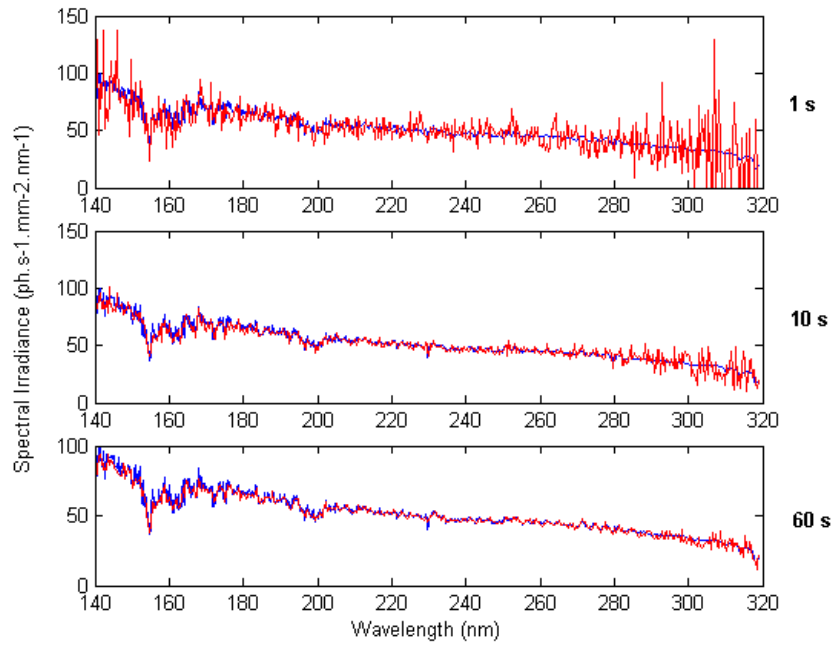


Figure 4.17: Results from the star radiometric modelling on the PHEBUS using SPICAM star O2 (blue line) with results from the radiometric model with different integration time (1 s, 10 s and 60 s) superimposed (red lines)

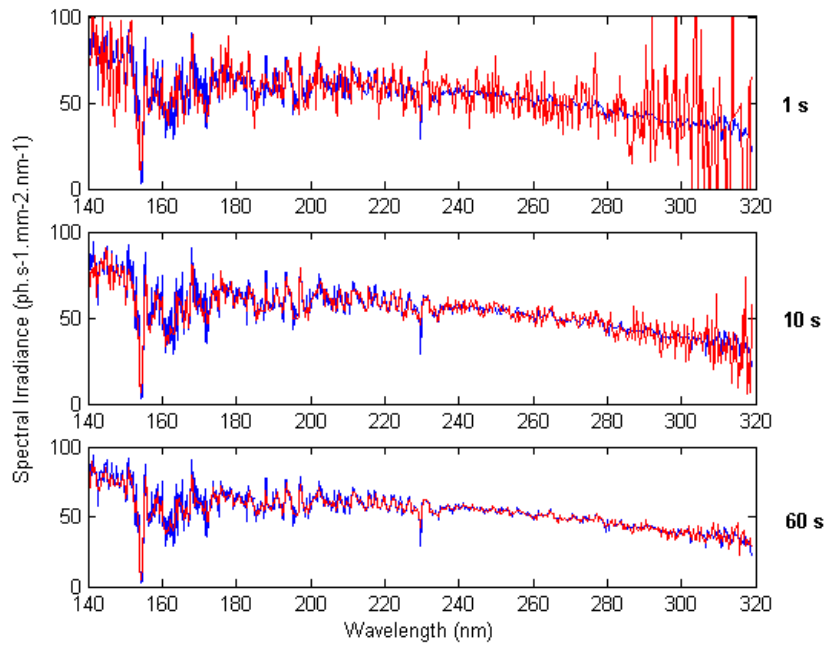


Figure 4.18: Results from the star radiometric modelling on the PHEBUS using SPICAM star O19 (blue line) with results from the radiometric model with different integration time (1 s, 10 s and 60 s) superimposed (red lines)

to observe in high spectral resolution the emissions of atoms and molecules in Mercury's exosphere (see Chassefière et al., 2010).

The optical layout and technical details of PHEBUS are described in the first part, as well as the theory behind the calibration of the instrument.

In the second part, a radiometric model accounting for the photometric characteristics of PHEBUS is presented, which has been developed in order to predict the brightness of possible emissions at Mercury. Using a combination of ray-tracing and numerical methods, the image recorded by PHEBUS can be simulated. The main objective is to anticipate realistic in-flight calibrations and prepare for observations in space, with recommendations on the choice of the detectors (CsI, CsTe or KBr). Simulations are presented with different noise levels.

Finally, the radiometric model is applied to two stars chosen from the SPICAM star catalogue out of 39 other stars, which are used to evaluate the radiometric model in order to prepare for in-flight calibration of the detectors.

Table B.1 show the expected brightness of emission lines measured by PHEBUS when orbiting Mercury, for wavelengths ranging from 30 nm to 323 nm, and spanning species from H, He, Na to K, Mg, O and C.

Chapter 5

Modelling Mercury's hydrogen exosphere

*"One day Spero came earlier than usual.
Eureka!, he cried.
But quickly restraining himself,
Perhaps, he added."*

5.1 Introduction

Mercury has a tenuous surface-bounded exosphere, meaning that neutral species interact with the surface more often than with each other. This exosphere was measured by Mariner 10 as to contain substantial parts of hydrogen, helium and oxygen (Broadfoot et al., 1974, 1976) and by ground-based measurements to contain sodium and potassium (Potter and Morgan, 1985, 1986), and calcium (Bida et al., 2000).

The source of the neutral species that populate the exosphere are most probably the solar wind for hydrogen (H) and helium (He), and the crust, for oxygen (O), potassium (K), calcium (Ca), sodium (Na) and magnesium (Mg). Upper limits of abundances and brightness of the main emissions observed at Mercury and the Moon, before MESSENGER, are shown in Table 5.1.

Brightness are expressed in a CGS unit of flux called Rayleigh (R), which represents the number of photons emitted in all directions per square centimeter of receiver per second (Hunten et al., 1956; Baker and Romick, 1976):

$$1 \text{ R} = 10^6 \text{ photons} \cdot \text{cm}^{-2} \text{ s}^{-1} \quad (5.1)$$

Table 5.1 gives only a schematic idea of the complexity of Mercury's exosphere as much is still unknown. For instance, the available observations and theories suggest a large day/night asymmetry of the hydrogen and helium exospheres, with higher densities of gases on the nightside.

TABLE I
Known Gases on Mercury and Moon

Species	Wavelength (Å)	Mercury ^a			Moon ^b	
		g^c (ph atoms ⁻¹ s ⁻¹)	Brightness (R)	N_0 (cm ⁻³)	N_0 (Day) (cm ⁻³)	N_0 (Night) (cm ⁻³)
H	1216	5.3×10^{-3}	70, 720	23, 230 ^d	<10	—
He	584	5.1×10^{-5}	70	6.0×10^3	2×10^3	4×10^4
O	1304	2.1×10^{-5}	63	4.4×10^4	—	—
Na	5890, 5896	2.45, 1.22	$1-10 \times 10^5$	$1.7-3.8 \times 10^4$	—	—
K	7664, 7699	3.24, 1.67	5×10^3	5×10^2	—	—
Ar ^e	869	5.5×10^{-8}	—	$<6.6 \times 10^6$	1.6×10^3	4×10^4

^aDensities or upper limits based on resonance scattering.

^bDensity or upper limits based on *in situ* measurements.

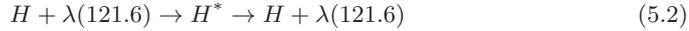
^cScattering coefficient (photons atoms⁻¹ s⁻¹) at Mercury aphelion and no Doppler shift. For Na and K they vary (see Sec. IV).

^dHot and cold components.

^eMercurian values inferred from lunar values.

Table 5.1: Known gases on Mercury (Mariner 10) and the Moon (measurements from Hodges et al. 1974), Table I from Hunten et al. (1988).

The most intense spectral line observed in the ultraviolet spectrum of Mercury is hydrogen Lyman- α , at 121.6 nm and produced by resonant scattering of the solar flux by hydrogen atoms (Hunten et al., 1988).



On Mercury hydrogen emissions are difficult to observe due to the fact that they intermingle with the interplanetary background. Therefore modelling is necessary to separate the contributions. Sodium emissions (Na D_1 and D_2 at 589.0 and 589.6 nm, on the contrary, are easier to observe due to their high efficiency to resonantly scatter the solar flux and have therefore been more thoroughly explored (discovery: Potter and Morgan, 1985; further studies: Sprague et al., 1997; Killen et al., 1999; Potter and Killen, 2008; Potter et al., 2007; Leblanc et al., 2008).

The same goes for the modelling of the exospheric hydrogen of Mercury. The first models were rudimentary and dealt mostly with He because of the lack of reliable physical parameters describing the gas-surface interactions (Shemansky and Broadfoot, 1977).

The knowledge acquired from the exploration of the Moon, and albedo and geology similarities between Mercury and the Moon (see also Table 5.1), justified at the time the direct translation of Moon models to the Mercury environment, despite the sheer difference in proximity to the Sun (surface temperature), the presence of a magnetic field and the need to simplify the surface composition.

Hodges and Johnson (1968) and Hodges (1972) derived the general theory of exospheric transport for heavy gases such as Ne which were expected to obey temperature relations in exospheres ($T_s^{-5/2}$ distribution law¹). Hodges (1973) then developed a Monte-Carlo ballistic lunar model for hydrogen (H and H₂) and helium. The calculated densities of helium were in good agreement with the measurements performed by the Apollo 17 lunar surface mass spectrometer. Based on his calculations and the limits set by the Apollo mission, Hodges (1973) hypothesised that thermal escape of hydrogen at the Moon should occur mostly through H₂ while the solar wind may be the main source of atomic H.

¹For description of this law please see equation (5.36.) in part 5.2.5

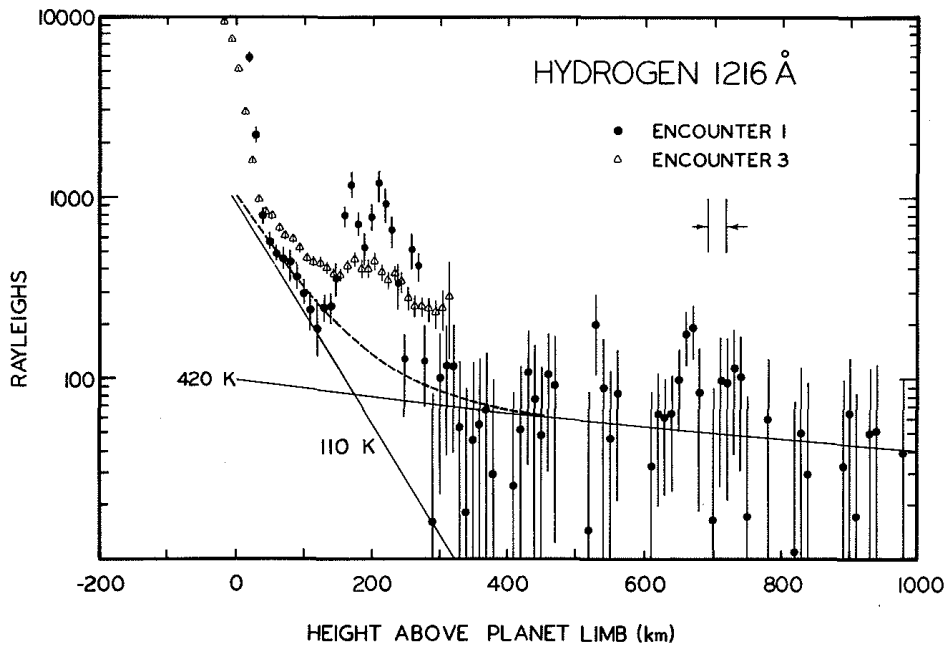


Figure 5.1: Altitude emission profile of HI Ly- α in Rayleigh above the subsolar limb measured by Mariner 10 UV spectrometer (Broadfoot et al., 1976). The two-temperature fit of Shemansky and Broadfoot (1977) is shown. The appearance of the heightened values, commonly referred to as "the bump", at 200 km is said to be instrumental whereas the low altitude emission could have been significantly polluted by surface reflected flux.

Attempts to detect HI Ly- α on the Moon were prevented by the large interplanetary background contribution as well as the geocorona: no statistical dataset is available on atomic hydrogen that could validate the exospheric models on this species and serve as a useful comparison with Mercury.

Early ground-based attempts to detect an atmosphere on Mercury proved unsuccessful leading to the need of in-situ or remote sensing measurements from space. So far only two planetary missions have been launched to explore Mercury: Mariner 10 in 1973 and MESSENGER in 2004.

During three flybys from 1974 to 1975, all occurring at aphelion with the identical hemisphere illuminated, Mariner 10 gave the first recorded measurements of hydrogen brightness in limb configuration. Figure 5.1 shows the altitude brightness profile of HI Ly- α above the subsolar point from the first and third encounters. Large noise levels are seen at higher altitudes due to the Ly- α interplanetary background contribution.

To explain the profiles, Shemansky and Broadfoot (1977) postulated the presence of two different populations of hydrogen, one cold at 110 K and one hot at 420 K which are fitted in Figure 5.1. The cold population has never been physically modelled.

Hydrogen spectral lines, including HI Ly- α , lie in the middle of the spectral range of the EUV channel of PHEBUS (55 – 155 nm), on board the ESA/JAXA mission BepiColombo (probable launch 2014). PHEBUS is a UV spectrometer specially designed to study Mercury's exosphere. One of the difficulties when observing Mercury's exospheric

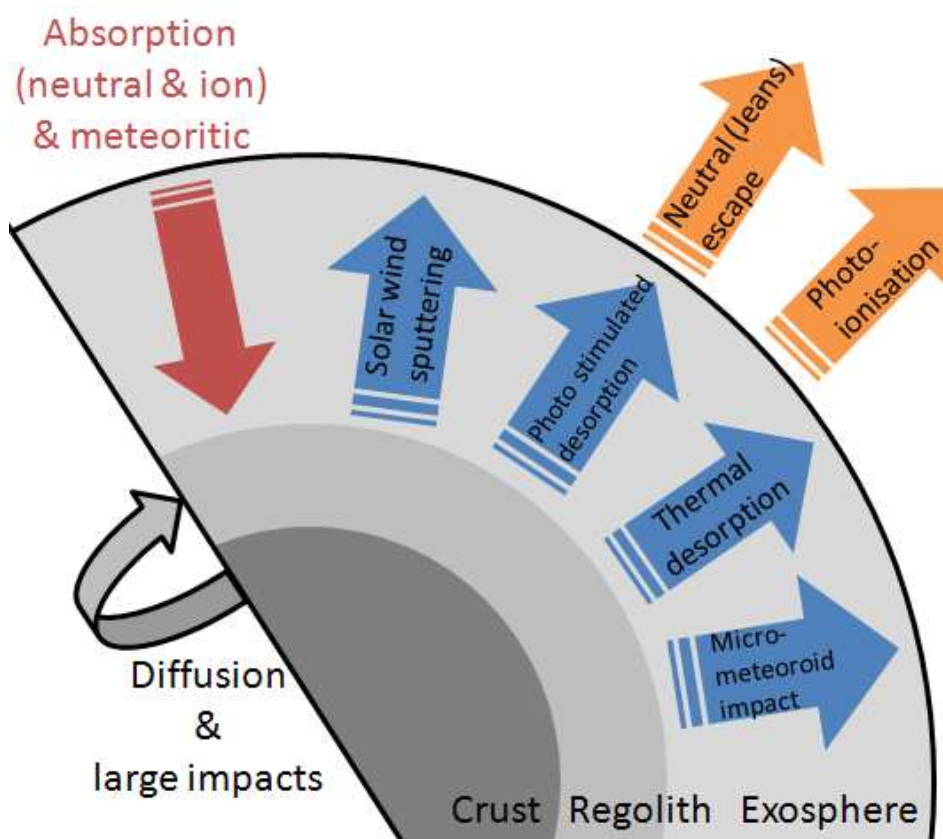


Figure 5.2: Probable source and sink processes for a surface bounded exosphere applied to Mercury (Image adapted from Leblanc et al. (2007)).

hydrogen is the bright interplanetary emissions which intensities are non negligible with respect to the expected brightness of Mercury's exospheric hydrogen.

As mentioned above, a detailed model of neutral H densities and of HI Ly- α is therefore needed to distinguish interplanetary background from exospheric H. Since the main source of Mercury's exospheric hydrogen is solar wind implantation, the study of hydrogen may serve as a tracer of the solar wind, its variability, its region of impact and its intensity.

In the creation of the exosphere of Mercury, many processes contribute to the release of particles. There are several different ejection processes on Mercury (Smyth and Marconi, 1995; Leblanc et al., 2007) most of them are summarised in Figure 5.2. Depending on species, local time, orbital position and solar wind conditions, different processes will dominate.

All these mechanisms eject particles from the surface, see Figure 5.2, with a process specific energy in different spatial directions and characteristic time spans.

TABLE V
 Estimated Atmospheric Physical Properties on Mercury

	H	He	O	Na	K	Notes
SCALE HEIGHTS (km)						
Subsolar H_s	1330	330	83	58	33	a
Antisolar, H_a	230	57	14	10	6	b
Dayside content (10^{27} atoms) N_d	4	100	140	60	0.7	c
Nightside content (10^{27} atoms) N_n	4	670	2200	60	0.7	c
PHOTOIONIZATION TIME (s)	5.5×10^6	3.8×10^6	8.8×10^5	12,800	7500	d
PRODUCTION RATES, (10^{22} s^{-1})						
Radiogenic, P_r	—	0.7–4.6	—	—	—	e
Sputtering, P_{sp}	—	—	30–300	3–30	<1	f
Photosputtering, $P_{\phi s}$	—	—	?	$10, <2000$	—	f,g
Meteoritic, P_m	—	—	—	2–14	0.3	h
Interplanetary medium, P_{ipm}	1.4	0.2	—	—	—	e,o
Solar wind + magnetosphere, P_{sw}	230–850	10–37	—	—	—	e,i
LOSS RATES, (10^{22} s^{-1})						
Jeans	<<80	—	—	—	—	j
Photoionization	<0.14	<13	<50	≤ 600	≤ 10	k
Solar-wind, magnetosphere ionization	0.09	0.06	1.3	0.04	.0008	l
Radiation pressure, nonthermal atoms	(8–70) $\times 10^3$	(7–70) $\times 10^3$	>7000.	?	>3.	m
ATMOSPHERIC LIFETIME (hr)						

a: $T = 575 \text{ K}$; b: $T = 100 \text{ K}$; c: From Table I and above scale heights. Area of a hemisphere = $3.75 \times 10^{17} \text{ cm}^2$. Night/day density ratio taken as 1 for H, 50 for He, 100 for O, and 1 for Na, K; d: Kumar (1976) and Sec. VI; e: Goldstein et al. (1981); f: Ip (1986); g: McGrath et al. (1986); h: Sec. VI; Morgan et al. (1987); i: H value assumed to be 23 times He; j: Sec. VI; k: Upper limits assume no recycling of ions from magnetosphere to surface; l: He value from (e); others are probably comparable if scaled by abundances; m: Smyth (1986); Ip (1986); n: Ratio of estimated content to loss rate. It does not include possible losses of source atoms. o: Assumed deposition efficiency 0.3.

Table 5.2: Sinks and sources of the exosphere of Mercury (Hunten et al., 1988)

Solar wind sputtering

The solar wind, composed mainly of electrons, protons and heavier ions², interacts directly with the regolith surface and releases neutral atoms into the exosphere.

This is because the incident plasma ions, that reach the exobase carry momentum. This momentum is directly transferred to an atmospheric atom or molecule in a elastic collision, which in turn can instigate a collision cascade (Johnson, 1994). The cascade causes atoms and molecules at the exobase to be knocked into ballistic trajectories that either populate the corona (McGrath and Johnson, 1987) or can escape the gravitational field (Sieveka and Johnson, 1984).

Depending on the solar wind pressure the compression and deformation of the magnetosphere will allow energetic particles to enter Mercury's close environment and impact the surface. For a slow solar wind speed of 400 km/s the precipitation of protons on the surface will be mostly distributed in oval-shaped areas in the north and south hemispheres³. For a fast solar wind of 800 km/s most of the dayside will be impacted by protons of higher energies (Kallio and Janhunen, 2003).

Micro-meteoroid vaporisation

Micro-meteoroids, of radius range $10^{-8} - 0.1\text{m}$, impact on the surface of Mercury and can be responsible for the local release of volatiles trapped in the surface through vaporisation. The impact velocities vary from 0-80 km/s leading to a deposition rate $4.752 \cdot 10^8$ g/year (Cremonese et al., 2005). In the process the high temperatures produced ranging between 2500 K and 5000 K (Eichhorn, 1978), can lead the ejected volatiles to escape into the exosphere as in the example of sodium, with a production rate ranging from $2.07 \cdot 10^6$ N $\text{cm}^{-2}\text{s}^{-1}$ to $3.9 \cdot 10^8$ N $\text{cm}^{-2}\text{s}^{-1}$ (Borin et al., 2010).

The main supply of atomic hydrogen from these micro-meteoroids may come from H₂O vapour deposited by them at their impact on the surface. H₂O is primarily photodissociated into H and OH and the corresponding production rate of H has an upper source limit of $240 \cdot 10^{22}$ atoms s^{-1} (Hunten et al., 1988)

Photon stimulated desorption

Photon stimulated desorption involves solar photons on the dayside of the planet (McGrath et al., 1986, Potter and Morgan, 1985 and Ip, 1990). This process releases neutral atoms into the exosphere with energies around 1 eV (Yakshinskiy and Madey, 1999 and Leblanc et al., 2007) and contributes to the formation of Mercury's sodium corona. Photodesorption is directly proportional to the flux of photons so that its efficiency increases with increasing solar zenith angle and decreases as the inverse square of the heliocentric distance (Lammer et al., 2003).

Chemical sputtering

Ejection by chemical sputtering occurs when reactive species such as H, C, O and S penetrate the surface and interact chemically with the regolith (Thomas, 1974 and Potter, 1995). The ejection takes place in several steps: surface implantation of the reactive species, chemical reaction with the target atoms and molecules and finally desorption.

²less than 5%

³at so called cusps region.

For instance, the release of water vapour (H_2O) is assumed to be coming from solar wind hydrogen atoms (H) with silicate molecules (Na_2SiO_3).

Thermal processes

At Mercury, trace atoms or molecules that are bound to or adsorbed on the surface can be desorbed thermally (Hunten and Sprague, 1997, 2002). Whereas thermal desorption refers to ejection of a trace species, like Na at Mercury, sublimation describes ejection of the principal species. Thermally desorbed species that are fully accommodated have roughly Maxwellian velocity distributions, typically given as a normalized flux distribution (Leblanc et al., 2007). When a particle interacts and is fully accommodated to the surface the particle will stick to the surface.

The probability per unit time, dP/dt , of ejection for thermal desorption is proportional to the surface concentration c_j of a species j , to the vibrational frequency on the surface ν_j , and to an exponential function of the surface binding energy. This ejection is dependent on T_s is the surface temperature and the Boltzmann constant (k_B).

Applied to Mercury's regolith, in reality, there exists an exchange of energy between the particle and the surface as the particles can be scattered by the surface lattice and since the expression above is a probability of ejection, the shallowest binding sites are depleted first so that, in the absence of replenishment, the ejection rate can decrease with time.

In the case of hydrogen, it is most probable that thermal desorption is the main channel of ejection (Hunten et al., 1988), which therefore, is assumed in the model to be the only ejection process. This important mechanism for hydrogen will be detailed in Chapter 5.2.4. H can however be ejected under various forms, molecular or atomic.

H and H_2 ejection

The production and dynamics of neutral hydrogen is not well understood: it is assumed in the following sections that it is released from the surface as atomic H, however it is also probably partly released as molecular H_2 (Hunten et al., 1988).

The possible contribution of H_2 ejection is not taken into account in the model, despite the suggestion by Crider and Vondrak (2002) that H, from a surface like the Moon, could be produced in very large quantities as H_2 (60%), as desorbing H (27%), as OH (10%) and as H_2O (2%). To be visible for Mariner 10, the H_2 molecules have to be dissociated when in the exosphere.

Photo-dissociation times of H_2 are between $1.2 \cdot 10^7$ s (quiet sun) and $5.23 \cdot 10^6$ s (active Sun) at 1 AU (Huebner et al., 1992) and gives photo-ionisation times that are equal to $1.8 \cdot 10^7$ s (quiet sun) and $8.7 \cdot 10^6$ s (active sun).

Dissociation energy is dependent on the vibrational state of the molecule but should be much larger than the escape energy of H at Mercury (~ 0.09 eV) (Huebner et al., 1992). When dissociated the H atoms gain energy from the dissociation and therefore, most of the produced H_2 -dissociation are very energetic and should quickly escape or re-impact Mercurys exosphere.

The fraction of dissociated atoms can probably be compared in a crude approximation to ionisation rates for hydrogen: depending on the velocity distribution, ionised hydrogen atoms may amount from 30% to 60% of the total hydrogen population. If we assume that the population of dissociated hydrogen molecules can be equivalent to the ionised hydrogen atom population, half of this amount of newly isotropic dissociated hydrogen will be directly escaping to space, while maybe half will be directed to the surface with very high energy. As they then hit the surface at these energies they will just bounce off and escape again leaving the escaped percentage of dissociated hydrogen to nearly 100%.

H_2 dissociation energy into $\text{H} + \text{H}$ has been measured and calculated to be $36\,118\text{ cm}^{-1}$ (4.47 eV) (Stoicheff (2001)), which means that on average, these new-born hydrogen atoms will be given 2.2 eV each, to be compared with the escape energy of one hydrogen atom (0.09 eV).

Therefore H_2 products should not contribute significantly to the profile of Mariner 10 observations below 1000 km in altitude⁴, as discussed in Chapter 5.5.4. Therefore, we neglect this contribution in the simulation.

Jeans escape

The basic concepts of planetary atmospheric escape were given by Jeans (1925) as individual molecules, in the high tail of the distribution, may reach escape velocity if the energy is high enough. These molecules are at a level in the atmosphere where the mean free path is comparable to the scale height.

In a quantity of gas the velocity of individual molecules varies continuously as they collide with one another, gaining and losing kinetic energy. The variation in kinetic energy among the molecules is described by the Maxwell distribution. The kinetic energy and mass of a molecule determine its velocity by $E_{kin} = \frac{1}{2}mv^2$. The more massive a molecule of a gas is, the lower the average velocity of the molecules is at a given temperature. A lower average velocity gives makes it less likely that any of the molecules reach escape velocity.

This is why hydrogen escapes from a given atmosphere more easily than for example sodium. Also, if the planet has a higher mass, the escape velocity is greater, and fewer particles will escape.

Jeans escape was later extended to the collisionless thermal escape model by Chamberlain (1963) and Chamberlain and Hunten (1987) as applicable to Mercury for the case of perfect accommodation.

Ionisation

Ionisation can be an important loss mechanism for particles in ballistic motion around Mercury. Ions created by photoionisation, called photo-ions, may be accelerated by the solar wind convection electric field and escape. Since this an important loss mechanism for hydrogen, ionisation will be detailed in Chapter 5.2.6.

Section I presents all the physical inputs and the problematics around the modelling of the hydrogen exosphere at Mercury, while section II focuses on the step-by-step implementation of the hydrogen Monte Carlo model built during this PhD work.

⁴ H_2 has much smaller time of residence in Mercury's exosphere and much more energy so that it won't produce the 104 – 132 K observed profile.

5.2 SECTION I: The physics behind

5.2.1 Definitions and basic exospheric theory

The exosphere of a planet, also known as planetary corona, is the collisionless region of the atmosphere (Chamberlain, 1963; Hunten et al., 1988). The escape velocity is defined as:

$$V_{esc}(r) = \sqrt{\frac{2GM_M}{r}} \quad (5.3)$$

where M_M is the mass of Mercury and r the distance from the centre of Mercury. It represents the limit velocity allowing the particles to escape from the gravitational attraction of the planet, represented by the acceleration of gravity g_M at the surface of Mercury:

$$g_M = \frac{G M_M}{r_M^2} = 370 \text{ cm s}^{-2} \quad (5.4)$$

with the gravitational constant: $G = 6.674 \cdot 10^{-11} \text{ m}^3 \text{ kg}^{-1} \text{ s}^{-2}$

the mass of Mercury: $M_M = 3.302 \cdot 10^{23} \text{ kg}$

the radius of Mercury: $r_M = 2439.7 \cdot 10^3 \text{ m}$

As the only force applied in the exosphere is gravity, each atmospheric species behaves independently and their density follows as a first approximation an exponential decrease governed by their own scale height H_i :

$$H_i = \frac{k_B T_\infty}{m_i g_M} \quad (5.5)$$

m_i is the mass of the particle (for example hydrogen) and T_∞ the exospheric temperature.

The density n_i of neutral species such as hydrogen defines the collision depth τ :

$$\tau = \int n_i(z) \sigma dz \quad (5.6)$$

where σ is the collision cross section, which is linked in turn to the mean free path ℓ :

The mean free path, ℓ_i , is the average distance travelled by a particle before colliding with other particles:

$$\ell_i = \frac{1}{n \sigma_i} \quad (5.7)$$

Where the total neutral density is n and σ_i is the collision cross section of the species i with other particles.

From equations 5.5 and 5.7, the dimensionless Knudsen number (K_i) can be built which defines the lower limit of an exosphere as the quota of mean free path and scale height

$$K_i = \frac{\ell_i}{H_i} \quad (5.8)$$

The exobase is defined as the altitude at which $K_i \approx 1$ while if $K_i \gg 1$, the regime is non-collisional. For Mercury the exobase is at the surface.

Many exospheric models start with the pioneering work of Jeans (1925) and later Chamberlain (1963) who solved the collisionless Boltzmann equation (also known as Liouville) and gave analytical expressions describing the densities and temperatures of the neutral species. These expressions are valid in specific conditions that will be discussed later in this chapter.

The knowledge of the physical conditions at the exobase, given by the velocity distribution of ejected particles (see section 5.2.2) is the first step in the classical exospheric theory in order to determine their subsequent motion in the exosphere. Particles are then acted upon by external forces such as gravity and solar radiation pressure take into account in Newton's equations of motion (see section 5.2.4). Some may re-impact the surface in due time and provide a source of hydrogen atoms released in the exosphere through the accurate description of surface-gas exchanges (accommodation at the surface, see section 5.2.5). Others will be lost to the exosphere through photoionisation (see section 5.2.6).

All these mechanisms describe the temporal evolution of hydrogen particles and the next sections aim at following them from their ejection from the surface, their deterministic ballistic motion in the exosphere, to their eventual re-impact at the surface or loss to the exosphere.

5.2.2 Mechanisms of ejection from the surface: Maxwell-Boltzmann distributions

Early assumptions on the Lunar and later on the Mercurian exosphere have stated that the gas-surface interaction can be represented by a true exobase theoretical approach. Although this assumption can be deemed too simplistic in its approach, it still serves as an important reminder that the surface is not an impenetrable boundary and that porosity has to be taken into account.

The modelling of Mercury and the Moon exospheres of hydrogen and helium remains difficult without a good knowledge of the distribution of the particles ejected from the surface. Previous studies have used two different energy distributions: the Maxwell-Boltzmann distribution (hereafter MB) and the Maxwell Boltzmann flux distribution (hereafter MBF) and sometimes a mixture of both distributions (Smith et al., 1978). These distributions have been studied and compared by Smith et al. (1978). In particular, these authors underlined that:

- A MB distribution assumes that the exospheric particles re-impacting a surface are fully thermalised before being ejected, that is particles are in thermodynamic equilibrium with the surface. Such a distribution does not produce a barometric variation of the exospheric density as demonstrated by Brinkmann (1970). MB distributions have been used by Hodges et al. (1980) when modelling the Lunar hydrogen exosphere. Hodges et al. suggested that re-impacting particles will remain a long enough time in the surface to collide several times with it leading to a local thermodynamic equilibrium. However, this assumption of long residence time has been criticised by Shemansky and Broadfoot (1977).

Assuming this assumption is fulfilled, Hodges et al. (1980) and later Kunc and Shemansky (1981) however showed that the surface-gas interaction would not produce a MB distribution because not only free-free collisions but also free-bound (absorption events) collisions would occur. In the latter case, the characteristic Debye temperature of the surface will define the maximum energy transfer per collision for weak interaction between light low-energy particles and the surface (Shemansky and Broadfoot, 1977) leading to the depletion of the energetic tail of the distribution with respect to that of the impacting particles.

The MB distribution is defined as:

$$f_{MB}(E) = \frac{2}{\pi^{1/2}} \cdot \frac{1}{k_B T_s} \left(\frac{E}{k_B T_s} \right)^{1/2} e^{-\left(\frac{E}{k_B T_s}\right)} \quad (5.9)$$

where E is the energy, k_B the Boltzmann constant and T_s the surface temperature.

- An MBF distribution was suggested as physically more correct than an MB distribution because it can produce the expected barometric density variation in specific cases (Brinkmann, 1970). However this distribution implies that there is a statistical equilibrium between surface and exosphere, an assumption which has no reason to be verified since gas-surface interactions are not constrained by the exospheric distribution but rather by the surface property (Shemansky and Broadfoot, 1977).

The MBF distribution is defined as:

$$f_{MBF}(E) = \frac{E}{(k_B T_s)^2} e^{-\left(\frac{E}{k_B T_s}\right)} \quad (5.10)$$

As shown by Shemansky and Broadfoot (1977) and Kunc and Shemansky (1981) from theoretical calculations of surface-gas interaction and by Smith et al. (1978) by comparison with the helium exospheres at both Moon and Mercury, the acting distribution of light atoms when ejected from a surface with low energy is neither MB nor MBF, the physics of the interaction being highly dependent on the structure and composition of the upper surface, on its roughness, on its porosity and ultimately on its temperature. So far no study has ever been published on the dependency of this distribution to these surface parameters.

On a physical and mathematical level, the link between MB and MBF distribution can be explained. In a MB distribution, the quantity $f_{MB}(v_i) d^3v$ represents the mean number of particles per unit volume between v and $v + dv$, while the MBF distribution expresses the number of particles passing through per second in a unit area.

The relationship between the MB and MBF distributions is then that of a function to its integral in velocity phase space, which volume is defined as:

$$d^3v = \sin(\theta) d\theta d\phi v^2 dv, \quad (5.11)$$

where θ and ϕ are the ejection angles from a plane surface (θ is the angle between the velocity vector of the ejecta and the normal to the surface). Within this volume, particles are moving with an associated flux $\Phi(v)$ in $\text{cm}^{-2} \text{s}^{-1}$ so that:

$$\begin{aligned} \Phi(v) &= \int f_{MB}(v) v \cos(\theta) d^3v \\ &= \iint_{\theta=-\pi/2}^{\pi/2} \int_{\phi=0}^{2\pi} f_{MB}(v) v \cos(\theta) \sin(\theta) d\theta d\phi v^2 dv \end{aligned} \quad (5.12)$$

$$\begin{aligned} &= 2\pi \int f_{MB}(v) v^3 dv \\ &= \int f_{MBF}(v) dv \end{aligned} \quad (5.13)$$

because $\int_{-\pi/2}^{\pi/2} \sin(\theta) \cos(\theta) d\theta = 1$ and $\int_0^{2\pi} d\phi = 2\pi$.

Equation (5.13) can be expressed according to the particles' kinetic energy $E = m_H v^2/2$ of mass m_H in order to retrieve equation (5.10).

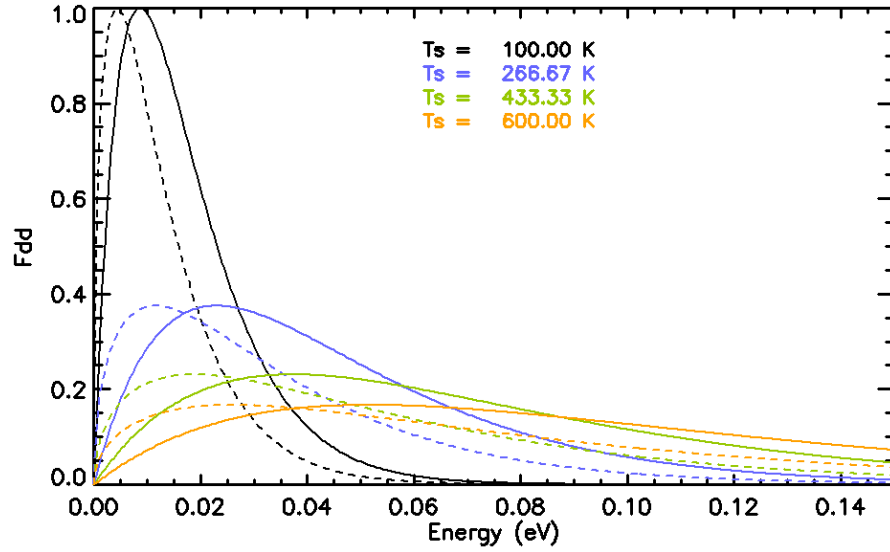


Figure 5.3: MB (dashed line) and MBF (solid line) energy distribution of the particles when ejected from various surface temperature T_s . The peak of the distribution is at $k_B \cdot T_s/2$ in the case of MB distribution and at $k_B \cdot T_s$ in the case of MBF distribution.

According to Leblanc and Johnson (2003), the precise angular form of the MBF distribution applied to light species and for a surface temperature T_s is:

$$f(E, \theta) = 2\cos(\theta) \frac{E}{(k_B T_s)^2} e^{-E/k_B T_s} \quad (5.14)$$

where θ is the ejection angle with respect to the normal to the surface.

Equation (5.14) can be divided into a function depending on θ and a function f_1 depending on E :

$$f_1(E) = \frac{2E}{(k_B T_s)^2} e^{-E/k_B T_s} \quad (5.15)$$

The distribution $f_1(E)$ is plotted in Figure 5.3 for both MB and MBF distributions.

As can be seen, the knowledge of the surface temperature (exobase) determines the actual shape of the distribution.

5.2.3 Temperature mapping

A realistic mapping of the surface temperature is crucial in order to consistently describe the thermal exchanges at the surface (desorption/adsorption). The model based on Leblanc and Johnson (2003) and Wurz and Lammer (2003) was adopted where the temperature of the surface T_s depends on the solar zenith angle and the solar photon flux intensity as derived from infrared measurements on Mariner 10 (Chase et al., 1976).

On the dayside the surface temperature is given by:

$$T_s(\text{long}, \text{lat}) = T_1 + T_0 \times (\cos(\text{lat}) \times \cos(\text{long}))^{1/4} \quad (5.16)$$

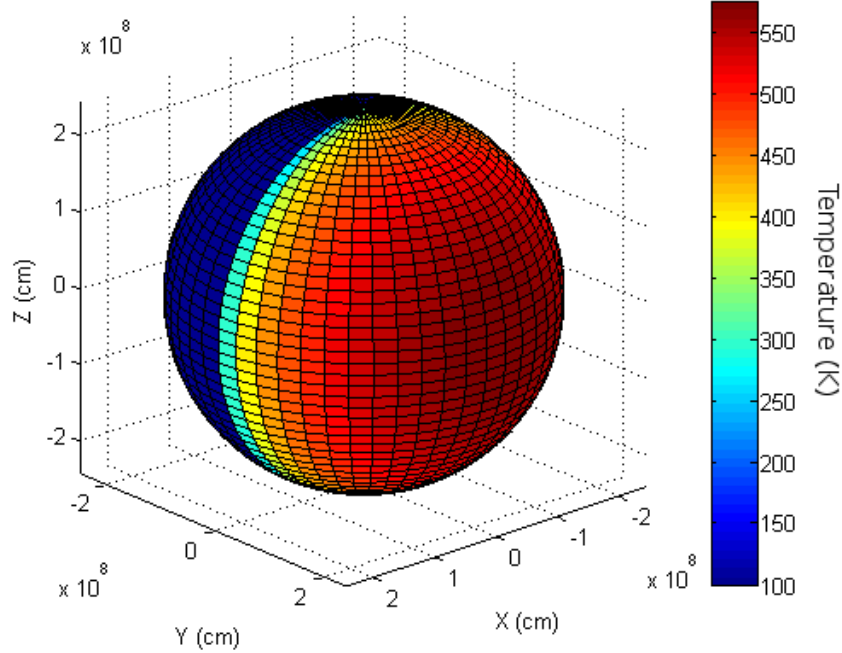


Figure 5.4: Surface temperature map applied in the simulation, where positive y-axis is pointing towards the Sun. The maximum temperature at the subsolar point is 575 K (dark red) while the nightside temperature is a static value of 100 K (blue).

with $T_1 = 100$ K and T_0 varying from 600 K at the perihelion to 475 K at the aphelion, see Figure 5.4.

This formula is originally deduced from Butler (1997) and parametrized in order to reproduce the subsolar point temperature variation with respect to Mercury's heliocentric distance from ~ 575 K at aphelion to ~ 700 K at perihelion (Hale and Hapke, 2002).

On the nightside the temperature is assumed to be constant, $T_s = 100$ K.

5.2.4 Ballistic motion of particles in the exosphere and external conditions

When air friction is negligible, as it is in the tenuous exosphere of Mercury, the motion of a particle of mass m_i under the influence of gravity is determined completely by the Newton equation and the knowledge of the launch speed and the launch angle.

As explained in section 5.2.2, these dynamics start with the ejection of the particle from a surface with a given temperature and velocity distribution (see Figure 5.5). The particle is ejected as a source particle and can, while in flight, either escape or return to the surface. The external forces applied to its trajectory is gravitation and, as explained below, solar radiation pressure.

When the particle on a re-impacting trajectory interacts once again with the surface, it may accommodate with the surface, take the temperature of the surface or a fraction of

In a general way, the acceleration of an atom due to resonant scattering of solar radiation is expressed as (Smyth, 1979, Potter and Morgan, 1987):

$$a_{sol} = \frac{hc}{\lambda_i} \frac{\pi e^2}{m_e m_i c^2} \frac{\pi \Phi_{\lambda_i}}{d^2} f_i \quad (5.20)$$

e and m_e are the charge and mass of the electron, λ_i and f_i are the wavelength and the quantum oscillator strength of the resonant transition, hc/λ_i represents the change of momentum of the target atom. For HI Ly- α transition ($^2S-^2P_{1/2}$), $\lambda_i = 121.6$ nm and $f_i = 0.416$. $\pi\Phi_{\lambda_i}$ is the solar flux at the wavelength of the resonance line at 1 AU, expressed in photons $\text{cm}^{-2} \text{s}^{-1}$ in the rest frame of the hydrogen atom. d is the heliocentric distance expressed in AU.

The solar radiation acceleration depends on the solar flux, which in turn is varying with heliocentric distance (factor 1.52 from perihelion to aphelion of Mercury). It also depends on the planet's radial velocity, that varies with the elliptic orbit of Mercury around the Sun.

While the maximum solar radiation acceleration can reach 200 cm s^{-2} for Na atoms (Smyth, 1986), it is only $\sim 4 \text{ cm s}^{-2}$ for hydrogen H atoms, much smaller than Mercury's gravity (370 cm s^{-2}).

In order to constrain the motion of hydrogen particles at the exobase and in the exosphere of Mercury, a precise evaluation of sources and sinks must be carried out. This is what the next two sections present and detail.

5.2.5 Sources of hydrogen at Mercury: Thermal processes

Apart from solar wind sputtering, micro-meteoroid vaporisation, photon-stimulated desorption and chemical sputtering, one source of hydrogen at Mercury can be considered dominant: thermal desorption. The quantitative inclusion of thermal desorption is made in two steps: first by calculating the residence time in the surface with respect to the surface temperature and second by calculating the probability of ejection.

Residence time

When a particle interacts with the surface the standard exospheric theory assumes that the particle is fully accommodated to the surface. This means that the particle will stick to the surface. In reality there exists an exchange of energy between the particle and the surface as the particles can be scattered by the surface lattice.

A characteristic time for surface accommodation is the residence time, which is the time a particle resides at the surface before being (re-)ejected (Hunten et al., 1988).

This residence time is depending on the surface temperature and can be expressed as following:

$$\tau_{ads} = \tau_0 e^{D_0/k_B T_s} \quad (5.21)$$

where τ_0 is the vibration time for the van der Waals potential (around 10^{-13} s)

D'_0 is the "depth to $\nu = 0$ " here used as $D_0/k_B =$ heat of adsorption expressed as an equivalent temperature, k_B is the Boltzmann constant and T_s is the local surface temperature.

Numerical values are taken from Table 5.3.

Therefore equation (5.21) takes the form:

$$\tau_{ads} = \tau_0 e^{D'_0/T_s} \quad (5.22)$$

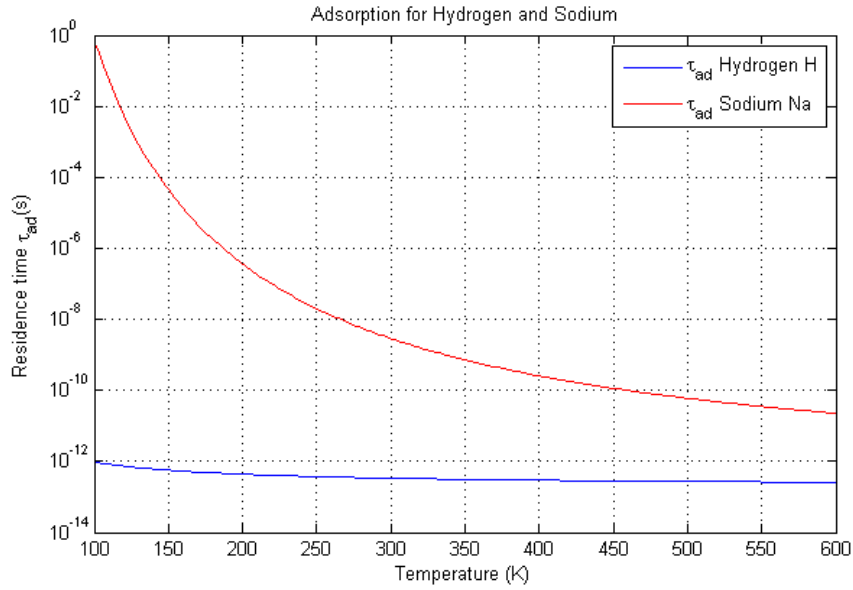


Figure 5.6: Residence time for adsorption for hydrogen and sodium calculated between 100 and 600 K, with the data of Table 5.3.

The lower the surface temperature, the more likely the atom will be adsorbed in the surface on impact. With a residence time of $\sim 10^{-13}$ s at most, see Figure 5.6, it is very unlikely that hydrogen will be adsorbed at all in the surface of Mercury, whatever the surface temperature and night/day conditions. Compared to hydrogen, sodium behaves very differently, with residence times ranging between 0.71 s at $T = 100$ K and 2.26×10^{-11} s at $T = 600$ K which means that on the nightside of the planet, impacting Na atoms will have a relatively large probability to be adsorbed.

The calculation of residence time, according to classical theory, is however subject to discrepancy when applied to more complex environments. Many unknowns, such as the composition of the surface, the variations in surface temperature and the energy of the particles can all affect the result. Recent studies on alkali atoms such as Na show possible variations in residence time ranging from 10^{-9} s to 10^{-13} s (Holmlid, 2006; Killen et al., 2007). However, a commensurate change in the residence time from 10^{-13} s to a few orders of magnitude larger, as these latter studies would suggest, would not affect the probability of adsorption of hydrogen atoms in the simulation as it would require much larger changes than that.

Ejection probability

At each time step, the parameter indicative of the probability, that a particle on the surface is ejected is calculated. This probability is based on the time of residence τ_{ads} , calculated above, of a particle in the surface using the mathematical description and the values from Hunten et al. (1988) and shown in (Table 5.3).

The probability of ejection of a test particle from Mercury's surface during a time step Δt is then:

$$P_E = \frac{\Delta t}{\tau_{ads}} \quad (5.23)$$

Considering the maximum surface temperature, $T = 600$ K, the maximum ejection probability for hydrogen particles is, using Table 5.3 and with $\Delta t = 0.2$ s:

$$P_E^{max} = \frac{0.2}{2.6 \cdot 10^{-13}} = 7.7 \cdot 10^{11} \quad (5.24)$$

The minimum ejection probability achievable P_E^{min} , for a surface temperature of $T = 100$ K is in the same way:

$$P_E^{min} = \frac{0.2}{9.5 \cdot 10^{-13}} = 2.1 \cdot 10^{11} \quad (5.25)$$

This means that in all conditions found at Mercury, the probability of hydrogen atoms to be ejected or re-ejected from the surface is 100%.

Surface-gas interactions then need to be evaluated in order to calculate the energy of the bouncing re-ejected particle. This is done in the next subsection by introducing the concept of accommodation coefficient.

Surface accommodation on re-impact

Besides the issue of the choice of the adequate energy distribution for ejected particles, the hydrogen exospheres and the interaction of particles with the surface have previously been described assuming:

- A saturated surface, that is, each time a light particle impacts the surface, a new one is ejected,
- Full absorption of the impacting particle by the surface so that the re-ejected particle is ejected at the energy of the surface.

It was later demonstrated by Shemansky and Broadfoot (1977) that these assumptions are probably incorrect because light species have a very short time of residence in the surface. Moreover, these authors suggested that even if multiple collisions occur, the high-energy tail of the distribution of the particle will be depleted with respect to a Maxwellian gas, because there is an upper limit on the quantity of energy that can be delivered from a surface to an impacting low-energy light atom whereas the energy loss by this same atom into the surface is not limited.

Following this idea, Hunten et al. (1988) suggested that the behaviour of an atom at the surface of a planet such as Mercury could be modelled as having a specific potential energy as illustrated by Figure 5.7. A particle colliding with the surface will lose or gain energy and will be adsorbed only if enough energy is lost and falls below zero: see the potential well in Figure 5.7. Otherwise, the incoming particle will simply be scattered off the surface.

When a particle is bound at the surface the potential energy is at its minimum and equivalent to a vibration at $k_B T$. The minimum energy needed to extract an atom from the surface is E_a , the activation energy, corresponding to the right-hand side of Figure 5.7.

Accommodation coefficient

The approach chosen in this work is based on the concept of two exospheric populations of particles. As suggested by Hunten et al. (1988), the hydrogen exosphere is supposed to be produced from:

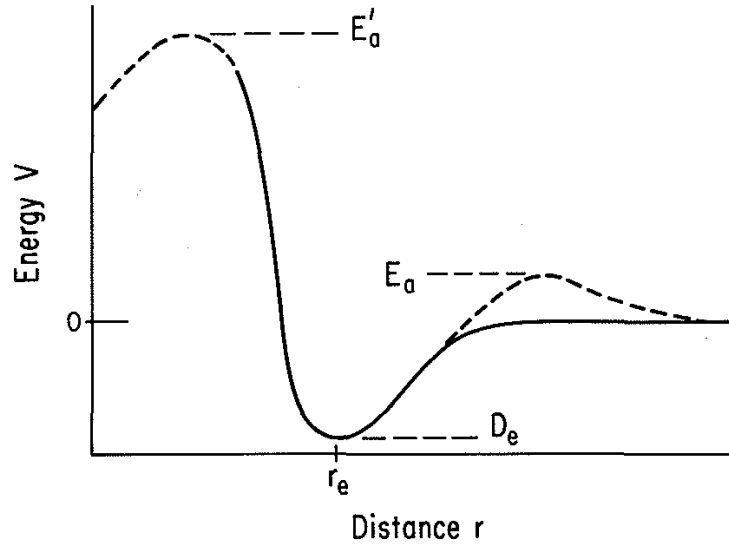


Figure 5.7: Potential energy curve for an atom at the surface. Well depth D_e and distance r_e from the well, activation energy E_a and diffusion activation energy through lattice E'_a (Image Hunten et al (1988))

- *Source particles*, which are absorbed particles ejected from the surface (thence following MB or MBF-type distributions),
- *Ambient particles*, which are exospheric particles that are moving around Mercury.

Ambient particles can then in turn re-impact the surface. When impacting, they will not be fully (energetically) accommodated to the surface but only partially as suggested by Shemansky and Broadfoot (1977) leading to night/day asymmetries of the hydrogen exosphere.

A particle which arrives in contact with the surface will make a certain number of collisions with the surface before being re-ejected. One can simply model the energy exchange between surface and the particle by introducing the accommodation coefficient α as defined by Knudsen in 1911 (see Hunten et al 1988):

$$\alpha = \frac{E_2 - E_0}{E_1 - E_0} \quad (5.26)$$

where

E_0 is the energy of the impacting particle

E_2 is the energy of the particle after re-ejection. E_1 is the thermal energy of the surface:

$$E_1 = k_B T_s \quad (5.27)$$

where

T_s is the surface temperature,

k_B the Boltzmann constant.

So:

$$E_2 = \alpha(k_B T_s - E_0) + E_0 \quad (5.28)$$

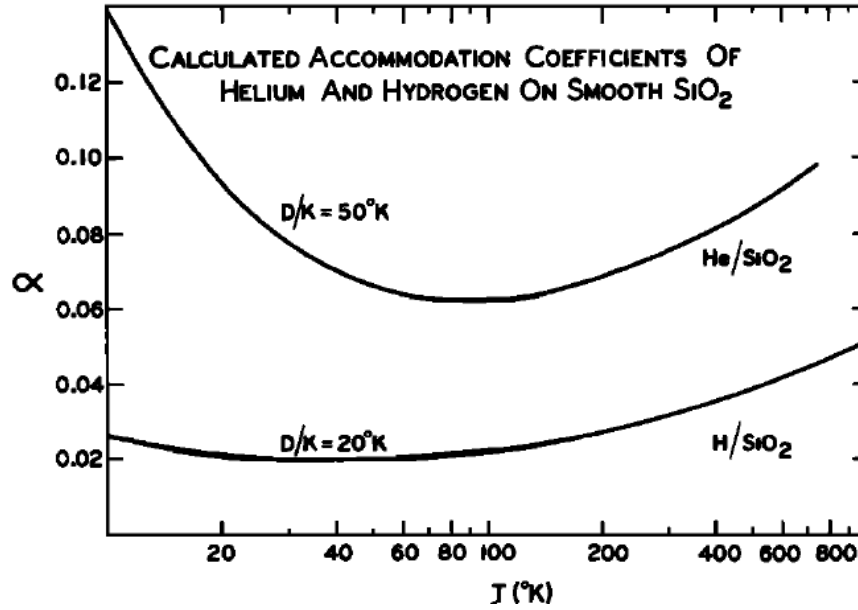


Figure 5.8: Calculated accommodation coefficients for helium and hydrogen on smooth SiO_2 . Temperature scale is gas temperature (Image Shemansky and Broadfoot (1977)).

Laboratory measurements of the accommodation coefficients for several species have been performed (Frisch and Stern, 1931; Estermann and Stern, 1930; Roberts, 1930, 1932) and despite several attempts it has been concluded that it is extremely difficult to measure it correctly. The value also changes with the surface composition and since most of the measurements have been made using single surface compositions, it is highly volatile to apply it directly to the mixed composition of Mercury's surface. For example values of α for helium on alkaline metals are in the range of 0.02 – 0.1 (Trilling, 1970) where the last value was also achieved by Shemansky and Broadfoot (1977) as an application to the Moon. They also state that atomic hydrogen would have values of α a factor of at least 2 times below that of Helium, as can be seen in Figure 5.8.

In the accommodation approach adopted in the present model, the energy E_2 is defined from a MB or MBF distribution at the surface temperature T_s , so that if $\alpha = 1$, the same distribution as for that of the source particles is derived. In this way, a partial thermalisation of the exospheric particles at the surface is introduced, the α coefficient defining to which extent the high-energy tail of the distribution will be depleted as suggested by Shemansky and Broadfoot (1977).

The value for α of 0.08 for hydrogen that is used in the Monte Carlo simulation SPERO is taken from Table 5.3 as stated by Hunten et al. (1988).

Accommodation coefficient limits: Debye temperature

As mentioned above, one of the largest factors of uncertainty is the energy accommodation coefficient α . In our model this quantity is based on the classical calculations of Kunc and Shemansky (see Hunten et al., 1988) for hydrogen on an α quartz surface for a temperature of 600 K.

TABLE IV
Gas-Surface Physical Interaction Parameters for α Quartz^a

Species	H	He	O	Na	K
Well depth ^b D_e (K)	254	102	920	3000	2800
Well distance ^b r_e (Å)	3.39	2.57	3.11	3.48	4.04
Depth to $v = 0$ ^b D_0 (K)	156	54	837	2900	2720
Vibration period $\tau(10^{-13}\text{s})$	2.0	4.7	2.7	1.8	2.5
600 K adsorption time τ_a (s)	2.6×10^{-13}	5.1×10^{-13}	1.3×10^{-12}	2.3×10^{-11}	2.3×10^{-11}
100 K adsorption time τ_a (s)	9.5×10^{-13}	8.1×10^{-13}	1.8×10^{-9}	0.71	0.16
600 K accom- modation coefficient α	0.08	0.05	0.11	0.62	0.26

^aSources: Kunc and Shemansky (1985) for helium; Shemansky and Kunc (in preparation) for all others.

^b D_e , r_e , are illustrated in Fig. 13. D_0 is the dissociation energy to the separated-atom limit from the lowest vibrational level.

Table 5.3: Gas-surface physical interactions, Table IV from Hunten et al 1988

In the present SPERO model, this coefficient is directly applied for a temperature gradient of 100–600 K although the value given in Hunten et al. (1988) is theoretically only applicable for 600 K, leading to a possible discrepancy in the ejection or adsorption percentage, which in turn could affect the shape of the density profile. Energy exchange reactions with the surface is limited to single phonons⁵, a quantum of the lattice vibrations in a solid, which in turn are defined by the characteristic Debye temperature of the solid.

To apply the energy accommodation coefficient for a surface, a macroscopic T_s is assumed. This might be too simple an assumption in the case of Mercury since the regolith surface of Mercury is much more complicated than assuming a simple quartz surface.

The conclusion of such preliminary reasoning could be that, instead of using an accommodation coefficient based on a macroscopic temperature T_s , a molecular temperature describing the heat capacity of a solid medium such as a crystal should be applied, called the "Debye temperature".

The Debye temperature Θ is the intrinsic temperature of the molecules located in the surface as opposed to the macroscopic temperature of the surface governing the calculation of the accommodation coefficient. Θ is the highest achievable temperature due to a single normal mode of vibration:

$$\Theta \equiv \frac{h\nu_m}{k_B} \quad (5.29)$$

where: h is Planck's constant

k_B is Boltzmann's constant

and ν_m is the maximal vibrational frequency defined as:

$$\nu_m = \frac{9N_A\rho}{4\pi m} \left(\frac{1}{v_s^3} + \frac{2}{v_p^3} \right)^{-1} \quad (5.30)$$

⁵An assumption by Shemansky and Broadfoot (1977) and discussed by Hodges (1980)

where: N_A is Avogadro's number
 ρ is the density
 m is the atomic weight
 v_s is the S-wave speed⁶
 v_p is the P-wave speed⁷

With these definitions the accommodation coefficient can be redefined as a reduction of the classical formula of London (see Devonshire, 1937):

$$\alpha_{\ominus} = \left(\frac{3}{8}\right) \left(\frac{1}{m_i^{1/3} M_i}\right) \left(\frac{8\pi h^2 \kappa^2 T_i}{k_B \Theta^2}\right)^{3/2} \quad (5.31)$$

where: m_i is the mass of the gas atom
 M_i is the mass of the surface atom
 $1/\kappa$ is the equilibrium internuclear distance
 T_i is the gas temperature

At low finite temperatures, where a majority of collisions are adsorption collisions, the energy that is delivered to the gas is limited by the potential well depth of the gas-surface system. At high temperatures, such as the dayside of Mercury where adsorption collisions are not in majority, the energy transfer is controlled by the Debye characteristic temperature of the solid (Kunc and Shemansky, 1981) as clearly seen in Figure 5.9.

A low accommodation coefficient implies rapid transport of gases. Despite the opposing effect that surface roughness and scattering angles have, this leads to an increased mobility of the particles and a higher escape rate. Thus the quality of the surface does not only affect the accommodation coefficient but also the angular scattering distribution, which both have transport properties and therefore should therefore also affect the equilibrium energy distribution as mentioned in Chapter 5.5.1.

Shemansky and Broadfoot (1977) pointed out that Debye temperature effects on the energetic tail and accommodation coefficient act in a similar way on the density distribution of the light species in the exosphere.

Complete accommodation

In the case of fully accommodated particles at the surface the classical exospheric theory (Hodges and Johnson, 1968; Hodges, 1980) leads to an approximation of the density variation with respect to surface temperature. Following this theory, the surface density depends on the surface temperature and follows the relation $T_s^{-5/2}$. Exospheric particles are bouncing from place to place on the exobase-surface with a characteristic length of each hop equal to the scale height of the neutral atmosphere (H_i , equation (5.5)). As the motion of particles follows a random walk (stochastic condition), the number of hops between two hemispheres of the planet (separated by a r_M) is of the order of (Hunten et al., 1988):

$$\Delta^2 = \frac{R_M^2}{H_i^2} \quad (5.32)$$

⁶S-waves are transverse waves, which means that particles in the medium move at right angles to the energy that is being transferred.

⁷P-waves are compression waves, which means that particles in the medium move in the same direction as the energy that is being transferred.

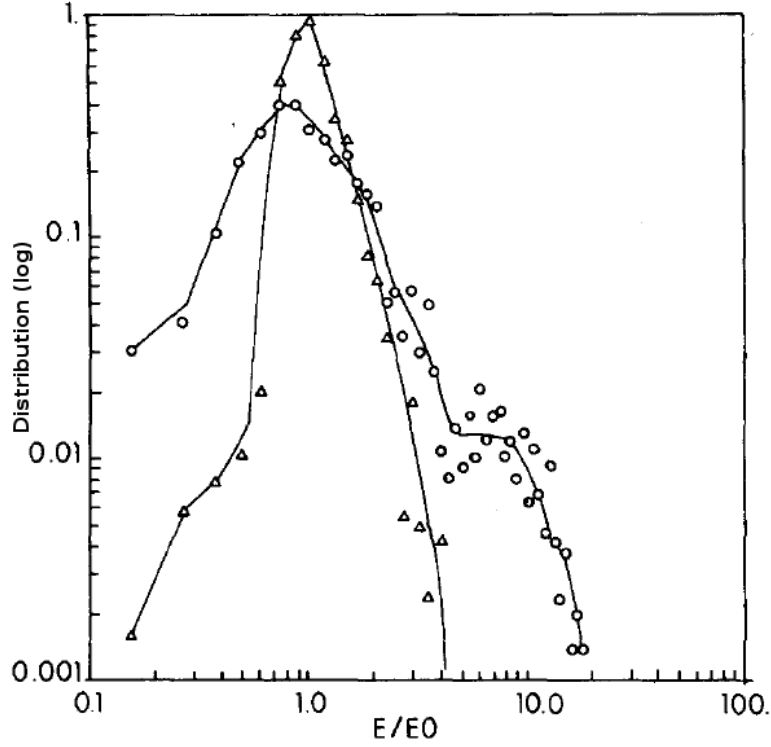


Figure 5.9: Energy distribution of helium atoms scattered from an α -quartz surface. Incident atoms with energy of 600 K, surface temperature of 600 K. Triangles is distribution calculated for correct Debye characteristic temperature for quartz ($\Theta = 470K$) while circles is for $\Theta = 210K$ (Image Kunc and Shemansky (1981))

The distance between two hemispheres (day/night) is of the order of R_M , the radius of Mercury.

The characteristic time t_{ff} of a hop done by a particle thermalised with the surface is the ballistic/free fall time defined as:

$$t_{ff} = \sqrt{2} \frac{v_i}{g} \cos(45^\circ) = \frac{2}{g} \left(\frac{k_B T_\infty}{m_i} \right)^{1/2} = 2 \left(\frac{H_i}{g} \right)^{1/2} \quad (5.33)$$

when the motion is projected at 45° from the horizontal (average angle of ejected particle) with characteristic speed v_i . v_i is the thermal velocity $v_i = \sqrt{(2k_B T_\infty/m_i)}$ for the temperature at the exobase equal, for Mercury, to the surface temperature ($T_\infty = T_s$).

From equation 5.32 and equation 5.33 the migration time from hemisphere to hemisphere can be deduced

$$t_m = t_{ff} \Delta^2 = 2 g R_M^2 \left(\frac{m_i}{k_B T_\infty} \right)^{3/2} \quad (5.34)$$

The number flux ϕ_{hemi} of particles i travelling from one hemisphere to another is

$$\phi_{hemi} = \frac{N_i}{t_m} = \frac{n_i H_i}{t_m} \quad (5.35)$$

where N_i the integrated column density of gas (in cm^{-2}) above the surface and n_i the

number density in cm^{-3} . In the steady-state case, the flux ϕ_{hemi} is constant and hence:

$$n_i T_{\infty}^{-5/2} = C^{st} \quad (5.36)$$

On Earth, this first-order approximation for hydrogen is valid and known as the “zero net ballistic flow” condition (Quesette, 1972). On Mercury this relation can serve as a useful starting point for comparison in the case of full accommodation $\alpha = 1$.

Now that the ejection sources and particle-surface interactions have been clarified with respect to probabilities of ejection and the limitations to the accommodation approach adopted in this study, the only remaining factor influencing the formation of the hydrogen exosphere and its maintenance over time is how hydrogen is lost to the exosphere.

5.2.6 Sinks of hydrogen at Mercury: Ionisation

Apart from Jeans escape taken into account when calculating the trajectories of the particles (neutral escape), and which is dominant for hydrogen (H) and helium (He), one other loss process can be considered for hydrogen: ionisation. Again, the calculation of this effect in the Monte Carlo model at each time step of the orbit can be done in two steps: first by calculating the time before ionisation with respect to the heliocentric distance, and second by deriving from it the probability of ionisation of a hydrogen particle, which will then be lost to the neutral exosphere.

Characteristic time before ionisation

Ionisation can be an important loss mechanism for particles in ballistic motion around Mercury.

The time before ionisation of an hydrogen atom at 1 AU at quiet solar conditions, counting from the sun, is $\tau_{\text{ion}_{1\text{AU}}} = 7.8 \times 10^6$ s (Fulle et al., 2007).

The value for $\tau_{\text{ion}_{\text{Mercury}}}$ is calculated by $\tau_{\text{ion}_{1\text{AU}}}$ scaled to $1/d^2$, where d is the heliocentric distance (Fulle et al., 2007):

$$\tau_{\text{ion}_{\text{Mercury}}} = \tau_{\text{ion}_{1\text{AU}}} \cdot \frac{d_{\text{Mercury}}^2}{d_{1\text{AU}}^2} \quad (5.37)$$

with the values above and the following

$$d_{1\text{AU}} = 1 \text{ AU} = 149.6 \cdot 10^{11} \text{ cm}$$

$$d_{\text{Mercury}}(\text{aphelion}) = 0.467 \text{ AU} = 69.8 \cdot 10^{11} \text{ cm}$$

The calculation gives the value:

$$\tau_{\text{ion}_{\text{Mercury}}} = 1.69 \cdot 10^6 \text{ s} \quad (5.38)$$

at the surface of Mercury, which is essentially the lifetime of H atoms against ionisation. It is around 3 times less than the recommended value of Hunten et al. (1988) of $\sim 5.5 \cdot 10^6$ s using a different reference for ionisation times.

The maximum photoionisation loss rate for H is then equal to the number of atoms, assumed to be $4 \cdot 10^{27}$ from the measurements of Mariner 10 summarised in Table 5.2, divided by the ionisation time and multiplied by the maximum loss efficiency, assumed to be of the order of 2. The result gives $0.47 \cdot 10^{22} \text{ s}^{-1}$ to compare with the value $0.14 \cdot 10^{22} \text{ s}^{-1}$ calculated by Hunten et al. (1988) in an identical way but with different inputs.

This high loss rate makes photoionisation the second most efficient escape mechanism after Jeans escape.

Charge-exchange reactions may be considered too, however Killen and Ip (1999) showed that the charge-exchange reaction rate is very small compared to photoionisation and can be safely neglected for most species.

5.2.7 Deriving emission line brightness: radiative transfer and optical thickness (*with Jean-Yves Chaufray*)

Radiative transfer of resonance line

A planetary Lyman- α radiation is produced by resonant scattering of solar photons by atomic hydrogen in the planetary exosphere. A hydrogen atom, initially at ground electronic state, can absorb a photon and be excited to first electronic state. This excitation is instantaneously followed by the emission of a new photon associated to the de-excitation of the hydrogen atom to ground state.

All the hydrogen atoms do not have the same velocity, but have velocities in different direction described by the velocity function distribution. These movements create a Doppler broadening of the emission lines. Moreover, emission lines also have a natural broadening due to Heisenberg uncertainties.

To compute the planetary Lyman- α radiation, the radiative transfer equation, which describes the transport of photons in a material medium (Chandrasekhar, 1950), must be solved. If an isotropic emission is assumed, the formal solution of the radiative transfer equation, giving the brightness $I(r, \Omega)$ along a line of sight is given by:

$$I(r, \Omega) = \frac{1}{4\pi} \iint \epsilon_\lambda(r + s\Omega) \exp[-\tau_\lambda(r, r + s\Omega)] ds d\lambda \quad (5.39)$$

where the brightness is integrated over the line spectral profile, Ω is the direction of the line of sight and r the position of the observer. The distance between the observer and a point on the line of sight is s varying from 0 (observer position) to infinity. ϵ is the local emissivity (in photons/cm³/s/nm) at wavelength λ and τ , $(r, r + s\Omega)$ is the optical thickness between the observer position r and the point on the line of sight at $r + s\Omega$ for wavelength λ .

The optical thickness is a dimensional number measuring the transparency of a medium. When $\tau \ll 1$ at all wavelengths, the medium is said optically thin and else the medium is said optically thick.

The optical thickness between two points is given by:

$$\tau_\lambda(r, r + s\Omega) = \int_0^s \sigma_\lambda(r + s'\Omega) n(r + s'\Omega) ds' \quad (5.40)$$

where $n(s')$ is the local density of hydrogen atoms and σ_λ is the scattering cross section. This cross section measures the efficiency for a hydrogen atom to absorb a photon. Due to natural and Doppler broadening, the typical profile of the scattering cross section is a Voigt profile.

In the exosphere of Mercury, the hydrogen density is very small (Hunten et al., 1988), and then optical thickness is expected to be much less than 1 at all wavelengths and so

the medium optically thin. If the optically thin condition is fulfilled, the emissivity ϵ integrated over wavelengths is directly proportional to the hydrogen density and can be written

$$\epsilon(r) = \frac{1}{4\pi} gn(r) \quad (5.41)$$

where g is the excitation factor expressed in s^{-1} . It represents the number of hydrogen atoms excited by the solar radiation per second.

The value of the excitation factor during Mariner 10 mission has been estimated to $5.3 \cdot 10^{-3} s^{-1}$ (Shemansky, see Hunten et al., 1988). For an optically thin medium, the brightness along the line of sight (for a limb observation) is then given by

$$I(r, \Omega) = \frac{1}{4\pi} gN \quad (5.42)$$

where N is the hydrogen slant density.

Macroscopic quantities can be calculated depending on the path of the particles. Densities are one of these outputs. In order to derive from these exospheric H densities the brightness of H I Lyman-alpha, one of the most intense resonant lines in the FUV spectrum –that will be measured by PHEBUS and that was recorded by Mariner 10–, the assumption of an optically thick or thin medium must first be tested, which can be done using a radiative transfer approach for a resonant line.

Radiative transfer: Modeling

The model is decomposed in two parts. In a first part the local emissions are computed using a Monte Carlo scheme. In the second part, the formal solution of radiative transfer is computed using equation (5.39) by integrating the local emissivity along the line of sight. This division is usually used in radiative transfer modelling of resonant line.

The Monte Carlo code used to compute local spectral emissivity is based on the model used by Chaufray et al. (2009) and have been adapted to describe the Lyman- α line in the exosphere of Mercury. In this model, the Lyman- α albedo of the surface of Mercury is assumed to be close to the albedo of the Moon which is 4% (Chassefiere et al. 2010) and the density and temperatures are the outputs of the exospheric model with rescaling of the density to arbitrary value. This rescaling factor is a free parameter adjusted to fit Mariner 10 observations.

In this model, test particles representative of solar photons are followed along their trajectory. Their scattering by hydrogen atoms in the exosphere of Mercury is described as well as their reflection and absorption on the surface. The Mariner 10 geometry of observation is approximated as during the Mariner 10 observation.

Optically thin medium: g-values

When an atmosphere can be regarded as optically thin, that is when the *mean free path* (ℓ_i , see equation 5.7) \gg *scale height* (H_i , see equation 5.5) and there is no particle collisions, the need for radiative transfer diminishes and instead the exospheric emissions can be calculated using "g-values", or "solar photon scattering probabilities".

A definition of the g-value is provided by Chamberlain (1961) as "*the number of photons that would be scattered per second per unit atom if there were no deactivation*" (Chamberlain (1961), p. 424), which Killen et al. (2009) developed by taking into account

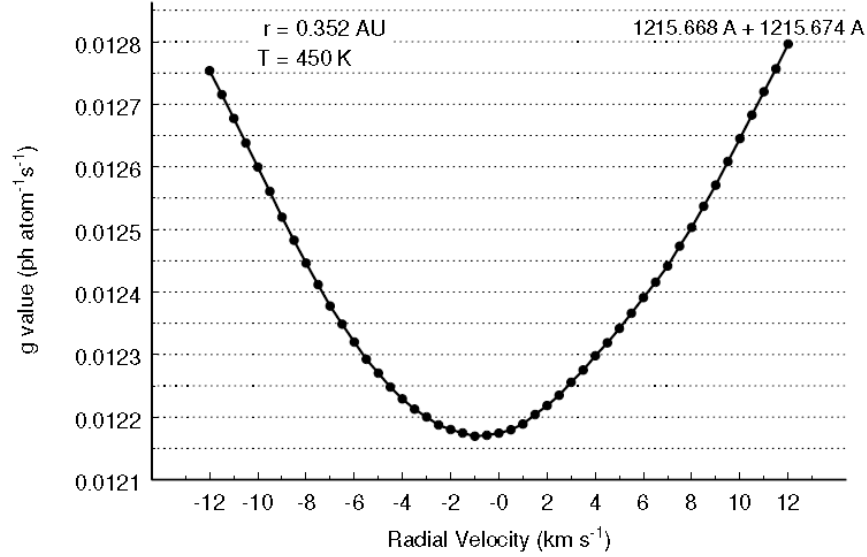


Figure 5.10: The variation in g_g for the hydrogen Lyman- α as a function of radial velocity (Image Killen et al. (2009))

radiationless deactivation, the distribution of population in states of the excited species, and the kinetic temperature of the fluorescent volume. However, they assume isotropic scattering, and do not address polarization effects or the scattering phase function.

With the assumption above, Chamberlain (1961) calculated the g-value for hydrogen to $1 \cdot 10^{-3} \text{ s}^{-1}$ while Killen et al. (2009) arrive at a g-value for hydrogen of $6.7 \cdot 10^{-3} \text{ s}^{-1}$ for aphelion conditions. This can be compared to the value calculated by Shemansky (1988), g-value = $5 \cdot 10^{-3} \text{ s}^{-1}$ and which is used in this thesis to simulate the hydrogen data from Mariner 10, as closely as possible.

The Killen value allows for higher intensity than the Shemansky value and differs at aphelion as $\sim 5\%$ lower than at perihelion, depending on the radial velocity (-12 km/s to +12 km/s). In Figure 5.10 the varying of the g-value for hydrogen, according to the radial velocity of the gas envelope/planet as it orbits the Sun, is shown.

So assuming, with high probability, that Mercury's exosphere is an optically thin medium, the total column amount of a given species is given in terms of the solar forced g-value defined as an emission probability per atom ($\text{photon s}^{-1} \text{atom}^{-1}$). Therefore the abundance of a species (N_g) can be used to obtain emission brightness (I_g) with the g-value (g_g) through the relation (see Killen et al., 2009):

$$N_g \propto I_g / g_g \quad (5.43)$$

For hydrogen to yield an emission intensity in Rayleigh ($10^6 \text{ photons/cm}^2/\text{s}$) for Lyman- α a 121.6 nm, the (in this case simulated) column density (n_H in atoms/cm²) is then simply multiplied by the g-value (g in photons/atom/s) in a straightforward way.

5.3 SECTION II: Monte Carlo model

The 3D exospheric model *SPERO - Simulation and Parsing of Exospheric neutRals at Oms*, was developed in Fortran 90 during the thesis to compute densities, velocities and temperatures of hydrogen atoms in the exosphere of Mercury.

5.3.1 Coordinate system

A reference frame is built for Mercury and will be used in the rest of this manuscript. x lies along the tangential velocity vector of the planet Mercury in its orbit with respect to the Sun, y toward the Sun and z points toward the North hemisphere. In this representation:

- The latitude is equivalent to the polar angle θ which varies from 0° (north pole) to 180° , (south pole)
- The longitude is equivalent to the azimuthal angle ϕ with 90° the dawn terminator, 0° the sub solar line, -90° the dusk terminator and $\pm 180^\circ$ the midnight line.

This gives:

$$lat = 90^\circ - \theta \quad (5.44)$$

and

$$long = \phi - 90^\circ \quad (5.45)$$

The subsolar point, that is the point directly under the Sun at noon and at the equator, is defined in this reference frame as $lat = 0$ and $long = 0$.

5.3.2 Flow of program

The purpose of the simulation is to launch a large amount of particles at the same time and follow their ballistic trajectories from ejection off the surface of Mercury until they either re-impact, are ionised or escape at a set limit radius, see Figure 5.13. To solve the equations of motion, with applied forces, a transport equation (central force/exchange force algorithm) is solved at each time step using a Monte Carlo technique.

Monte Carlo methods are stochastic methods that depend on repeated random sampling.

The key element of a Monte Carlo simulation is a generator of random numbers. In SPERO a double precision routine (see Numerical recipes, 1996) is used to generate random numbers which are used as input into the central force algorithm.

Monte Carlo simulations are by nature time and computational intense but the results are usually accurate with a large statistical basis.

As inputs in the simulation the several characteristic parameters must be taken into account: the residence time of adsorption of a particle in the surface, the time for a particle to be photoionised while moving in its ballistic trajectory and the accommodation coefficient representing the energy exchange between the particle and the surface at re-impact.

Figure 5.12 shows the different conditions encountered by particles all along their path, whether they are ejected in ballistic trajectories or adsorbed in the surface.

Since it is assumed that the main ejection process is thermal desorption the initial ejection and re-ejection are both depending on the surface temperature, calculated and explained in paragraph 5.2.3.

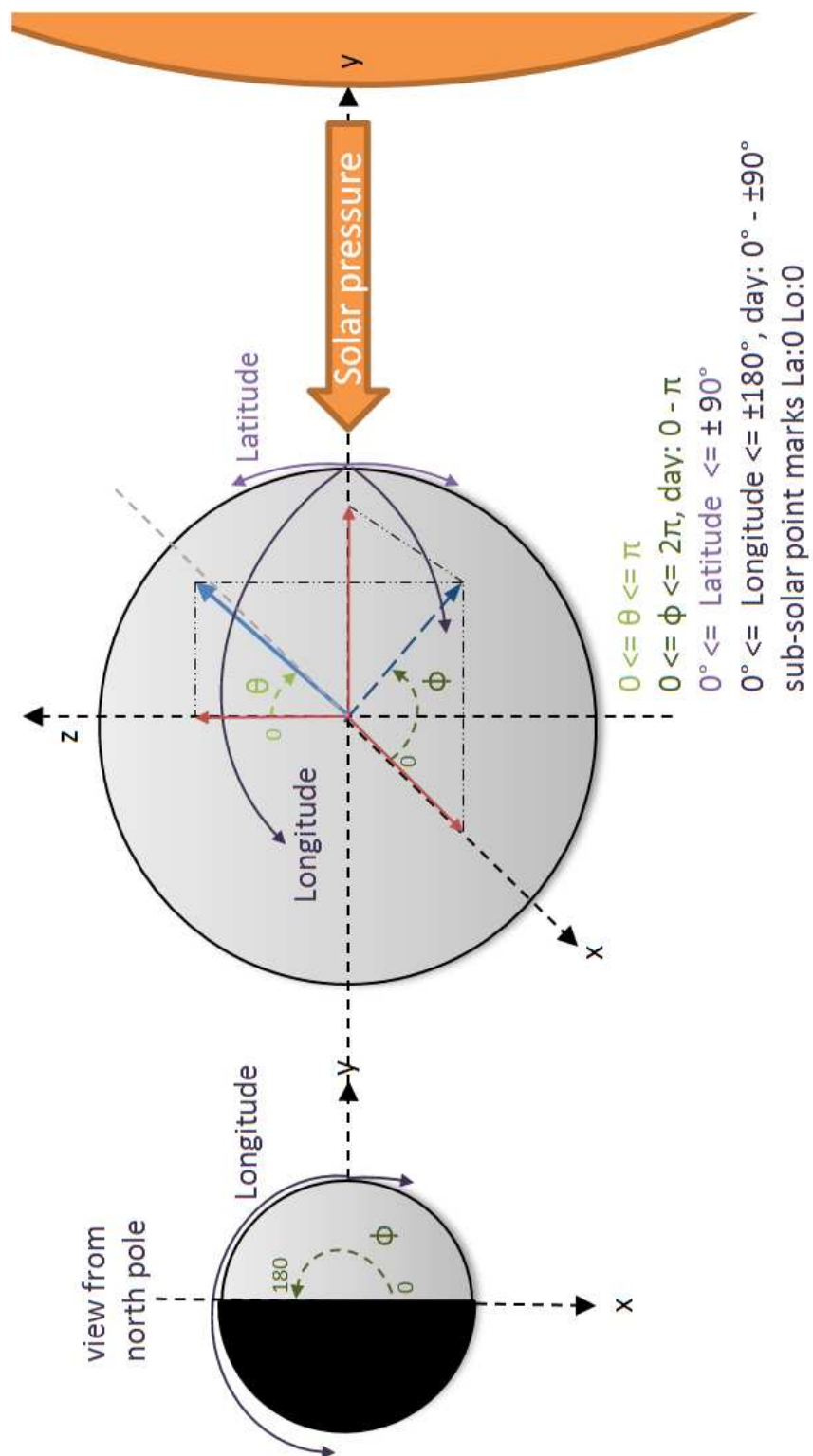


Figure 5.11: Overview of coordinate system used for Mercury in the simulation and this thesis.

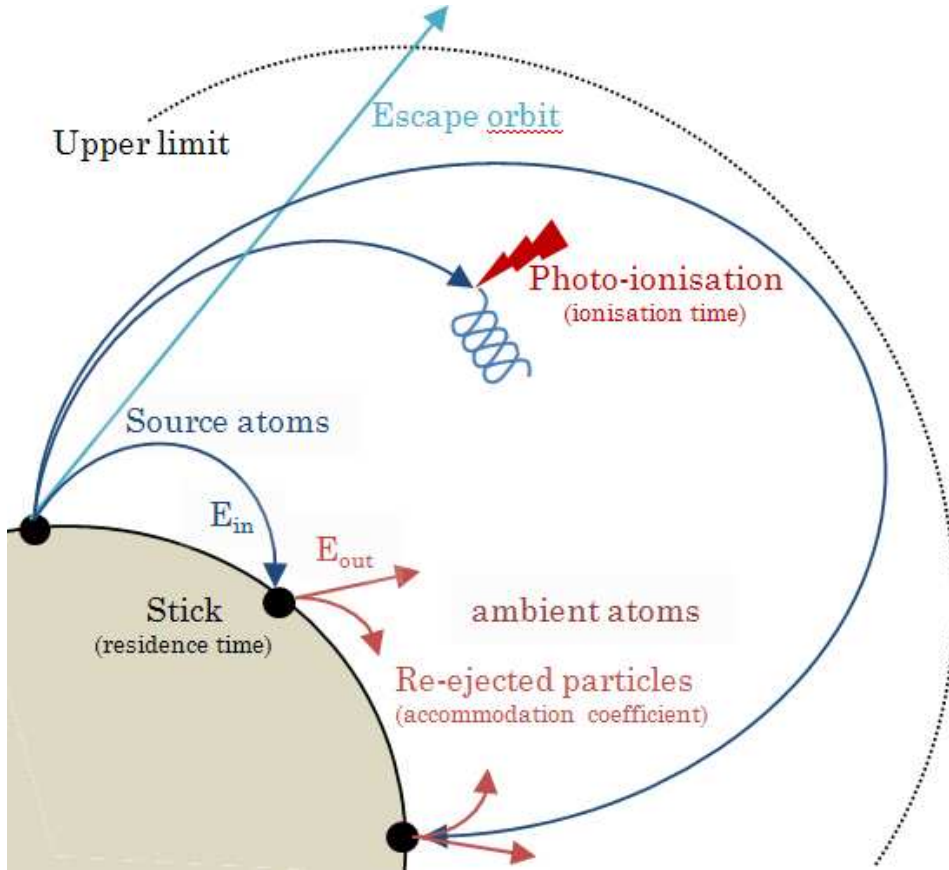


Figure 5.12: The different conditions encountered by neutral particles along their ballistic trajectories, from ejection to escape, ionisation or re-impact.

Algorithm

A typical run starts with an array of a fixed amount of particles, randomly located at the surface within the launch area predefined. For each particle's known coordinate (r_i, θ_i, ϕ_i) the corresponding temperature T_s , at the surface, is derived from the temperature mapped over the surface.

From this initial temperature the corresponding energy distribution is calculated and a random value within this distribution is picked, E_{out} . This energy is used to calculate the vector components of velocities in radial direction (V_r) while the angular vector components at launch ($\theta_{init}, \phi_{init}$) are calculated using a random value defined by $\theta_{init} = \arccos(\sqrt{\mathfrak{R}})$ and $\phi_{init} = 2\pi \cdot \mathfrak{R}$, where \mathfrak{R} is a random number from 0 – 1.

To get the same density of ejecta at the surface, we applied the arcsine transformation that converts a binomial random variable into one that is nearly normally distributed. An element of surface between (ϕ_1, ϕ_2) and (θ_1, θ_2) has a surface of $(\phi_2 - \phi_1) \times (\cos \theta_1 - \cos \theta_2)$, therefore if θ is defined as $\arccos(\mathfrak{R})$ it will induce a distribution of ejecta with a constant density at the surface (Settaouti and Settaouti, 2008). Using either arcsin or arccos makes no difference since they both give a random uniform distribution.

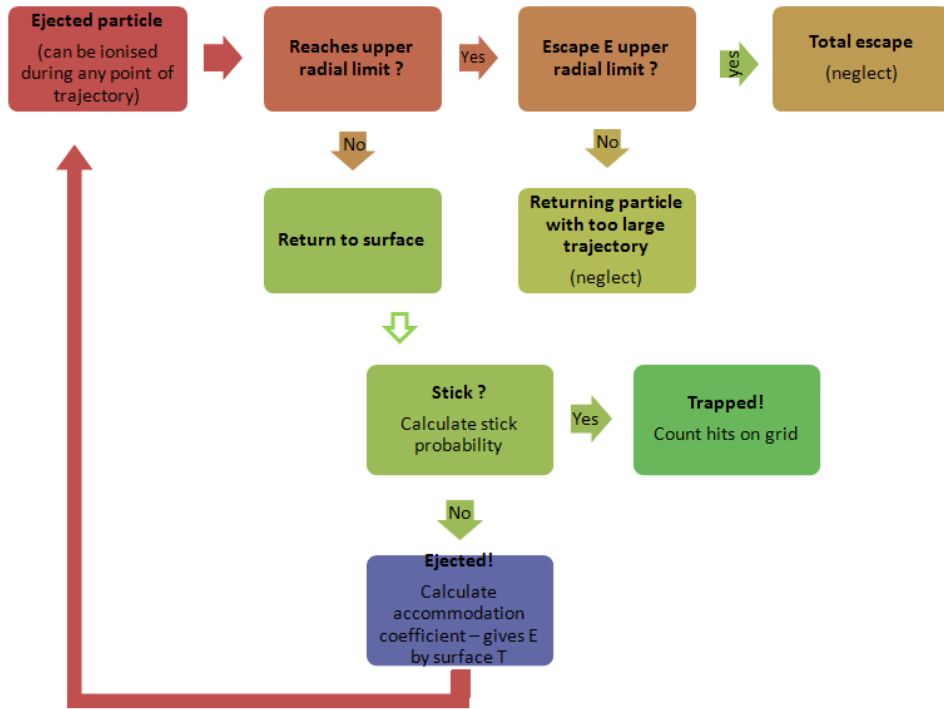


Figure 5.13: Simplified flow scheme for the model SPERO.

The particles then follow their ballistic trajectories, affected by the gravity field of Mercury (g_M) and the solar radiation pressure (V_{sol}) until they get ionized, escape outside the set radial limit or re-impact the surface.

As illustrated by Figure 5.13 the program operates according to Table 5.4.

Weight

Every “test” particle that is ejected represents a large amount of hydrogen particles. These test particles are adorned with a weight w . At every time step t test particles are created simulating a given supply of hydrogen particles. The weight w is calculated in order to reproduce a given flux of ejecta from the surface:

$$w = \Phi \cdot \frac{t_1 - t_0}{N_i} \quad (5.46)$$

where N_i is the number of particles inserted in the run, Φ is the number of particles ejected per second, t_0 and t_1 the start and stop time of the simulation. Φ is a free parameter that will be adjusted in order to reproduce the Mariner 10 emission intensity.

When a particle is ionised or escape, a new particle is re-injected at the surface, in order to keep the same number of test particles in the simulation at any time and to increase the statistics.

Starting parameters

Amount of initiated particles (array)
 Choice of launch area
 Time of run is set to reach steady state
 Time step ($dtmi$) is defined to 0.2
 Radial grid is defined to 20 resolution
 Longitude and latitude grid is defined to $\sim 1.2^\circ$

Time initialisation of all particles in array:

New particle is placed on surface ($r = 1 \cdot r_M$) within launch area
 Re-ejected particles are ejected from the same place as they impacted
 $T_{surface}$ from particle coordinate, gives E_{out}^a which gives V_{init}^b
 θ_{init}^c and ϕ_{init}^c are given

EJECTION

Particle follows ballistic trajectory in steps of $dtmi$ with applied forces
 ESCAPED *new particle inserted*
 SUPPRESSED *new particle inserted*
 IONISED *new particle inserted*

Accumulation in exospheric density files and temperature and velocity(x,y,z) files

RE-IMPACT on surface ($r < 1 \cdot r_M$, lat/long as trajectory determines)

$T_{surface}$ is extracted from particle coordinate, gives ejection energy E_{out}
 New Vr_{init} is calculated with accommodation coefficient α
 θ_{init} and ϕ_{init} are given, as before

STICKING (probability) *new particle inserted* OR particle is re-ejected

Calculation of temperature and velocity(x,y,z) files

Normalisation with flux ejected, volume and amount of particle inserted

Table 5.4: Numerical algorithm of SPERO simulation. ^a Particle ejection energy, ^b Particle velocity, ^c Particles launch angles in spherical coordinates

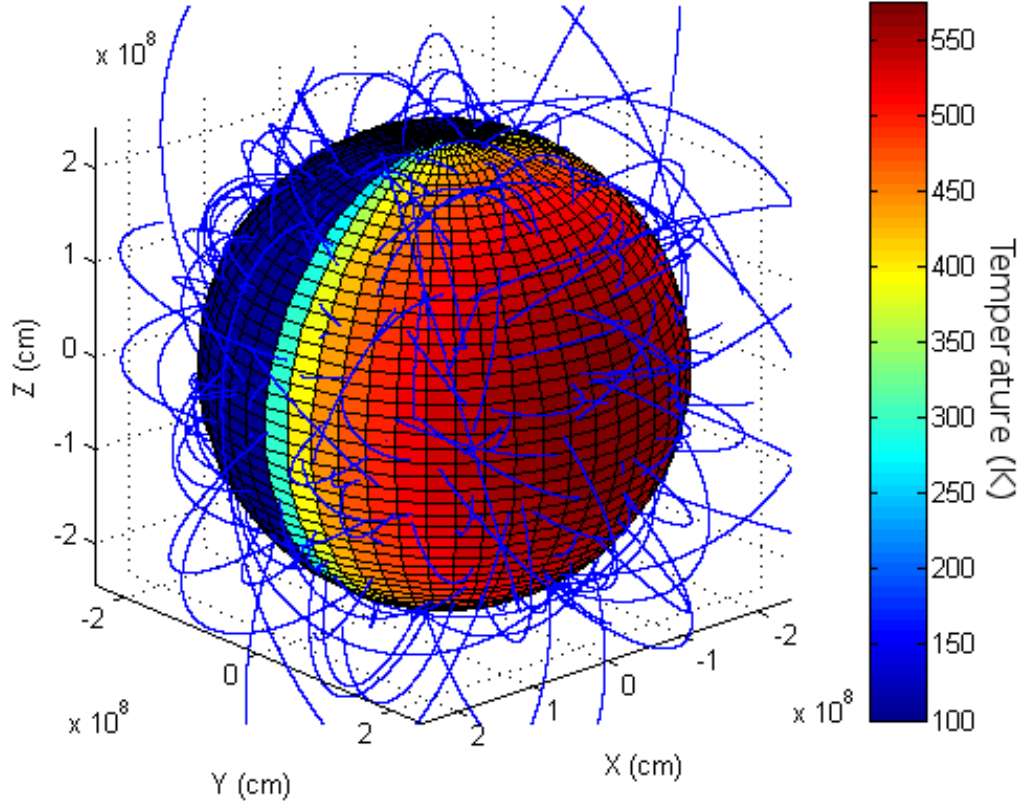


Figure 5.14: Typical ballistic trajectories for 100 particles with energies given by the mapped temperature.

5.3.3 Time evolution of the particle

Theoretical determination of the time step Δt

Particles are moving in ballistic orbits, see Figure 5.14, where a typical time interval Δt between two iterations is defined in order to get a required accuracy. The calculation stops when they end their trajectory either at the surface or at a limit outside of Mercury (8 radii).

In SPERO, the time step should also be short enough so that even the fastest particle has at least one time step inside every grid interval.

In our approach, the highest energy E_{max} a particle can have is 1 eV ⁸, corresponding to a maximum velocity V_{max} :

$$V_{max} = \sqrt{\frac{2E_{max}}{m_H}} = 13.8 \text{ km s}^{-1} \quad (5.47)$$

Since the smallest grid cell size is that of the r direction, Δr , and that the cell size should

⁸In the case of 600 K MBF distribution the probability of having a particle with more than 1 eV is less than $10^{-7} \%$

be larger than the distance travelled by the fastest particle $\Delta r > \Delta t \times V_{max}$.

More precisely, Δt should be smaller by a factor 0.5 or less, because the fastest particle ideally travels less than half the smallest cell size, which gives:

$$\Delta t \leq 0.5 \cdot \frac{\Delta r}{V_{max}} = 0.72 \text{ s} \quad (5.48)$$

A small time step is preferable but a compromise between computer runtime for the simulation and accuracy of the results has to be reached. Thus, in the simulation, a time step $\Delta t \approx 0.2$ s is agreed upon. This time step was compared to the simulated trajectory with the analytical solution for a simple case by simulating ballistic trajectory in a plane and for a constant gravity acceleration and no solar pressure.

Steady state

The definition of steady state in the simulation is when the amount of particles ionised, escaped or suppressed divided by total amount of particles ejected, is not changing any more. This usually is at least a few times the ionisation time (t_{ion}).

Also proof of steady state is the convergence of the density curves. To illustrate this, density profiles for example subsolar and antisolar points can be plotted for different times and when the curves converge the steady state is set to be reached.

5.3.4 Euler solution to ballistic motion

The motion of the particles on Mercury follows mainly ballistic trajectories in a gravity field, already described in section 5.2.4 by equation (5.17):

$$m_i \frac{d\vec{v}}{dt} = m_i \vec{g} + \sum_j \vec{F}_j$$

In cartesian coordinates (x,y,z) , equation (5.17) becomes:

$$\begin{cases} m_i \frac{dv_x}{dt} = m_i g_x \\ m_i \frac{dv_y}{dt} = m_i g_y - F_{sol,y} \\ m_i \frac{dv_z}{dt} = m_i g_z \end{cases} \quad (5.49)$$

In order to solve the ordinary differential equation (5.49), an explicit or implicit numerical scheme can be chosen. For a time-dependent differential equation of the general form $dy/dt = f(y)$, the expansion in Taylor series for t near zero, or $t = h$ with $h \ll 1$, yields:

$$\begin{aligned} y(t) &= y(0) + h f(y) + \dots \\ &\approx y_0 + h f(y_0) \end{aligned} \quad (5.50)$$

The expansion can be made at any t so that:

$$y_{n+1} = y_n + h f(y_n) \quad (5.51)$$

which advances a solution from y_n to y_{n+1} iteratively by a step h . Equation (5.51) is known as the forward implementation of Euler's method.

For the equation of motion, this is equivalent to finding the new position and velocity vectors (v_x, v_y, v_z) , and applying the iterative transformation at each time t and for a time step Δt :

$$\begin{cases} x(t + \Delta t) = x(t) + v_x(t + \Delta t) \Delta t \\ y(t + \Delta t) = y(t) + v_y(t + \Delta t) \Delta t \\ z(t + \Delta t) = z(t) + v_z(t + \Delta t) \Delta t \end{cases} \quad (5.52)$$

where the velocity components (v_x, v_y, v_z) at time $t + \Delta t$ were preliminary obtained using the same Euler method:

$$\begin{cases} v_x(t + \Delta t) = v_x(t) + \frac{dv_x}{dt} \Delta t \\ v_y(t + \Delta t) = v_y(t) + \frac{dv_y}{dt} \Delta t \\ v_z(t + \Delta t) = v_z(t) + \frac{dv_z}{dt} \Delta t \end{cases} \quad (5.53)$$

The components dv_i are directly obtained by calculating the second part of the equation of motion (the forces applied), with $dv_i/dt = \sum_k F_{i,k}/m_i$.

As equations 5.52 are a numerical approximation of the sought solution, the Euler algorithm has to be checked with respect to convergence and accuracy.

The advantage of the Euler method in SPERO is manifold: it is easy to implement and to modify in the simulation, its accuracy and stability is satisfactory.

As the Euler forward method is more than adequate for solutions such as the one implemented here, there is no need to use higher order functions such as Runge-Kutta. Although the result could be more stable and conserve the energy better, methods like the Runge-Kutta are very time consuming.

Before making the choice of Euler forward method, I made a small study of the accuracy, energy conservation and runtime for three methods: Euler forward method, Runge-Kutta 2 and Runge Kutta 4. Without going into details, the conclusion was that due to the simplicity of the ballistic trajectories as applied in the simulation, the Euler forward method was giving the same answer down to the sixth decimal as compared to Runge-Kutta 2 and Runge-Kutta 4, for a runtime that was at least four times as short as the same run for the two other methods.

Ejection of particles: MBF and MB distributions

At the heart of Monte Carlo simulations lies the concept of continuous random variables, noted here for instance X . In order to have a complete description of the probability distribution of X , the knowledge of both the probability density function (PDF), noted $f(X)$ and the cumulative distribution function (CDF), noted $F(X)$ is necessary. The CDF describes the probability \Pr that a random variable with a given probability distribution will be found at a value less or equal to x :

$$F(x) = \Pr(X \leq x) \quad (5.54)$$

The link between the CDF and the PDF is then simply that of a primitive to its derivative, see Figure 5.15:

$$f(x) = \frac{dF(x)}{dx} \iff F(x) = \int_{-\infty}^x f(x) dx \quad (5.55)$$

One interpretation of the CDF is that its inverse F^{-1} –if it exists– maps the distribution function variable such as velocity to a uniformly distributed set of numbers, typically

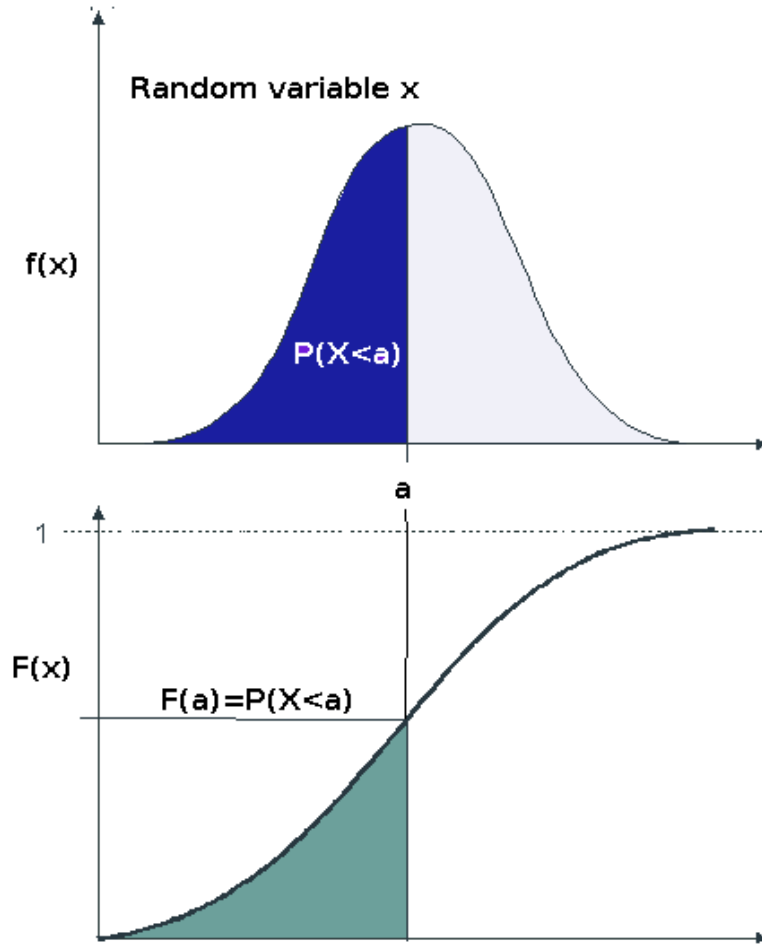


Figure 5.15: Relation of Cumulative Distribution Function (CDF), bottom, to Probability Distribution Function (PDF), top.

normalized between 0 and 1. This is exactly what is needed to determine a random energy from the day distribution, which gives the velocity distribution of ejected particles (hydrogen) from the surface at a given temperature.

To use this property in Monte Carlo calculations, the cumulative distribution function $F(E)$ has to be built by calculating the primitive of the distribution as an example for MBF:

$$F(E) = \int_0^E f_1(E) dE \quad (5.56)$$

with:

$$f_1(E) = \frac{2E}{(k_B T_s)^2} e^{-E/k_B T_s}$$

After some substitutions, and taking the boundary condition that $F(0) = 0$, the following appears:

$$F(E) = -2e^{-E/k_B T} \left(1 + \frac{E}{k_B T} \right) + 2 \quad (5.57)$$

The random choice of an energy E in the inverse CDF will result in a uniformly random energy obeying the probability distribution function $F(E)$, and ultimately will be distributed according to $f_1(E)$. Indeed, if U is a uniform random variable between 0 and 1, then $F^{-1}(U)$ follows the distribution F .

This fundamental property of the CDF can be proved by remarking that by definition of the inverse of F , $F^{-1}(U) = \{x \mid F(x) = U\}$, $0 < U < 1$. It follows that the requested probability is:

$$\Pr(F^{-1}(U) \leq x) = \Pr(\{y \mid F(y) = U\} \leq x) \quad (5.58)$$

$$= \Pr(U \leq F(x)) \quad (5.59)$$

$$= F(x) \quad (5.60)$$

using the fact that F is monotonic and can be applied to both sides of the internal equation $\{y \mid F(y) = U\} \leq x$, and that $\Pr(U \leq y) = y$, since U is uniform on the unit interval.

The algorithm can be sketched as follows:

- Generation of a random number U from the standard uniform distribution,
- Computation of the value X_c so that $F(X_c) = U$ (inverse transform sampling),
- X_c is the random number drawn from the distribution described by F .

The advantage of this technique is to get a quick analytical expression to randomize the energies at ejection of the particles without the use of a complex algorithm that would significantly slow down the runs.

For more complex and usually multi-variable functions, this can also be achieved by using the Gaussian random deviates technique (Box-Muller transform) as explained in Hodges (1973) or for instance, the efficient ziggurat algorithm (Marsaglia and Tsang, 2000).

Upper boundary

A criterion to define the upper boundary where the simulation is not following the particles anymore is that the particles lost⁹ in the simulation are mostly escaping particles. Escaped particles are defined as energetic particles reaching the set limit with energy larger than the escape energy. Suppressed particles are defined as the particles reaching the same set limit as the escaping particles but having energy less than the escaping energy at the limit.

The kinetic energy for hydrogen is defined by

$$E_{kin} = \frac{m_h \cdot v^2}{2} \quad (5.61)$$

which in turn yields the velocity as

$$v = \sqrt{2 \cdot E_{kin} / m_h} \quad (5.62)$$

The potential energy is

$$E_{pot} = \frac{G \cdot m_M \cdot m_h}{r_M} \quad (5.63)$$

⁹lost means here that the simulation no longer follows the trajectory of these particles but deem them lost in the simulation and are replaced by a new particle.

where

G is the gravitational constant at $6.6726 \cdot 10^{-11} m^3/kg/s^2$

m_h is the mass of hydrogen = $1.6725 \cdot 10^{-27} kg$

m_M is the mass of Mercury = $3.3022 \cdot 10^{23} kg$

r_M is the radius of Mercury = $2439.7 \cdot 10^3 m$

So the escape velocity of Hydrogen, or other atoms, at the surface of Mercury is therefore $4.25 \cdot 10^3 m/s$.

Translated into energy by equation (5.61), $E_{esc_surf} = 1.511 \cdot 10^{-20} J$ which is the same as $0.094eV$.

The upper radial limit has been decided to 8 radii from the surface, based on the runs made and a comparison to the ratio of escaped/suppressed particles in the run.

Using the criteria that the particles, counted as escaped and lost, must reach at least $8 \cdot r_M$ and that they must have an energy of at least the E_{esc} at that distance becomes

$$v_{esc_8radius} = -\sqrt{\frac{2G \cdot m_M}{8 \cdot r_M}} = 1.50 \cdot 10^3 m/s \quad (5.64)$$

Translated into energy by equation (5.61), $E_{esc_8radius} = 1.889 \cdot 10^{-21} J$ which is the same as $0.0118eV$.

5.3.5 Outputs

Density grid

Densities, temperatures and velocities are calculated in 3D around Mercury, taking into account accommodation coefficient of the surface, solar pressure, ionisation and surface densities once the simulation has reached a steady state.

A (r, θ, ϕ) grid is defined. The original resolution of the latitude and longitude is 50 km on surface level, which corresponds to $\sim 1.2^\circ$, see Figure 5.16. The radial distance is set to be between the surface ($1r_M$) and ($8r_M$) with a grid resolution of 20 km.

For the density grid, particles are recorded within each cell of the grid they pass through and for each given time step (dt). The accumulation is done during a given time $t_{simulation}$ so that the final density $n(i)$ in cell i of coordinates (r, θ, ϕ) is

$$n(i) = \sum_n \delta t \quad (5.65)$$

where the sum is on the number of all the time steps spent by any particle in cell i and n is the total number of time spent by a particle in this cell.

The densities are then normalised by

$$n(i)_n = \frac{n(i) \cdot w}{Vol(i)} \quad (5.66)$$

w is the weight

$Vol(i)$ is the volume of the cell i

For the temperature grid, the kinetic temperature density $t(i)$ is

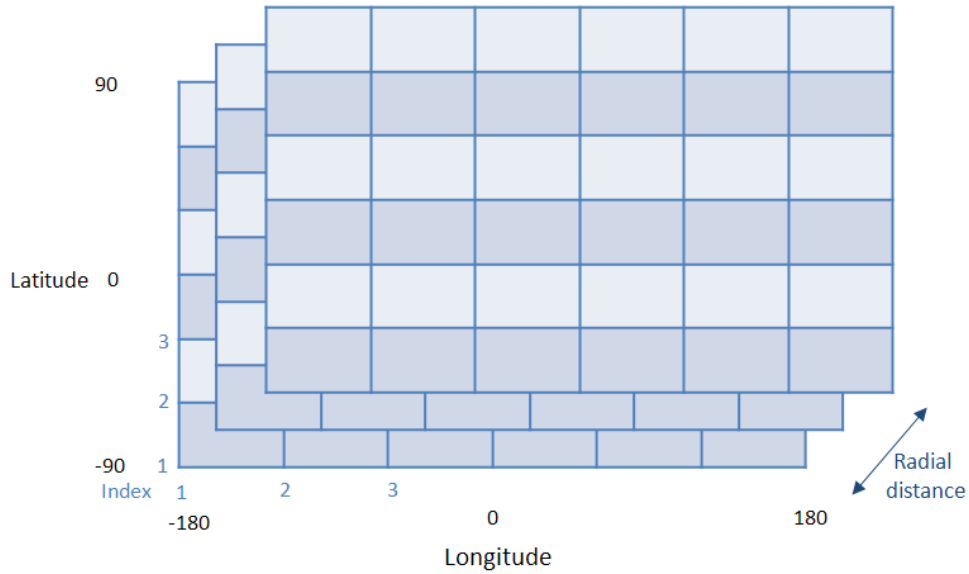


Figure 5.16: Theoretical representation of the 3D density grid.

$$t(i) = \sum n(i) \cdot \delta t \cdot (V(x)^2 + V(y)^2 + V(z)^2) \quad (5.67)$$

where

$V(x/y/z)$ is the velocity vector for each time step as

$$V'(x/y/z) = V(x/y/z) + V(x/y/z)dt \quad (5.68)$$

and then normalised

$$V(x/y/z)_n = \frac{V'(x/y/z)}{n(i)} \quad (5.69)$$

5.4 Validation

5.4.1 Convergence criteria

As mentioned in section 5.3.3, the convergence of the density curves demonstrates to at which altitude the simulation is reliable. In Figure 5.17 and Figure 5.18, the accumulated density altitude profiles are plotted at subsolar and antisolar points at different time intervals in the simulation. Convergence is reached at run times longer than 1500h for an altitude of up to 2000 km, for the nominal run, with 1000 test-particles. With 2000 particles, we reached a steady state up to $3 r_M$ on the density within 750 hours of simulation.

5.4.2 Chamberlain

To make sure the program correctly calculates densities of hydrogen around Mercury, a comparison to Chamberlain profiles for hydrogen has been done.

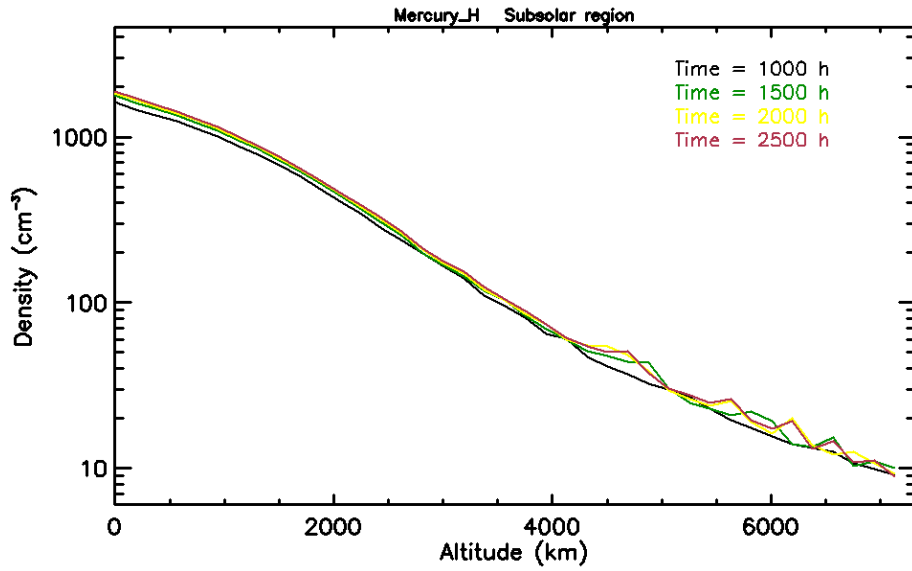


Figure 5.17: Density profile of neutral hydrogen at subsolar. Convergence is apparent at runtime longer than 1000 h for an altitude of up to 6000 km.

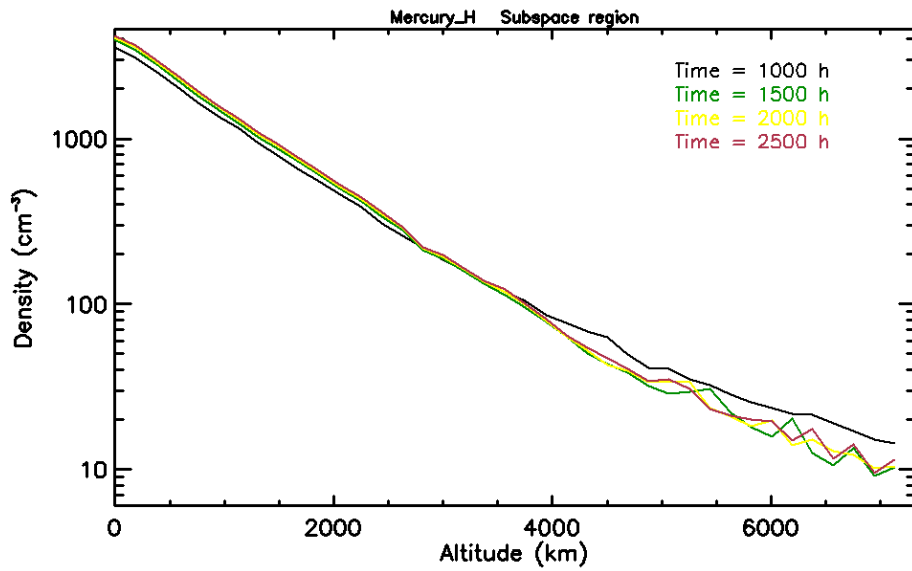


Figure 5.18: Density profile of neutral hydrogen at antisolar point. Convergence is apparent at runtime longer than 1000 h for an altitude of up to 6000 km.

A Chamberlain model is a standard model for exospheres assuming:

- spherical symmetry,
- uniform conditions and steady-state,
- a Maxwellian velocity distribution at the exobase,
- no collisions at all above the exobase,
- and that particles are only moving under the gravitational force (neglecting all other effects such as solar pressure)

The exobase is classically assumed to be a sharp transition, referred to in the Chamberlain formalism as the 'critical level'.

The mathematical analysis of the collisionless exosphere follows the description of Chamberlain (1963). This approach consists in the adding of two controlling factors – gravitational attraction and thermal energy– and the use of Liouville's equation to derive the density distributions and escape flux. The collisionless Boltzmann equation, also called Liouville's equation, is:

$$\frac{\partial f}{\partial t} + \frac{d\vec{r}}{dt} \cdot \frac{\partial f}{\partial \vec{r}} + \frac{d\vec{p}}{dt} \cdot \frac{\partial f}{\partial \vec{p}} = 0 \quad (5.70)$$

This equation implies that the density in the phase space stays constant with time. In the Chamberlain formalism, particles moving under the effect of the gravitational field in a collisionless region are, depending on their energy, either:

- *ballistic*, meaning captive particles in elliptic motion intersecting the critical level (coming from the exobase),
- *satellite*, meaning captive particles in elliptic motion above the critical level, or
- *escaping*, meaning having enough energy to escape the gravitational attraction of the planet in a hyperbolic motion.

Classical exospheric theory: equations of motion

The trajectory of an exospheric particle of mass m_i in polar coordinates $(\vec{u}_r, \vec{u}_\theta)$ is comprised into a plane so that:

$$m_i \frac{d\vec{p}}{dt} = m_i (\ddot{r} - r\dot{\theta}^2) \vec{u}_r = -\frac{GMm_i}{r^2} \vec{u}_r = \left(\frac{dp_r}{dt} - \frac{P_\chi}{m_i r^3} \right) \vec{u}_r \quad (5.71)$$

for a radial distance r from the center of a planetary body of mass M . G the gravitational constant. The conservation of angular momentum $\vec{L} = \vec{r} \times \vec{p}$ leads to the expression $P_r = L_r/m_i = r^2\dot{\theta}$ being a constant (Kepler's second law).

In a steady equilibrium state, $\partial f/\partial t = 0$ and equation (5.70) can be re-written, in polar coordinates:

$$\frac{dr}{dt} \frac{\partial f}{\partial r} + \frac{dp_r}{dt} \frac{\partial f}{\partial p_r} = 0 \quad (5.72)$$

which simply becomes from equation (5.71):

$$\frac{dr}{dt} \frac{\partial f}{\partial r} + \left(\frac{P_\chi}{m_i r^3} - \frac{GMm_i}{r^2} \right) \frac{\partial f}{\partial p_r} = 0 \quad (5.73)$$

Chamberlain (1963) assumed an isotropic, Maxwellian distribution of velocities for temperatures T_∞ at and below the critical level r_0 :

$$f(r_0, p_r, P_\chi) = \frac{n_0 e^{-p_r^2/2m_i k_B T_\infty} e^{-P_\chi^2/2m_i k_B T_\infty r_0^2}}{(2\pi m_i k_B T_\infty)^{3/2}} \quad (5.74)$$

n_0 is the density at the exobase, k_B Boltzmann's constant and T_∞ the exospheric temperature. By differentiating equation (5.74) with respect to p_r :

$$\frac{\partial f}{\partial p_r} = -\frac{p_r}{m_i k_B T_\infty} f \quad (5.75)$$

Substituting this equation in equation (5.73) yields:

$$\frac{df/f}{dr} = \frac{d(\ln f)}{dr} = -\left(\frac{GMm_i}{k_B T_\infty r^2} - \frac{P_\chi^2}{m_i k_B T_\infty r_0^3} \right) \quad (5.76)$$

which is independent of p_r . Since dependence of f on p_r does not depend on altitude, this equation is valid everywhere from the exobase and upwards. The integration of equation (5.76) from r_0 to r using equation (5.74) as boundary condition gives the variation of the distribution function with altitude:

$$f(r, p_r, P_\chi) = \frac{n_0 e^{-(\beta_0 - \beta)} e^{-p_r^2/2m_i k_B T_\infty} e^{-P_\chi^2/2m_i k_B T_\infty r^2}}{(2\pi m_i k_B T_\infty)^{3/2}} \quad (5.77)$$

where the convenient quantity β has been introduced. β is the escape parameter defined in the Jeans formalism as the potential energy in units of $k_B T_\infty$ and depending on the distance r :

$$\beta(r) = \frac{GMm_i}{k_B T_\infty r} = \frac{V_{esc}^2}{U^2} \quad (5.78)$$

The escape velocity, as shown before, is $V_{esc} = \sqrt{2GM/r}$ whilst the most probable Maxwellian velocity is $U = \sqrt{2k_B T_\infty/m_i}$.

Exospheric density

Under these conditions, the altitude profile of exospheric densities is found by integrating the distribution function f over momentum space, giving the analytical equation:

$$n(r) = \iiint f(r, p_r, P_\chi) P_\chi dp_r dP_\chi = n_0 e^{-(\beta_0 - \beta)} \quad (5.79)$$

This equation, known as the isothermal barometric formula, is valid in the case of independent p_r and P_χ momenta taking all values allowed by the equation of motion, that is $-\infty < p_r < \infty$ and $0 < P_\chi < \infty$.

Equation (5.79) remains true regardless of the precise form of the distribution function as long as the gas pressure is isotropic and the mean kinetic energy is proportional to the temperature (perfect-gas law). When $r \rightarrow \infty$, $\beta \rightarrow 0$ and the barometric law predicts that a finite pressure and density are reached. However, this tendency is not observed in a realistic exosphere and at sufficient distances above the exobase, the barometric law breaks down.

In practice in the exosphere, not all particle momenta (p_r, P_χ) are allowed due to the gravitational force and particles follow trajectories which fill conic sections in velocity phase space (see Goldstein, 1950).

The integration of equation (5.77) then takes the general form:

$$n(r) = n_0 e^{-(\beta_0 - \beta)} \zeta(\beta) \quad (5.80)$$

which is the product of a partition function ζ by the barometric density law.

The function ζ is the partition function in the velocity phase space corresponding to the fraction of the isotropic Maxwellian distribution that is actually present. It can be

expressed as the sum of the partition functions of the three motions, ballistic (b), satellite (s) and escaping (e) of the particles:

$$\begin{aligned}\zeta(\beta) &= \zeta_b(\beta) + \zeta_s(\beta) + \zeta_e(\beta) \\ &= \frac{2\pi}{r^2(2\pi m_i k_B T_\infty)^{3/2}} \iint e^{-\frac{p_r^2}{2m_i k_B T_\infty} - \frac{P_\chi^2}{2m_i k_B T_\infty r^2}} P_\chi dP_\chi dp_r\end{aligned}\quad (5.81)$$

An adequate change of variables, expressing energies in units of $k_B T_\infty$ so that the radial dimensionless velocity is $w_r = v_r/U$ and the dimensionless transverse velocity, defined as $w_t = v_t/U$, enables to rewrite the partition function as:

$$\zeta(\beta) = \frac{1}{\pi^{3/2}} \iiint e^{-w^2} w^2 \sin \theta dw d\theta d\phi \quad (5.82)$$

where $w = \sqrt{w_r^2 + w_t^2}$ is the module of the dimensionless velocity and the angle θ is defined so that $w_r = w \cos \theta$ and $w_t = w \sin \theta$.

Distribution of particles in the velocity phase space

The type of conic section described by the motion of particles in velocity space depends on its total energy and its momentum and may be precisely computed. By conservation of the angular momentum (M) and the total energy (E):

$$\left\{ \begin{array}{l} \mathbf{M}: r v_i(r) \sin \theta = C^{st} \iff \frac{w(r)}{\beta(r)} \sin \theta = C^{st} \\ \mathbf{E}: \frac{1}{2} m_i v_i(r)^2 - \frac{GMm_i}{r} = C^{st} \iff w^2(r) - \beta(r) = C^{st} \end{array} \right. \quad (5.83)$$

Different regions in velocity space can be isolated and are shown in Figure 5.19:

- **Escaping/bound particles:** All non-escaping particles bound to the planet have velocities smaller than the escape energy V_{esc} corresponding to a dimensionless velocity $w^2 < \beta$. These particles have the equivalent of a negative total energy and are confined on elliptic trajectories inside a circle of radius $\sqrt{\beta}$ in the velocity phase space (w_r, w_t) defined by $w_r^2 + w_t^2 = \beta$. Particles outside this circle will follow hyperbolic trajectories and may escape with positive energy.
- **Satellite/particles intersecting the exobase:** One limit condition for the motion of particles is when it intersects the exobase with velocity w_0 . If it coincides with the exobase, the angle θ will take the limit value $\theta_0 = \pi/2$. Following along a trajectory from the exobase, a particle of characteristics (w, β) will satisfy the new conservative energy-momentum equations derived from equation (5.83):

$$\left\{ \begin{array}{l} \mathbf{M}: \frac{w_0}{\beta_0} = \frac{w}{\beta} \sin \theta \\ \mathbf{E}: w_0^2 - \beta_0 = w_r^2 + w_t^2 - \beta \end{array} \right. \quad (5.84)$$

Combining both equations leads to the equation of a hyperbola of the form $x^2/a^2 - y^2/b^2 = 1$:

$$\frac{\beta_0 + \beta}{\beta^2} w_t^2 - \frac{1}{\beta_0 - \beta} w_r^2 = 1 \quad (5.85)$$

This hyperbola, of eccentricity $\epsilon = \sqrt{1 + b^2/a^2} = \beta_0/\beta$, defines in the velocity space (w_r, w_t) the limit between two populations of particles: satellite particles (not intersecting the exobase, that is outside the hyperbola) and particles intersecting

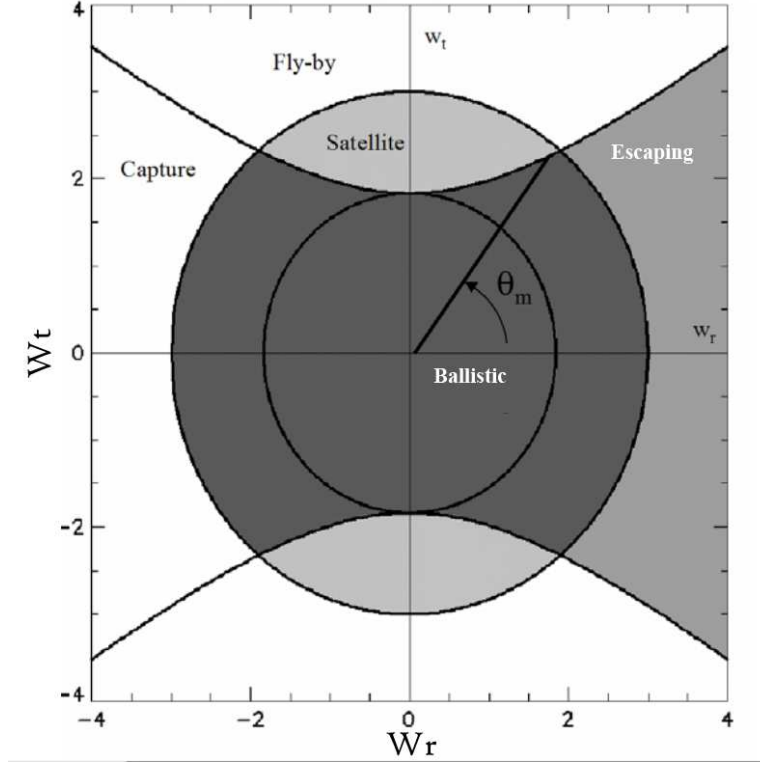


Figure 5.19: The different classes of orbits (ballistic, escaping, satellite) represented in the normalised velocity phase space (w_r, w_t) . The small circle has for radius $\sqrt{\beta^2/(\beta + \beta_0)}$, the bigger circle has for radius $\sqrt{\beta}$ (Image adapted from Chaufray (2007)).

the exobase (inside the hyperbola), see Figure 5.19. θ_m is the polar angle of the hyperbola given by:

$$\cos \theta_m = \sqrt{1 - \frac{\beta^2}{\beta_0^2} \left(1 + \frac{\beta_0 - \beta}{w^2}\right)} \quad (5.86)$$

Following the study of the classes of particles with respect to allowed values in the phase space, the analytical expressions of ζ can be derived from triple integrals in phase space and expressed by gamma functions Γ . They are described for instance in Chamberlain (1963), Fahr and Shizgal (1983) or Chaufray (2007).

Comparison between simulation and the classical theory

In the case of this study, Mercury's exospheric hydrogen, n_0 is the density at the surface of Mercury (exobase), $M = M_M$ the mass of Mercury, $m_i = m_H$ the mass of hydrogen and $T_\infty = T_s$ the surface temperature. At the critical level $r_0 = R_M$, $\beta_0 = GM_M m_H / (k_B T_\infty R_M)$, where R_M is Mercury's radius.

A typical Chamberlain profile at the subsolar point is shown in Figure 5.20 for $T_\infty = 100$ K and $T_\infty = 600$ K compared to the output densities of SPERO in the corresponding

Simulation density profiles (black, green) compared to Chamberlain profiles (red, blue) for two temperatures

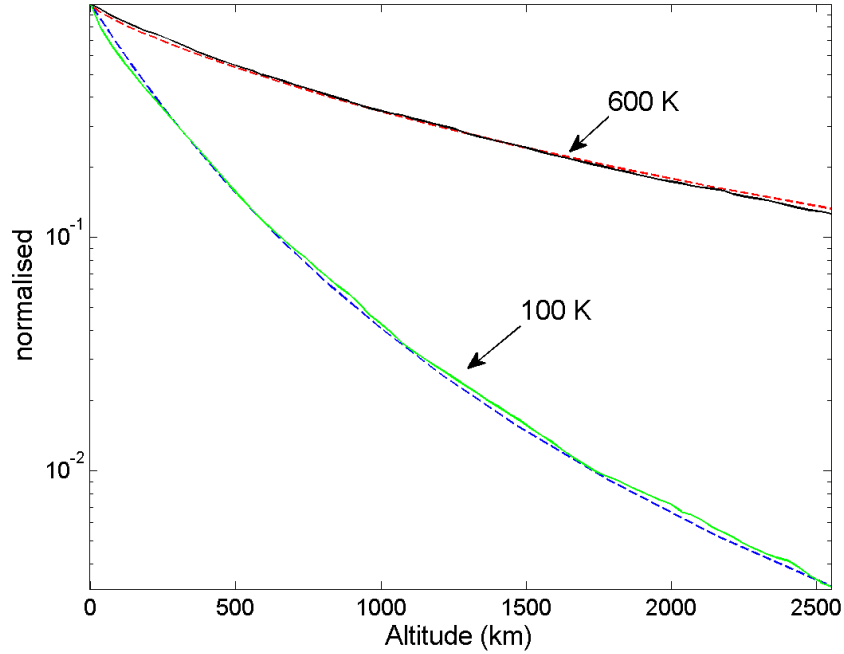


Figure 5.20: Chamberlain profile comparison for temperatures of 100 K and 600 K, to a simulation run for a converging run of 2500 h for the same temperatures.

conditions of complete absorption at the surface for a converging runtime of 2500 h, which is simulation time equivalent to 4 days computer time.

As pointed out above, the Chamberlain formulation is valid for spherical symmetry at the exobase producing one exobase density and one constant temperature T_∞ . In order to simulate this behaviour in SPERO, conditions were changed at the exobase in order to have the same flux everywhere and the same surface temperature (equivalent to the exospheric temperature).

Figure 5.20 shows an excellent agreement between the two models, which demonstrates as a validation procedure that the model SPERO correctly computes:

- the trajectory of the particles,
- the density in the exosphere,
- the energy distribution of the particle at ejection.

Another test of the validity of the approach of SPERO relies on the comparison to the density relation provided by Hodges and Johnson (1968) in the case of particles fully accommodated to the surface, related to the number of hops.

5.4.3 Thermalisation at surface

The variation of the density close to the surface with respect to longitude at the equator should follow a $T_s^{-5/2}$ relation or close in case of perfect thermalisation (Hodges and

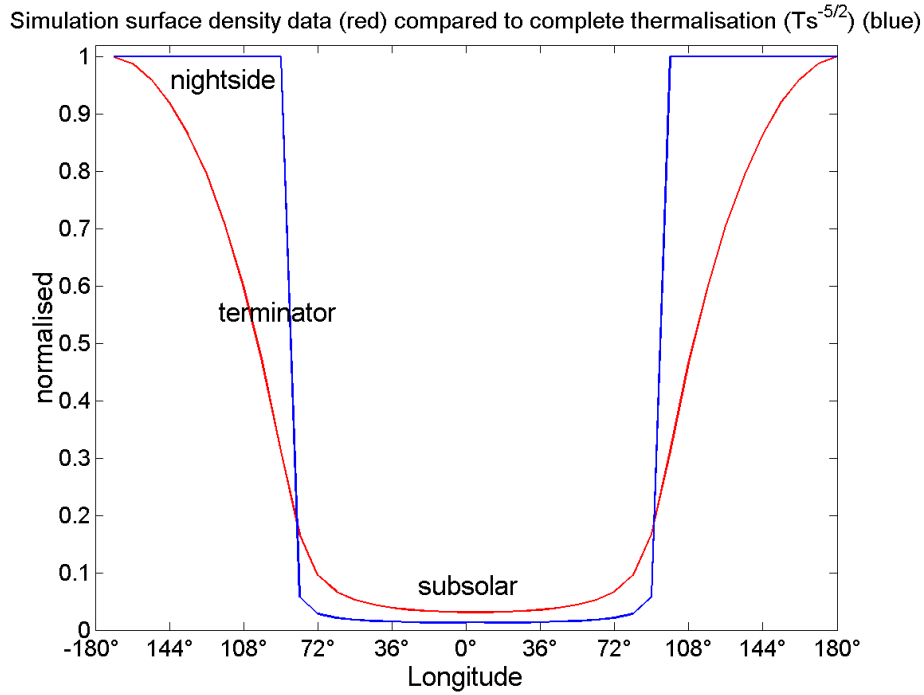


Figure 5.21: $T_s^{-5/2}$ profile comparison to simulation run, both curves have been normalised with the max value.

Johnson, 1968; Hodges et al., 1974) as explained in section 5.2.5, equation (5.36).

The thermalisation is connected to the gradient of surface temperature. In the following, the temperature map that was mapped for Mercury with nightside uniformly at 100 K and the dayside as a temperature gradient. The accommodation of the particle is set as being complete, see section 5.2.5, as supposed in Hodges et al. (1974) model. Then the density close to the surface is calculated, normalized by the nightside peak density and compared to the relation suggested by Hodges et al. (1974).

In Figure 5.21 the density at a radial distance close to the surface along the entire equator is compared with the relation suggested by Hodges et al. (1974). The important parameter in the comparison is the relative variation of the density from noon (maximal surface temperature) to midnight (minimum surface temperature). As shown in Figure 5.21, this ratio is relatively well reproduced by the simulation, showing that the modelling of the global day to night sides migration is well done.

5.5 Sensitivity study

A nominal case is compared to other cases where small changes are implemented in the code such as a change of accommodation coefficient, change of solar radiation pressure and other factors defined later on in the following chapters.

The nominal run have the following characteristics:

- Start amount of particles/particles always in run: 2000

- Time step: 0.2 s
- Run time: 2500 h, which is the convergence time
- Ejection area: dayside uniform placement
- Velocity distribution: MBF or MB
- Accommodation coefficient $\alpha = 0.08$ as stated by Hunten (1988)
- Solar radiation pressure: 1 % g_M

Output from nominal MBF run

- Total amount of particles injected into simulation: 33169
- Escaped amount of particles: 21413 ($\sim 65\%$)
- Ionised amount of particles: 9756 ($\sim 29\%$)
- Ejection rate from surface¹⁰: $2.4 \cdot 10^9$ H/cm²/s

Output from nominal MB run

- Total amount of particles injected into simulation: 15525
- Escaped amount of particles: 4711 ($\sim 30\%$)
- Ionised amount of particles: 8813 ($\sim 57\%$)
- Ejection rate from surface¹¹: $3.1 \cdot 10^5$ H/cm²/s

Due to the difficulty of constraining certain factors the model is subject to a certain sensitivity. These factors can be nominated as a "free" parameter. The two "free" parameters of largest importance in the simulation are the "accommodation coefficient" and "distribution functions".

To understand the impact of these "free" parameters simulations are realised which density profiles, with changed parameters, at subsolar and midnight are compared to the nominal simulation, such as the velocity distribution functions or the accommodation coefficient, in the following chapters.

5.5.1 MB and MBF Velocity distribution functions

As explained previously, the accommodation factor is adjusted in order to reproduce as much as possible the observations (see following sections). Since we do not address the detailed description of the gas-surface interaction, our aim is to propose a reasonable solution for the hydrogen exosphere based on a simplified parametric analysis.

Several aspects of Mercury hydrogen exosphere will be described:

- Its dependency on the ejection distribution MB vs MBF (spatial scales and escape),
- Its dependency on the source regions (uniform dayside or localized at high latitudes). We will study that dependency for MB and MBF as well.

These previous analysis are aimed to better constrain comparisons with Mariner 10 observations. In particular, it will be used to provide some clues on the energy distribution role, before concluding on the accommodation of the particles at the surface.

¹⁰As scaled to reproduce Mariner 10 profile

¹¹As scaled to reproduce Mariner 10 profile

MB vs MBF: spatial distribution and escape rates

A case with a preferential ejection of hydrogen atoms from dayside hemisphere ($3.7 \cdot 10^{17} \text{ cm}^2$) is shown in this section. In this scenario, we supposed that hydrogen atoms are ejected in the exosphere by the solar photons and by evaporation. Since it is believed that most hydrogen atoms could come from solar wind implantation, another case with a preferential ejection from a region representative of the region impacted by solar wind will be done as well (roughly the cusp regions, Sarantos et al. 2007).

Figure 5.22 and Figure 5.23 display the results obtained after a run lasting 2500 hours of simulated time with 2000 particles maintained permanently in the simulation. The density calculated has been obtained following the method described in section 5.3.5 and the convergence checked by comparing the density profiles at various times of the simulation and by calculating the evolution of the loss rates.

In the case of MB (Figure 5.22), 15524 test-particles were injected in the simulation and followed up to the moment they either escaped (4711 test-particles) or were ionized (8813 test-particles), 2000 test-particles being still in the exosphere when we stopped the simulation. The ejection rate from the bombarded surface is $3.1 \cdot 10^5 \text{ H/cm}^2/\text{s}$ in order to reproduce the typical range of dayside density reported by Mariner 10 at the subsolar point, that is $1.1 \cdot 10^{23} \text{ H/s}$. Therefore, for MB distribution, the loss is largely dominated by ionization with a loss rate of $0.7 \cdot 10^{22} \text{ H/cm}^2/\text{s}$ and the neutral escape is $0.4 \cdot 10^{22} \text{ H/cm}^2/\text{s}$.

The ionization loss rate calculated in our simulation supposes that none of these ions are reabsorbed by the surface. Goldstein et al. (1981) as an example suggested that up to 50% of the newly created He ion might be lost, a percentage that is difficult to constrain without self-consistently coupling exospheric and magnetospheric models. Other percentages have been also suggested for Na ions going from 60% (Killen et al. 2004) to less than 15% (Delcourt et al. 2003). It implies that from the $0.7 \cdot 10^{22} \text{ H/s}$ ionized in Mercury's exosphere it is probable that a significant percent should be recycled into the surface.

In the case of MBF distribution (Figure 5.23), 33169 test-particles were injected in the simulation and followed up to the moment they either escaped (21413 test-particles) or were ionized (9756 test-particles). The ejection rate from the bombarded surface is $2.4 \cdot 10^9 \text{ H/cm}^2/\text{s}$, that is, $8.9 \cdot 10^{26} \text{ H/s}$ in order to reproduce the typical range of dayside density reported by Mariner 10 at the subsolar point. Therefore, for MBF distribution, the loss is largely dominated by neutral escape with a loss rate of $6.1 \cdot 10^{26} \text{ H/s}$ and the ion escape are $2.8 \cdot 10^{26} \text{ H/s}$. We found therefore in the case of MBF distribution a ~ 20 times larger neutral escape than in the case of MB distribution, as suggested by Smith et al. (1978).

Figure 5.24 and Figure 5.25 displays the derived density range at various positions in the equatorial plane of Mercury. We found density at the surface subsolar plane around 200 H/cm^3 in the case of MB and around 120 H/cm^3 in the case of MBF. These densities have to be compared to the 250 H/cm^3 suggested by the original analysis of Mariner 10 observations. Our new analysis of Mariner 10 profiles suffered however from a relatively poor agreement with the observations as explained in section 5.5.4.

As shown in Figure 5.24, the simulated densities display a significant day to nightside contrast in density with a nightside density ~ 213 times larger than on the dayside in the case of MB distribution and by only a factor 2 in the case of MBF distribution. The thermal accommodation relation between temperature and density would predict a factor ~ 80 (Hodges et al. 1973). Therefore, the contrast between subsolar and antisolar densities is smaller in the case of partial thermalisation than predicted in the case of a complete thermalisation at the surface (Figure 5.21).

As explained in introduction, Hodges et al. (1973) theory implicitly supposed a MB distribution with a complete thermal accommodation ($\alpha = 1$). In our case, since we

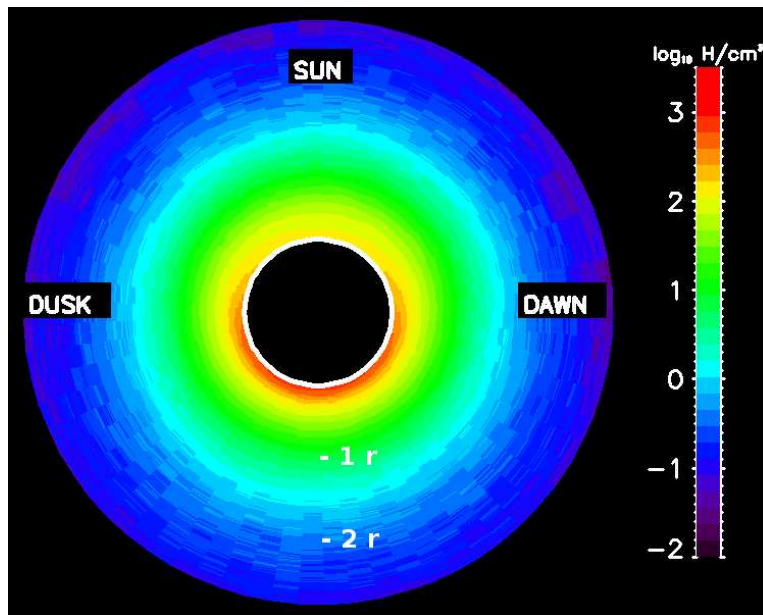


Figure 5.22: Density distribution in \log_{10} of H/cm^3 in the equatorial plane extending to three $radius_{Mercury}$, calculated using MB distribution. The Sun is at the top of each figure. The two simulations were scaled (in term of ejection flux in order to reproduce the observed dayside subsolar point made by Mariner 10).

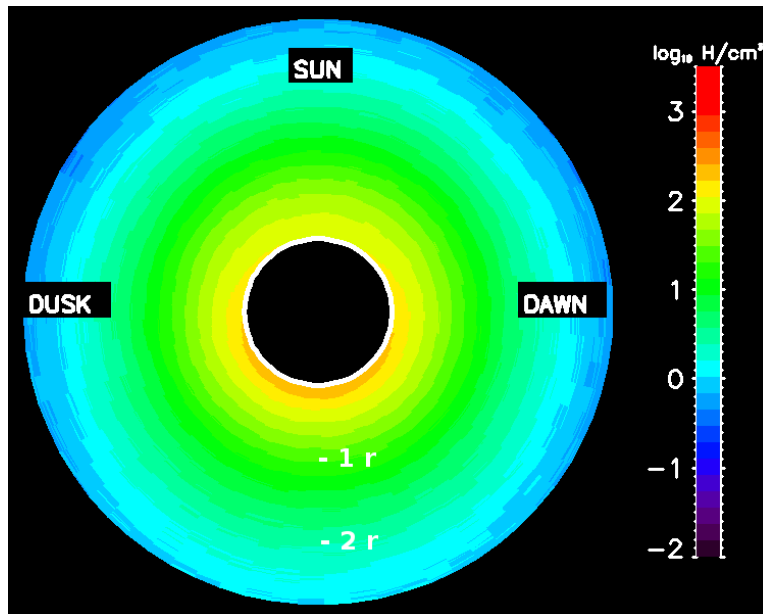


Figure 5.23: Density distribution in \log_{10} of H/cm^3 in the equatorial plane extending to three $radius_{Mercury}$, calculated using MBF distribution. The Sun is at the top of each figure. The two simulations were scaled (in term of ejection flux in order to reproduce the observed dayside subsolar point made by Mariner 10).

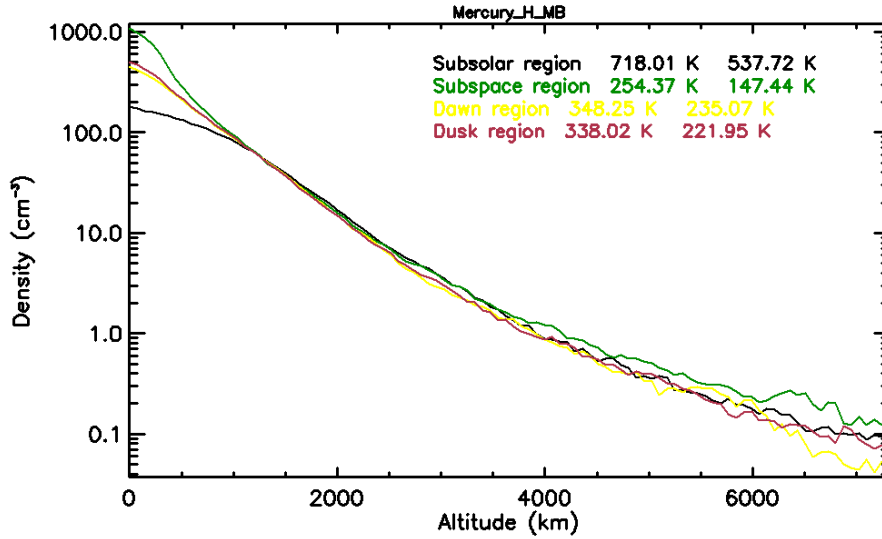


Figure 5.24: Density profiles at the subsolar (black line), antisolar (green line), dawn (yellow line) and dusk (red line) points in the equatorial region for MB distribution. The two temperatures indicated for each line are derived from a barometric law with a specific scale height $H = kT/mg$ (see equation 5.5) for altitudes 0-200 km and 300-800 km.

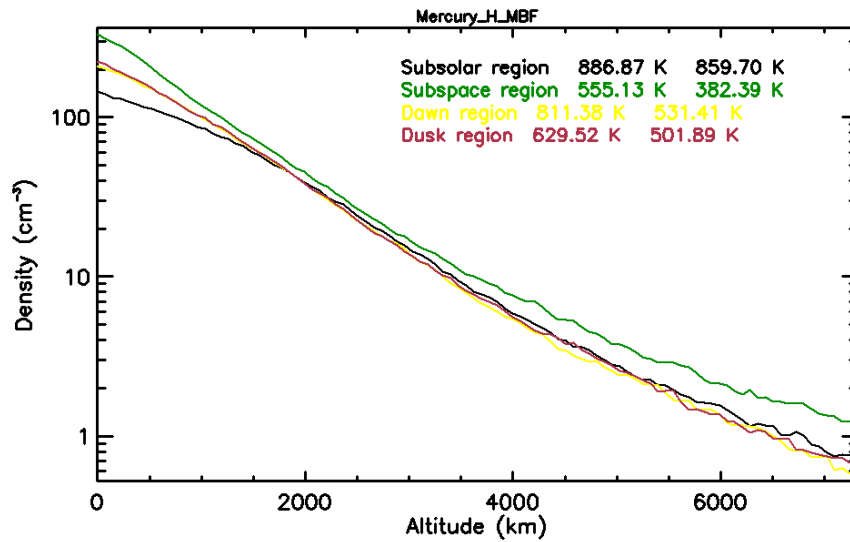


Figure 5.25: Density profiles at the subsolar (black line), antisolar (green line), dawn (yellow line) and dusk (red line) points in the equatorial region for MBF distribution. The two temperatures indicated for each line are derived from a barometric law with a specific scale height $H = kT/mg$ (see equation 5.5) for altitudes 0-200 km and 300-800 km.

supposed a weak accommodation, day to night sides migration and density contrast is reduced. Smith et al. (1978) made a similar calculation for Mercury He exosphere supposing a complete thermal accommodation. These authors found a day to night sides density ratio of 140 to 150 in the case of MBF distribution and of 270 in the case of MB distribution.

The origin of the day to night asymmetry is better evidenced in Figure 5.26 and Figure 5.27 showing the mean sunward velocity distribution around Mercury for both distributions. Both panels displayed the same global trend. There is clearly a set of particles moving toward the Sun which are particles ejected from the dayside with enough energy to escape Mercury. The rest of the equatorial plane is mainly populated by particles with almost no global motion with respect to Mercury, that is, a region with a mixture of particles moving away and toward Mercury surface.

There is also a global day to night sides motion of the hydrogen particles (in agreement with the density plot) as suggested by the negative velocity (between -0.1 and -0.3 km/s) in the terminator regions which are the regions indicated by dawn and dusk. The main difference between the two panels is the magnitude of the velocity which is larger for MB distribution than for MBF. Such a difference is mainly due to the fact that region far from Mercury are populated much more efficiently by a MBF distribution than by a MB distribution. As an example, above 1000 km in altitude, it is needed 0.026 eV for a H atom to reach such an altitude. Only 10% of the particles ejected following a MB distribution at 100 K can reach 1000 km in altitude and 20% of the particles ejected following a MBF distribution at 100 K (Figure 5.3).

In another way, it implies that the source region of the particles reaching $1 R_M$ from the surface is essentially the subsolar region for MB case and the whole dayside for MBF case. As a consequence, $1 R_M$ region is populated essentially by particles ejected from 400-600 K region for MB ejection whereas it is populated by a much larger range of surface temperature in the case of MBF ejection. Such a situation is also illustrated by the map of the temperature around Mercury in both cases (Figure 5.28 and Figure 5.29). As shown the average exospheric kinetic temperature is much hotter from a MBF ejecta distribution (Figure 5.29) than with a MB ejecta distribution (Figure 5.28). Kinetic temperatures are also in closer agreement with surface temperature in the MBF case than in the MB one.

The comparison between Figure 5.28 and Figure 5.29 also shows that the kinetic temperature derived from the MBF case is much continuous with a decrease from the surface with altitude contrary to the MB case. Actually, as shown in Figure 5.24 and Figure 5.25, the density profile is closer to a barometric profile in MBF case than in MB case. However, the temperatures derived from a scale height altitude analysis are significantly larger than both surface and kinetic calculated temperatures. It shows that the calculated exosphere in the case of MBF is not barometric.

In the case of MB, the contrast between kinetic temperatures shown in Figure 5.28, surface temperature and scale height temperature (Figure 5.24 and Figure 5.25) is even more important. Kinetic temperatures between 150 K on dayside to 50 K on nightside are calculated in the exosphere, whereas scale height temperatures from 500 to 100 K are calculated. Actually, the profiles of the density shown in Figure 5.24 and Figure 5.25 are significantly different from a barometric profile, showing a strong discontinuity of the subsolar profile. This is also illustrated in Figure 5.28 and Figure 5.29 where various concentric regions of temperature are obvious (not due to a lack of statistic), illustrating the mixture of regions mainly populated by specific region of the surface, as an example, nightside region close to the surface.

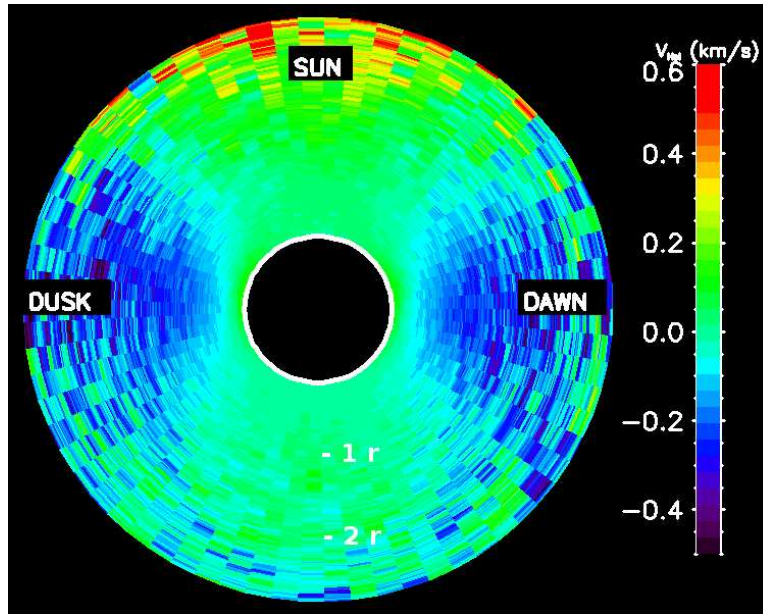


Figure 5.26: Sunward/Antisunward velocity component distribution in km/s in the equatorial plane extending to three $\text{radius}_{\text{Mercury}}$, for MB distribution. The Sun is at the top of each figure. The velocity is expressed in Mercury's frame. Positive velocity are for particles moving toward the Sun.

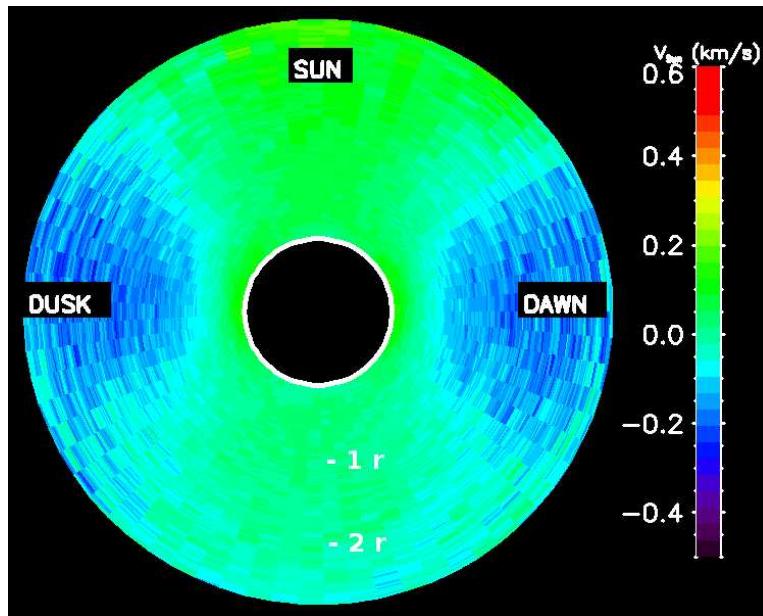


Figure 5.27: Sunward/Antisunward velocity component distribution in km/s in the equatorial plane extending to three $\text{radius}_{\text{Mercury}}$, for MBF distribution. The Sun is at the top of each figure. The velocity is expressed in Mercury's frame. Positive velocity are for particles moving toward the Sun.

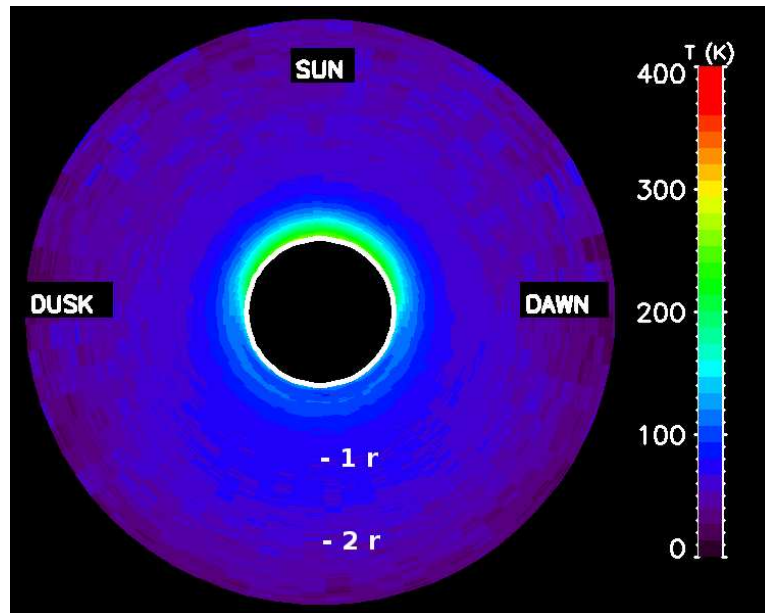


Figure 5.28: Kinetic temperature distribution in K in the equatorial plane extending to three $\text{radius}_{Mercury}$, for MB distribution.

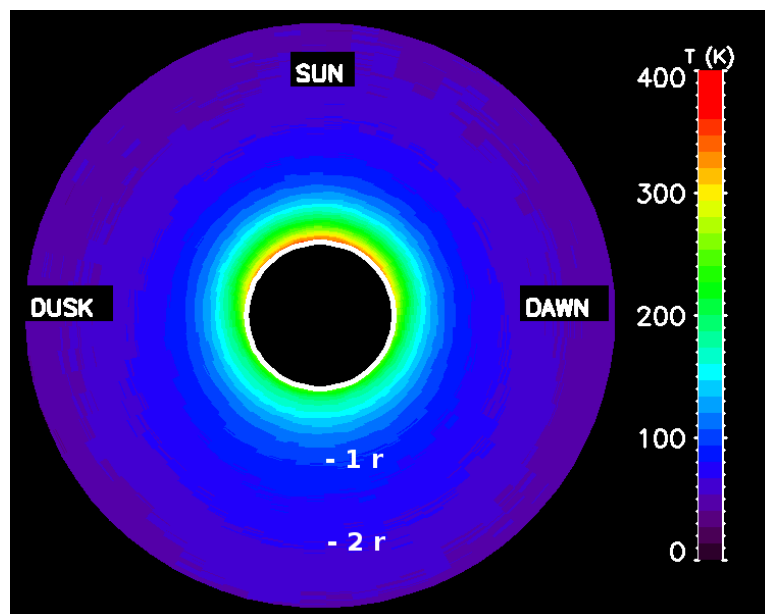


Figure 5.29: Kinetic temperature distribution in K in the equatorial plane extending to three $\text{radius}_{Mercury}$, for MBF distribution.

5.5.2 Accommodation coefficient

In short, the accommodation coefficient is a macroscopic classical quantity that in simplistic cases is directly applicable within margins. However in more complex cases, such as this case of hydrogen at Mercury, the accommodation coefficient seems to lose meaning. The reason is that the surface reactions on Mercury seem to be more complex than earlier assumed.

In Figure 5.30 and Figure 5.31, two nominal cases are compared to two runs of changed accommodation coefficient, from the nominal value of $\alpha = 0.08$ to the higher value of $\alpha = 0.5$ - which is very close to the accommodation value for sodium of $\alpha = 0.62$. The densities were calculated for both MB and MBF distributions.

Despite the obvious differences in densities between the MBF and the MB distributions, it is clear that for both distributions a difference in the accommodation coefficient leads to a flattening of the curves and a larger density quota between day- and nightside although this quota is smaller for the MB distribution.

This density change is particularly true for the MB distribution, that gives a much higher density closer to the surface than the MBF distribution but gets an enormous increase in densities at higher altitudes for an increased accommodation coefficient. In the nominal case the "correct" value for $\alpha = 0.08$ which is very low, is used, leading to the particles returning to the surface and impacting, takes the energy of the surface to a lower degree than if one would compare to the much higher value of $\alpha = 0.5$.

A high accommodation coefficient implies that the particles take the energy of the surface, or thermalise, to a higher degree than a low coefficient.

This dependence can be seen clearly in the flattening of the subsolar densities and the extension to several thousands of km. As the accommodation coefficient is higher ($\alpha = 0.5$) than the usual one for hydrogen ($\alpha = 0.08$), particles take on the higher energies from the dayside to a larger degree. Particles with higher energies will have higher velocities, and thus travel further from the surface and in both Figures this is seen as an extension to higher altitudes.

Similarly the nightside lower energy (100 K) have more particles take on the lower energy and thus the densities fall off at lower altitudes than for the nominal case. The particles all have low energies and cannot reach very far from the surface before they fall back and re-impact on the surface. Indeed particles with such a low energy will most probably "hop around" on the nightside of Mercury until they are ionised or reach the dayside with higher energies.

What is also clear is that a higher accommodation coefficient "smooths out" the differences between the MB and the MBF distributions. This could be one of the reasons that hydrogen is so hard to fit to existing data, for any of these distributions, while successful models (and comparisons to data) have been done for sodium and other species with much higher accommodation coefficient (Na has an $\alpha = 0.62$ to compare to H $\alpha = 0.08$). The differences in the velocity distributions simply doesn't show as much when the accommodation with the surface takes over.

5.5.3 Source regions

Source regions refer to the areas on Mercury's surface where the particles can be ejected in the simulation. The nominal run has been chosen to eject particles from the dayside, only because this is compliant with the arrival of the solar wind at Mercury. However this area covers the entire dayside uniformly, which is maybe not the truth. Therefore ejection

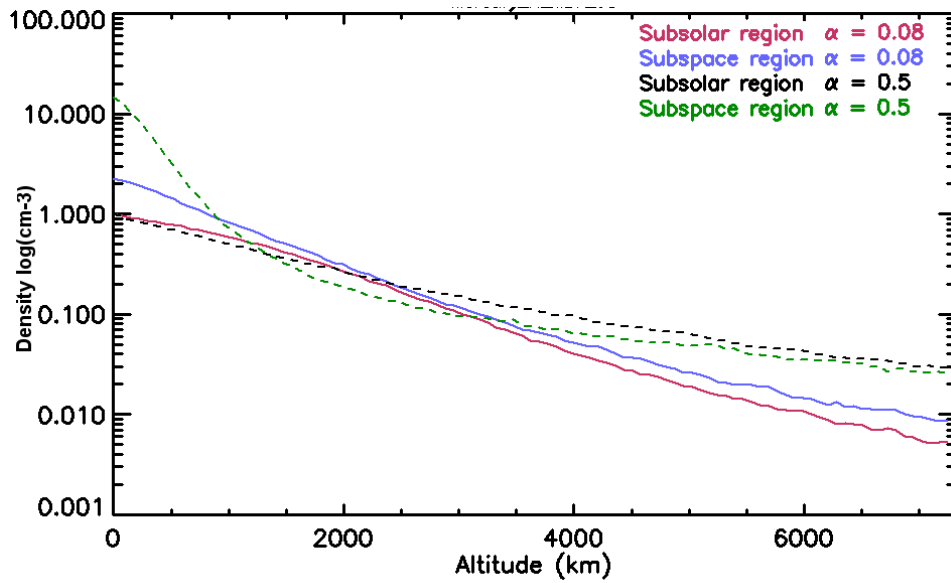


Figure 5.30: Nominal case and case for changed accommodation coefficient to $\alpha = 0.5$ for MBF distribution. Both curves are normalised to nominal case subsolar value, for comparison. The two temperatures indicated for each line are derived from a barometric law with a specific scale height $H = kT/mg$ (see equation 5.5) for altitudes 0-200 km and 300-800 km.

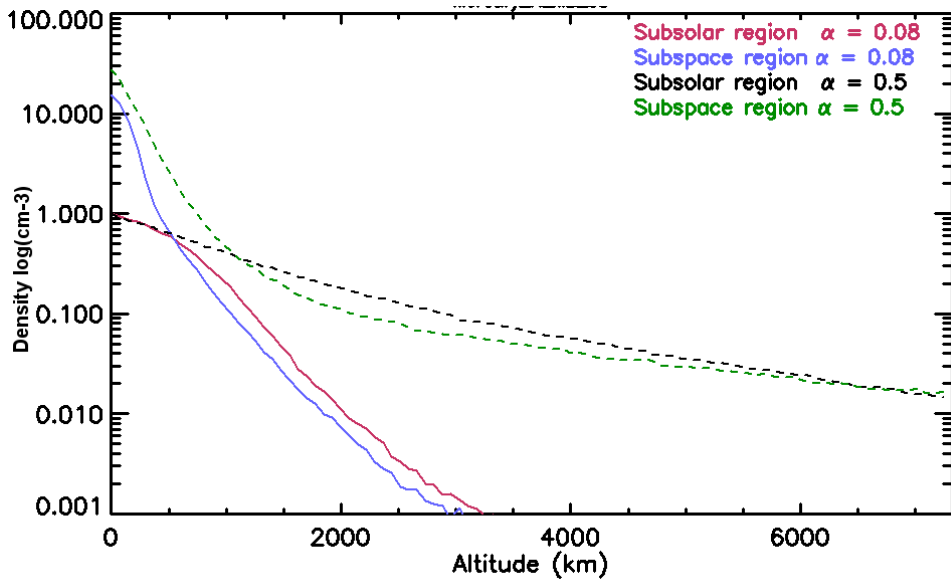


Figure 5.31: Nominal case and case for changed accommodation coefficient to $\alpha = 0.5$ for MB distribution. Both curves are normalised to nominal case subsolar value, for comparison. The two temperatures indicated for each line are derived from a barometric law with a specific scale height $H = kT/mg$ (see equation 5.5) for altitudes 0-200 km and 300-800 km.

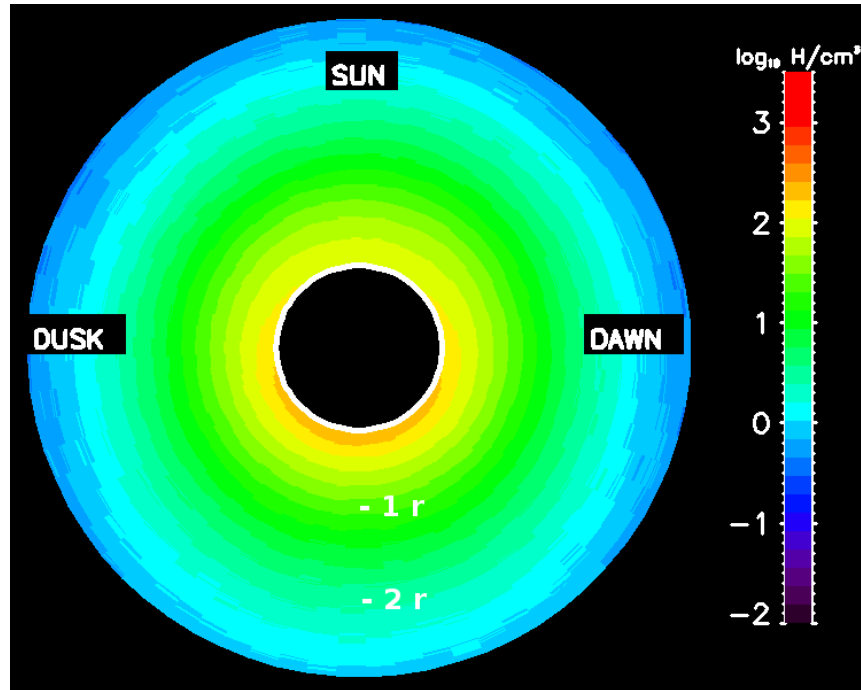


Figure 5.32: Exospheric hydrogen density in \log_{10} of H/cm^3 in the equatorial plane extending to three $radius_{Mercury}$, calculated using MBF distribution with ejection from a region defined as between -60 and 60 in longitude and 27 and 54 in latitude.

from smaller areas, or even other parts of the planet, such as the nightside, can be realised to simulate other conditions than the nominal one.

We ran a case with a preferential ejection of hydrogen atoms from high latitude Northern hemisphere from a region defined as between -60 and 60 in longitude and 27 and 54 in latitude (a surface of $3.8 \cdot 10^6 \text{ km}^2$ that is around 5% of Mercurys surface).

Such a surface is set to represent the typical surface area impacted by solar wind particles at Mercury (Sarantos et al., 2007). In this scenario, solar wind protons impacted preferentially Mercurys surface within this region. Such protons are either reflected by the surface as protons, for example between 0.1 to 1% of the impacting solar wind protons are observed to be reflected at the surface (Saito et al., 2008), or as neutral particles. Wieser et al. (2009) as an example reported that up to 20% of the impinging protons were backscattered by the Lunar surface as neutral particles with energy above 25 eV. At such energy, this neutral hydrogen would escape Mercury since the escape energy of a H atoms at the surface is less than 0.1 eV and thus will not contribute significantly to the local density of Mercurys exosphere. The remaining 80% of protons impacting Mercurys surface will not be re-emitted directly but will be physi-sorbed or chemi-sorbed. We therefore explicitly supposed that the main source of hydrogen at Mercury is solar wind protons implanted in the surface.

These particles are later ejected from the surface by thermal desorption (evaporation) producing the low energy component that has been observed by Mariner 10.

Figure 5.32 displays the associated global hydrogen density distribution of the H atoms

associated with such a localized ejection source. The global shape of the distribution does not display significant signature of such a localized source. In fact, the density is increased locally only within the first 1000 km within the region of ejection. Above 500 km, the density is globally symmetric with respect to the Sun-Mercury axis in the case of MB, and above 1000 km in the case of MBF.

In the MBF case, after 2500 hours of run, a stationary state was reached with 33664 test-particles inserted during the run, with 9771 test-particles lost by ionization and 243893 test-particles lost by thermal escape. The ejection rate from the bombarded surface is $7.7 \cdot 10^6$ H/cm²/s in order to reproduce the typical range of dayside density reported by Mariner 10 at the subsolar point, that is, $2.9 \cdot 10^{23}$ H/s. It implies that during that run $8.5 \cdot 10^{22}$ H/s were lost by ionization and $2.05 \cdot 10^{23}$ H/s lost as neutral. As for the MB case; there is a minor difference with the uniform case because in that case the H atoms are ejected from a surface which is slightly hotter than in the uniform dayside ejection rate, leading to a small increase of the neutral escape.

Even if a localized source for the H exosphere is probable, it will therefore be difficult to identify such a source region when probing Mercurys exosphere. These simulations suggest that above 500-1000 km in altitude, no signature in the density spatial distribution will be available to trace back the main origin of Mercurys exosphere.

5.5.4 Comparison to Mariner 10 data

In order to compare to Mariner 10 observed profile, we reconstituted an approximate trajectory of Mariner 10 during its third flyby. Mariner 10 made two flybys with observation of the Lyman- α , which were close to each other. Figure 5.33 reproduce the trajectory of Mariner 10 during the third flyby as projected into the equatorial plane.

We also reconstituted the field of view of the UV spectrometer during that flyby. The important part is when the field of view of the UV spectrometer observed the dayside. From these fields of view, we then calculated the column density that should have been measured during this flyby, as can be seen in Figure 5.34.

We then used the g-value calculated by Shemansky (1988) for Lyman- α emission during this flyby, namely g-value = $5 \cdot 10^{-3} \text{ s}^{-1}$ to convert this column density into emission intensity (in Rayleigh). Figure 5.35 reproduce the line-of-sight emission intensity as calculated for the two simulations for uniform dayside source and MB/MBF distributions.

As shown in Figure 5.35, there are essentially three parts in Mariner 10 profile. Below 30 km, the measured brightness is probably due to surface reflected contamination which was not efficiently suppressed. Between 30 km and 300 km, the measured profiles suggest a slope following a 102/134 K barometric scale height. The bump around 200 km should not be considered since it has been reported as being due to instrumental effects. Above 300 km in altitude, the measured intensities became very noisy so that any comparison would be limited. We will therefore concentrate our analysis on the region between 30 and 300 km in altitude.

According to the Figure 5.35, we can already conclude that:

- None of the simulations reproduce the measured profile from Mariner 10
- The MB profile is steeper than the MBF profile because the MBF energetic tail is more important than the MB energetic tail
- MBF and MB profiles seem to reproduce the slope above 300 km. However, comparison between simulation and observation remains limited because of the relatively low signal noise ratio of the observations.

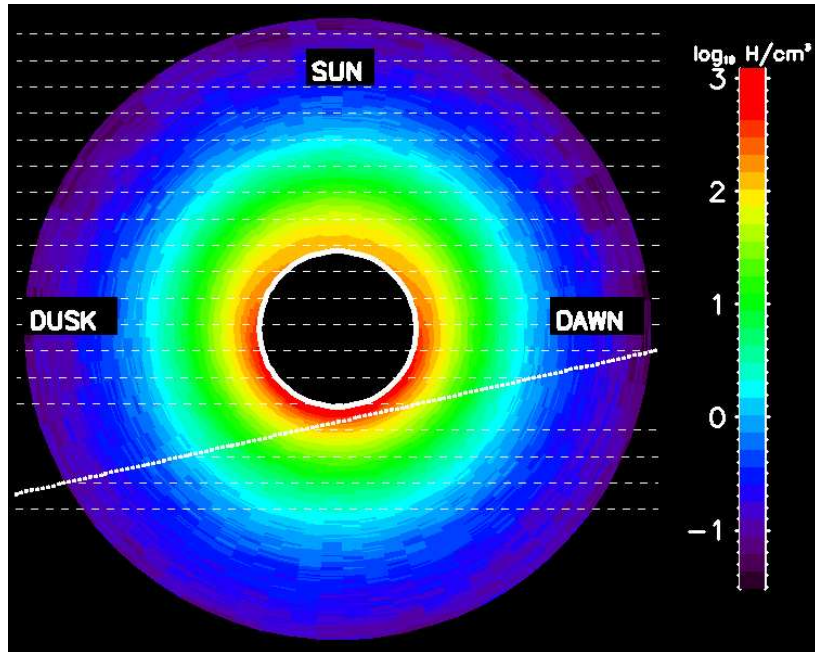


Figure 5.33: Equatorial hydrogen density, extending to three $r_{Mercury}$, as simulated with a MB distribution (same as Figure 5.32). Solid white line is the approximative trajectory of Mariner 10 during its third fly-by (assumed to be within the equatorial plane for simplification). The dashed lines represent the simulated field of view of the UV spectrometer during this fly by.

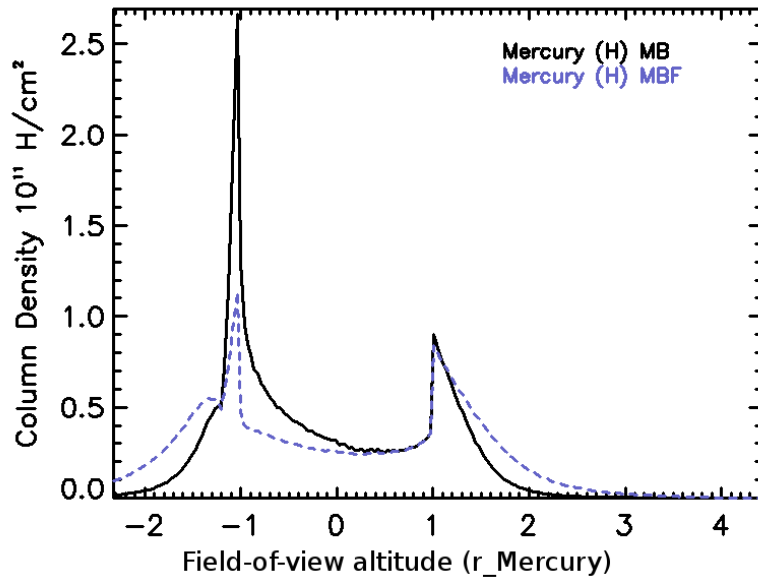


Figure 5.34: Hydrogen column density simulation data with the same field-of-view as seen during Mariner 10 flyby encounter III (Figure 5.33) for both MBF and MB distributions.

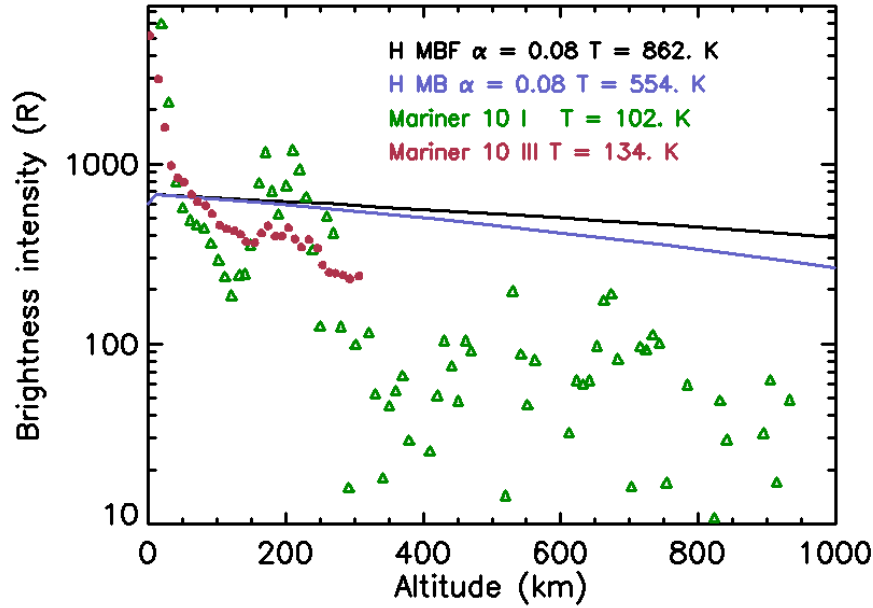


Figure 5.35: Comparison between the measured Lyman- α emission brightness measured during Mariner 10 flyby (circles is first flyby, triangles is third flyby) and the simulated equivalent emission using MB (black line) and MBF distributions (blue line). Temperatures are calculated from scale height analysis between 100 and 320 km in altitude. The simulated profiles were normalized to the brightness intensity measured at 50 km in altitude.

- The less noisy part of Mariner 10 profile is being 30 and 300 km in altitude. It suggests a 102/134 K slope of the emission brightness profile, which is not reproduced by the simulations.

Higher accommodation does not improve the comparison (Figure 5.36 and Figure 5.37). Far from the surface, the profile is flatter than in Figure 5.35 and the equivalent temperatures are higher. Indeed, a higher accommodation implies a more efficient thermalisation of the particle. The consequence is a larger day/night sides migration (as discussed in the previous sections). Therefore, around the subsolar region, the profile in density is more dominated by source particles (ejected at the surface temperature) than by ambient particles. The profile is therefore flatter at large distance from the surface than in the case of a lower accommodation. In other way, a large accommodation coefficient means that the exosphere is more representative of the surface below it. As a consequence, energy accommodation cannot explain the observed profiles.

It has been suggested by Shemansky and Broadfoot (1977) that the energy distribution of the rejected particles should be truncated in energy due to the energy exchange with the surface, which is limited by the Debye temperature of the surface.

We arbitrarily fixed this limit at various energies, that is, we limit the energy distribution of the particles rejected from the surface after impacting it. We then simulated the associated exospheric density and brightness profile. Figure 5.38, Figure 5.39, Figure 5.40 and Figure 5.41 display the effect of including such a truncation in energy in a MBF distribution (Figure 5.38 and Figure 5.39) and in a MB distribution (Figure 5.40 and

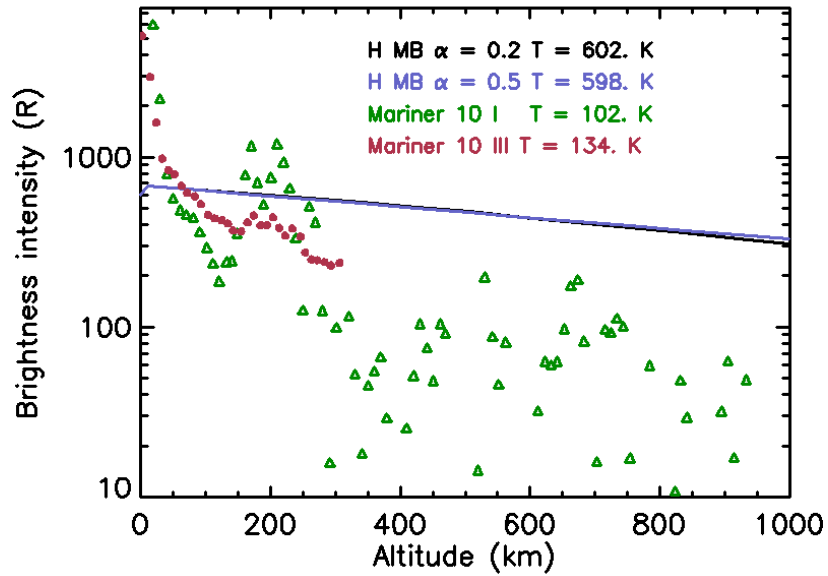


Figure 5.36: Comparison between the measured Lyman- α emission brightness measured during Mariner 10 flyby (green triangles) and the simulated equivalent emission using an accommodation factor of 0.2 (black line) and an accommodation factor of 0.5 (blue line) for a MB distribution. Temperatures are calculated from scale height analysis between 100 and 320 km in altitude.

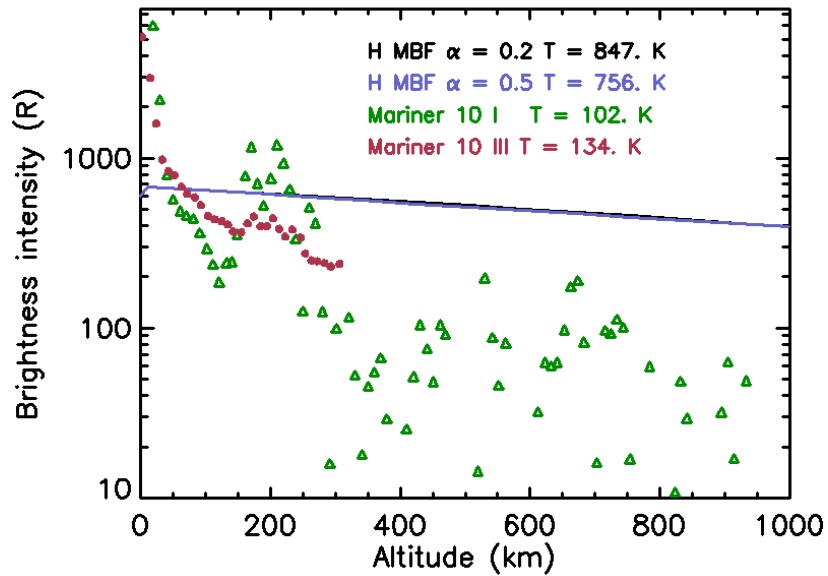


Figure 5.37: Comparison between the measured Lyman- α emission brightness measured during Mariner 10 flyby (green triangles) and the simulated equivalent emission using an accommodation factor of 0.2 (black line) and an accommodation factor of 0.5 (blue line) for a MBF distribution. Temperatures are calculated from scale height analysis between 100 and 320 km in altitude.

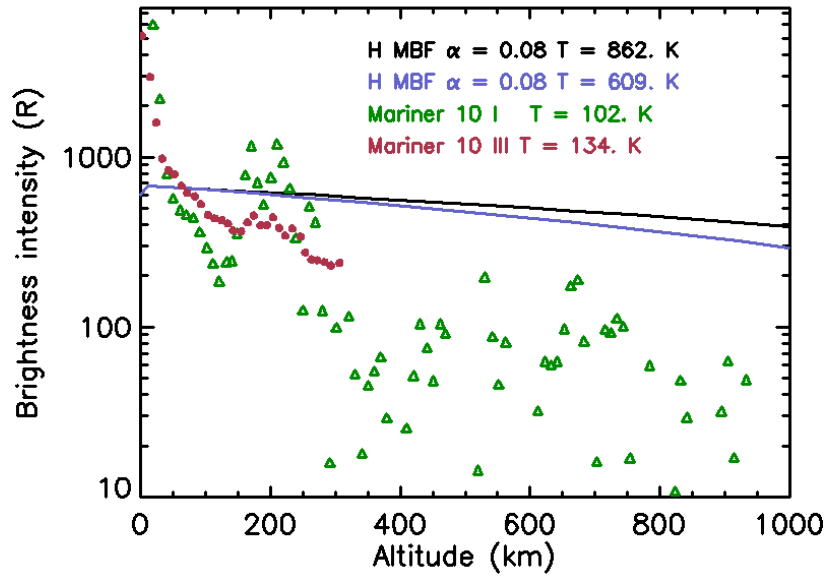


Figure 5.38: Comparison between the measured Lyman- α emission brightness measured during Mariner 10 flyby (green triangles) and the simulated profile using MBF with accommodation of 0.08 and no truncation in energy (black line) and a MBF simulation with a truncation of the rejected distribution at 0.08 eV (blue line). Temperatures are calculated from scale height analysis between 100 and 320 km in altitude.

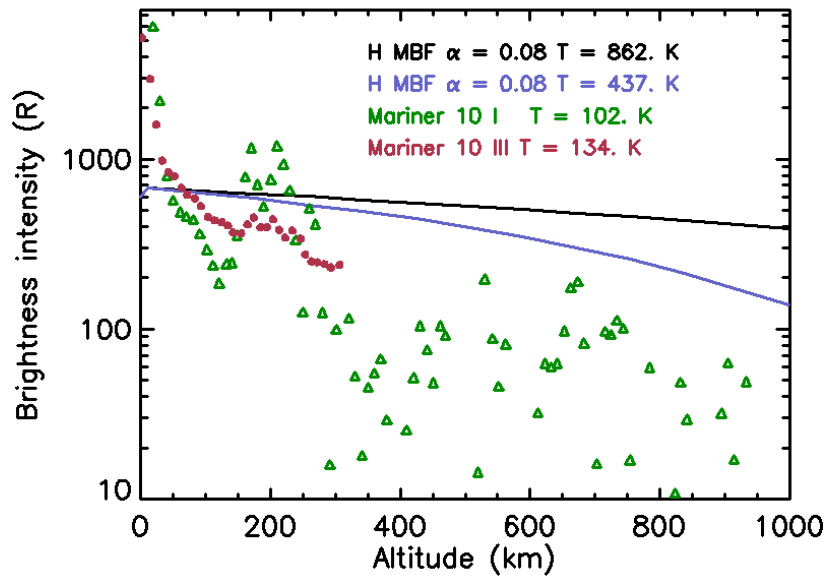


Figure 5.39: Comparison between the measured Lyman- α emission brightness measured during Mariner 10 flyby (green triangles) and the simulated equivalent emission using MBF and an accommodation factor of 0.08 (black line) same as Figure 5.36 but with a truncation in energy at 0.06 eV (blue line) and of 0.04 eV (black line). Temperatures are calculated from scale height analysis between 100 and 320 km in altitude.

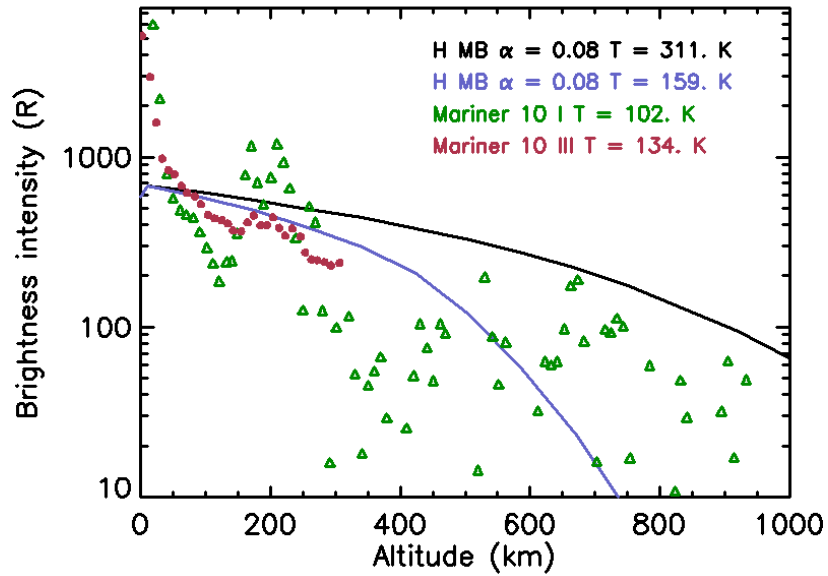


Figure 5.40: Comparison between the measured Lyman alpha emission brightness measured during Mariner 10 flyby (green triangles) and a simulation using MB distribution truncated in energy at 0.08 eV (dark line) and 0.04 eV (blue line) and accommodation factor of 0.08. Temperatures are calculated from scale height analysis between 100 and 320 km in altitude.

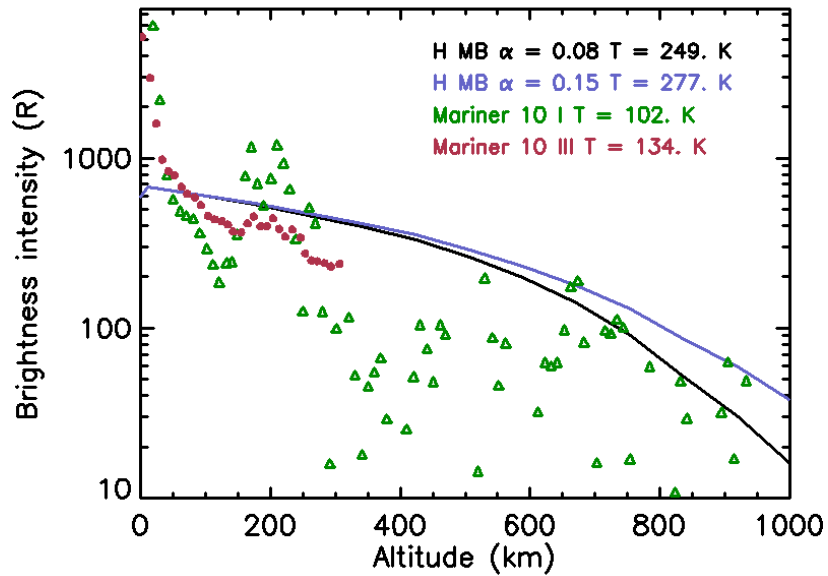


Figure 5.41: Comparison between the measured Lyman alpha emission brightness measured during Mariner 10 flyby (green triangles) and MB distribution, accommodation factor of 0.08 (black line) and of 0.15 (blue line) and truncation in energy at 0.06 eV. Temperatures are calculated from scale height analysis between 100 and 320 km in altitude.

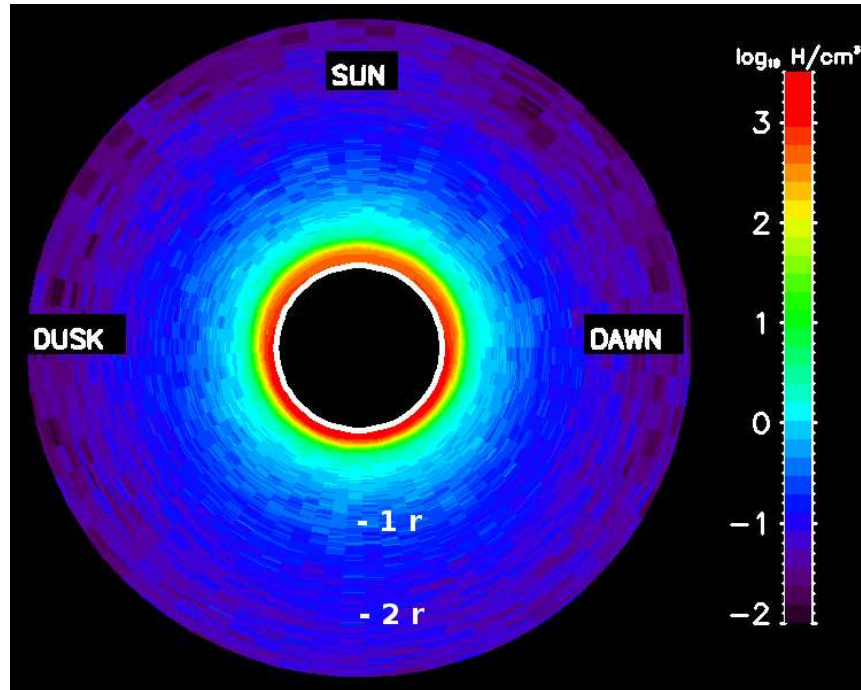


Figure 5.42: Density distribution in \log_{10} of H/cm^3 in the equatorial plane extending to three $\text{radius}_{\text{Mercury}}$, calculated using MB distribution for an accommodation coefficient of 0.08 and an energy truncation at 0.04 eV. The Sun is at the top of the figure.

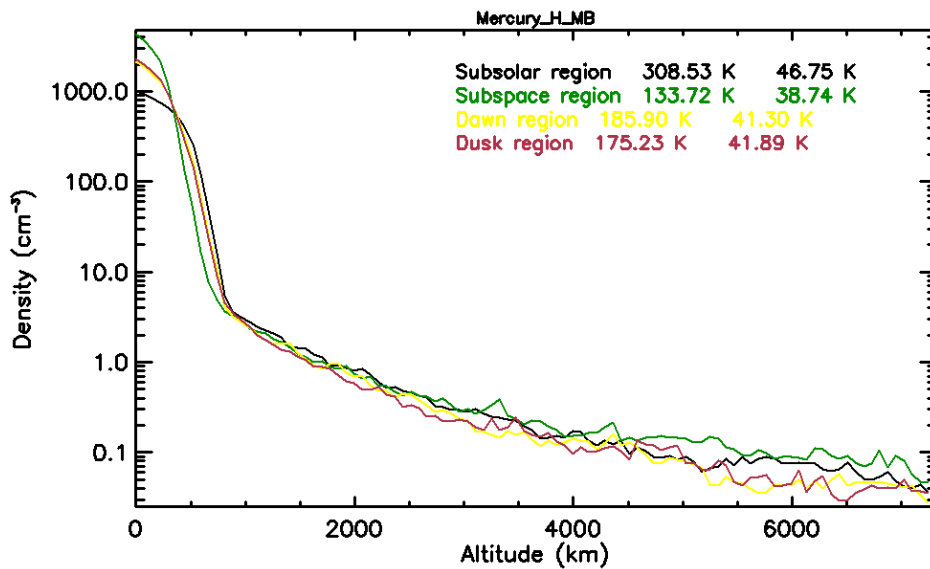


Figure 5.43: Density profiles for Figure 5.42 for an accommodation coefficient of 0.08 and an energy truncation at 0.04 eV at the subsolar (black line), antisolar (green line), dawn (yellow line) and dusk (red line) points in the equatorial region.

Figure 5.41).

In these cases, the scale height and associated temperature between 30 and 300 km (indicated on each figure and for each simulation) decreases significantly. It is therefore clear from this work that the energy distribution of the particle re-ejected from a surface can be truncated in energy in order to superficially reproduce the H density profile below 300 km in altitude. This is, however, with a certain reservation to the accuracy of the Mariner 10 hydrogen profile. In another way, if the energy truncation does indeed reproduce the curve, the result suggests that we could retrieve some characteristics of the hydrogen exosphere - surface interaction thanks to the detailed observation and modeling of Mercury's exosphere.

From Figure 5.38, Figure 5.39, Figure 5.40 and Figure 5.41, it appears that up to an energy truncation of 0.04 eV (Figure 5.39) is needed to reproduce the 102/134 K profiles observed by Mariner 10. Such a cut in energy can be easily understood since 0.035 eV is the energy needed to reach 1600 km in altitude. With 0.04 eV energy cut, we therefore do not allow the ambient particles to reach altitudes higher than 2000 km in altitude, only source particle being able to do so.

Figure 5.40 suggests that the measured emission above 600 km is not compatible with the profile between 30 and 300 km in altitude, the source population being not large enough with respect to the ambient one. Such a conclusion is also suggested by the large dispersion of the measured emission above 400 km in altitude which suggests that the emission brightness should decrease significantly with altitude above that altitude. Actually, the apparent constant emission brightness intensity above 400 km measured by Mariner 10 suggests that the measured emission is dominated by the interplanetary background emission rather by Mercury's exosphere emission.

Figure 5.42 and Figure 5.43 display the shape of Mercury's exosphere in the case corresponding to Figure 5.40 (blue line). As shown in Figure 5.42 and Figure 5.43, the main remarkable feature of the exosphere in that case is the much smaller day to night sides contrast (factor 4). Figure 5.43 also shows that in that case we found a much denser exosphere close to the surface at both subsolar and antisolar points. This is compensated by a strong variation of the density around 200 km in altitude.

Unfortunately, the only profile of the H exosphere available so far does not allow us to be more conclusive on the structure of the H exosphere. In another way, if Mariner 10 profile is confirmed by the forthcoming observations by MESSENGER (which UV spectrometer won't be able to probe altitude close to the surface because of the lack of a large baffle) and by BepiColombo (PHEBUS being specially equipped for that kind of measurement), we should expect to be able to retrieve essential information on the physics of the exosphere/surface interaction. Any future observations of the Lyman alpha emission above Mercury's surface associated with an accurate correction due to the interplanetary emission should provide key information on the origins of Mercury's exosphere.

5.5.5 Prediction of expected PHEBUS signal

As noted in Chapter 4, it is of great benefit to be able to, at some level, predict a signal of an instrument built for a specific purpose. PHEBUS has been constructed with both the environment around Mercury in mind, and the ability to make high resolution spectrography of ultraviolet signatures in the exosphere of Mercury. The technical specifications of the optical part of PHEBUS is called the instrument function and is a measurement of the ideal resolution the spectrograph could have in an ideal environment.

To be able to understand what type of emissions and their resolution and strength PHEBUS should be able to detect, the emission densities can be convoluted with the

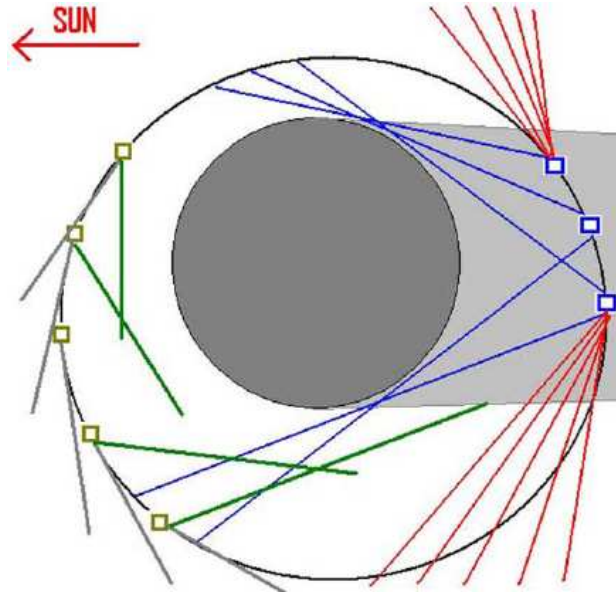


Figure 5.44: Schematic view of the different observation modes. Blue lines are grazing sounding mode at twilight, red lines are vertical scanning mode, grey lines are along-orbit sounding mode with LOS parallel to the velocity vector (Image adapted from Chassefiere et al. (2010))

instrument function and thus giving an ideal image of the best possible detection the PHEBUS could have. Of course, once in space and in the extreme environment around Mercury, this will not be completely true with so many unknown factors affecting the instrument, but it will give a measure of the upper limit estimate of PHEBUS detection.

A schematic view of the different observation modes for the PHEBUS can be seen in Figure 5.44 where the mode that scans the furthest from the surface of Mercury is the "Vertical scanning mode". In this mode a vertical scan of the atmosphere, between the lowest admissible altitude (0 km if the spacecraft is in the shadow of the nightside, and a yet undefined value if it is on the dayside) to typically 1000 km altitude (Chassefiere et al., 2010).

This leaves PHEBUS open to scan for hydrogen from 0-1000 km from the surface, which is the same range as Mariner 10 had.

We ran a "best fit" case according to the Mariner 10 comparison in chapter 5.5.4; MB distribution, dayside SZA dependent launch area, 0.08 accommodation coefficient and cut in energy at 0.04. Then we reused the profile that was deduced from Mariner 10's line-of-sight for the third flyby, for further details please see Chapter 5.5.4. The simulated column density with the same field-of-view as the flyby above, can be seen in Figure 5.34. This column density (n_H in atoms/cm²), for Lyman- α , was then multiplied by the g-value (g in photons/atom/s) to yield an emission intensity in Rayleigh (10⁶ photons/cm²/s).

$$I_H = n_H \cdot g$$

To arrive at count rates or counts/second, the instrument function (f_{EUV}) of PHEBUS which is ~ 0.148 counts/s/R for Lyman- α at 121.6 nm, needs to be multiplied with the emission rates:

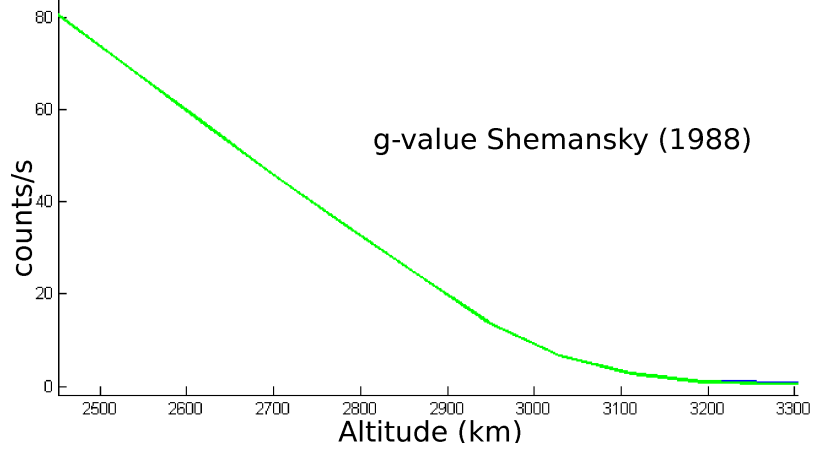


Figure 5.45: Counts/second for Lyman- α emissions as viewed by PHEBUS EUV detector. The g-value is from Shemansky (1988).

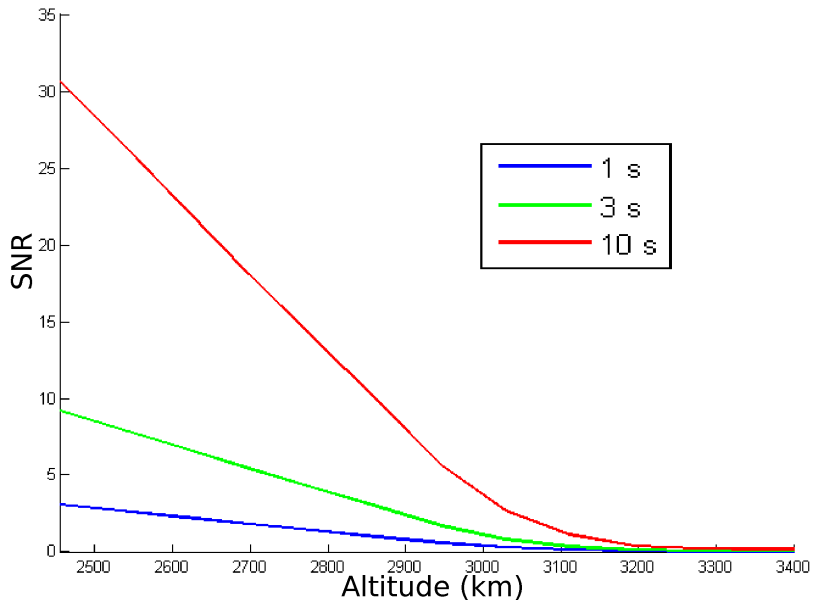


Figure 5.46: Signal-to-noise ratio for g-value from Shemansky (1988) as depicted in Figure 5.45 for three different accumulation times (1 s, 3 s and 10 s).

$$\text{counts/s} = I_H * f_{EUV}$$

We used the g-value calculated by Shemansky (1988), $g\text{-value} = 5 \cdot 10^{-3} \text{ s}^{-1}$ and the emission intensities can be seen in Figure 5.45.

It is clear that with these theoretical results, PHEBUS will have no, at least theoretical, problems detecting hydrogen in the exosphere around Mercury, however higher accumulation times are needed to resolve the emissions that are further away from the surface, since they have to exceed the noise of the static interplanetary background of 25 R.

Signal-to-Noise ratio

The signal-to-noise ratio (SNR) is

$$SNR = S/\sqrt{S + S_b}$$

where S is the mean signal and S_b is the noise of the background, in this case $\sqrt{600} \approx 25 \text{ counts/s}$.

In Figure 5.46 the signal-to-noise ratio for different accumulation times are shown as applied to the PHEBUS.

For even just a few seconds ($\sim 10s$) of exposure the PHEBUS should have > 20 in SNR for a Lyman- α signal for distances as far as 2500 km ($\sim 1r_M$) from the surface. For altitudes as high as 3000 km PHEBUS would have a $SNR > 3$, which was one of the criteria when designing PHEBUS.

5.6 Summary

It is clear, and in accordance with previous conclusions, such as Shemansky and Broadfoot (1977), that modelling hydrogen in the exosphere of Mercury does not follow standard classical theories. Hydrogen is having a much more complex behaviour than previously thought. It seems that the gas-surface interactions for this species are undeveloped, at this time.

There is a large discrepancy in the choice of velocity distribution, since neither MB nor MBF distribution give a density profile that fits the current Mariner 10 profile. As can be seen in Figure 5.22 and Figure 5.23 the two distributions yield completely different profiles for hydrogen in the simulation. However, for hydrogen it seems that the use of the MB distribution rather than the MBF, is more justified in view of the current results.

Despite the obvious differences in densities between the MBF and the MB distributions, it is clear, that for both distributions, a difference in the accommodation coefficient leads to a flattening of the curves and a larger density quota between day- and nightside. A higher accommodation coefficient also "smooths out" the differences between the MB and the MBF distributions. This could be one of the reasons that hydrogen is so hard to fit to existing data since hydrogen has such a small accommodation to the surface of Mercury.

The change of surface accommodation coefficient does not change the fit of the curves enough to reproduce the Mariner 10 profile as seen in Figure 5.41 which has a much higher accommodation coefficient.

It was suggested by Shemansky and Broadfoot (1977) that the energy distribution of the rejected particles should be truncated in energy due to the energy exchange with the surface, which is limited by the Debye temperature of the surface.

A "best fit" to reproduce the 102/134 K profiles, of Mariner 10's hydrogen data, apparently needs an energy truncation of 0.04 eV (Figure 5.39). Such a cut in energy can be easily understood since 0.035 eV is the energy needed to reach 1600 km in altitude. With 0.04 eV energy cut, the ambient particles are not allowed to reach altitudes higher than 2000 km in altitude, only source particle being able to do so. It is therefore clear from this work that the energy distribution of the particle re-ejected from a surface should probably be truncated in energy in order to reproduce the H density profile below 300 km in altitude.

The hydrogen profile of the H exosphere from Mariner 10 is the only one available so far, and in combination with our model, does not allow us to be more conclusive on the structure of the H exosphere. Hopefully the Mariner 10 data can be confirmed by forthcoming observations by MESSENGER and especially by BepiColombo, which will have PHEBUS on board, which was specially designed for these types of observations.

PHEBUS will, according to the calculations of emission intensity of Lyman- α and the low signal-to-noise ratio of > 3 for altitudes as high as 3000 km, have a good chance to record hydrogen in Mercury's exosphere as can be seen in Figure 5.46.

Chapter 6

Conclusion

“The Universe is made one by an invisible, imponderable, immaterial force which puts its atoms in motion. If one single atom should cease to be moved by this force, the universe would come to a stop.”

This thesis, carried out in Service d’Aéronomie/LATMOS, deals with two aspects of neutral hydrogen at Mercury, observational and theoretical - The preparation of the in-flight calibration of the EUV/FUV spectrometer PHEBUS on board BepiColombo that has been developed specifically to observe hydrogen and other ultraviolet emissions, and the construction of a Monte Carlo model of the neutral hydrogen exosphere of Mercury.

The neutral hydrogen around Mercury is of special interest since it is one of the most abundant species on Mercury and because most of the data recorded by the first mission to Mercury, Mariner 10 in the 1970s, are almost only of hydrogen. Also, at the moment of writing this thesis, another mission to Mercury, NASA’s MESSENGER, has just made its third flyby and is about to enter orbit. MESSENGER will have the opportunity to record hydrogen and other emissions, that could be used for further refinement of the model developed in this thesis.

ESA is also developing a mission to Mercury, BepiColombo, that is set to launch in 2014. On board, the ultraviolet spectrometer PHEBUS will be able to also record hydrogen and other species with its very sensitive detectors and clever technical solutions to minimise the stray light inside the instrument, making it an ideal instrument for these types of observations.

The in-flight calibration of the PHEBUS, described in Chapter 4 is a very important step for any instrument that will encounter a space environment.

As PHEBUS is an EUV/FUV instrument I had to search for suitable calibration sources such as the very hot and rare Wolf-Rayet stars. As a basis for this search, I analysed the possible star spectra given by the star occultation analysis of SPICAV and SPICAM, described in Chapter 3.

Since PHEBUS is modelled after both these instruments, it was very suitable to use their gained knowledge of calibration to make the calibration of PHEBUS smoother.

After analysing the suitability of calibration objects, I then applied the radiometric model,

developed by N. Rouanet, to the chosen stars to estimate the sensitivity and accuracy of PHEBUS, in calibration aspects.

Since the PHEBUS is built for EUV/FUV range it is obvious that hydrogen at 121,6 nm, will be observed. Hydrogen is abundant around Mercury but can very easily fade into the interstellar background, if the instrument is not sensitive enough¹. However, since there has only been one mission so far to Mercury and because hydrogen is almost impossible to observe from Earth, it was clear that a model of the hydrogen in the exosphere of Mercury could greatly improve the calibration of PHEBUS.

The modelling of the hydrogen exosphere described in Chapter 5 describes, for the first time, the behaviour of neutral hydrogen in the exosphere of Mercury.

The model SPERO, Simulation and Parsing of Exospheric neutRal atOms, that I developed in the course of this thesis, is a full 3-D Monte Carlo numerical model that calculates the ballistic orbits of hydrogen particles released from the surface of Mercury up until a set altitude. The model is also very easily adaptable to other neutral atoms such as helium or other rocky bodies such as the Moon. An article applying the model to helium is currently in preparation (Leblanc et al., 2011) since the scope of this thesis was too limited to address this subject.

The particles are affected by gravity, radiation pressure and ionisation until they either escape at a set upper limit or re-impact the surface. If they re-impact the surface they accommodate to the surface temperature and are re-ejected with energies that are equivalent to this temperature.

As the result was compared to the measurements of Mariner 10, it appears that hydrogen does not seem to follow the classical exospheric theory applied where thermal desorption is the main surface release mechanism. An article is in preparation where the results of this study will be addressed (Simon Wedlund et al., 2011).

The sensitivity study presented in Chapter 5.5 can be concluded in two remarks:

- Gas-surface interactions are poorly understood and badly constrained. Since they determine how hydrogen atoms are distributed at the exobase (*in the choice of MB or MBF velocity distribution*) and how they accommodate with respect to surface temperature (*accommodation coefficient*), they have a large impact on the densities presented.
- The point above leads to the need for more observations (*remote and/or in situ*) and more laboratory experiments on gas-surface interactions, such as the reaction of hydrogen with various regolith surfaces (*porosity, chemical reactions, energy exchange*).

These two points will hopefully be clarified by forthcoming missions such as MESSENGER and BepiColombo, since the hydrogen profile from Mariner 10, in combination with our model, does not allow us to be more conclusive on the structure of the hydrogen exosphere as of now.

¹This is what happened to Mariner 10, which spectra of hydrogen is most likely saturated by interstellar background or reflection of the surface of Mercury

Appendix A

SPICAM star table of 39 stars with flux above 800 R at 164 nm

SPI nr	HR nr	Name	Type	V Mag	RA (deg)	Dec (deg)
2	264	Gam Cas	B0IVe	2.47	14.18	60.72
5	472	Alp Eri	B3Vpe	0.46	24.43	-57.24
8	1203	Zet Per	B1Ib	2.85	58.53	31.88
9	1220	Eps Per	B0.5V	2.89	59.46	40.01
12	1713	Bet Ori	B8Ia:	0.12	78.63	-8.2
14	1790	Gam Ori	B2III	1.64	81.28	6.35
16	1852	Del Ori	O9.5I	2.23	83	-0.3
17	1879	Lam Ori	O8III	3.54	83.78	9.93
18	1899	Iot Ori	O9III	2.77	83.86	-5.91
19	1903	Eps Ori	B0Ia	1.7	84.05	-1.2
20	1948	Zet Ori	O9.7I	2.05	85.19	-1.94
21	2004	Kap Ori	B0.5I	2.06	86.94	-9.67
25	2294	Bet CMa	B1III-	1.98	95.68	-17.96
28	2491	Alp CMa	A1Vm	-1.46	101.29	-16.72
29	2618	Eps CMa	B2II	1.5	104.66	-28.97
36	3165	Zet Pup	O5f	2.25	120.9	-40
41	3734	Kap Vel	B2IV-	2.5	140.53	-55.01
44	4199	The Car	B0Vp	2.76	160.74	-64.39
46	4621	Del Cen	B2IVn	2.6	182.09	-50.72
48	4730	Alp1 Cru	B0.5I	1.33	186.65	-63.1
49	4731	Alp2 Cru	B1V	1.73	186.65	-63.1
53	4853	Bet Cru	B0.5I	1.25	191.93	-59.69
55	5056	Alp Vir	B1III	0.98	201.3	-11.16
56	5132	Eps Cen	B1III	2.3	204.97	-53.47
57	5191	Eta UMa	B3V	1.86	206.88	49.31
59	5231	Zet Cen	B2.5I	2.55	208.88	-47.29
60	5267	Bet Cen	B1III	0.61	210.96	-60.37
62	5440	Eta Cen	B1.5V	2.31	218.88	-42.16
65	5469	Alp Lup	B1.5I	2.3	220.48	-47.39
70	5944	Pi Sco	B1V+B	2.89	239.71	-26.11
71	5953	Del Sco	B0.3I	2.32	240.08	-22.62
73	5984	Bet1 Sco	B1V	2.62	241.36	-19.81
74	6084	Sig Sco	B1III	2.89	245.3	-25.59
76	6165	Tau Sco	B0V	2.82	248.97	-28.22
77	6175	Zet Oph	O9.5V	2.56	249.29	-10.57
84	6527	Lam Sco	B2IV+	1.63	263.4	-37.1
86	6580	Kap Sco	B1.5I	2.41	265.62	-39.03
89	7121	Sig Sgr	B2.5V	2.02	283.82	-26.3
91	7790	Alp Pav	B2IV	1.94	306.41	-56.74

Table A.1: SPICAM star table of 39 stars with flux above 800 R at 164 nm. (Dimarellis 2003). Type = Spectral type, V Mag = Visual magnitude, RA = Right ascension, Dec = Declination

Appendix B

PHEBUS radiometric simulation brightness of emission lines

Wavelength (nm)	Species	Brightness (Rayleigh)
30.40000	He II	1.6E-03
37.20750	Na II	8.9E-03
58.40000	He I	1.8E+02
73.60000	Ne I	1.4E-01
74.40000	Ne I	9.3E-02
76.93530	O I	7.2E-02
76.94080	O I	2.2E-01
77.07930	O I	2.2E-02
77.10250	O I	6.4E-03
77.10560	O I	3.6E-02
79.15140	O I	8.4E-02
79.19730	O I	2.8E-01
80.42700	O I	4.1E-02
80.47790	O I	1.1E-02
80.48480	O I	6.9E-02
81.06650	O I	8.3E-03
81.10510	O I	2.7E-02
81.67200	O I	1.5E-03
81.67720	O I	2.2E-02
81.68620	O I	1.2E-01
87.77980	O I	9.3E-01
87.78790	O I	2.7E+00
88.59730	N I	3.0E-02
88.62260	N I	5.8E-02
88.63330	N I	8.7E-02
88.74580	N I	2.3E-02
88.80240	N I	1.7E-02
88.83720	N I	8.1E-03
90.36230	C II	1.7E-02
90.39620	C II	3.2E-02
90.62070	N I	7.5E-02
90.64320	N I	1.5E-01
90.66190	N I	2.3E-01
90.96970	N I	7.0E-02
91.02780	N I	4.8E-02
91.06450	N I	2.3E-02
94.51910	C I	2.3E+00

Wavelength (nm)	Species	Brightness (Rayleigh)
102.50000	H I	5.5E-01
102.57620	O I	8.5E+00
102.57629	O I	1.0E-01
102.57629	O I	1.5E+00
104.80000	Ar I	7.1E-03
106.66600	Ar I	3.1E-03
113.40000	N I	2.6E+01
118.88330	C I	2.4E-01
119.00210	C I	2.1E-02
119.22180	C I	2.6E-02
119.30310	C I	4.0E+00
119.39950	C I	6.3E-01
119.95500	N I	1.7E+00
120.02230	N I	1.2E+00
120.07100	N I	1.3E+00
121.55000	H I	1.3E+02
123.60000	Kr I	1.7E-02
125.05840	S II	4.6E-01
125.38110	S II	1.3E+00
125.95190	S II	2.7E+00
126.07350	C I	2.7E+00
126.57000	H ₂	1.5E+00
127.64830	C I	1.3E-01
127.72450	C I	5.0E+00
128.01350	C I	8.5E-01
129.56530	S I	3.1E+00
129.61730	S I	8.4E-01
130.34301	S I	5.2E+00
130.40000	O I	2.1E+02
131.65420	S I	1.0E+00
131.66150	S I	7.7E-02
131.66210	S I	5.7E-03
132.88340	C I	2.9E+00
133.45320	C II	7.5E-01
133.57260	Cl I	3.8E-03
136.57000	H ₂	1.4E+00
140.15140	S I	7.3E-01

Wavelength (nm)	Species	Brightness (Rayleigh)
142.50300	S I	6.3E+00
142.51880	S I	4.3E-01
142.52190	S I	4.7E-02
146.20000	H ₂	1.3E+00
147.39940	S I	9.9E+00
147.43781	S I	1.3E+00
147.45699	S I	7.9E-02
148.00000	Xe I	2.2E+00
151.00000	CO	1.2E+03
152.67070	Si II	2.1E-03
154.67000	H ₂	1.4E+00
156.03090	C I	7.9E+01
160.75000	H ₂	4.8E+00
160.80000	H ₂	1.5E+00
165.60000	C I	6.3E+02
167.07870	Al II	4.8E-02
180.73110	S I	2.8E+02
181.40000	S I	1.6E-01
182.00000	S I	7.6E+02
190.02860	S I	1.7E-01
193.10000	C I	1.6E+03
196.89189	Ni I	5.5E-02
199.43000	Ni I	5.9E-02
202.58240	Mg I	1.1E+03
205.20740	Ni I	2.3E-01
205.39519	Ni I	1.4E-02
208.41211	Fe I	7.5E+00
211.83159	Al I	4.3E+01
212.96631	Al I	5.9E+01
213.20171	Fe I	4.8E+00
213.85930	Fe I	1.6E+00
214.55549	Al I	1.1E+02
215.07949	Ca I	1.9E+00
216.67729	Fe I	1.3E+02
216.88259	Al I	1.2E+02
219.91819	Al I	6.5E+00
220.46670	Al I	3.5E+02
220.79780	Si I	1.1E+03

Wavelength (nm)	Species	Brightness (Rayleigh)
224.91799	Fe II	4.0E-02
225.07900	Fe I	2.7E+00
225.48000	Ni I	1.8E+00
225.80071	Al I	1.5E+01
225.95110	Fe I	1.2E+01
226.14309	Ni I	1.1E+00
226.34641	Al I	4.3E+02
227.54661	Ca I	1.2E+01
227.60259	Fe I	1.4E+01
228.99839	Ni I	3.1E+01
232.00339	Ni I	1.7E+02
234.34961	Fe II	1.2E+00
234.55430	Ni I	2.5E+01
234.75139	Ni I	3.5E+00
236.70510	Al I	6.3E+02
237.20691	Al I	2.7E+01
237.37361	Fe II	4.5E-01
238.20391	Fe II	4.2E+00
239.85591	Ca I	9.6E+00
243.37649	Na I	1.1E+01
243.37681	Na I	5.5E+00
243.65940	Na I	1.2E+01
243.65969	Na I	6.2E+00
243.87681	Si I	6.7E+01
244.00100	Na I	1.5E+01
244.00129	Na I	7.7E+00
244.41890	Na I	2.0E+01
244.41919	Na I	1.0E+01
244.93770	Na I	2.0E+01
244.93821	Na I	1.0E+01
245.59309	Na I	2.5E+01
245.59370	Na I	1.2E+01
246.26470	Fe I	1.1E+02
246.43789	Na I	3.2E+01
246.43870	Na I	1.6E+01
247.55359	Na I	5.4E+01
247.55471	Na I	2.7E+01
248.32710	Fe I	1.1E+03
249.07129	Na I	5.4E+01

Wavelength (nm)	Species	Brightness (Rayleigh)
249.07271	Na I	2.8E+01
250.11321	Fe I	1.6E+02
251.21340	Na I	1.1E+02
251.21550	Na I	5.4E+01
251.43159	Si I	4.3E+03
252.28491	Fe I	5.7E+02
252.60000	Si I	1.4E+03
254.38411	Na I	2.2E+02
254.38721	Na I	1.1E+02
256.79819	Al I	7.8E+02
258.58760	Fe II	2.7E+00
259.38689	Na I	7.3E+02
259.39189	Na I	3.7E+02
259.93960	Fe II	6.5E+00
265.24751	Al I	5.4E+02
268.03411	Na I	3.9E+03
268.04331	Na I	1.9E+03
271.90271	Fe I	1.4E+03
274.12029	Li I	1.8E+00
274.12029	Li I	3.7E+00
279.55281	Mg II	4.1E+02
280.27051	Mg II	1.9E+02
283.54570	Fe I	2.4E+01
285.20000	Mg I	1.3E+05
285.28110	Na I	6.4E+03
285.30120	Na I	3.1E+03
287.41721	Fe I	5.7E+01
291.21570	Fe I	1.5E+02
293.69031	Fe I	6.9E+02
294.26699	K I	8.9E-01
294.27219	K I	4.4E-01
296.32100	K I	1.5E+00
296.32830	K I	7.5E-01
296.68979	Fe I	1.5E+03
298.35701	Fe I	1.1E+03
299.21179	K I	2.5E+00
299.22219	K I	1.2E+00
301.91431	Ni I	3.2E+01
303.18669	Ni I	1.6E+01
303.47620	K I	5.4E+00
303.49209	K I	2.7E+00

Wavelength (nm)	Species	Brightness (Rayleigh)
308.21509	Al I	2.9E+04
308.50000	OH	4.3E+02
309.20000	Al I	7.2E+03
310.17891	K I	8.4E+00
310.20459	K I	4.2E+00
314.51121	Ni I	1.7E-01
319.32261	Fe I	5.4E+01
321.71541	K I	3.7E+01
321.76201	K I	1.8E+01
322.16509	Ni I	2.0E+01
322.69829	Ni I	3.2E+00
323.26570	Li I	1.6E+01
323.26570	Li I	3.3E+01
323.29341	Ni I	1.3E+02

Table B.1: Brightness of emission lines between 30 and 323 nm, as simulated by the radiometric model of PHEBUS.

Appendix C

SPICAV star table of 183 stars with flux above 60 R at 164 nm

SPICAM O nr	HR nr	RA (deg)	Dec (deg)
98	15	2.1	29.09
99	153	9.24	53.9
100	179	10.52	50.51
101	496	25.92	50.69
102	542	28.6	63.67
103	779	39.87	0.33
104	801	40.86	27.71
105	936	47.04	40.96
106	985	50	65.65
107	1122	55.73	47.79
108	1131	56.08	32.29
109	1142	56.22	24.11
110	1165	56.87	24.1
111	1228	59.74	35.79
112	1239	60.17	12.49
113	1273	62.17	47.71
114	1423	67.28	-13.05
115	1463	69.08	-3.35
116	1497	70.56	22.96
117	1520	71.38	-3.25
118	1542	73.51	66.34
119	1552	72.8	5.61
120	1567	73.56	2.44
121	1617	75.36	-7.17
122	1641	76.63	41.23
123	1679	77.29	-8.75
124	1735	79.4	-6.84
125	1756	79.89	-13.18
126	1765	80.44	-0.38
127	1770	80.71	3.54
128	1789	81.19	1.85
129	1810	81.91	21.94
130	1811	81.71	3.1
131	1839	82.7	5.95
132	1855	82.98	-7.3
133	1868	83.38	-1.16
134	1876	83.71	9.49
135	1887	83.76	-6
136	1892	83.85	-4.84
137	1897	83.85	-5.42
138	1910	84.41	21.14
139	1931	84.69	-2.6
140	1949	85.19	-1.94

SPICAV star table of 183 stars with flux above 60 R at 164 nm

SPICAM O nr	HR nr	RA (deg)	Dec (deg)
141	1956	84.91	-34.07
142	1996	86.5	-32.31
143	2084	89.5	25.95
144	2106	89.38	-35.28
145	2159	91.89	14.77
146	2199	92.99	14.21
147	2205	92.97	-6.55
148	2344	96.99	-4.76
149	2361	97.04	-32.58
150	2387	97.96	-23.42
151	2456	100.24	9.9
152	2538	102.46	-32.51
153	2571	103.39	-20.22
154	2648	105.73	-4.24
155	2745	108.56	-26.35
156	2749	108.7	-26.77
157	2781	109.67	-24.56
158	2782	109.68	-24.95
159	2787	109.58	-36.73
160	2845	111.79	8.29
161	2961	114.86	-38.31
162	3034	117.02	-25.94
163	3055	117.31	-46.37
164	3084	118.16	-38.86
165	3089	118.27	-49.61
166	3090	118.33	-48.1
167	3116	119.33	-44.11
168	3117	119.19	-52.98
169	3129	119.56	-49.24
170	3159	120.08	-63.57
171	3206	122.37	-47.35
172	3237	123.37	-35.9
173	3240	123.49	-36.32
174	3294	125.63	-48.49
175	3447	130.07	-52.92
176	3454	130.81	3.4
177	3457	130.15	-59.76
178	3468	130.9	-33.19
179	3476	130.92	-49.82
180	3498	131.68	-56.77

SPICAM O nr	HR nr	RA (deg)	Dec (deg)
181	3527	132.64	-46.53
182	3659	137.74	-58.97
183	3663	137.82	-62.32
184	3819	143.54	-51.26
185	3940	149.22	-54.57
186	4133	158.2	9.31
187	4140	158.01	-61.69
188	4234	161.45	-80.54
189	4390	170.25	-54.49
190	4537	177.42	-63.79
191	4590	180.21	-19.66
192	4638	182.91	-52.37
193	4662	183.95	-17.54
194	4679	184.61	-64
195	4743	187.01	-50.23
196	4773	188.12	-72.13
197	4787	188.37	69.79
198	4848	191.59	-56.49
199	4898	193.65	-57.18
200	4942	196.73	-49.91
201	5035	200.66	-60.99
202	5190	207.38	-41.69
203	5248	209.57	-42.1
204	5249	209.67	-44.8
205	5285	211.51	-41.18
206	5354	214.85	-46.06
207	5395	216.53	-45.22
208	5425	218.15	-50.46
209	5453	219.47	-49.43
210	5471	220.49	-37.79
211	5626	227.21	-45.28
212	5664	229.24	-60.96
213	5680	229.7	-60.5
214	5685	229.25	-9.38
215	5708	230.67	-44.69
216	5781	233.97	-44.96
217	5793	233.67	26.71
218	5812	234.66	-29.78
219	5904	238.4	-25.33
220	5928	239.22	-29.21

SPICAM O nr	HR nr	RA (deg)	Dec (deg)
221	5948	240.03	-38.4
222	5987	241.65	-36.8
223	5993	241.7	-20.67
224	6028	243.08	-27.93
225	6092	244.93	46.31
226	6141	247.55	-25.11
227	6143	247.85	-34.7
228	6252	253.08	-38.02
229	6396	257.2	65.71
230	6431	259.33	33.1
231	6588	264.87	46.01
232	6743	271.66	-50.09
233	6787	272.19	20.81
234	6897	276.74	-45.97
235	7029	281.08	-35.64
236	7074	283.05	-62.19
237	7298	288.44	39.15
238	7565	297.77	22.61
239	7623	299.93	-35.28
240	7739	303.82	25.59
241	8047	314.96	47.52
242	8053	315.3	46.16
243	8146	319.48	34.9
244	8154	319.61	43.95
245	8260	324.27	-19.47
246	8335	326.7	49.31
247	8353	328.48	-37.36
248	8539	336.32	1.38
249	8622	339.82	39.05
250	8762	345.48	42.33
251	8781	346.19	15.21
252	8797	346.65	59.42
253	9071	359.75	55.76

Table C.1: SPICAV star table of 183 stars with flux above 60 R at 164 nm. (E. Villard 2007). RA=Right ascension, Dec=Declination

Appendix D

Short-term variations of Mercury's sodium Na exosphere observed with very high spectral resolution

Leblanc, F., Doressoundiram, A., Schneider, N., Massetti, S., Wedlund, M., Lopez Ariste, A., Barbieri, C., Mangano, V., Cremonese, G., Short-term variations of Mercury's Na exosphere observed with very high spectral resolution, Geophys. Res. Lett., 36, 7201, 2009. Copyright [2009] American Geophysical Union.

Reproduced by permission of American Geophysical Union.



Short-term variations of Mercury's Na exosphere observed with very high spectral resolution

F. Leblanc,¹ A. Doressoundiram,² N. Schneider,³ S. Massetti,⁴ M. Wedlund,¹
A. López Ariste,⁵ C. Barbieri,⁶ V. Mangano,⁴ and G. Cremonese⁷

Received 9 March 2009; revised 9 March 2009; accepted 20 March 2009; published 15 April 2009.

[1] Short time variations of Mercury's exosphere cannot be tracked easily from ground based observatories because of the difficulty of distinguishing them from Earth atmospheric effects. On July 13th 2008, using THEMIS solar telescope, we were able to simultaneously measure brightness, Doppler shift and width of the exospheric sodium D₂ emission line during half a day with a resolving power of $\sim 370,000$. Mercury's exosphere displayed an emission brightness peak in the Northern hemisphere which vanished in few hours and a more persistent Southern Hemispheric peak. The bulk Doppler shift of the exosphere suggests a period of strong escape from Mercury. The global changes of the Doppler shift and of the Doppler width suggest that a cloud of sodium atoms ejected before or at the beginning of our sequence of observations passed through THEMIS field of view moving anti-sunward. A preferentially southern ejection of sodium atoms leading to the observed persistent southern emission peak is consistent with the orientation of the Interplanetary Magnetic Field during that period. **Citation:** Leblanc, F., A. Doressoundiram, N. Schneider, S. Massetti, M. Wedlund, A. López Ariste, C. Barbieri, V. Mangano, and G. Cremonese (2009), Short-term variations of Mercury's Na exosphere observed with very high spectral resolution, *Geophys. Res. Lett.*, 36, L07201, doi:10.1029/2009GL038089.

1. Introduction

[2] Mercury's sodium exosphere was observed by *Potter and Morgan* [1990] to be variable on timescales of an Earth day (that is ~ 10 minutes of Mercury solar time) with high latitude peaks in emission brightness appearing and disappearing in few Earth days. *Potter et al.* [2006] suggested that the solar wind might play a key role in producing such observed localized peaks and their short time variability. The reconnection between the interplanetary magnetic field (IMF) lines and Mercury's magnetic field lines would allow the solar wind to penetrate through Mercury's magnetospheric cusps [*Massetti et al.*, 2007]. The solar wind particles would then impact Mercury's surface inducing the sputtering of surface Na atoms leading

to localized increases of the sodium exospheric density at high latitudes.

[3] Following *Massetti et al.* [2007], the solar wind density and velocity control the efficiency of the solar wind sputtering whereas the IMF orientation controls the size and position of the region where the solar wind particles impact Mercury's surface. When the radial component of the IMF is sunward and is the dominant component, the solar wind particles are predicted to preferentially impact the Southern hemisphere in a region whose size and position are driven by the two other components of the IMF. An opposite situation (anti-sunward IMF radial component) was encountered during MESSENGER first flyby with a more intense northern sodium emission than southern [*McClintock et al.*, 2008].

[4] The solar wind and IMF conditions changing on time scales much shorter than one Earth day, the exospheric signatures of the solar wind sputtering at Mercury should also change within few Earth hours. One of the problems with tracking short time variations from Earth is that, in few hours, Mercury is observed through various atmospheric conditions which are a significant potential source of misinterpretation.

[5] In this paper, we discuss the first simultaneous observations of Mercury's sodium brightness, Doppler shift and width during more than 10 continuous hours thanks to the very high resolution of THEMIS solar telescope and its capability to image Mercury's exosphere throughout daylight. Section 2 provides the information on these observations and the analysis performed, and sections 3 and 4 report discussion and conclusions, respectively.

2. Observations and Analysis

[6] THEMIS [*López Ariste et al.*, 2000] is a French-Italian solar telescope on the Canary Island of Tenerife with a 0.9 m primary mirror (with a central obscuration of 0.4 m) and a 15.04 m focal length. The slit size was $0.25'' \times 69.6''$ and the spectral resolution of 15.9 mÅ provided $\sim 370,000$ resolving power. One camera is used to measure the D₂ at 5890 Å Na emission line covering a spectral range of ~ 4 Å and is composed of 512 by 512 pixels at 7.8 mÅ/pixel spectral dispersion. The observation was obtained on the 13th July 2008 between 06:19 and 18:22 UT (08:19–20:22 local time). Mercury's true anomaly angle (TAA) was between 308.8 and 311.5°, the phase angle was between 67.3° and 65.4° and Mercury's radius (R_M) was 3.05''. We were facing the dusk side of Mercury and were seeing 70% of Mercury's illuminated disk. Mercury's heliocentric distance was 0.33 AU and its heliocentric radial velocity was between -7.8 and -7.5 km/s (towards the Sun). The slit was oriented along

¹LATMOS/IPSL, Université Versailles Saint Quentin, CNRS, Verrières-le-Buisson, France.

²LESIA, Observatoire de Paris, Meudon, France.

³LASP, University of Colorado, Boulder, Colorado, USA.

⁴IFSI, INAF, Rome, Italy.

⁵THEMIS, UPS853, CNRS, La Laguna, Spain.

⁶Department of Astronomy, University of Padova, Padova, Italy.

⁷Osservatorio Astronomico di Padova, INAF, Padova, Italy.

Table 1. Subsequent Scans of July 13th 2008^a

Scan n°	Time (UT, LT±2h)	Type of Scan	Seeing (")	Average Emission (kR)	Average Doppler Shift (km/s)	Average Doppler Width (km/s)	North/South Hemispheric Emissions Ratio
3	06:19–06:50	HR, 9 positions separated by 0.5"	3.50 ± 0.28	N/A	-1.07 ± 0.02	2.90 ± 0.31	0.93
4	06:53–08:05	HR, 21 positions separated by 0.25"	1.50 ± 0.58	2.81 ± 0.28	-0.98 ± 0.02	2.79 ± 0.28	0.94
8	08:16–09:28	HR, 21 positions separated by 0.25"	1.33 ± 0.38	2.74 ± 0.15	-1.18 ± 0.01	2.84 ± 0.03	0.90
10	09:33–10:45	HR, 21 positions separated by 0.25"	1.50 ± 0.36	2.61 ± 0.15	-1.04 ± 0.01	2.87 ± 0.25	0.91
12	10:50–12:02	HR, 21 positions separated by 0.25"	1.67 ± 0.34	3.08 ± 0.13	-0.85 ± 0.01	2.78 ± 0.12	0.90
13	12:05–13:31	HR, 25 positions separated by 0.25"	1.83 ± 0.63	2.61 ± 0.32	-0.89 ± 0.01	2.74 ± 0.12	0.93
16	13:38–15:03	HR, 25 positions separated by 0.25"	1.67 ± 0.38	<2.60 ± 0.15	-0.89 ± 0.01	2.84 ± 0.27	0.78
17	15:05–16:31	HR, 25 positions separated by 0.25"	2.33 ± 0.47	2.73 ± 0.25	-0.97 ± 0.01	2.87 ± 0.27	0.81
21	16:55–17:38	LR, 12 positions separated by 0.5"	1.50 ± 0.42	3.28 ± 0.19	-0.98 ± 0.04	2.38 ± 0.45	0.82
22	17:39–18:22	LR, 12 positions separated by 0.5"	2.16 ± 0.53	3.11 ± 0.30	-1.05 ± 0.04	2.51 ± 0.45	0.75

^aThe average emission has been calculated by summing all the ADU measured within all the pixels of the scan, then by multiplying by the angular size of a pixel and then by dividing by the angular size of Mercury apparent disk. The average Doppler shift and width are calculated by fitting by a Gaussian distribution the sum of all spectra measured within all pixels with signal/noise ratio larger than 150 (Figure 3). Uncertainty on the Doppler shift and width (one standard deviation from Gaussian fit) should be considered as relative uncertainty. HR and LR are for high and low resolution respectively. Scan 16 did not cover the whole exosphere so that the average emission should be considered as a lower limit. For scan 3, coverage and seeing precluded a good estimate of the calibration. The method to calculate uncertainties on emission brightness and seeing is described by *Leblanc et al.* [2008].

Mercury's North/South axis and Mercury's exosphere was scanned with the slit automatically moved between each position in a direction perpendicular to the slit. Because the sky conditions were deteriorating, the two last scans were performed with lower resolution (220,000 and 27 mÅ spectral resolution) with a slit of 0.5" × 118" size. Details on each scan are provided in Table 1.

[7] The telescope provided tip-tilt corrections at ~1 kiloHertz. At each slit position, ten individual exposures of twenty seconds were taken with negligible overhead for CCD readout and slit motions. The data were bias corrected and flat fielded. The flat field was obtained by observing the Sun using a special mode avoiding solar bright or dark spots. Spectral calibration was carefully performed, during the whole sequence of observation, using solar spectra obtained at four different times. The sky background was calculated from two segments at each end of the slit interpolated over the whole slit by fitting these two parts with a second degree polynomial. In order to subtract the reflected solar spectrum from Mercury's surface, we used the solar spectrum obtained for the closest atmospheric terrestrial conditions (similar air mass and zenith angle), shifted in wavelength, and scaled to the measurements. The exospheric emission line is then integrated subtracting an average background level calculated outside the emission line. We then fitted the emission line with a Gaussian function and derived the Doppler shift and the spectral full width at half maximum (FWHM) of the emission line after correction by the effect of the point spread function of the instrument. The Doppler shift of Mercury's exospheric line in Mercury's frame was determined using JPL/Horizon ephemerides. We estimated the uncertainty on the Doppler shift as ~0.25 km/s. The brightness calibration is based on the Hapke theoretical model of the reflected solar light from Mercury's surface, which has the advantage of avoiding any uncertainty due to Earth's atmospheric absorption [*Sprague et al.*, 1997]. We have also developed a method to evaluate the uncertainty on the absolute calibration due to the uncertainty of position of the slit on Mercury's illuminated disk [*Leblanc et al.*, 2008].

3. Results

[8] Figure 1 shows the measured emission brightness during six of the best scans described in Table 1. The quality of the images is validated by our estimate of the seeing value and by the image of the continuum [*Leblanc et al.*, 2008]. As shown in Table 1, 4th column, these scans were obtained for comparable atmospheric conditions. As displayed in Figure 1, there are distinct Northern and Southern exospheric peaks structure during scans 4 and 8, followed by a progressive disappearance of the northern peak in less than five hours, whereas the southern peak is still evident up to scan 22 (more than 11 hours later, see also Table 1 last column). The average emission brightness intensity (Table 1: fifth column) displays minima during scans 10 and 13–16, a significant maximum during scan 12 and an increase from scan 17 up to the end of the observation.

[9] In Figure 2, the spatial distribution of the Doppler shift associated to each plot of Figure 1 is shown. In Table 1 (6th column) we also provide the Doppler shift of the sum

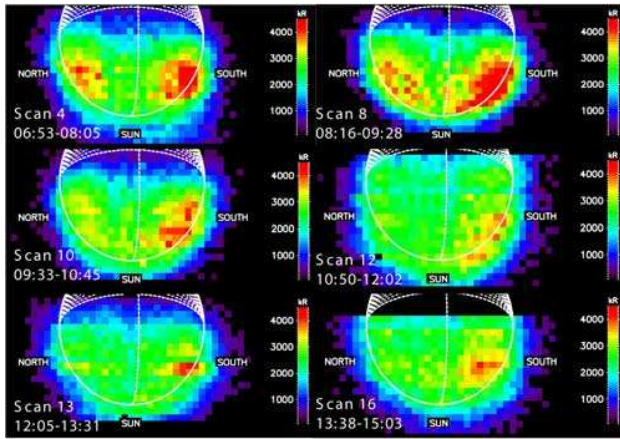


Figure 1. Emission brightness during the six consecutive scans on the 2008/07/13. Mercury's disk is plotted. The white dashed lines are longitudes on the nightside region. The scan of Mercury is done from bottom to top of each panel. Only pixels where the signal/noise ratio was greater than 150 are plotted.

of all pixels for each scan (Figure 3). This Doppler shift is always negative and displays minima at scan 8 and at the end of the observation and a maximum at scan 12. A positive Doppler shift corresponds to atoms moving away from the observer and mainly anti-sunward. The Doppler shift as seen from Earth depends on the angle between the line of sight and the vector normal to the surface, the sodium atoms being ejected preferentially perpendicularly to the surface. Since sodium atoms are also pushed anti-sunward by the solar radiation pressure, such a Doppler shift will also depend on the angle between the line of sight and the solar zenith angle. For quiet conditions, we should observe a globally negative Doppler shift of the atoms along the line of sight with maxima at the solar limb and in the anti-solar direction (bottom and top parts of each panel) and

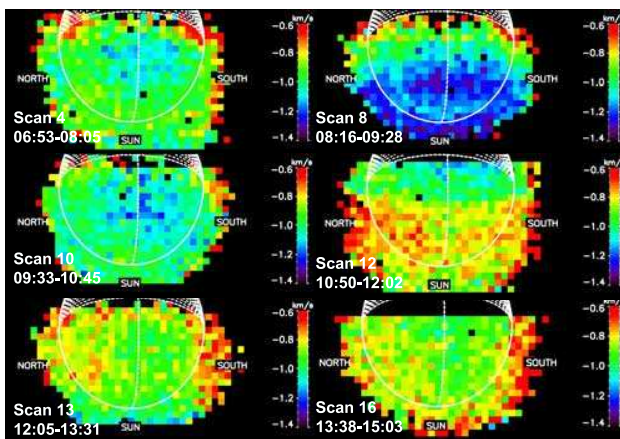


Figure 2. Doppler shift of the Na D_2 emission line in Mercury's frame. A positive Doppler shift means that the Na atoms move on average away from the observer whereas a negative Doppler corresponds to Na atoms moving towards the observer. Only pixels where the signal/noise ratio was greater than 150 are plotted.

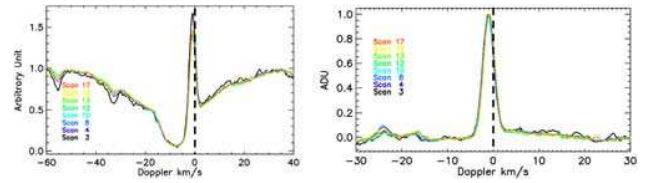


Figure 3. Spectra of the measured signal obtained by summing all pixels with signal/noise ratio larger than 150. (left) The sky contribution to the measured spectra was subtracted but not the solar reflected light on Mercury's surface. (right) Same as Figure 3 (left) but with the solar reflected light on Mercury's surface subtracted. Each spectrum is plotted in Mercury's exospheric frame (zero Doppler shift, vertical dashed line).

a minimum at the sub-Earth point. Such a minimum of the Doppler shift at the center of the apparent disk is observed in Figure 2, for scans 4, 8 and 10 as well as for scans 13 to 17. A globally negative Doppler shift (Figure 3) implies also that a significant part of the observed exosphere was not dominantly gravitationally bounded to Mercury. In the contrary, we should have observed a globally null Doppler shift in Mercury's frame.

[10] *Leblanc et al.* [2008] observed an enlargement of the Doppler spectral line in association with peak of emission brightness and interpreted this as the signature of an energetic process of ejection. The Doppler width distribution during the 6 scans displayed Figures 1 and 2 is shown in Figure 4. We observe a slightly hotter southern hemisphere than the northern during the whole sequence of observation. Two episodes of increase of the Doppler width appear also to occur during scans 8 and 10 and during scans 16 and 17 in Figure 4 (also evident in the average Doppler width displayed 7th column of Table 1). Therefore, during these two periods of maximum Doppler width, it is probable that solar wind sputtering increased leading to a local increase of the Doppler width and to the Doppler shift minima during scan 8 and less evidently during scans 16–17. The association between Doppler width and peak of emission is not as clear for these observations as for the one reported by *Leblanc et al.* [2008]. This can be explained by worse seeing conditions, Mercury being also closer to the Earth in 2007, but also as a signature of the weakness of the energetic processes during our observation. Moreover, most of the atoms producing the southern and northern brightness peaks were probably ejected before the start of our observation, so that they either already moved away from the region of ejection for the most energetic particles as suggested by Figure 4 or partially thermalized by reimpacting the surface.

[11] Scan 12 is the only scan which does not display a clear minimum of the Doppler shift at the center of the apparent disk. We interpret it as the path of another cloud of sodium moving anti-sunward, with positive Doppler shift as suggested by the peak of the average brightness, Figure 1, during scan 12 but without brighter high latitude peaks. Such atoms may have been ejected before scan 10, as suggested by the increase of the Doppler width. The rate of ejection towards the observer between scans 4 and 10, should have peaked during scan 8, as suggested by the contrast between the emission brightness of the high latitude

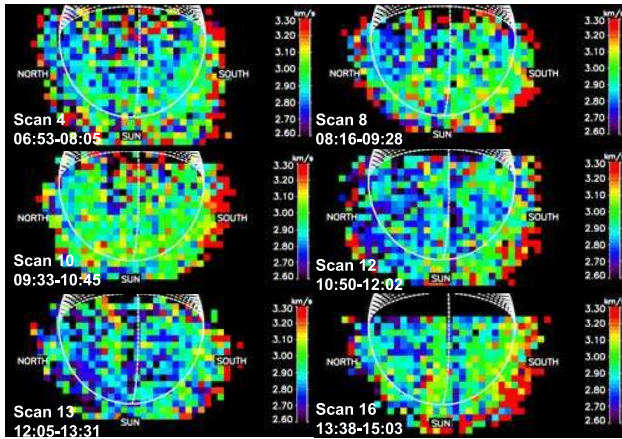


Figure 4. Doppler Width of the spectral Na D₂ emission line. Only pixels where the signal/noise ratio was greater than 150 are plotted.

peaks with the rest of the exosphere. An episode of strong ejection during scan 8 is also suggested by the minimum of the Doppler shift close to the subsolar region. The minimum of average emission brightness during scan 10 (Table 1, 5th column) could have been due to those atoms ejected before scan 10 being slowed down by solar radiation pressure (around -180 cm s^{-2} at TAA = 310° [Smyth and Marconi, 1995]) down to a null velocity with respect to the Sun (and therefore passing through a minimum of the number of solar photons a sodium atom could scatter) before moving anti-sunward. The minimum of the Doppler width during scan 13 would be then the signature of a quiet period during which energetic ejection decreased. If f_1 represents the total number of atoms of the bulk exosphere with a Doppler shift V_1 and f_2 the atoms in the cloud moving with a Doppler shift of V_2 , then the average measured Doppler shift observed during scan 12 would be equal to $V = (V_1 \times f_1 + V_2 \times f_2)/(f_1 + f_2)$ if the exosphere is assumed to be optically thin. V_1 is the average Doppler shift measured when no second population is present, that is $V_1 \sim -0.9 \text{ km/s}$ (scan 13). The cloud population when ejected from the surface should have a velocity of the order of -1.2 km/s (scan 8) and should reimpact the surface with a similar velocity, that is, $V_2 \sim +1.2 \text{ km/s}$, implying, $f_1 \sim 41 \times f_2$ ($V = -0.85 \text{ km/s}$ for scan 12). Therefore, apart from any consideration of scattering efficiency, the increase of exospheric atoms needed to produce the Doppler shift signature observed during scan 12 (f_2) should represent only few percent of the total exospheric sodium atomic population (f_1) in good agreement with the total emission brightness variation (Table 1, 5th column). A similar episode of ejection apparently occurred after scan 16 (from the Doppler width increase) but will be not discussed here because the conditions of observation worsened after scan 16.

[12] In summary, the presence of a persistent peak in emission brightness in the southern hemisphere during more than 11 hours seems to be due to at least two consecutive events of solar wind sputtering and preferentially in the Southern hemisphere. The Northern peak remained visible from Earth for a few hours which suggests that after being initiated by a dramatic increase of the ejection rate, probably before the start of our observation (if not we would have

seen a signature in the Doppler width during scan 4), the peak in exospheric density progressively fades away during several hours being partially maintained by recycling and induced diffusion in the surface. In the contrary, the apparently more persistent southern peak might be explained by one or more subsequent episodes of preferentially southern ejection as indicated by the Doppler width signatures. These episodes of ejection were probably weak as suggested by the lack of significant variation of the total emission brightness.

[13] It is possible to infer the variation and orientation of the IMF during the period of our observations by using Advanced Composition Explorer measurements (ACE, which was 20 Earth radii above the equatorial plane) and the Wilcox Solar Observatory solar data (WSO). At that time, WSO indicates that both Earth and Mercury were above the equatorial plane by 4° and 2.5° respectively. The correction due to the Earth–Sun–Mercury angle as well as to the propagation time of the solar wind between the Earth and Mercury was evaluated using the interplanetary discontinuity linked to the equatorial coronal hole recorded by the SoHO EIT instrument as a marker. Mercury on the July 13th appears to have encountered a period of variable sign of the radial magnetic field component but with long period of sunward and strong values. As stated in the introduction, a strong sunward radial component should induce a preferentially bombardment of the Southern hemisphere as supported by our observation.

4. Conclusions

[14] Eight consecutive images of the brightness, Doppler shift and width of Mercury's exospheric D₂ emission line have been obtained during almost eleven hours by THEMIS solar telescope using very high resolving power ($\sim 370,000$). Two high latitude peaks in emission brightness were visible at the beginning of our sequence of observation. The Northern hemispheric peak vanished during the first five hours of observation whereas the Southern peak lasted during the whole sequence. In the same time, the Doppler shift changed significantly as well as the Doppler width. These observations suggest that a strong ejection event occurred before or at the beginning of our sequence of observations producing in particular the Northern hemispheric peak. Such an event leads to the formation of a cloud of sodium atoms probably initially ejected towards the Sun, then slowed down and accelerated in the anti-sunward direction by the solar radiation pressure. This first event of ejection was then followed probably by a second episode of increased ejection rate preferentially from the Southern hemisphere.

[15] Baumgardner *et al.* [2008] and S. Okano *et al.* (personal communication, 2008) have recently observed Mercury's sodium tail and reported the presence of localized peak of density along the tail that they interpreted as potentially short time variation in Mercury's exosphere. We here show that indeed Mercury's exosphere significantly change in less than a few Earth hours.

References

Baumgardner, J., J. Wilson, and M. Mendillo (2008), Imaging the sources and full extent of the sodium tail of the planet Mercury, *Geophys. Res. Lett.*, *35*, L03201, doi:10.1029/2007GL032337.

- Leblanc, F., A. Doressoundiram, N. Schneider, V. Mangano, A. López Ariste, C. Lemen, B. Gelly, C. Barbieri, and G. Cremonese (2008), High latitude peaks in Mercury's sodium exosphere: Spectral signature using THEMIS solar telescope, *Geophys. Res. Lett.*, *35*, L18204, doi:10.1029/2008GL035322.
- López Ariste, A., J. Rayrole, and M. Semel (2000), First results from THEMIS spectropolarimetric mode, *Astron. Astrophys.*, *142*, 137–148.
- Massetti, S., S. Orsini, A. Milillo, and A. Mura (2007), Modelling Mercury's magnetosphere and plasma entry through the dayside magnetopause, *Planet. Space Sci.*, *55*, 1557–1568.
- McClintock, W. E., et al. (2008), Mercury's exosphere: Observations during MESSENGER's first Mercury flyby, *Science*, *321*, 92–94.
- Potter, A. E., and T. H. Morgan (1990), Evidence for magnetospheric effects on the sodium atmosphere of Mercury, *Science*, *248*, 835–838.
- Potter, A. E., R. M. Killen, and M. Sarantos (2006), Spatial distribution of sodium on Mercury, *Icarus*, *181*, 1–12.
- Smyth, W. H., and M. L. Marconi (1995), Theoretical overview and modeling of the sodium and potassium atmospheres of Mercury, *Astrophys. J.*, *441*, 839–864.
- Sprague, A. L., R. W. H. Kozlowski, D. M. Hunten, N. M. Schneider, D. L. Domingue, W. K. Wells, W. Schmitt, and U. Fink (1997), Distribution and abundance of sodium in Mercury's atmosphere, 1985–1988, *Icarus*, *129*, 506–527.
-
- C. Barbieri, Department of Astronomy, University of Padova, Vicolo Osservatorio 2, I-35122 Padova, Italy.
- G. Cremonese, Osservatorio Astronomico di Padova, INAF, Vicolo Dell'Osservatorio 5, I-35122 Padova, Italy.
- A. Doressoundiram, LESIA, Observatoire de Paris, 5, place Jules Janssen, F-92195 Meudon CEDEX, France.
- F. Leblanc and M. Wedlund, LATMOS/IPSL, Université Versailles Saint Quentin, CNRS, Réduit de Verrières BP 3, F-91371 Verrières-le-Buisson CEDEX, France. (francois.leblanc@latmos.ipsl.fr)
- A. López Ariste, THEMIS, UPS853, CNRS, C/Via Lactea s/n, E-38200 La Laguna, Spain.
- V. Mangano and S. Massetti, IFSI, INAF, Via del Fosso del Cavaliere, 100, I-00133 Roma, Italy.
- N. Schneider, LASP, University of Colorado, Campus Box 392, Boulder, CO 80309-0392, USA.

Bibliography

- [1] Gassendi and the Transit of Mercury. *Nature*, 128:787–788, November 1931.
- [2] W. S. Adams and T. Dunham, Jr. Note on the Spectrum of Mercury. *Publ. of the ASP*, 44:380, December 1932.
- [3] B. J. Anderson, M. H. Acuna, H. Korth, M. E. Purucker, C. L. Johnson, J. A. Slavin, S. C. Solomon, and R. L. McNutt. The Structure of Mercury’s Magnetic Field from MESSENGER’s First Flyby. *Science*, 321:82–, July 2008.
- [4] E. M. Antoniadi. *The planet Mercury*. 1974.
- [5] D. J. Baker and G. J. Romick. The rayleigh: interpretation of the unit in terms of column emission rate or apparent radiance expressed in SI units. *Appl. Optics*, 15:1966–1968, August 1976.
- [6] A. Balogh, R. Grard, S. C. Solomon, R. Schulz, Y. Langevin, Y. Kasaba, and M. Fujimoto. Missions to Mercury. *Space Sci. Reviews*, 132:611–645, October 2007.
- [7] A. R. Barakat and J. Lemaire. Monte Carlo study of the escape of a minor species. *Physical Review A*, 42:3291–3302, September 1990.
- [8] J.-L. Bertaux, O. Korablev, S. Perrier, E. Quémerais, F. Montmessin, F. Leblanc, S. Lebonnois, P. Rannou, F. Lefèvre, F. Forget, A. Fedorova, E. Dimarellis, A. Reberac, D. Fonteyn, J. Y. Chaufray, and S. Guibert. SPICAM on Mars Express: Observing modes and overview of UV spectrometer data and scientific results. *Journal of Geophys. Research (Planets)*, 111:E10S90, October 2006.
- [9] J.-L. Bertaux, F. Leblanc, O. Witasse, E. Quemerais, J. Lilensten, S. A. Stern, B. Sandel, and O. Korablev. Discovery of an aurora on Mars. *Nature*, 435:790–794, June 2005.
- [10] J.-L. Bertaux, D. Nevejans, O. Korablev, E. Villard, E. Quémerais, E. Neefs, F. Montmessin, F. Leblanc, J. P. Dubois, E. Dimarellis, A. Hauchecorne, F. Lefèvre, P. Rannou, J. Y. Chaufray, M. Cabane, G. Cernogora, G. Souchon, F. Semelin, A. Reberac, E. van Ransbeek, S. Berkenbosch, R. Clairquin, C. Muller, F. Forget, F. Hourdin, O. Talagrand, A. Rodin, A. Fedorova, A. Stepanov, I. Vinogradov, A. Kiselev, Y. Kalinnikov, G. Durry, B. Sandel, A. Stern, and J. C. Gérard. SPICAV on Venus Express: Three spectrometers to study the global structure and composition of the Venus atmosphere. *Planet. Space Sci.*, 55:1673–1700, October 2007.
- [11] F. W. Bessel. . Berliner Astronomisches Jahrbuch p. 253. 1813.
- [12] T. A. Bida, R. M. Killen, and T. H. Morgan. Discovery of calcium in Mercury’s atmosphere. *Nature*, 404:159–161, March 2000.
- [13] J. Bishop. Venus exospheric structure - The role of solar radiation pressure. *Planet. Space Sci.*, 37:1063–1077, September 1989.

-
- [14] P. Borin, M. Bruno, G. Cremonese, and F. Marzari. Estimate of the neutral atoms' contribution to the Mercury exosphere caused by a new flux of micrometeoroids. *Astro. and Astrophysics*, 517:A89+, July 2010.
- [15] D. Breuer, S. A. Hauck, M. Buske, M. Pauer, and T. Spohn. Interior Evolution of Mercury. *Space Sci. Reviews*, 132:229–260, October 2007.
- [16] R. T. Brinkmann. Departures from Jeans' escape rate for H and He in the Earth's atmosphere. *Planet. Space Sci.*, 18:449, April 1970.
- [17] A. L. Broadfoot, S. Kumar, M. J. S. Belton, and M. B. McElroy. Mercury's Atmosphere from Mariner 10: Preliminary Results. *Science*, 185:166–169, July 1974.
- [18] A. L. Broadfoot, D. E. Shemansky, and S. Kumar. Mariner 10 - Mercury atmosphere. *Geophys. Research Letters*, 3:577–580, October 1976.
- [19] A. L. Broadfoot, D. E. Shemansky, and S. Kumar. Mariner 10 UV Experiment: Helium on Mercury. In *Bulletin of the American Astronomical Society*, volume 8 of *Bulletin of the American Astronomical Society*, page 483, June 1976.
- [20] B. J. Butler. The migration of volatiles on the surfaces of Mercury and the Moon. *Journal of Geophys. Research*, 102:19283–19292, August 1997.
- [21] A. J. Butrica. *To See the Unseen: A History of Planetary Radar Astronomy*. January 1996.
- [22] J. W. Chamberlain. Planetary coronae and atmospheric evaporation. *Planet. Space Sci.*, 11:901, August 1963.
- [23] J. W. Chamberlain and F. J. Campbell. Rate of Evaporation of a Non-Maxwellian Atmosphere. *Astro. Phys. Journal*, 149:687, September 1967.
- [24] J. W. Chamberlain and D. M. Hunten. Theory of planetary atmospheres: an introduction to their physics and chemistry /2nd revised and enlarged edition/. *Orlando FL Academic Press Inc International Geophysics Series*, 36, 1987.
- [25] S. Chandrasekhar. The Theory of Axisymmetric Turbulence. *Royal Society of London Philosophical Transactions Series A*, 242:557–577, September 1950.
- [26] S. C. Chase, Jr., E. D. Miner, D. Morrison, G. Muench, and G. Neugebauer. Mariner 10 infrared radiometer results - Temperatures and thermal properties of the surface of Mercury. *Icarus*, 28:565–578, August 1976.
- [27] E. Chassefière, J.-L. Maria, J.-P. Goutail, E. Quémerais, F. Leblanc, S. Okano, I. Yoshikawa, O. Korablev, V. Gnedykh, G. Naletto, P. Nicolosi, M.-G. Pelizzo, J.-J. Correia, S. Gallet, C. Hourtoule, P.-O. Mine, C. Montaron, N. Rouanet, J.-B. Rigal, G. Muramaki, K. Yoshioka, O. Kozlov, V. Kottsov, P. Moisseev, N. Semena, J.-L. Bertaux, M.-T. Capria, J. Clarke, G. Cremonese, D. Delcourt, A. Doressoundiram, S. Erard, R. Gladstone, M. Grande, D. Hunten, W. Ip, V. Izmodenov, A. Jambon, R. Johnson, E. Kallio, R. Killen, R. Lallement, J. Luhmann, M. Mendillo, A. Milillo, H. Palme, A. Potter, S. Sasaki, D. Slater, A. Sprague, A. Stern, and N. Yan. PHEBUS: A double ultraviolet spectrometer to observe Mercury's exosphere. *Planet. Space Sci.*, 58:201–223, January 2010.
- [28] J. Y. Chaufray, R. Modolo, F. Leblanc, G. Chanteur, R. E. Johnson, and J. G. Luhmann. Mars solar wind interaction: Formation of the Martian corona and atmospheric loss to space. *Journal of Geophys. Research (Planets)*, 112:E09009, September 2007.
- [29] Jean-Yves Chaufray. *Etude de l'exosphère de Mars et de l'échappement de l'eau : Modélisation et analyse des données UV de SPICAM*. PhD thesis, l'Université Paris VI, 2009.

BIBLIOGRAPHY

- [30] M. T. Cicero, trans. F. Brooks. *De Natura Deorum (On the Nature of the Gods)*. London: Methuen, 1896.
- [31] F. Cipriani, F. Leblanc, and J. J. Berthelier. Martian corona: Nonthermal sources of hot heavy species. *Journal of Geophys. Research (Planets)*, 112:E07001, July 2007.
- [32] G. Colombo. Rotational Period of the Planet Mercury. *Nature*, 208:575, November 1965.
- [33] G. Colombo and I. I. Shapiro. The Rotation of the Planet Mercury. *SAO Special Report*, 188, November 1965.
- [34] A. C. M. Correia and J. Laskar. Mercury's capture into the 3/2 spin-orbit resonance as a result of its chaotic dynamics. *Nature*, 429:848–850, June 2004.
- [35] A. C. M. Correia and J. Laskar. Long-term evolution of the spin of Mercury. I. Effect of the obliquity and core-mantle friction. *Icarus*, 205:338–355, February 2010.
- [36] G. Cremonese, M. Bruno, V. Mangano, S. Marchi, and A. Milillo. Release of neutral sodium atoms from the surface of Mercury induced by meteoroid impacts. *Icarus*, 177:122–128, September 2005.
- [37] G. Cremonese, J. Warell, J. K. Harmon, F. Leblanc, M. Mendillo, and A. L. Sprague. Techniques and methods in ground-based observation of Mercury. *Planet. Space Sci.*, 58:61–78, January 2010.
- [38] D. H. Crider and R. R. Vondrak. Hydrogen migration to the lunar poles by solar wind bombardment of the moon. *Advances in Space Research*, 30:1869–1874, 2002.
- [39] D. C. Delcourt, S. Grimald, F. Leblanc, J.-J. Berthelier, A. Millilo, A. Mura, S. Orsini, and T. E. Moore. A quantitative model of the planetary Na⁺ contribution to Mercury's magnetosphere. *Annales Geophysicae*, 21:1723–1736, August 2003.
- [40] S. F. Dermott. Planetary science: How Mercury got its spin. *Nature*, 429:814–815, June 2004.
- [41] A. F. Devonshire. The Interaction of Atoms and Molecules with Solid Surfaces. VIII. The Exchange of Energy between a Gas and a Solid. *Royal Society of London Proceedings Series A*, 158:269–279, January 1937.
- [42] A. Dollfus. Observation visuelle et photographique des planètes Mercure et Vénus à l'Observatoire du Pic du Midi. *L'Astronomie*, 67:61, February 1953.
- [43] A. Dollfus. *Polarizations Studies of Planets*, page 343. 1961.
- [44] A. Dollfus and M. Auriere. Optical polarimetry of planet Mercury. *Icarus*, 23:465–482, November 1974.
- [45] D. L. Domingue, P. L. Koehn, R. M. Killen, A. L. Sprague, M. Sarantos, A. F. Cheng, E. T. Bradley, and W. E. McClintock. Mercury's Atmosphere: A Surface-Bounded Exosphere. *Space Sci. Reviews*, 131:161–186, August 2007.
- [46] A. Doressoundiram, F. Leblanc, C. Foellmi, A. Gicquel, G. Cremonese, J.-F. Donati, and C. Veillet. Spatial variations of the sodium/potassium ratio in Mercury's exosphere uncovered by high-resolution spectroscopy. *Icarus*, 207:1–8, May 2010.
- [47] J. A. Dunne and E. Burgess. The voyage of Mariner 10 : mission to Venus and Mercury. *NASA Special Publication*, 424, 1978.
- [48] B. R. Dyce, G. H. Pettengill, and I. I. Shapiro. Radar determination of the rotations of Venus and Mercury. *Astro. Journal*, 72:351, April 1967.
- [49] G. Eichhorn. Primary velocity dependence of impact ejecta parameters. *Planet. Space Sci.*, 26:469–471, May 1978.
- [50] I. Estermann and O. Stern. Beugung von Molekularstrahlen. *Zeitschrift fur Physik*, 61:95–125, January 1930.

-
- [51] H. J. Fahr and B. Szizgal. Modern exospheric theories and their observational relevance. *Reviews of Geophysics and Space Physics*, 21:75–124, February 1983.
- [52] G. Field. The Atmosphere of Mercury. In P. J. Brancazio & A. G. W. Cameron, editor, *The Origin and Evolution of Atmospheres and Oceans*, page 269, 1964.
- [53] G. B. Field. Atmosphere of Mercury. *Astro. Journal*, 67:575, November 1962.
- [54] J. L. Fox. The production and escape of nitrogen atoms on Mars. *Journal of Geophys. Research*, 98:3297–3310, February 1993.
- [55] M. Frassati, R. Braga, and R. Baum. A new optical map of the regolith albedo of Mercury. *Journal of the British Astronomical Association*, 112:125–129, June 2002.
- [56] Frisch and Stern. *Phys. Zeits.*, 32(670), 1931.
- [57] M. Fujimoto, W. Baumjohann, K. Kabin, R. Nakamura, J. A. Slavin, N. Terada, and L. Zelenyi. Hermean Magnetosphere-Solar Wind Interaction. *Space Sci. Reviews*, 132:529–550, October 2007.
- [58] M. Fulle, F. Leblanc, R. A. Harrison, C. J. Davis, C. J. Eyles, J. P. Halain, R. A. Howard, D. Bockelée-Morvan, G. Cremonese, and T. Scarmato. Discovery of the Atomic Iron Tail of Comet MCNaught Using the Heliospheric Imager on STEREO. *Astro. Phys. Journall*, 661:L93–L96, May 2007.
- [59] K.-H. Glassmeier, J. Grosser, U. Auster, D. Constantinescu, Y. Narita, and S. Stellmach. Electromagnetic Induction Effects and Dynamo Action in the Hermean System. *Space Sci. Reviews*, 132:511–527, October 2007.
- [60] B. E. Goldstein, S. T. Suess, and R. J. Walker. Mercury - Magnetospheric processes and the atmospheric supply and loss rates. *Journal of Geophys. Research*, 86:5485–5499, July 1981.
- [61] Herbert Goldstein. *Classical Mechanics*. Cambridge, MA: Addison-Wesley Press. 1950.
- [62] A. S. Hale and B. Hapke. A Time-Dependent Model of Radiative and Conductive Thermal Energy Transport in Planetary Regoliths with Applications to the Moon and Mercury. *Icarus*, 156:318–334, April 2002.
- [63] R. E. Hartle, S. A. Curtis, and G. E. Thomas. Mercury’s helium exosphere. *Journal of Geophys. Research*, 80:3689–3692, September 1975.
- [64] J. W. Head, S. L. Murchie, L. M. Prockter, M. S. Robinson, S. C. Solomon, R. G. Strom, C. R. Chapman, T. R. Watters, W. E. McClintock, D. T. Blewett, and J. J. Gillis-Davis. Volcanism on Mercury: Evidence from the First MESSENGER Flyby. *Science*, 321:69–, July 2008.
- [65] J. Hevelius. *Mercurius in sole visus*. [Gdansk]: auctoris typis et sumptibus, imprimebat Simon Reiniger, 1662.
- [66] R. Hobson. *The exact transmission of texts in the first millennium BCE - an examination of the cuneiform evidence from Mesopotamia and the Torah scrolls from the western shore of the Dead Sea*. PhD thesis, University of Sydney, Department of Hebrew, Biblical and Jewish Studies, 2009.
- [67] R. R. Hodges. Methods for Monte Carlo simulation of the exospheres of the moon and Mercury. *Journal of Geophys. Research*, 85:164–170, January 1980.
- [68] R. R. Hodges, J. H. Hoffman, and F. S. Johnson. The lunar atmosphere. *Icarus*, 21:415–426, April 1974.
- [69] R. R. Hodges, Jr. Response of lunar atmosphere to volcanic gas releases. *Planet. Space Sci.*, 20:1849, November 1972.
- [70] R. R. Hodges, Jr. Helium and hydrogen in the lunar atmosphere. *Journal of Geophys. Research*, 78:8055–8064, 1973.

BIBLIOGRAPHY

- [71] R. R. Hodges, Jr., J. H. Hoffman, F. S. Johnson, and D. E. Evans. Composition and Dynamics of Lunar Atmosphere. In *Lunar and Planetary Institute Science Conference Abstracts*, volume 4 of *Lunar and Planetary Institute Science Conference Abstracts*, page 374, March 1973.
- [72] R. R. Hodges, Jr. and F. S. Johnson. Lateral Transport in Planetary Exospheres. *Journal of Geophys. Research*, 73:7307–7317, 1968.
- [73] L. Holmlid. The alkali metal atmospheres on the Moon and Mercury: Explaining the stable exospheres by heavy Rydberg Matter clusters. *Planet. Space Sci.*, 54:101–112, January 2006.
- [74] W. E. Howard, III, A. H. Barrett, and F. T. Haddock. Measurement of Microwave Radiation from the Planet Mercury. *Astro. Phys. Journal*, 136:995, November 1962.
- [75] W. F. Huebner, J. J. Keady, and S. P. Lyon. Solar photo rates for planetary atmospheres and atmospheric pollutants. *Astrophysics and Space Science*, 195:1–289, September 1992.
- [76] T.E. Huff. *The Rise of Early Modern Science: Islam, China, and the West*. Cambridge, 1993.
- [77] D. M. Hunten, D. E. Shemansky, and T. H. Morgan. *The Mercury atmosphere*, pages 562–612. 1988.
- [78] D. M. Hunten and A. L. Sprague. Origin and character of the lunar and Mercurian atmospheres. *Advances in Space Research*, 19:1551, May 1997.
- [79] D. M. Hunten and A. L. Sprague. Diurnal variation of Na and K at Mercury. *Meteoritics and Planetary Science*, 37:1191–1195, September 2002.
- [80] D.M. Hunten, F.E. Roach, and J.W. Chamberlain. A photometric unit for the airglow and aurora. *Journal of Atmos. and Terrest. Physics*, 8(6):345 – 346, 1956.
- [81] W.-H. Ip. The sodium exosphere and magnetosphere of Mercury. *Geophys. Research Letters*, 13:423–426, May 1986.
- [82] W.-H. Ip. On solar radiation-driven surface transport of sodium atoms at Mercury. *Astro. Phys. Journal*, 356:675–681, June 1990.
- [83] J. H. Jeans. Highly-penetrating Radiation and Cosmical Physics. *Nature*, 116:861, December 1925.
- [84] R. E. Johnson. Plasma-Induced Sputtering of an Atmosphere. *Space Sci. Reviews*, 69:215–253, August 1994.
- [85] G. H. Jones, E. Roussos, N. Krupp, U. Beckmann, A. J. Coates, F. Crary, I. Dandouras, V. Dikarev, M. K. Dougherty, P. Garnier, C. J. Hansen, A. R. Hendrix, G. B. Hospodarsky, R. E. Johnson, S. Kempf, K. K. Khurana, S. M. Krimigis, H. Krüger, W. S. Kurth, A. Lagg, H. J. McAndrews, D. G. Mitchell, C. Paranicas, F. Postberg, C. T. Russell, J. Saur, M. Seiß, F. Spahn, R. Srama, D. F. Strobel, R. Tokar, J.-E. Wahlund, R. J. Wilson, J. Woch, and D. Young. The Dust Halo of Saturn’s Largest Icy Moon, Rhea. *Science*, 319:1380–, March 2008.
- [86] E. Kallio and P. Janhunen. Modelling the solar wind interaction with Mercury by a quasi-neutral hybrid model. *Annales Geophysicae*, 21:2133–2145, November 2003.
- [87] K. I. Kellermann. The Thermal Radio Emission from Mercury, Venus, Mars, Saturn and Uranus. *Icarus*, 5:478, 1966.
- [88] R. Killen, G. Cremonese, H. Lammer, S. Orsini, A. E. Potter, A. L. Sprague, P. Wurz, M. L. Khodachenko, H. I. M. Lichtenegger, A. Milillo, and A. Mura. Processes that Promote and Deplete the Exosphere of Mercury. *Space Sci. Reviews*, 132:433–509, October 2007.

-
- [89] R. Killen, D. Shemansky, and N. Mouawad. Erratum: "Expected Emission from Mercury's Exospheric Species, and Their Ultraviolet-Visible Signatures". *Astro. phys. Journal Suppl. Series*, 182:667, June 2009.
- [90] R. Killen, D. Shemansky, and N. Mouawad. Expected Emission from Mercury's Exospheric Species, and their Ultraviolet-Visible Signatures. *Astro. phys. Journal Suppl. Series*, 181:351–359, April 2009.
- [91] R. Killen, R. Vervack, N. Mouawad, and D. Crider. Monte Carlo Model of Mercury's Sodium Exosphere. In *37th COSPAR Scientific Assembly*, volume 37 of *COSPAR, Plenary Meeting*, page 1511, 2008.
- [92] R. M. Killen and W.-H. Ip. The surface-bounded atmospheres of Mercury and the Moon. *Reviews of Geophysics*, 37:361–406, 1999.
- [93] R. M. Killen, A. Potter, A. Fitzsimmons, and T. H. Morgan. Sodium D2 line profiles: clues to the temperature structure of Mercury's exosphere. *Planet. Space Sci.*, 47:1449–1458, December 1999.
- [94] R. M. Killen, A. E. Potter, D. M. Hurley, C. Plymate, and S. Naidu. Observations of the LCROSS Impact Event from the McMath-Pierce Solar Telescope: Sodium and Dust. In *Lunar and Planetary Institute Science Conference Abstracts*, volume 41 of *Lunar and Planetary Institute Science Conference Abstracts*, page 2333, March 2010.
- [95] R. M. Killen, A. E. Potter, P. Reiff, M. Sarantos, B. V. Jackson, P. Hick, and B. Giles. Evidence for space weather at Mercury. *Journal of Geophys. Research*, 106:20509–20526, September 2001.
- [96] R. M. Killen, M. Sarantos, A. E. Potter, and P. Reiff. Source rates and ion recycling rates for Na and K in Mercury's atmosphere. *Icarus*, 171:1–19, September 2004.
- [97] J. Kim, A. F. Nagy, J. L. Fox, and T. E. Cravens. Solar cycle variability of hot oxygen atoms at Mars. *Journal of Geophys. Research*, 103:29339–29342, December 1998.
- [98] J. F. Kordas, I. T. Lewis, B. A. Wilson, D. P. Nielsen, H.-S. Park, R. E. Priest, R. F. Hills, M. J. Shannon, A. G. Ledebuhr, and L. D. Pleasance. Star tracker stellar compass for the Clementine mission. In W. J. Fowski and M. M. Birnbaum, editor, *Society of Photo-Optical Instrumentation Engineers (SPIE) Conference Series*, volume 2466 of *Society of Photo-Optical Instrumentation Engineers (SPIE) Conference Series*, pages 70–83, June 1995.
- [99] N. A. Kozyrev. The Atmosphere of Mercury. *Sky and Telescope*, 27:339, June 1964.
- [100] S. Kumar. Mercury's atmosphere - A perspective after Mariner 10. *Icarus*, 28:579–591, August 1976.
- [101] S. Kumar, D. M. Hunten, and A. L. Broadfoot. Non-thermal hydrogen in the Venus exosphere - The ionospheric source and the hydrogen budget. *Planet. Space Sci.*, 26:1063–1075, November 1978.
- [102] J. A. Kunc and D. E. Shemansky. The interaction of helium with α -quartz. *Journal of Chem. Physics*, 75:2406–2411, September 1981.
- [103] H. Lammer, P. Wurz, M. R. Patel, R. Killen, C. Kolb, S. Massetti, S. Orsini, and A. Milillo. The variability of Mercury's exosphere by particle and radiation induced surface release processes. *Icarus*, 166:238–247, December 2003.
- [104] U. J. Le Verrier. Theorie DU mouvement de Mercure. *Annales de l'Observatoire de Paris*, 5:1, 1859.
- [105] F. Leblanc, E. Chassefière, R. E. Johnson, D. M. Hunten, E. Kallio, D. C. Delcourt, R. M. Killen, J. G. Luhmann, A. E. Potter, A. Jambon, G. Cremonese, M. Mendillo, N. Yan, and A. L. Sprague. Mercury's exosphere origins and relations to its magnetosphere and surface. *Planet. Space Sci.*, 55:1069–1092, June 2007.

BIBLIOGRAPHY

- [106] F. Leblanc, J. Y. Chaufray, and J. L. Bertaux. On Martian nitrogen dayglow emission observed by SPICAM UV spectrograph/Mars Express. *Geophys. Research Letters*, 34:L02206, January 2007.
- [107] F. Leblanc, J. Y. Chaufray, J. Lilensten, O. Witasse, and J.-L. Bertaux. Martian dayglow as seen by the SPICAM UV spectrograph on Mars Express. *Journal of Geophys. Research (Planets)*, 111:E09S11, August 2006.
- [108] F. Leblanc, D. Delcourt, H. Lammer, K. Torkar, Berthelier J.-J., Vaisberg O., and Woch J. Ion of planetary origins at Mercury: some estimates. In *Notes du Pole de Planétologie de l'IPSL, l'Institut Pierre-Simon Laplace, 2004*, Notes du Pole de Planétologie de l'IPSL, 2004.
- [109] F. Leblanc and A. Doressoundiram. Mercury exosphere. II. The sodium/potassium ratio. *Icarus*, 211:10–20, January 2011.
- [110] F. Leblanc, A. Doressoundiram, N. Schneider, V. Mangano, A. López Ariste, C. Lemen, B. Gelly, C. Barbieri, and G. Cremonese. High latitude peaks in Mercury's sodium exosphere: Spectral signature using THEMIS solar telescope. *Geophys. Research Letters*, 35:L18204, September 2008.
- [111] F. Leblanc, A. Doressoundiram, N. Schneider, S. Massetti, M. Wedlund, A. López Ariste, C. Barbieri, V. Mangano, and G. Cremonese. Short-term variations of Mercury's Na exosphere observed with very high spectral resolution. *Geophys. Research Letters*, 36:L07201, April 2009.
- [112] F. Leblanc and R. E. Johnson. Mercury's sodium exosphere: new insights. In *AAS/Division for Planetary Sciences Meeting Abstracts #34*, volume 34 of *Bulletin of the American Astronomical Society*, page 847, September 2002.
- [113] F. Leblanc and R. E. Johnson. Mercury's sodium exosphere. *Icarus*, 164:261–281, August 2003.
- [114] F. Leblanc and R. E. Johnson. Mercury exosphere I. Global circulation model of its sodium component. *Icarus*, 209:280–300, October 2010.
- [115] F. Leblanc, J. G. Luhmann, R. E. Johnson, and M. Liu. Solar energetic particle event at Mercury. *Planet. Space Sci.*, 51:339–352, April 2003.
- [116] F. Leblanc, O. Witasse, J. Lilensten, R. A. Frahm, A. Safaenili, D. A. Brain, J. Mouginot, H. Nilsson, Y. Futaana, J. Halekas, M. Holmström, J. L. Bertaux, J. D. Winningham, W. Kofman, and R. Lundin. Observations of aurorae by SPICAM ultraviolet spectrograph on board Mars Express: Simultaneous ASPERA-3 and MARSIS measurements. *Journal of Geophys. Research (Space Physics)*, 113:A08311, August 2008.
- [117] S. Lebonnois, E. Quémerais, F. Montmessin, F. Lefèvre, S. Perrier, J.-L. Bertaux, and F. Forget. Vertical distribution of ozone on Mars as measured by SPICAM/Mars Express using stellar occultations. *Journal of Geophys. Research (Planets)*, 111:E09S05, September 2006.
- [118] H.-S. Liu and J. A. O'Keefe. Theory of Rotation for the Planet Mercury. *Science*, 150:1717, December 1965.
- [119] A. López Ariste, J. Rayrole, and M. Semel. First results from THEMIS spectropolarimetric mode. *Astro. and Astrophysics*, 142:137–148, February 2000.
- [120] Lyot. La couronne solaire étudiée en dehors des éclipses. *Bulletin Astronomique*, 6:305–316, 1930.
- [121] G. Marsaglia and W. W. Tsang. The ziggurat method for generating random variables. *J. Statis. Softw.*, 5(8):1–7, 2000.
- [122] S. Massetti, S. Orsini, A. Milillo, and A. Mura. Modelling Mercury's magnetosphere and plasma entry through the dayside magnetopause. *Planet. Space Sci.*, 55:1557–1568, September 2007.

-
- [123] W. E. McClintock, R. J. Vervack, E. T. Bradley, R. M. Killen, N. Mouawad, A. L. Sprague, M. H. Burger, S. C. Solomon, and N. R. Izenberg. Messenger observations of mercury's exosphere: Detection of magnesium and distribution of constituents. *Science*, 324(5927):610–613, 2009.
- [124] H. McEwen. La planète Mercure et la rotation des satellites: étude basée sur les résultats obtenus avec la grande lunette de l'Observatoire de Meudon. *Nature*, 135:85–86, January 1935.
- [125] M. A. McGrath and R. E. Johnson. Magnetospheric plasma sputtering of Io's atmosphere. *Icarus*, 69:519–531, March 1987.
- [126] M. Michael and R. E. Johnson. Energy deposition of pickup ions and heating of Titan's atmosphere. *Planet. Space Sci.*, 53:1510–1514, December 2005.
- [127] A. Milillo, P. Wurz, S. Orsini, D. Delcourt, E. Kallio, R. M. Killen, H. Lammer, S. Massetti, A. Mura, S. Barabash, G. Cremonese, I. A. Daglis, E. Angelis, A. M. Lellis, S. Livi, V. Mangano, and K. Torkar. Surface-Exosphere-Magnetosphere System Of Mercury. *Space Sci. Reviews*, 117:397–443, April 2005.
- [128] F. Montmessin, E. Quémerais, J. L. Bertaux, O. Korablev, P. Rannou, and S. Lebonnois. Stellar occultations at UV wavelengths by the SPICAM instrument: Retrieval and analysis of Martian haze profiles. *Journal of Geophys. Research (Planets)*, 111:E09S09, September 2006.
- [129] V. I. Moroz. Infrared Spectrum of Mercury ($\lambda=1.0\text{-}3.9\mu$). *Soviet Astronomy*, 8:882, June 1965.
- [130] A. Mura, A. Milillo, S. Orsini, and S. Massetti. Numerical and analytical model of Mercury's exosphere: Dependence on surface and external conditions. *Planet. Space Sci.*, 55:1569–1583, September 2007.
- [131] A. Mura, P. Wurz, H. I. M. Lichtenegger, H. Schleicher, H. Lammer, D. Delcourt, A. Milillo, S. Orsini, S. Massetti, and M. L. Khodachenko. The sodium exosphere of Mercury: Comparison between observations during Mercury's transit and model results. *Icarus*, 200:1–11, March 2009.
- [132] S. L. Murchie, T. R. Watters, M. S. Robinson, J. W. Head, R. G. Strom, C. R. Chapman, S. C. Solomon, W. E. McClintock, L. M. Prockter, D. L. Domingue, and D. T. Blewett. Geology of the Caloris Basin, Mercury: A View from MESSENGER. *Science*, 321:73–, July 2008.
- [133] A. F. Nagy and P. M. Banks. Diurnal variation of the H+ flux between the ionosphere and the plasmasphere. *Journal of Geophys. Research*, 77:4277–4279, 1972.
- [134] A. F. Nagy, J. Kim, and T. E. Cravens. Hot hydrogen and oxygen atoms in the upper atmospheres of Venus and Mars. *Annales Geophysicae*, 8:251–256, April 1990.
- [135] S. Orsini, L. G. Blomberg, D. Delcourt, R. Grard, S. Massetti, K. Seki, and J. Slavin. Magnetosphere-Exosphere-Surface Coupling at Mercury. *Space Sci. Reviews*, 132:551–573, October 2007.
- [136] G. H. Pettengill and R. B. Dyce. A Radar Determination of the Rotation of the Planet Mercury. *Nature*, 206:1240, June 1965.
- [137] R. F. Poppen, U. Fink, and H. P. Larson. A New Upper Limit for an Atmosphere of CO₂ on Mercury. In *Bulletin of the American Astronomical Society*, volume 5 of *Bulletin of the American Astronomical Society*, page 302, March 1973.
- [138] A. Potter and T. Morgan. Discovery of sodium in the atmosphere of Mercury. *Science*, 229:651–653, August 1985.
- [139] A. E. Potter. Chemical sputtering could produce sodium vapor and ice on Mercury. *Geophys. Research Letters*, 22:3289–3292, December 1995.

BIBLIOGRAPHY

- [140] A. E. Potter, C. M. Anderson, R. M. Killen, and T. H. Morgan. Ratio of sodium to potassium in the Mercury exosphere. *Journal of Geophys. Research (Planets)*, 107:5040, June 2002.
- [141] A. E. Potter and R. M. Killen. Observations of the sodium tail of Mercury. *Icarus*, 194:1–12, March 2008.
- [142] A. E. Potter, R. M. Killen, and T. H. Morgan. Solar radiation acceleration effects on Mercury sodium emission. *Icarus*, 186:571–580, February 2007.
- [143] A. E. Potter, R. M. Killen, and M. Sarantos. Spatial distribution of sodium on Mercury. *Icarus*, 181:1–12, March 2006.
- [144] A. E. Potter and T. H. Morgan. Potassium in the atmosphere of Mercury. *Icarus*, 67:336–340, August 1986.
- [145] A. E. Potter and T. H. Morgan. Variation of sodium on Mercury with solar radiation pressure. *Icarus*, 71:472–477, September 1987.
- [146] A. E. Potter and T. H. Morgan. Evidence for suprathreshold sodium on Mercury. *Advances in Space Research*, 19:1571, May 1997.
- [147] L. M. Prockter, C. M. Ernst, B. W. Denevi, C. R. Chapman, J. W. Head, C. I. Fassett, W. J. Merline, S. C. Solomon, T. R. Watters, R. G. Strom, G. Cremonese, S. Marchi, and M. Massironi. Evidence for Young Volcanism on Mercury from the Third MESSENGER Flyby. *Science*, 329:668–, August 2010.
- [148] E. Quémerais, J.-L. Bertaux, O. Korabely, E. Dimarellis, C. Cot, B. R. Sandel, and D. Fussen. Stellar occultations observed by SPICAM on Mars Express. *Journal of Geophys. Research (Planets)*, 111:E09S04, September 2006.
- [149] J. A. Quessette. Atomic Hydrogen Densities at the Exobase. *Journal of Geophys. Research*, 77:2997–3000, 1972.
- [150] J. K. Roberts. The Exchange of Energy between Gas Atoms and Solid Surfaces. *Royal Society of London Proceedings Series A*, 129:146–161, September 1930.
- [151] J. K. Roberts. The Exchange of Energy between Gas Atoms and Solid Surfaces. II. The Temperature Variation of the Accommodation Coefficient of Helium. *Royal Society of London Proceedings Series A*, 135:192–205, February 1932.
- [152] Y. Saito, S. Yokota, T. Tanaka, K. Asamura, M. N. Nishino, M. Fujimoto, H. Tsunakawa, H. Shibuya, M. Matsushima, H. Shimizu, F. Takahashi, T. Mukai, and T. Terasawa. Solar wind proton reflection at the lunar surface: Low energy ion measurement by MAP-PACE onboard SELENE (KAGUYA). *Geophys. Research Letters*, 35:L24205, December 2008.
- [153] G. Saliva. Theory and Observation in Islamic Astronomy - the Work of Ibn-Al of Damascus. *Journal for the History of Astronomy*, 18:35, February 1987.
- [154] B. R. Sandel and A. L. Broadfoot. Statistical performance of the intensified charged coupled device. *Appl. Optics*, 25:4135–4140, November 1986.
- [155] G. V. Schiaparelli. Sulla rotazione di Mercurio. *Astronomische Nachrichten*, 123:241, December 1889.
- [156] J.H. Schröter. *Hermographische Fragmente zur genaueren Kenntnis des Planeten Merkur*. Göttingen, 1800.
- [157] A. Settaouti and L. Settaouti. Simulation of the transport of sputtered atoms and effects of processing conditions. *Applied Surface Science*, 254:5750–5756, July 2008.
- [158] D. E. Shemansky and A. L. Broadfoot. Interaction of the surfaces of the moon and Mercury with their exospheric atmospheres. *Reviews of Geophysics and Space Physics*, 15:491–499, November 1977.

-
- [159] E. M. Sieveka and R. E. Johnson. Ejection of atoms and molecules from Io by plasma-ion impact. *Astro. Phys. Journal*, 287:418–426, December 1984.
- [160] C. Simon, O. Witasse, F. Leblanc, G. Gronoff, and J.-L. Bertaux. Dayglow on Mars: Kinetic modelling with SPICAM UV limb data. *Planet. Space Sci.*, 57:1008–1021, July 2009.
- [161] J. A. Slavin, M. H. Acuna, B. J. Anderson, D. N. Baker, M. Benna, S. A. Boardsen, G. Gloeckler, R. E. Gold, G. C. Ho, H. Korth, S. M. Krimigis, R. L. McNutt, J. M. Raines, M. Sarantos, D. Schriver, S. C. Solomon, P. Trávníček, and T. H. Zurbuchen. MESSENGER Observations of Magnetic Reconnection in Mercury’s Magnetosphere. *Science*, 324:606–, May 2009.
- [162] J. A. Slavin, M. H. Acuna, B. J. Anderson, D. N. Baker, M. Benna, G. Gloeckler, R. E. Gold, G. C. Ho, R. M. Killen, H. Korth, S. M. Krimigis, R. L. McNutt, L. R. Nittler, J. M. Raines, D. Schriver, S. C. Solomon, R. D. Starr, P. Trávníček, and T. H. Zurbuchen. Mercury’s Magnetosphere After MESSENGER’s First Flyby. *Science*, 321:85–, July 2008.
- [163] J. A. Slavin, B. J. Anderson, D. N. Baker, M. Benna, S. A. Boardsen, G. Gloeckler, R. E. Gold, G. C. Ho, H. Korth, S. M. Krimigis, R. L. McNutt, L. R. Nittler, J. M. Raines, M. Sarantos, D. Schriver, S. C. Solomon, R. D. Starr, P. M. Trávníček, and T. H. Zurbuchen. MESSENGER Observations of Extreme Loading and Unloading of Mercury’s Magnetic Tail. *Science*, 329:665–, August 2010.
- [164] J. A. Slavin, B. J. Anderson, T. H. Zurbuchen, D. N. Baker, S. M. Krimigis, M. H. Acuna, M. Benna, S. A. Boardsen, G. Gloeckler, R. E. Gold, G. C. Ho, H. Korth, R. L. McNutt, J. M. Raines, M. Sarantos, D. Schriver, S. C. Solomon, and P. Trávníček. MESSENGER observations of Mercury’s magnetosphere during northward IMF. *Geophys. Research Letters*, 36:L02101, January 2009.
- [165] G. R. Smith, D. E. Shemansky, A. L. Broadfoot, and L. Wallace. Monte Carlo modeling of exospheric bodies - Mercury. *Journal of Geophys. Research*, 83:3783–3790, August 1978.
- [166] W. H. Smyth. Io’s sodium cloud - Explanation of the east-west asymmetries. *Astro. Phys. Journal*, 234:1148–1153, December 1979.
- [167] W. H. Smyth. Nature and variability of Mercury’s sodium atmosphere. *Nature*, 323:696–699, October 1986.
- [168] W. H. Smyth and M. L. Marconi. Theoretical overview and modeling of the sodium and potassium atmospheres of mercury. *Astro. Phys. Journal*, 441:839–864, March 1995.
- [169] S. C. Solomon, R. L. McNutt, T. R. Watters, D. J. Lawrence, W. C. Feldman, J. W. Head, S. M. Krimigis, S. L. Murchie, R. J. Phillips, J. A. Slavin, and M. T. Zuber. Return to Mercury: A Global Perspective on MESSENGER’s First Mercury Flyby. *Science*, 321:59–, July 2008.
- [170] H. Spinrad, G. B. Field, and P. W. Hodge. Spectroscopic Observations of Mercury. *Astro. Phys. Journal*, 141:1155, April 1965.
- [171] A. L. Sprague, D. M. Hunten, and F. A. Grosse. Upper Limit for Lithium in Mercury’s Atmosphere. *Icarus*, 123:345–349, October 1996.
- [172] A. L. Sprague, R. W. H. Kozlowski, D. M. Hunten, N. M. Schneider, D. L. Domingue, W. K. Wells, W. Schmitt, and U. Fink. Distribution and Abundance of Sodium in Mercury’s Atmosphere, 1985-1988. *Icarus*, 129:506–527, October 1997.
- [173] S. A. Stern. The Lunar Atmosphere and Its Intimate Connection to the Lunar Surface: A Review. In *Workshop on New Views of the Moon II: Understanding the Moon Through the Integration of Diverse Datasets*, page 8012, September 1999.

BIBLIOGRAPHY

- [174] B. P. Stoicheff. On the dissociation energy of molecular hydrogen. *Canadian Journal of Physics*, 79:165–172, February 2001.
- [175] R. G. Strom, C. R. Chapman, W. J. Merline, S. C. Solomon, and J. W. Head. Mercury Cratering Record Viewed from MESSENGER's First Flyby. *Science*, 321:79–, July 2008.
- [176] R. G. Strom and A. L. Sprague. *Exploring Mercury. The iron planet*. 2003.
- [177] D. Tedlock. *Popol Vuh: The definitive edition of the Mayan book of the dawn of life and the glories of gods and kings*. Touchstone; Original edition 1985, Re-ed. 1996.
- [178] G. E. Thomas. Mercury: Does Its Atmosphere Contain Water? *Science*, 183:1197–1198, March 1974.
- [179] L. Trilling. The interaction of monatomic inert gas molecules with a continuous elastic solid. *Surface Science*, 21:337–365, July 1970.
- [180] R. J. Vervack, W. E. McClintock, R. M. Killen, A. L. Sprague, B. J. Anderson, M. H. Burger, E. T. Bradley, N. Mouawad, S. C. Solomon, and N. R. Izenberg. Mercury's Complex Exosphere: Results from MESSENGER's Third Flyby. *Science*, 329:672–, August 2010.
- [181] M. Wieser, S. Barabash, Y. Futaana, M. Holmström, A. Bhardwaj, R. Sridharan, M. B. Dhanya, P. Wurz, A. Schaufelberger, and K. Asamura. Extremely high reflection of solar wind protons as neutral hydrogen atoms from regolith in space. *Planet. Space Sci.*, 57:2132–2134, December 2009.
- [182] P. Wurz and H. Lammer. Monte-Carlo simulation of Mercury's exosphere. *Icarus*, 164:1–13, July 2003.
- [183] B. V. Yakshinskiy and T. E. Madey. Photon-stimulated desorption as a substantial source of sodium in the lunar atmosphere. *Nature*, 400:642–644, August 1999.
- [184] L. Zelenyi, M. Oka, H. Malova, M. Fujimoto, D. Delcourt, and W. Baumjohann. Particle Acceleration in Mercury's Magnetosphere. *Space Sci. Reviews*, 132:593–609, October 2007.